POLITECNICO DI TORINO
Repository ISTITUZIONALE

Temperature dependence of material behaviour at high strain-rate Proceedings of 24th DYMAT Technical Meeting 9-11 September 2019, Stresa (Italy)

Original
Temperature dependence of material behaviour at high strain-rate Proceedings of 24th DYMAT Technical Meeting 9-11 September 2019, Stresa (Italy) / Scapin, Martina; Peroni, Lorenzo. - ELETTRONICO. - (2019), pp. 1-160.

Availability:
This version is available at: 11583/2768212 since: 2019-11-20T11:00:45Z

Publisher:
Politecnico di Torino

Published
DOI:

Terms of use:
openAccess

This article is made available under terms and conditions as specified in the corresponding bibliographic description in the repository

Publisher copyright

(Article begins on next page)

04 August 2020

Proceedings of 24th DYMAT Technical Meeting

Temperature dependence of material behaviour at high strain-rate

9-11 September 2019, Stresa, Italy

ISBN 978-88-85745-27-8

Scientific Committee

Pr. N. Bahlouli, University of Strasbourg, France
Dr. E. Buzaud, CEA, Gramat, France
Pr. E. Cadoni, University if Applied Sciences and Arts of Southern Switzerland, Switzerland
Dr. A. Cosculluela ,CEA, Bordeaux, France
H.D.R. H. Couque, Nexter Munitions, Bourges, France
Pr. P. Forquin, Université Joseph Fourier, France
Pr. F. Galvez, Universidad Politecnica de Madrid, Spain
Dr. S. Guerard, Ecole Nationale Supérieure d'Arts et Métiers, France
Pr. S. Hiermaier, Fraunhofer Institute for High-Speed Dynamics, Ernst-Mach-Institut, Germany
Pr. M. Hokka, Tampere University of Technology, Finland.
Pr. L. Kruszka, The Jaroslaw Dabrowski Military University of Technology, Poland
Pr. M. Langseth, Norwegian University of Science and Technology, Norway
Pr. E. Markiewicz, Université de Valenciennes, France
Pr. L. Peroni, Politecnico di Torino, Torino, Italy
Pr. P. Verleysen, Ghent University, Belgium
Dr. S. M. Walley, University of Cambridge, United Kingdom

Organizing Committee

Pr. L. Peroni, Politecnico di Torino, Torino, Italy
Dr. M. Scapin, Politecnico di Torino, Torino, Italy
Pr. E. Cadoni, University of Applied Sciences and Arts of Southern Switzerland, Switzerland
Dr. D. Forni, University of Applied Sciences and Arts of Southern Switzerland, Switzerland

Contacts

Prof. Lorenzo Peroni
lorenzo.peroni@polito.it
Phone: +39 011 0903540

Dr. Martina Scapin
martina.scapin@polito.it
Phone: +39 011 0903543

Department of Mechanical and Aerospace Engineering
Corso Duca degli Abruzzi 24, 10129 Turin, Italy

Sponsors

FLIR SYSTEMS™

THE GLOBAL LEADER IN INFRARED CAMERAS

iX Cameras

Photron

SHIMADZU

Excellence in Science

HADLAND® IMAGING

CAMERAS • SYSTEMS • ACCESSORIES

MatchID

Metrology beyond colors

H.-D. RUDOLPH GmbH

optische Messgeräte

Preface

In recent years, interest in material characterization at high strain-rates while varying the temperature has been continuously increasing. Consequently, the study and modelling of material behavior in such conditions has been promoted. In many applications such as machining, metal forming, high velocity impact or high energy deposition of metals, materials are deformed at very high rates. This produces self-heating to high temperatures due to adiabatic processes. In this case, the stress-strain response will be a balance between the effects of hardening (due to strain and strain-rate) and thermal softening. In other cases, the working temperature may be different to room temperature. Hence both the mechanical response of the material and the effect of strain-rate should be investigated in the domain of interest. At high temperature, materials generally become much more ductile and can also exhibit microstructural changes due to recrystallization phenomena. By contrast, at low temperatures the material strength usually increases and the mechanical behavior changes from ductile to brittle.

From these considerations, it appears evident that temperature and strain-rate are variables of fundamental importance in the prediction of the mechanical response of materials, playing an important role in many deformation processes. Hence, it is clear there is a need to define proper material models which could be implemented in numerical Finite Element simulations from which it should be possible to predict and estimate the responses of structures, components and materials under different loading conditions and scenarios. Of course, the development of methodologies and facilities for the complete investigation of the mechanical response of materials in the whole temperature and strain-rate field of interest is required and has to be addressed, by also taking into account the fact that temperature and strain-rate are mutually related. This means that the thermal effects obtained from quasi-static tests cannot always be used to predict material response under dynamic loading conditions. Moreover, this reveals that in order to consider the coupled effects of temperature and strain-rate, material models should be used in which the thermal component of stress is also considered.

Lorenzo Peroni, Martina Scapin

POLITECNICO
DI TORINO

European association for the promotion of research into the dynamic behavior of materials and its applications

President:	Eric Buzaud	*France*
Vice-President:	Francisco Galvez	*Spain*
Treasurer:	Antonio Cosculluela	*France*
Secretary:	Stephen M. Walley	*United Kingdom*
Vice-Secretary:	Nadia Bahlouli	*France*
Vice-Treasurer:	Sandra Guerard	*France*
Vice-President Web:	Stefan Hiermaier	*Germany*
Vice-President Edition:	Hervé Couque	*France*
Vice-President International Affairs:	Ezio Cadoni	*Italy*

Journal of Dynamic Behavior of Materials

Editor-in-Chief: ERIC N. **BROWN**

ISSN: 2199-7446 (Print) 2199-7454 (Online)

Description

Profiles international developments in the study of dynamic behavior of materials.

Covers the science and engineering of material and structural response to dynamic loading focused on high strain-rate, impact, blast, penetration, shock response, and extreme conditions.

Includes new results on material response and development of techniques, methods, and diagnostics for the study of materials in the dynamic regime

Journal of the Dynamic Behavior of Materials is a peer reviewed archival journal on the science and engineering of material and structural response to dynamic loading focused on high strain-rate, impact, blast, penetration, and shock response. The journal publishes experimental, theoretical, modeling and simulation, and interdisciplinary work focused both on advancement of new techniques and application of techniques to new materials and structures. Experimental techniques will include, but not be limited to, small-scale tests for constitutive response of material such as Split Hopkinson Pressure Bar, Kolsky Pressure Bar, gas-gun and powder-gun driven plate impact, direct and flier plate drive high-explosive experiments, direct and flier plate drive laser experiments, and drop tower; small-scale integrated tests for validation of material constitutive models such as Taylor Anvil, Dynamic-Tensile-Extrusion, high-explosive driven perturbed plate experiments, shock tube loading; and integrated structure level experiments as blast, impact, crash, and penetration mechanics. The journal also covers diagnostics for dynamics experiments to include but not be limited to high-speed photography, dynamic radiography, velocimetry (PDV, mPDV, VISAR, lineVISAR, etc), gages, pins, etc. Hybrid experimental-computational papers are also encouraged. In addition to primary research articles, The Journal of Dynamic Behavior of Materials publishes review articles, brief technical notes, and applications articles that discuss important emerging technologies.

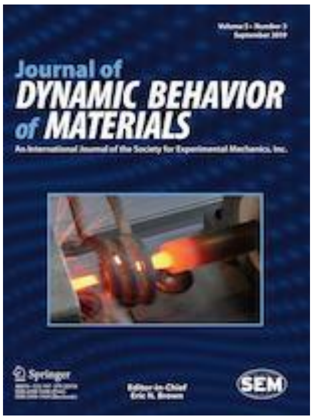

Special Issue on: "Temperature dependence of material behaviour at high strain-rate"

Editors:

M. Scapin, P. Verleysen, M. Hokka, N. Bahlouli

Contents

M. Scapin, L. Peroni, C. Torregrosa, A. Perillo-Marcone, M. Calviani	Effects of strain rate and temperature on the mechanical response of pure tungsten	**DYMAT2019_SI01**
R. S. Potter, J. M. Cammack, C. H. Braithwaite, P. D. Church, S. M. Walley	Problems associated with making mechanical measurements on water-ice at quasistatic and dynamic strain rates	**DYMAT2019_SI02**
M. J. Perez-Martin, J. K. Holmen, S. Thomesen, O. S. Hopperstad, T. Børvik	Dynamic behaviour of a high-strength structural steel at low temperatures	**DYMAT2019_SI03**
E. Cadoni, D. Forni	Austenitic stainless steel under extreme combined conditions of loading and temperature	**DYMAT2019_SI04**
N. I. Vazquez-Fernandez, G. Correa Soares, J. L. Smith, J. D. Seidt, M. Isakov, A. Gilat, V.T. Kuokkala, M. Hokka	Adiabatic heating of austenitic stainless steels at different strain rates	**DYMAT2019_SI05**
B. Song, B. Sanborn	A Modified Johnson-Cook Model for Dynamic Response of Metals with an Explicit Strain- and Strain-Rate-Dependent Adiabatic Thermosoftening Effect	**DYMAT2019_SI06**
M. Peroni, G. Solomos	Advanced experimental data processing for the identification of thermal and strain-rate sensitivity of a nuclear steel	**DYMAT2019_SI07**
M. Pasquali, A. Bertarelli, C. Accettura, E. Berthome, L. Bianchi, P. Bolz, F. Carra, C. Fichera, M. I. Frankl, T. Furness, G. Gobbi, P. Grosclaude, J. Guardia-Valenzuela, M. Guinchard, M. D. Jedrychowsky, F. J. Harden, A. Lechner, P. Mollicone, P. D. Pastuszak, M. Portelli, S. Redaelli, E. Rigutto, O. Sacristan de Frutos, P. Simon	Dynamic response of advanced materials exposed to high-energy particle beam impacts	**DYMAT2019_SI08**
A. Bragov, L. Igumnov, A. Konstantinov, A. Lomunov, E. Rusin	Effects of high strain rate and self-heating on plastic deformation of metal materials under fast compression loading	**DYMAT2019_SI09**
G. C. Ganzenmüller, S. Patil, M. Maurer, M. Sauer, M. Jung, S. Hiermaier	The Freiburg Glassy Polymer Model	**DYMAT2019_SI10**
G. Correa Soares, M. Patnamsetty, P. Peura, M. Hokka	Effects of Adiabatic Heating and Strain Rate on the Dynamic Response of a CoCrFeMnNi High-Entropy Alloy	**DYMAT2019_SI11**

T. Tancogne-Dejean, X. Li, M. Diamantopoulou, C. C. Roth, D. Mohr	High Strain Rate Response of Additively-Manufactured Plate-Lattices: Experiments and Modeling	**DYMAT2019_SI12**
E. Farotti, E. Mancini, T. Bellezze, M. Sasso	Investigation of the effects of mold temperature, test temperature and strain rate on mechanical behavior of a polymer	**DYMAT2019_SI13**
C. Francart, Y. Demarty, N. Bahlouli, S. Ahzi	Constitutive modelling of thermal mechanical inelastic flow behavior of an epoxy resin from low to high strain rates	**DYMAT2019_P01**
V. Kotov, V. V. Balandin, V Vl. Balandin, A. Bragov, A. Lomunov	Numerically analyzing the inverse experiment methodology as applied to the investigation of dynamic penetration into water-saturated soils at negative temperatures	**DYMAT2019_P02**
A. Bragov, V. V. Balandin, V. Vl. Balandin, V. Kotov, S. Litvinchuk	Analyzing resistance to penetration of a conical striker into sand at positive and negative temperatures, based on the results of inverse experiments	**DYMAT2019_P03**
S. Chandran, W. Liu, J. Lian, S. Münstermann, P. Verleysen	Thermal effects on the dynamic damage and fracture of a dual phase automotive steel	**DYMAT2019_P04**
A. Abedini, C. Butcher, M. Worswick	Influence of Strain Rate on Fracture Behaviour of Ultra-High Strength Steel Sheet	**DYMAT2019_P05**
A. Bragov, A. Konstantinov, S. Litvinchuk, A. Lomunov, E. Rusin	The temperature effect of pulse pressing on structure and mechanical properties of compacts	**DYMAT2019_P06**
G. Mirone, R. Barbagallo	Coupling of temperature, strain and strain rate effects on the flow stress of a stainless steel	**DYMAT2019_P07**
P. Longère	Temperature evolution and consequences in adiabatic shear localization onset and development	**DYMAT2019_P08**
T. Holmquist	The thermal softening response of soda-lime glass inferred from plate-impact experiments, ballistic tests, and computational analysis	**DYMAT2019_P09**
T. Fíla, J. Falta, S. Bronder, P. Koudelka, P. Zlámal, M. Adorna, O. Jiroušek, A. Jung	Hybrid Polymer-Nickel Auxetic Structures: Testing Using Open Hopkinson Bar, Digital Image Correlation and High-speed Thermography	**DYMAT2019_P10**
L. Le Barbenchon, P. Viot, J. Girardot, J.-B. Kopp	Behaviour of bio-based cellular materials under severe loadings Effect of temperature and strain rate	**DYMAT2019_P11**
J. L. Smith, J. D. Seidt, A. Gilat, V.-T. Kuokkala	Using Full-Field Strain and Temperature Measurements to Determine the Taylor-Quinney Coefficient in Dynamic Tensile Tests	**DYMAT2019_P12**

P. Koudelka, T. Fila, J. Falta, J. Sleichrt, P. Zlamal, A. Mauko, M. Adorna, M. Neuhauserova, O. Jirousek	Temperature Dependent Compressive Characteristics of Additively Manufactured Stainless-steel Auxetic Lattices at High Strain-rate	**DYMAT2019_P13**
W. Moćko, M. Jabłońska	Viscoplastic response of high manganese steels at a wide range of temperatures	**DYMAT2019_P14**
R. Sancho, F. Gálvez	Analysing and modelling the yield-strength anomaly at high strain-rates	**DYMAT2019_P15**
B. Sanborn, B. Song, D. Susan, K. Johnson, J. Dabling, J. Carroll, A. Brink, S. Grutzik, A. Kustas	Dynamic Temperature-Dependent Tensile Behavior of Soft Ferromagnetic Alloy Fe-Co-2V	**DYMAT2019_P16**
C. Sauer, A. Heine, W. Riedel, N. Hartmann, W. Harwick, S. Kilchert, N. Ledford, M. Sauer	Non-monotonous strain rate dependence of yield stress for tungsten heavy alloy	**DYMAT2019_P17**
G. Haugou, H. Morvan, E. Markiewicz, R. Bertolini, S. Bruschi	Characterisation of material behaviour at low temperatures using Split Hopkinson Pressure Bar for calibrating cryogenic machining numerical simulations	**DYMAT2019_P18**
J. Mespoulet, P.L. Hereil, H. Couque, A. Hocini, P. Langlois, G. Dirras	Investigation of a Severe Plastic Deformation process of structural hardened aluminum grades using a heated direct impact technique to annihilate Adiabatic Shear Bands formation	**DYMAT2019_A01**
L. Farbaniec, D.E. Eakins	Thermomechanical properties of hexagonal close-packed metals under high strain rate loading: a novel approach to diagnostic and full-field measurements of temperature and strain fields	**DYMAT2019_A02**
S. Ulan kyzy, R. Völkl, O. Munz, T. Fischer, U. Glatzel	Dynamic properties of honeycomb liner materials Hastelloy X and Haynes 214	**DYMAT2019_A03**
G. Mohanty, A. Lambai, R. Ramachandramoorthy, J. Michler	Interplay of temperature, strain rate and orientation: Case study on elevated temperature, high strain rate micromechanical tests on fcc metallic systems	**DYMAT2019_A04**
R. Ramachandramoorthy, G. Mohanty, J. Schwiedrzik, D. Frey, J.-M. Breguet, J. Michler	Micromechanical exploration of the combined effects of high strain rate and high temperature: A novel experimental technique	**DYMAT2019_A05**
A. Cohen, A. Yosef-Hai, D. Levi-Hevroni, M. Oblinado, A. Rack	Fast X-ray imaging as a diagnostic tool for high temperature high strain rate loaded materials	**DYMAT2019_A06**
C. C. Roth, T. Fras and D. Mohr	On the impact behavior of aluminum alloy AA7020-T6	**DYMAT2019_A07**
X. Li, C. C. Roth, D. Mohr	Fracture of Dual Phase Steel under Extreme Loading Conditions: Experiments and Simulations	**DYMAT2019_A08**
C. Bernard, K. Ravi, K. Ogawa, O. Lame, J.-Y. Cavaillé	Thermomechanical behavior of UHMWPE during Cold-spray process	**DYMAT2019_A09**

C. Montenegro, J. Osorio, J. Casas, S. Abolghasem	Microstructure prediction in high strain-rate deformation of Al6063-O using artificial neural network and finite element analysis	**DYMAT2019_A10**
K.T. Ramesh	Thermal softening and rate sensitivity of bcc metals: experiments and mechanism-based modeling	**DYMAT2019_A11**
S. Boubanga-Tombet, S. Ravindran, A. Kidane, F. Marcotte	High-Speed Infrared investigations of local heating in a Graphite-Fiber-PDMS Composite material Under dynamic loading	**DYMAT2019_A12**

Effect of strain-rate and temperature on mechanical response of pure tungsten

M. Scapin*, L. Peroni, C. Torregrosa, A. Perillo-Marcone, M. Calviani

Abstract. This paper presents the results obtained from the investigation of the mechanical behaviour of two different batches of pure tungsten specimens. The interest in pure tungsten is due to its special properties, which has led to it finding applications in several fields, including nuclear physics. At this moment, it is used as a core material for fixed particle producing targets in several accelerator facilities around the world and it is a candidate for future ones. In these facilities, tungsten directly interacts with high energy proton beams and, consequently, is subjected to considerable deformation at high strain-rates and temperatures. From these considerations, there comes the need to properly investigate the material response under these extreme conditions. For this purpose, an ad-hoc testing campaign was performed on small dog-bone specimens in tension. The results will be applicable to the ongoing design of CERN's AD-target as well as to other future tungsten targets operating at high power and dynamically loaded in multiple accelerator facilities.

Due to tungsten's high Ductile-to-Brittle Transition temperature, it was not possible to test it at temperatures less than 250 °C. Tests were performed at two different strain-rates (nominal value of 1 s^{-1} and 10^3 s^{-1}) reaching a maximum temperature of 1000 °C. The dynamic tests were performed by using a Hopkinson Bar setup in the direct impact configuration. Both at low and high strain-rates, heating of the specimen was achieved using an induction coil system. A numerical inverse procedure was applied to analyse the experimental data with the aim to obtain the equivalent stress versus effective plastic strain at the different loading conditions to be used for calibration of the strength model and for the evaluation of strain-rate and thermal softening sensitivities of the material.

Published in Journal of Dynamic Behavior of Materials
https://doi.org/10.1007/s40870-019-00221-y

---

* Corresponding author: martina.scapin@polito.it, Department of Mechanical and Aerospace Engineering, Politecnico di Torino

DYMAT2019 SI02

Problems associated with making mechanical measurements on water-ice at quasistatic and dynamic strain rates

R. S. Potter, J. M. Cammack, C. H. Braithwaite, P. D. Church, S. M. Walley*

Abstract. Space penetrators are a potential method of inserting instrumentation onto ice covered bodies in the Solar System. Part of a study to see whether this is feasible involves numerically simulating impact of the penetrator into ice at impact velocities of a few hundred metres per second. In order to do this accurately, it is necessary to have a constitutive model for water ice that is valid at the strain rates and temperatures relevant to impact in the Outer Solar System. This paper reports certain issues and difficulties that arose during a study to obtain this data.

Published in Journal of Dynamic Behavior of Materials
https://doi.org/10.1007/s40870-019-00202-1

---

* Corresponding author: smw14@cam.ac.uk, SMF Fracture and Shock Physics Group, The Cavendish Laboratory

DYMAT2019 SI03

Dynamic Behaviour of a High-Strength Structural Steel at Low Temperatures

M. J. Perez-Martin[*], J. K. Holmen, S. Thomesen, O. S. Hopperstad, T. Børvik

Abstract. The main objective of this experimental study is to determine the effect of low temperatures on the mechanical behaviour of Strenx 960 Plus high-strength structural steel at different strain rates and stress triaxialities. For this purpose, a comprehensive experimental campaign was designed to characterise the material at a wide range of temperatures and loading rates. The stress triaxiality was varied by testing specimens with different geometry. First, to determine the ductile-to-brittle transition temperature, instrumented Charpy V-notch impact tests were carried out at a range of temperatures from + 20 °C down to − 90 °C. The impact energy dropped gradually with decreasing temperature, but a clear transition temperature could not be identified. A fractography study exhibited a clear dimple structure, revealing predominantly ductile fracture at all temperatures. Then, uniaxial tension tests on smooth and pre-notched axisymmetric specimens under both quasi-static and dynamic loading rates were carried out at room temperature and low temperatures. These tests were conducted to characterise the rate-dependence of the stress–strain behaviour and the failure strain. The results revealed that under quasi-static conditions the flow stress increased with decreasing temperature, while the failure strain was nearly independent of the temperature. Dynamic tensile tests using the same specimen geometries were conducted in a split Hopkinson tension bar at + 20 °C and − 40 °C. The material exhibited a positive strain rate sensitivity at all investigated temperatures. This experimental study reveals that the Strenx 960 Plus steel retains its ductility at temperatures as low as − 40 °C. Brittle failure could not be observed even with combined high strain rate, high stress triaxiality and low temperature.

Published in Journal of Dynamic Behavior of Materials
https://doi.org/10.1007/s40870-019-00206-x

---

[*] Corresponding author: mariajesus.perez@ntnu.no, Centre for Advanced Structural Analysis (CASA) / Norwegian University of Science and Technology (NTNU)

Austenitic Stainless Steel Under Extreme Combined Conditions of Loading and Temperature

E. Cadoni[*], D. Forni

Abstract. The use of stainless steel rebars is required when reinforced concrete structures are subjected to harsh environmental conditions during their lifetime. Some special infrastructures in addition to these climatic factors can be also subjected to extreme limit states of loading and temperature as in the case of fire followed by blast. This study deals with the mechanical behaviour of austenitic stainless reinforcing steel at three high strain rates (250, 400 and 800 1/s) combined to elevated temperature ranging from 200 to 1000 °C. Proof and ultimate tensile strengths, ductility parameters, strain rate and temperature effects as well as strain hardening rate have been determined and discussed. The increase of the temperature leads to increased plastic strain rate, increased reduction area and decrease in yield and ultimate tensile strengths. An increase of the ductility parameters is observed in particular after the temperature of 600 °C. Based on these experimental results new reduction factors have been proposed in case of dynamic loading. Finally, material parameters for two constitutive models have been calibrated to provide prevision useful in the design of reinforced concrete structures subjected to combined action of fire and blast.

Published in Journal of Dynamic Behavior of Materials
https://doi.org/10.1007/s40870-019-00205-y

---

[*] Corresponding author: ezio.cadoni@supsi.ch, SUPSI - University of Applied Sciences of Southern Switzerland

Adiabatic Heating of Austenitic Stainless Steels at Different Strain Rates

N. I. Vazquez-Fernandez[*], G. C. Soares, J. L. Smith, J. D. Seidt, M. Isakov, A. Gilat, V.T. Kuokkala, M. Hokka

Abstract. This work focuses on the effect of strain rate on the mechanical response and adiabatic heating of two austenitic stainless steels. Tensile tests were carried out over a wide range of strain rates from quasi-static to dynamic conditions, using a hydraulic load frame and a device that allowed testing at intermediate strain rates. The full-field strains of the deforming specimens were obtained with digital image correlation, while the full field temperatures were measured with infrared thermography. The image acquisition for the strain and temperature images was synchronized to calculate the Taylor–Quinney coefficient (β). The Taylor–Quinney coefficient of both materials is below 0.9 for all the investigated strain rates. The metastable AISI 301 steel undergoes an exothermic phase transformation from austenite to α'-martensite during the deformation, which results in a higher value of β at any given strain, compared to the value obtained for the more stable AISI 316 steel at the same strain rate. For the metastable 301 steel, the value of β with respect to strain depends strongly on the strain rate. At strain rate of 85 s^{-1}, the β factor increases from 0.69 to 0.82 throughout uniform elongation. At strain rate of 10^{-1} s^{-1}, however, β increases during uniform deformation from 0.71 to a maximum of 0.95 and then decreases to 0.91 at the start of necking.

Published in Journal of Dynamic Behavior of Materials
https://doi.org/10.1007/s40870-019-00204-z

---

[*] Corresponding author: naiara.vazquezfernandez@tuni.fi, Tampere University, Faculty of Engineering and Natural Sciences (ENS), Tampere, Finland

A Modified Johnson–Cook Model for Dynamic Response of Metals with an Explicit Strain- and Strain-Rate-Dependent Adiabatic Thermosoftening Effect

B. Song[*], B. Sanborn

Abstract. Metallic alloys are extensively utilized in applications where extreme loading and environmental conditions occur and engineering reliability of components or structures made of such materials is a significant concern in applications. Adiabatic heating in these materials during high-rate deformation is of great interest to analysts, experimentalists, and modelers due to a reduction in strength that is produced. Capturing the thermosoftening caused by adiabatic heating is critical in material model development to precisely predict the dynamic response of materials and structures at high rates of loading. In addition to strain rate effect, the Johnson–Cook (JC) model includes a term to describe the effect of either environmental or adiabatic temperature rise. The standard expression of the JC model requires quantitative knowledge of temperature rise, but it can be challenging to obtain in situ temperature measurements, especially in dynamic experiments. The temperature rise can be calculated from plastic work with a predetermined Taylor-Quinney (TQ) coefficient. However, the TQ coefficient is difficult to determine since it may be strain and strain-rate dependent. In this study, we modified the JC model with a power-law strain rate effect and an explicit form of strain- and strain-rate-dependent thermosoftening due to adiabatic temperature rise to describe the strain-rate-dependent tensile stress–strain response, prior to the onset of necking, for 304L stainless steel, A572, and 4140 steels. The modified JC model was also used to describe the true stress–strain response during necking for A572 and 4140 steels at various strain rates. The results predicted with the modified JC model agreed with the tensile experimental data reasonably well.

Published in Journal of Dynamic Behavior of Materials
https://doi.org/10.1007/s40870-019-00203-0

---

[*] Corresponding author: bsong@sandia.gov, Sandia National Laboratories

Advanced Experimental Data Processing for the Identification of Thermal and Strain-Rate Sensitivity of a Nuclear Steel

M. Peroni[*], G. Solomos

Abstract. The knowledge of material mechanical behaviour in different physical conditions is necessary to accurately simulate structural response using finite element methods, especially when complex physical processes, such as strain-hardening, large strains etc., are involved. In this context, the material characterization at different temperatures and strain-rates is indispensable, but it is equally essential to properly transform the test data into efficient constitutive equations capable to accurately reproduce the material response. As an alternative to the conventional analytical approach of the stress–strain curve fitting, this investigation examines the adoption of an inverse method that exploits a FEM model to accurately keep account of the specimen stress, strain, and temperature fields. The material parameters of the selected constitutive model are then obtained by using an optimization algorithm that iteratively changes the parameter values to minimize a target function. The algorithm has been implemented in MATLAB using the LS-DYNA FEM solver. In the paper, this method has been applied to the experimental data produced in a test campaign (EU project LISSAC) for a ferritic steel normally employed in nuclear pressure vessels. These data refer to tensile testing under several strain-rate and temperature conditions and include both smooth and notched cylindrical specimens. The constitutive models of Johnson–Cook and Zerilli–Armstrong have been considered for the demonstration of the methodology. The efficiency of the approach in determining the model parameters is critically assessed.

Published in Journal of Dynamic Behavior of Materials
https://doi.org/10.1007/s40870-019-00207-w

---

[*] Corresponding author: marco.peroni@ec.europa.eu, European Commission - Joint Research Centre

DYMAT2019 SI08

Dynamic Response of Advanced Materials Impacted by Particle Beams: The MultiMat Experiment

M. Pasquali*, A. Bertarelli, C. Accettura, E. Berthome, L. Bianchi, P. Bolz, F. Carra, C. Fichera, M. I. Frankl, T. Furness, G. Gobbi, P. Grosclaude, J. Guardia-Valenzuela, M. Guinchard, M. D. Jedrychowsky, F. J. Harden, A. Lechner, P. Mollicone, P. D. Pastuszak, M. Portelli, S. Redaelli, E. Rigutto, O. Sacristan de Frutos, P. Simon

Abstract. The introduction at CERN of new extremely energetic particle accelerators, such as the high-luminosity large hadron collider (HL-LHC) or the proposed future circular collider (FCC), will increase the energy stored in the circulating particle beams by almost a factor of two (from 360 to 680 MJ) and of more than 20 (up to 8500 MJ), respectively. In this scenario, it is paramount to assess the dynamic thermomechanical response of materials presently used, or being developed for future use, in beam intercepting devices (such as collimators, targets, dumps, absorbers, spoilers, windows, etc.) exposed to potentially destructive events caused by the impact of energetic particle beams. For this reason, a new HiRadMat experiment, named "MultiMat", was carried out in October 2017, with the goal of assessing the behaviour of samples exposed to high-intensity, high-energy proton pulses, made of a broad range of materials relevant for collimators and beam intercepting devices, thin-film coatings and advanced equipment. This paper describes the experiment and its main results, collected online thanks to an extensive acquisition system and after the irradiation by non-destructive examination, as well as the numerical simulations performed to benchmark experimental data and extend materials constitutive models.

Published in Journal of Dynamic Behavior of Materials
https://doi.org/10.1007/s40870-019-00210-1

---

* Corresponding author: michele.pasquali@cern.ch, CERN

Effects of high strain rate and self-heating on plastic deformation of metal materials under fast compression loading

A. Bragov*, L. Igumnov, A. Konstantinov, A. Lomunov, E. Rusin

Abstract. The results of dynamic tests for compression of four metals after annealing (aluminum alloy, copper, brass, stainless steel) in the range of strain rates 100–10000 s^{-1} are presented. To obtain dynamic true stress-true plastic strain curves a specific dynamic upsetting computation method was used starting from time variation of force pulse. The high-speed loading of specimens with a height to diameter ratio equal to 1.5 was carried out using three experimental devices: a drop-hammer with a free-falling mass, a ram impact machine with rubber accelerators and an impact machine with powder acceleration. A technique for direct measuring the specimen temperature during plasti deformation using an "artificial specimen" thermocouple (specimen-thermocouple) was proposed, in which the deformable metal itself is the "hot" junction, while the "cold" junction is connected to the measuring instrument. A thermoelectrode made of an alloy of noble metals tungsten and rhenium with a diameter of 0.1 mm was welded to the specimen by radiation from a pulsed YAG:Nd3+ laser. As a result of the tests, true dynamic stress-strain diagrams and flow stress versus strain rate were obtained. Experimental estimation concerning self-heating temperature variation corresponding to high-speed plastic deformation at room temperature is also developed. Experiments for determining the temperature effect of plastic deformation of the samples after annealing during cold settling showed that at the high speed of ~50 m/s and high strainrates of ~10000 s^{-1} the increase in temperature of the specimens compressed to a degree of deformation of 0.6 reached 55°C for an aluminum alloy, 60°C for copper, 80°C for brass and 140°C for stainless steel.

Published in Journal of Dynamic Behavior of Materials
https://doi.org/10.1007/s40870-019-00214-x

---

* Corresponding author: bragov@mech.unn.ru, Research Institute for Mechanics, Lobachevsky State University

A Simple Glassy Polymer Model
A practical framework for the strain-rate and temperature dependent behaviour of Polycarbonate

G. C. Ganzenmüller*, S. Patil, M. Maurer, M. Sauer, M. Jung, S. Hiermaier

Abstract. This work presents a simple and robust material model, suitable for dynamic simulations of glassy polymers such as Polycarbonate. The new model reduces the complex stress/strain behavior and its dependence on strain rate and temperature to a simple set of characteristics. Utilizing a time-temperature superposition principle, these characteristics serve as input for a purely empirical fitting approach, which provides an accurate representation of the material behaviour over a wide range of strain rates and temperatures. Calibration data including failure at high rates is obtained using a Split Hopkinson Tension Bar. To demonstrate the applicability of the new model, it is parameterized using high strain rate data and its simulation predictions compared to a gas gun impact experiment wherein a Polycarbonate plate is subjected to the impact of a steel sphere at temperatures between 23–80◦C and 56–75 m/s.

Published in Journal of Dynamic Behavior of Materials
https://doi.org/10.1007/s40870-019-00216-9

---

* Corresponding author: georg.ganzenmueller@inatech.uni-freiburg.de, Fraunhofer Ernst-Mach-Institute for High-Speed Dynamics, EMI

Effects of Adiabatic Heating and Strain Rate on the Dynamic Response of a CoCrFeMnNi High-Entropy Alloy

G. C. Soares*, M. Patnamsetty, P. Peura, M. Hokka

Abstract. This work presents a comprehensive analysis of the effects of strain and strain rate on the adiabatic heating and the mechanical behavior of a CoCrFeMnNi high-entropy alloy (HEA). In this investigation, compression tests were carried out at quasi-static and dynamic strain rates. The temperature of the specimens was measured using high speed infrared thermography. The high strain rate tests were conducted with a Split Hopkinson Pressure Bar, and the tests at lower strain rates were performed using a universal testing machine. The material exhibited a positive strain rate sensitivity, as true stress–strain plots were shifted upwards with the increase in strain rate. With exception of the isothermal tests, temperature rise and the Taylor–Quinney coefficient (β) were noticeably similar for the investigated strain rates. This study shows that the common assumption that β can be considered 0.9 and constant is possibly not very accurate for the CoCrFeMnNi alloy. The β is influenced by at least strain and strain rate.

Published in Journal of Dynamic Behavior of Materials
https://doi.org/10.1007/s40870-019-00215-w

---

* Corresponding author: guilherme.correasoares@tuni.fi, Tampere University, Faculty of Engineering and Natural Sciences (ENS)

High Strain Rate Response of Additively-Manufactured Plate-Lattices: Experiments and Modeling

T. Tancogne-Dejean, X. Li, M. Diamantopoulou, C. C. Roth, D. Mohr[*]

Abstract. Plate-lattices are a new emerging class of isotropic cellular solids that attain the theoretical limits for the stiffness of porous materials. For the same mass, they are significantly stiffer than random foams or optimal truss-lattice structures. Plate-lattice structures of cubic symmetry are fabricated from stainless steel 316L through selective laser melting. A special direct impact Hopkinson bar system is employed to perform dynamic compression experiments at strain rates of about 500/s. In addition, tensile specimens are manufactured for characterizing the stress-strain response of the additively manufactured cell wall material for strain rates ranging from 10^{-3} to 10^{3}/s. The results show that plate-lattices of a relative density of 23% crush progressively when subject to large strain compression. Their specific energy absorption increases by about 8% when increasing the applied strain rate from 0.001 to 500/s, which is primarily attributed to the strain rate sensitivity of the base material. Good quantitative and qualitative agreement between the experiments and the simulations is observed when using a detailed finite element model of the plate structures in conjunction with a modified Johnson-Cook model. The comparison of the simulation results for plate- and truss-lattices of the equal-density reveal a 45% increase in specific energy absorption. Compression experiments on Ti-6Al4V lattices revealed a low energy absorption due to the early fracture of the additively manufactured cell wall material.

Published in Journal of Dynamic Behavior of Materials
https://doi.org/10.1007/s40870-019-00219-6

---

[*] Corresponding author: dmohr@ethz.ch, ETH

Investigation of the Effects of Mold Temperature, Test Temperature and Strain Rate on Mechanical Behaviour of Polypropylene

E. Farotti*, E. Mancini, T. Bellezze, M. Sasso

Abstract. This paper investigates the time and temperature dependence of a ductile polymer, polypropylene, from the mechanical point of view. As the polymeric specimens have been manufactured by the injection molding process, the influence of Mold Temperature has been also subjected to the study. Compression tests have been performed both in quasi static and dynamic range ($10^{-3} \div 10^{3}$ s^{-1}), at different test temperatures (-20 ÷ 40 °C), and the results have been analysed in terms of Yield stress and failure behaviour. The strength of the polymer is strongly influenced from all the input parameters. Mold Temperature has a relevant effect only at room and high temperature. Polypropylene reveals a ductile to brittle transition when it is loaded at high rates, except when test temperature is high. The relation between Test Temperature, Strain Rate and Yield stress is found to be well described by the Ree-Eyring model, adapted to the two relaxation mechanisms involved.

Published in Journal of Dynamic Behavior of Materials
https://doi.org/10.1007/s40870-019-00218-7

---

* Corresponding author: e.farotti@pm.univpm.it, Università Politecnica delle Marche

Constitutive modelling of thermo-mechanical behavior of an epoxy resin from low to high strain rates

Charles Francart[1,2], *Yaël* Demarty[2], *Nadia* Bahlouli[1], *Saïd* Ahzi[1]

[1] ICUBE Laboratory, University of Strasbourg/CNRS, 2 rue Boussingault Strasbourg 67000, France
[2] Institut Saint Louis, 5 rue du Général Cassagnou, Saint-Louis 68300, France

Abstract. Epoxy resin is classically used to joint multilayer structures used for terminal ballistic and blast protection. These structures are subjected to severe loads. It is therefore essential to understand and characterize the epoxy which also has to sustain these loads. Due to the many possible multilayer configurations, it is necessary to use numerical simulations to identify trends before validating the best configurations through an expensive experimental campaign. We propose to study a new epoxy resin subjected to a wide range of strain rates and temperatures. In addition, this epoxy resin has as innovation a low glass transition temperature of the order of 60 °C. This particularity implies a modification of its mechanical behavior. A modeling of its thermo-mechanical behavior taking into account this low glass temperature is presented. A good correlation between experimental data and modeling is obtained.

1 Introduction

The epoxy resin studied in this work is used in different ballistic applications. It is therefore meaningful to investigate the mechanical behavior of such structure under high temperatures and high strain rates. The mechanical properties like stress-strain relation of the resin, like other polymers are sensitive to the strain rate and temperature. The sensitivity to the deformation rate and the temperature of the epoxy resins are weakly modeled in the literature. The main results concern more conventional polymers as in [1-4], which show an increase in the yield strength and the maximum stress as the strain rate increases. In [4], it shows an increase in modulus and maximum stress and a reduction in the tensile stress when the strain rate increases. The resins show a much more brittle response in tension than in compression. The mechanical behavior of the polymers exhibits strong nonlinearity in addition to a strong dependence on strain rate and temperature. Concerning the mechanical modeling of the polymers, models such as Ree-Eyring [5, 6] or cooperative models [7-9] (for the yield stress) coupled with a hyperelastic expression [10] (e.g. 8-chains model, Gent model ...) can be employed. The choice of the constitutive expressions has to be done with the consideration of the different deformation mechanisms. This can only be carried out through experimental mechanical characterization tests.

The thermo-mechanical response of the epoxy resin is investigated in compression loadings over a wide range of strain rates and temperatures. The low glass transition temperature of this epoxy needs a modification of constitutive equations used to describe the strain rate and temperature sensitivity. Thus, a new constitutive behavior model is proposed.

2 Sample preparation and physical material properties

The epoxy resin is a thermoset polymer processed by mixing two different components: a resin and a hardener for the polymerization. This epoxy resin has a very low pot time of 8 minutes (time during which the epoxy resin can be manipulated before the hardening) and reaches its optimum mechanical properties after around 3 days. The two components (1:1 ratio in mass) of the epoxy resin were mixed during 6 min (8 min of pot time) and the still liquid epoxy resin was next poured in wax molds. The bubbles have been removed with vibrations at very low ambient pressure. The samples were then machined for adjustment. The specific heat at room temperature of C_p=1000 J.kg^{-1}.K^{-1} was provided by the manufacturer. The density at room temperature was measured at ρ=1200 kg.m^{-3} using the Archimede's method. Differential scanning calorimetric test has revealed that this epoxy resin has a quite low temperature of glass transition of T_g=60°C=333 K.

3 Experimental methods

3.1. Quasi-static compression tests

The quasi-static compression tests have been carried out with an electro-mechanical Instron testing machine 5500 K9400 at the different true strain rates of 0.001/s, 0.01/s and 0.1/s on 1:1 ratio cylindrical specimens (h = 8 mm / Ø = 8 mm, Figure 1). LVDT Instron strain sensor has enabled to control the constant strain rate. The interfaces between the platens and the samples have been lubricated with petroleum jelly.

---

* Corresponding author: cfrancart@unistra.fr

3.2 Dynamic compression tests

The dynamical compression tests have been carried out at room temperature with a Split Hopkinson Pressure Bar setup (SHPB) (see Table 1) [11, 12].

Table 1. SHPB setup characteristics (mm)

Material	Input Bar	Output Bar	Striker	Sample size
High strength Steel	Ø = 12 L = 1400	Ø = 12 L = 1400	Ø = 12 L = 400	Ø = 8 L = 4

The raw wave signals from full Poisson's bridges of strain gages glued on the bars have been acquired. The signals have been magnified and displayed on a numerical oscilloscope at a sampling frequency of 2 MHz. The striker velocity measurement has been carried out with photodiode sensors. The interfaces between the samples and the bars have been lubricated with petroleum jelly.
Dynamic tests at high temperatures have been carried using a custom pulsated air flux system. The sample was heated alone (the bars were put in contact with it just before the test) and its temperature was monitored using a thermocouple set on its surface. Other dynamic tests at low temperatures have also been performed using liquid nitrogen and ethanol to adjust to the desired temperatures. The temperature of the sample was monitored using an infrared measuring device.

4 Experimental mechanical behavior

The true stress-strain compression curves obtained from the tests performed at low and high strain rates are plotted in Figure 1. Classical non-linear mechanical behavior is observed for the epoxy resin.
The curves can be decomposed in three main parts: elastic linear until threshold stress [13], strain softening [14, 15] followed by strain hardening [10]. The viscoelastic behavior is not addressed in this paper. Elastic modulus and yield stress are strain rate sensitive. As the strain rate increases, elastic modulus and yield stress increase too. Under quasi-static loading, the stress-strain curve at 0.001/s goes over the stress strain curves at 0.1/s at high strain level. This phenomenon can be attributed to the thermal softening. During the tests, an increase of temperature of 15°C was measured. The competition between the strain softening and strain hardening begins at low strain rate. Under dynamic loading, the strain softening manages to overcome the strain hardening at high strain due to the high adiabatic heating.

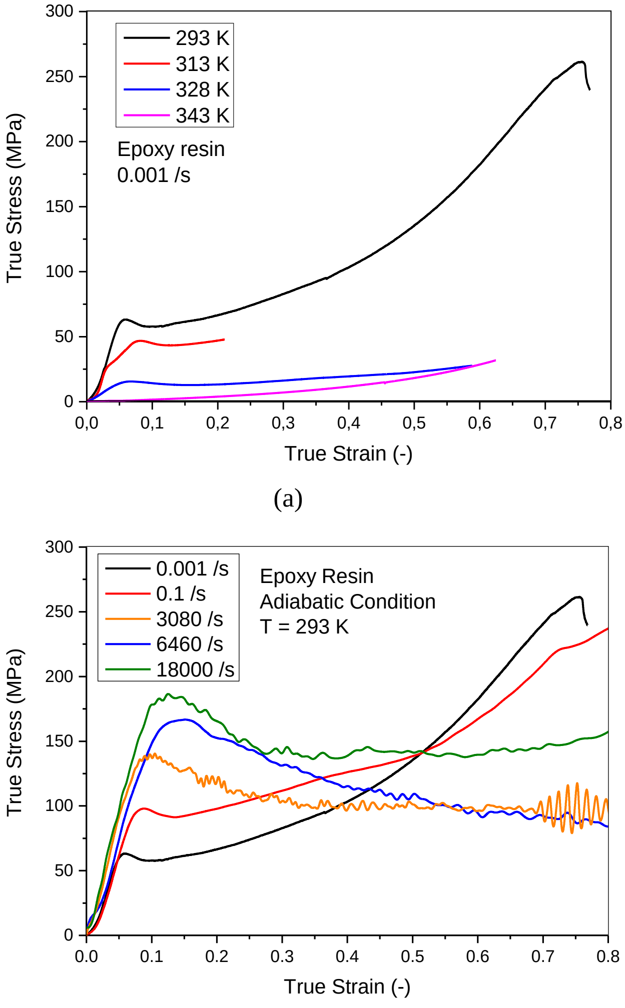

(a)

(b)

Fig. 1. True stress vs true strain curves of the epoxy resin for different strain rates at room temperature (a) and temperatures at low strain rate (b).

The evolution of the yield stress σ_y with the strain rate of the epoxy resin seems nonlinear for each tested temperatures (Figure 2). Two domains can be identified below and above approximately 10^2/s. The previously mentioned strong dependency of the threshold stress on the strain rate can be explained by the cross-linking [16] of the chains. Similarly, the motion inside the reticulated entities seems facilitated by increasing temperature as the free volume is growing.

The high non-linearity of σ_y towards temperature (Figure 2) is due to the fact that the glass transition temperature of the epoxy resin is relatively low (60°C). The mechanisms of chain diffusion from glassy state to rubber state greatly soften the polymer.

Concerning the strain hardening, the dependency to the strain rate [10, 14, 17] cannot be studied due to the low temperature of glass transition. Indeed, the adiabatic heating occurring at those rates of deformation leads to a rubber behavior of the polymer (Figure 1).
As mentioned previously, the behavior does not seem to present any visible strain hardening in dynamic conditions. However, the quasi-static tests enable to observe the high rate sensitivity of the overall mechanical behavior of the polymer.

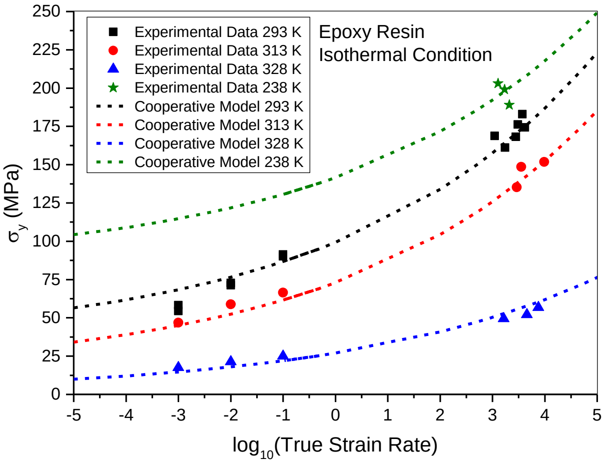

Fig. 2. Evolution of the yield stress of the epoxy resin with strain rates at different initial temperatures, with the application of the modified cooperative model (Eq 2) on the epoxy.

5 Constitutive modeling

The constitutive modeling is based on additive form following the equation Eq. 1.

$$\sigma(\varepsilon_p, \dot{\varepsilon}_p, T) = [\sigma_y(\dot{\varepsilon}_p, T) + \sigma_{hyp}(\varepsilon_p, \dot{\varepsilon}_p, T)]\psi(\varepsilon_p) \tag{1}$$

5.1 Yield stress modeling

The modeling of the threshold stress σ_y of polymer materials defines the global level of stress and is greatly dependent on the temperature and the strain rate [13, 14]. At the threshold stress, the motion inside the reticulated entities can be assumed irreversible. The model used in this work is the cooperative model [7-9] developed for amorphous polymers and based on the Ree-Eyring theory [5, 6]. This particular model takes into account the change of mechanical behavior before and after the temperature of glass transition through considerations on the evolution of the free volume [15, 18, 19] in the polymer with the temperature and the strain rate.

As shown by the experimental results on Figure 2, the temperature sensitivity of σ_y is highly non-linear for the range of tested temperatures. Therefore, the cooperative model is adapted to take into account such thermal behavior (Eq. 2) [7, 20]. The existence of a threshold stress has been observed only below the T_g in quasi-static condition and therefore the epoxy resin will be assumed as a purely hyperelastic material without threshold stress at low strain rates above T_g. The parameters, calculated with the tests using the least square method in Matlab optimization toolbox, are gathered in Table 2.

$$\begin{cases} \sigma_y(\dot{\varepsilon}_p, T < T_g - T_t) = \\ \left[\sigma_0 - mT + \dfrac{2k_bT}{V}\sinh^{-1}\left(\dfrac{\dot{\varepsilon}_p}{\dot{\varepsilon}_0 e^{-\frac{\Delta H_\beta}{RT}}}\right)^{\frac{1}{n}}\right] \\ * \left(1 - \dfrac{T}{T_g} e^{\theta^*\left(1-\frac{T_g}{T}\right)}\right) \\ \sigma_y(\dot{\varepsilon}_p, T \geq T_g - T_t) = \\ \dfrac{2k_bT}{V}\sinh^{-1}\left(\dfrac{\dot{\varepsilon}_p}{\dot{\varepsilon}_0 e^{-\frac{\Delta H_\beta}{RT_g}} e^{\frac{\ln(10)c_1^g(T-T_g)}{c_2^g+T-T_g}}}\right)^{\frac{1}{n}} \end{cases} \tag{2}$$

With $\sigma_0, m, V, n, \dot{\varepsilon}_0$ and ΔH_β model parameters. $R = 8.314$ J.mol^{-1}.K^{-1} is the constant of perfect gaz. σ_0 is a reference yield stress at 0 K, m is the temperature sensitivity, V is the activation volume of the chain motion, $\dot{\varepsilon}_0$ is a reference strain rate, ΔH_β is the β activation energy, θ^* the parameter modeling the nonlinear temperature sensitivity of the yield stress, T_t the temperature range between the beginning of the phenomenon of glass transition and T_g and n a phenomenological parameter linked to the level of reticulation of the chains [16].

Table 2. Cooperative model parameters of the epoxy resin.

σ_0 (MPa)	m (MPa/K)	V (m^3)	$\dot{\varepsilon}_0$ $(/s)$	ΔH_β (J/mol)	θ^* $(-)$
315.7	0.912	1.91e-29	4.92e9	5520	27.99
T_g (K)	c_1^g	c_2^g $(°C)$	n $(-)$	T_t (K)	/
333	17.44	51.6	10.83	8	/

5.2 Strain softening phenomenon

A strain-softening phenomenon [7, 14, 15, 21] can be observed for the epoxy resin. In this work, it is evaluated as the normalized energetic balance ψ between the global measured behavior σ_{exp} and the modeled behavior, which takes into account only the yield stress and the hyper elastic phenomena. It has been observed that the minimal energetic value is reached around a plastic strain of $\varepsilon_p \sim 0.125$ and stays quasi-constant up to around $\varepsilon_p \sim 0.3$. Therefore, it can be concluded that the epoxy resin (thermoset) releases its stored energy through the relaxation of chains over a relatively large strain range which leads to a decrease of the level of stress [14, 15, 22-24]. Therefore, to maintain the energy balance during the whole range of strain, the same quantity of released energy during the relaxation phenomenon has to be absorbed before the failure (Eq. 3).

$$\int_0^{\ln \varepsilon_p^f} \left(\frac{\sigma_{exp}}{\sigma_y + \sigma_{hyp}} - 1 \right) d\varepsilon_p = 0 \qquad (3)$$

The evolution of the energy balance ψ is modeled through Eq. 4. Only the strain sensitivity is taken into account in this work. Temperature and strain rate dependencies are assumed negligible in this work but still exist.

$$\psi(\varepsilon_p) = \frac{\sigma_{exp}}{\sigma_y + \sigma_{hyp}} = Ae^{B\varepsilon_p} + Ce^{D\varepsilon_p} \qquad (4)$$

With A, B, C and D phenomenological parameters. The parameters of the model are reported in Table 3.

Table 3. Energetic balance parameters of the epoxy resin.

$A\ (-)$	$B\ (-)$	$C\ (-)$	$D\ (-)$
0.2978	-12.91	0.6984	0.6644

5.3 Strain hardening

In this work, the model used for σ_{hyp} is the Gent model [25] which has been chosen due to its efficiency, simplicity of use and of implementation in numerical code.

5.4 Constitutive behavior of the epoxy resin

The mechanical behavior of the epoxy resin is complex. Indeed the significant differences between quasi-static and dynamic conditions are due to two properties of the material (Figures 3 and 4):

- The high level of reticulation of the thermoset polymers causes the high strain rate sensitivity of the yield stress.
- The low temperature of glass transition T_g causes a very high softening of the level of stress as soon as the temperature increases (due to adiabatic heating or environmental factors).

The model provides satisfying results to evaluate the level of stress of the epoxy resin over such wide ranges of temperatures and strain rates and up to very high strains (see Figure 4).

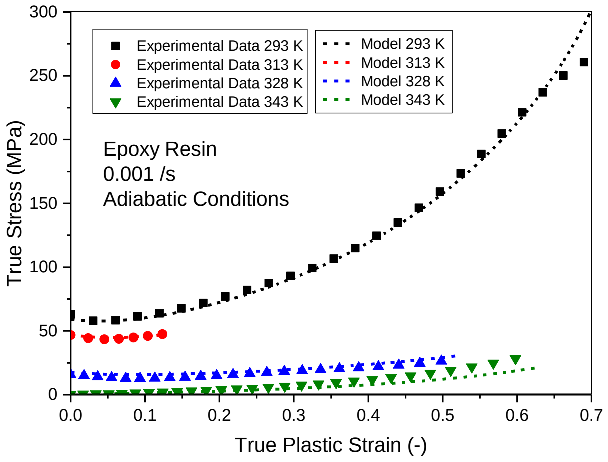

Fig. 3. Comparison of between the experimental data and the suggested model for the epoxy resin over wide range ranges of temperatures.

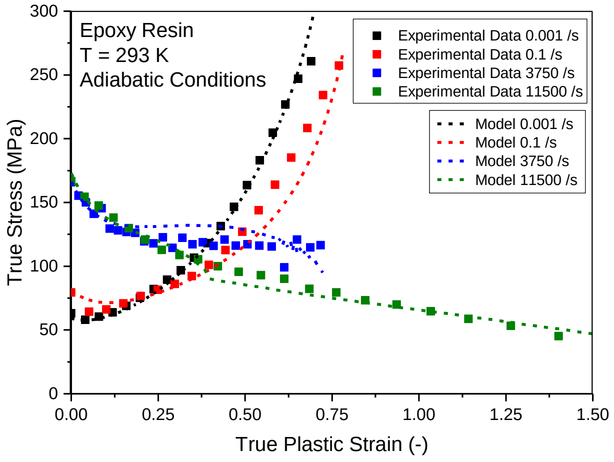

Fig. 4. Comparison of between the experimental data and the suggested model for the epoxy resin over wide range ranges of strain rates.

Conclusion

The work presented in this paper provides an overview of the mechanical behavior of an armor-bonding epoxy resin. Each main phenomenon responsible of the non-linear irreversible stress mechanical response have been discussed and a modeling has been suggested (yield stress, strain softening and hyperelasticity).

The particularities of the studied epoxy resin are its relative low temperature of glass transition ($T_g = 333\ K$) leading to a highly non-linear thermal behavior in the range of temperatures of interest and its very high level of chain cross-linking (entanglement). The increase of this latter leads to an increase of the strain rate sensitivity of the yield stress [8, 26]. The same goes for the temperature toward which the level of cross-linking is highly dependent and decreases rapidly when heat provided to the material increases [16].

The constitutive equations used for the modeling of the different phenomena have been developed to grasp its mechanical behavior with a high level of accuracy over wide ranges of temperatures and strain rates. These expressions aim to be implemented in a FEM software in order to numerically study the influence of epoxy joint in the mechanical performance of multilayer composite armor plates subjected to impact loading. Further mechanical characterizations on the studied epoxy resin with other kind of solicitations are under investigation to identify failure modes and model. A good compromise should be found to reach a satisfying description of the adhesive joint mechanical response under impact loading while keeping reasonable computing time.

This work was funded by the French-German Research Institute of Saint-Louis and experimental tests were carried out at the French-German Research Institute of Saint-Louis and at the ICube laboratory at Strasbourg.

References

1. Walley, S., et al., A study of the rapid deformation behaviour of a range of polymers. Philosophical Transactions of the Royal Society of London. Series A, Mathematical and Physical Sciences, 1989. 328(1597): p. 1-33.
2. Chen, W. and B. Zhou, Constitutive behavior of Epon 828/T-403 at various strain rates. Mechanics of time-dependent materials, 1998. 2(2): p. 103-111.
3. Chang, W. and J. Pan, Effects of yield surface shape and round-off vertex on crack-tip fields for pressure-sensitive materials. International journal of solids and structures, 1997. 34(25): p. 3291-3320.
4. Buckley, C.P., et al., Deformation of thermosetting resins at impact rates of strain. Part I: Experimental study. Journal of the Mechanics and Physics of Solids, 2001. 49(7): p. 1517-1538.
5. Eyring, H., Viscosity, plasticity, and diffusion as examples of absolute reaction rates. The Journal of Chemical Physics, 1936. 4(4): p. 283-291.
6. Ree, T. and H. Eyring, Theory of Non-Newtonian Flow. I. Solid Plastic System. Journal of Applied Physics, 1955. 26(7): p. 793-800.
7. Richeton, J., et al., Influence of temperature and strain rate on the mechanical behavior of three amorphous polymers: Characterization and modeling of the compressive yield stress. International Journal of Solids and Structures, 2006. 43(7–8): p. 2318-2335.
8. Richeton, J., et al., Modeling and validation of the large deformation inelastic response of amorphous polymers over a wide range of temperatures and strain rates. International Journal of Solids and Structures, 2007. 44(24): p. 7938-7954.
9. Gueguen, O., et al., Micromechanically based formulation of the cooperative model for the yield behavior of semi-crystalline polymers. Acta Materialia, 2008. 56(7): p. 1650-1655.
10. Boyce, M.C. and E.M. Arruda, Constitutive models of rubber elasticity: a review. Rubber chemistry and technology, 2000. 73(3): p. 504-523.
11. Jankowiak, T., A. Rusinek, and T. Lodygowski, Validation of the Klepaczko–Malinowski model for friction correction and recommendations on Split Hopkinson Pressure Bar. Finite Elements in Analysis and Design, 2011. 47(10): p. 1191-1208.
12. Davison, L., Fundamentals of Shock Wave Propagation in Solids, ed. Y.H. Lee Davison2008, Leipzig, Germany: Springer.
13. Ward, I.M., Review: The yield behaviour of polymers. Journal of Materials Science, 1971. 6(11): p. 1397-1417.
14. Rittel, D. and H. Maigre, An investigation of dynamic crack initiation in PMMA. Mechanics of Materials, 1996. 23(3): p. 229-239.
15. Struik, L.C.E., Dependence of relaxation times of glassy polymers on their specific volume. Polymer, 1988. 29(8): p. 1347-1353.
16. Gonzalez, L.Y.S., M.G. Botero, and M. Betancur, Hyperelastic Material Modeling. 2005.
17. James, H.M. and E. Guth, Theory of the elastic properties of rubber. The Journal of Chemical Physics, 1943. 11(10): p. 455-481.
18. Fox, T. and S. Loshaek, Influence of molecular weight and degree of crosslinking on the specific volume and glass temperature of polymers. Journal of Polymer Science, 1955. 15(80): p. 371-390.
19. Balluffi, R.W., Introduction to elasticity theory for crystal defects2012: Cambridge University Press.
20. Rittel, D. and A. Brill, Dynamic flow and failure of confined polymethylmethacrylate. Journal of the Mechanics and Physics of Solids, 2008. 56(4): p. 1401-1416.
21. Struik, L.C.E., Effect of thermal history on secondary relaxation processes in amorphous polymers. Polymer, 1987. 28(1): p. 57-68.
22. Hill, R., Continuum micro-mechanics of elastoplastic polycrystals. Journal of the Mechanics and Physics of Solids, 1965. 13(2): p. 89-101.
23. Xiao, C., J.Y. Jho, and A.F. Yee, Correlation between the shear yielding behavior and secondary relaxations of bisphenol a polycarbonate and related copolymers. Macromolecules, 1994. 27(10): p. 2761-2768.
24. Chen, L.P., A.F. Yee, and E.J. Moskala, The molecular basis for the relationship between the secondary relaxation and mechanical properties

of a series of polyester copolymer glasses. Macromolecules, 1999. 32(18): p. 5944-5955.

25. Horgan, C.O., The remarkable Gent constitutive model for hyperelastic materials. International Journal of Non-Linear Mechanics, 2015. 68(0): p. 9-16.
26. Grosso, G. and G.P. Parravicini, Chapter 1 - Electrons in One-Dimensional Periodic Potentials, in Solid State Physics (Second Edition), G. Grosso and G.P. Parravicini, Editors. 2014, Academic Press: Amsterdam. p. 1-65.

Numerically analyzing the inverse experiment methodology as applied to the investigation of dynamic penetration into water-saturated soils at negative temperatures

Vasiliy Kotov[1,*], *Vladimir V.* Balandin[1], *Vladimir Vl.* Balandin[1], *Anatoliy* Bragov[1], *Andrey* Lomunov[1]

[1]Research Institute of Mechanics, National Research Lobachevsky State University of Nizhny Novgorod, 603950, Nizhny Novgorod, Russian Federation

Abstract. The present paper numerically analyzes the applicability of the inverse experiment methodology for determining the force resisting penetration of a conical striker into frozen sand soil at a temperature of -18 ° C. The condition of the soil specimen prior to freezing is characterized as fully water-saturated. The deformational behavior of the soil is described in the framework of the model of compressible elastoplastic media with the plasticity condition depending on pressure. The dynamic compressibility diagram of the frozen soil includes the initial linearly elastic part. The errors in determining the force resisting penetration of a conical striker into frozen soil in the inverse experiment due to the effect of the waves reflected from the container walls was analyzed. The difference between maximal values of the force resisting penetration, obtained in the numerical calculations with the two versions of the boundary conditions, was used as a measure of the effect. For the problems of penetration of conical strikers into frozen and water-saturated soil, a fairly good agreement between the experimental data and numerical results can be obtained with the help of Grigoryan's model accounting for the pressure-dependent parameters.

1 Introduction

Determining the parameters of the laws of dynamic deformation for dry and water-saturated soils under varied parameters of temperature is of great scientific and applied importance. In the middle of the last century the stress and velocity fields were determined in field experiments as a result of spherical explosion of blasting charges in frozen soil. A substantial dependence of the wave parameters on temperature and soil characteristics in the initial non-frozen condition: humidity, porosity, fractional and component composition and others, was determined.

The inverse experiment methodology [1–3] with measuring bar has proved very effective in determining the force characteristics of penetration of rigid cylindrical strikers with heads of various geometries. It allows to measure integral loads at the initial nonstationary stage of penetration. Earlier, experimental data were obtained on strain-rate dependences of dynamic penetration of cylindrical solids with flat, hemispherical and conical heads into dry and water-saturated sand at positive temperatures [4 - 7].

A significant disadvantage of the inverse techniques is the necessity to accelerate soil containers of considerable mass and small geometrical dimensions that leads to the effect of the container walls on the integral loads and final penetration depths [8]. Earlier, the effect of the boundaries on the maximal and quasi-stationary values of the force resisting penetration of a 20 mm-dia hemispherical striker into dry sand, determined in inverse experiments, was studied. It was found that, if a boundary condition modeling the effect of a rigid container was used in computations, the quasi-stationary value of the force resisting penetration exceeds the analogous value calculated for penetration into a half-space by 20% at impact velocities over 100 m/s and then decreases with the increasing impact velocity. The computations of the process of penetration into dry soil conducted without a container showed lower values of the resistance force.

A qualitatively similar picture is observed when analyzing the process of penetration into frozen soil. The quantitative differences are explained by the fact that the longitudinal wave velocity in frozen soil (3000-4000 m/s) is an order of magnitude higher than the propagation velocity of small-amplitude waves in dry sand, which is 300-400 m/s.

In this paper the process of penetration of a conical striker along the normal line to the free surface was numerically analyzed in an axisymmetric formulation, using software package Dinamika-2 of the Research Institute for Mechanics of Nizhny Novgorod Lobachevsky State University, and in a 3D formulation in the framework of software product LS-Dyna. The relations of the soil media model were numerically realized in the framework of the modified Godunov scheme, implemented in the applied software package Dynamika-2 of the Research Institute for Mechanics of Nizhny Novgorod Lobachevsky State University. The earlier computations of the processes of impact and penetration of axisymmetric strikers into soft soil media showed good agreement between the numerical results and experimental data. The impact and penetration velocities are varied during the calculations from 150 to 300 m/s, with the cone basis diameters of 10, 12 and 20

---

[*] Corresponding author: vkotov@inbox.ru

mm. Computational geometry is determined by the size of the container used in the inverse experiment. The deformation of the container was neglected, the effect of the container walls was modeled by two choices of the boundary conditions: free surface (the absence of the walls) and “impermeability” along the normal line and free sliding in the tangential direction.

2 Mathematical formulation of the impact and penetration problem

Grigoryan's mathematical model of the dynamics of soil media [9] can be written in the cylindrical coordinate system rOz (where Oz is the symmetry axis) as the system of differential equations expressing the laws of conservation of mass, pulse and maximal density attained in the process of actively loading the soil, as well as equations of plastic flow theory with the von Mises–Schleicher plasticity condition

$$
\begin{gathered}
d\rho / dt + \rho(u_{r,r} + u_{z,z}) = -(\rho u_r)/r\,, \\
\rho du_r / dt - \sigma_{rr,r} - \sigma_{rz,z} = (\sigma_{rr} - \sigma_{\theta\theta})/r\,, \\
\rho du_z / dt - \sigma_{rz,r} - \sigma_{zz,z} = (\sigma_{rz})/r\,, \qquad (1) \\
d\rho_* / dt = d\rho / dt H(\rho - \rho_*) H(d\rho / dt)\,, \\
D_J s_{ij} + \lambda s_{ij} = 2Ge_{ij},\ (i, j = r, z)\,, \\
s_{ij} s^{ij} \le \tfrac{2}{3}\sigma_T^2\,,
\end{gathered}
$$

Where the following notation is used: t is time, ρ_0, ρ and ρ_* are the initial, current and maximal density attained in the loading process, u_i, σ_{ij}, s_{ij}, e_{ij} are the components of the velocity vector, Cauchy stress tensor, and deviators of the stress and strain rate tensors, respectively, H is the Heaviside function, D_J is the Yaumann derivative, $d\ /dt$ is the total derivative with respect to time, G is the shear modulus, σ_T is the yield strength, and sums are taken over repeated indices. Parameter $\lambda = 0$ in case of elastic strain and $\lambda > 0$ if the von Mises–Schleicher plasticity condition is satisfied.

The system of differential equations (1) is closed with finite relations, determining pressure p and plasticity condition of the soil

$$
\begin{gathered}
p = f_1(\rho, \rho_*) H(\rho_* - \rho) H(\rho_0 - \rho)\,, \qquad (2) \\
\sigma_T = f_2(p)\,.
\end{gathered}
$$

The system of equations (1), (2) of soil dynamics is complemented with initial and boundary conditions. On the head part of the striker, contacting with the soil medium, a contact algorithm of "impermeability" is used along the normal line with "sliding in the tangential direction with dry friction" in accordance with the Coulomb friction model with a constant friction coefficient k_f. Over the free surfaces of the soil and the striker, normal and tangential stresses were set to be equal to zero. The outer boundaries of the analyzed region of the soil corresponded to the geometry of the container used in the inverse experiment. Deformation of the container was neglected, and the effect of the container walls was modeled by two versions of the boundary conditions: 1) “impermeability” along the normal line and free sliding in the tangential direction (boundary condition 1) and 2) free surface, corresponding to the absence of walls (boundary condition 2). At an initial time, the stresses and velocity of the soil particles are equal to zero. The striker was assumed to be rigid, moving at a constant speed, equal to the impact velocity.

Let us concretize the assignment of functions f_1 and f_2 in Grigoryan's model of soil media (1), (2).

The dynamic compressibility of the soil, as well as some other compressible materials, is characterized by shock adiabat, represented by the linear dependence of the shock wave velocity D as a function of the mass velocity u:

$$D = A + Bu \qquad (3)$$

Here the value of the constant A is approximately equal to the propagation velocity of the plane compression wave in soil under small pressures, B characterizes the ultimate compressibility of soil. The shock adiabat, represented in the form of a linear dependence (3), and the Hugoniot conditions for a shock wave $\sigma = \rho_0 Du$, $\theta = u/D$ imply the well-known relation between the stress σ □ and the bulk strain θ.

$$\sigma(\theta) = \frac{\rho_0 A^2 \theta}{(1 - B\theta)^2}\,, \quad \theta = 1 - \frac{\rho_0}{\rho}\,, \qquad (4)$$

The shear resistance of the medium is determined by the fractional-rational dependence of the yield strength as a function of pressure

$$f_2(p) \equiv \sigma_0 + kp/(1 + kp/\Delta\sigma)\,, \quad \Delta\sigma = \sigma_M - \sigma_0 \qquad (5)$$

The coefficients σ_0, σ_M and k characterize adhesion, maximal value of yield strength and the internal friction of the soil.

The pressure is described with following equation

$$
p(\theta) = f_1(\theta) \equiv \begin{cases} K\theta, & -\theta_e < \theta < \theta_e \\ K\theta_e + \dfrac{\rho_0 a^2 \theta}{(1 - b\theta)^2}, & \theta \ge \theta_e \end{cases} \qquad (6)
$$

Here K, a and b are constant coefficients, the value θ_e limits an elastic behavior of the soil. The method for determining the coefficients a and b based on the known dependency parameters (3)-(5) is given in [16].

Unloading the medium from a state characterized by pressure and density values p_* and ρ_* is assumed to be linear

$$p - p_* = \frac{K}{\rho_0}(\rho - \rho_*) \qquad (7)$$

3 Formulation of numerical modeling problems

The relations (1), (2) were realized within the framework of the methodology [10], based on the modified Godunov scheme, implemented in the applied software package Dynamika 2 of the Research Institute for Mechanics, Nizhny Novgorod Lobachevsky State

University [11]. The earlier computations of the processes of impact and penetration of axisymmetric strikers into soft soil media [4] showed good agreement between the numerical results and experimental data.

To increase the reliability of the results of numerical analyses, the problem of penetration of a conical striker into an elastoplastic medium modeling frozen soil was analyzed in a fully 3D formulation, using commercial software product LS-DYNA. The striker was modeled by a non-deformable rigid body (*MAT_RIGID), the soil was modeled by an elastoplastic medium, the behavior of which is described in the framework of the model *MAT_SOIL_AND_FOAM.

The problem was analyzed in FSI (Fluid Structure Interaction) formulation, where the equations of motion of the striker were integrated in Lagrangian coordinates, while the equations for the soil were solved on the Eulerian grid. The interaction between the striker and an elastoplastic medium was realized using a special type of contact (CONSTRAINED_LAGRANGE_IN_SOLID). The formulation and solution of the problem of penetration corresponds to the one given earlier [12].

The parameters of the soil model (5), (6) are the following: ρ_0=2100 kg/m3, p_e=6 MPa, K=21000 MPa, G=7875 MPa (determined by the value of Poisson's ratio 1/3), a=1400 m/s, b =4, σ_0=15 MPa, k =0.5, σ_M =50 MPa, k_f =0.2.

The choice of values of the parameters is determined by the following reasons. Up to stress values of $\sigma*$=15-21 MPa, which correspond to compressive strength of the frozen soil, the soil behaves like a linearly elastic medium. Under conditions of uniaxial stress we have $p_e = \sigma^*/3$, at pressure $p_e << \sigma_M$ $\sigma^* = \sigma_0 + kp_e$ is also correct, whence it follows that $\sigma_0 = (1-k/3)\sigma^*$. The results of dynamic tests [13-15] also indicate stress-rate dependence of the deformation diagrams of frozen soil, resulting in the approximately 1.5-fold increase of compressive strength in the strain-rate range from 300 to 1000 1/s. It is to be noted that the strength values of the frozen soil obtained in both static and dynamic tests are characterized by considerable scatter. In the present paper, the average strength value σ^*=18 MPa was assumed. Strain-rate dependence was not accounted for in the first approximation. At pressures of about 200 MPa and a temperature of –18°C, ice-water transition takes place, and the behavior of the frozen soil becomes similar to that of water-saturated soil, the parameters of the equation of state for which were determined by us earlier [16]. The longitudinal wave velocity *c*, determined by the inclination of the deformation diagram (6) at its initial part, amounts $\sqrt{(K+4G/3)/\rho_0}$ =3.8 km/s, while the shear wave velocity is $\sqrt{G/\rho_0}$ =1.9 km/s. When the compression strength is exceeded, the longitudinal wave velocity drops to the value of 1.5 km/s, which corresponds to failure of the skeleton of the frozen soil.

The rectangular section of the cylindrical area of the soil is divided by a difference grid into square cells with the side size of d /*n*, where *n* is the number of cells. The convergence of the used Godunov scheme [10] was analyzed by a series of numerical computations on condensing grids. The change in quasistationary force depending on the cell size d /*n* appeared to be close to linear one with a reliability of at least 0.95, whereas the difference in values of the forces at *n* = 200 from the predicted values was 10-15%.

Fig. 1 presents the forces resisting to penetration into the frozen soil of the conical striker with an apex angle of 60 degrees and basis diameter of d =20 mm in a rigid jacket at velocities of 150 m/s (curves *1*, *2*) and 300 m/s (curves *3*, *4*). The curves *1*, *3* represent the results obtained in calculations employing the applied software package Dynamika 2, while the curves *2*, *4* represent the results obtained within the framework of software product LS-DYNA. The soil occupied a cylindrical area with a diameter of 54 mm and a height of 65 mm. It is to be noted that, the curves are almost fully coincident at the stage of penetration of the conical part of the striker and the numerical results after separation of the flow are in good agreement.

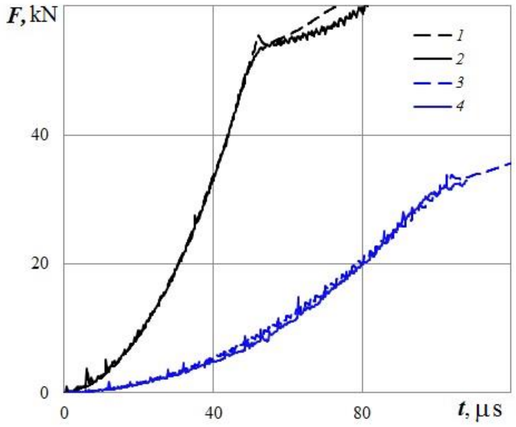

Fig. 1. The forces resisting to penetration into the frozen soil of the conical striker with an apex angle of 60 degrees and basis diameter of *d*=20 mm in a rigid jacket at velocities of 150 m/s (curves 1, 2) and 300 m/s (curves 3, 4)

4 Results of numerical computations

The results of numerical calculations of penetration of conical strikers with an apex angle of 60 degrees and basis diameters of *d*=10, 12 and 20 mm at penetration velocities of V_0=150 and 300 m/s are given onwards. Two versions of the boundary conditions modeling absolutely elastic and absolutely rigid containers are analyzed.

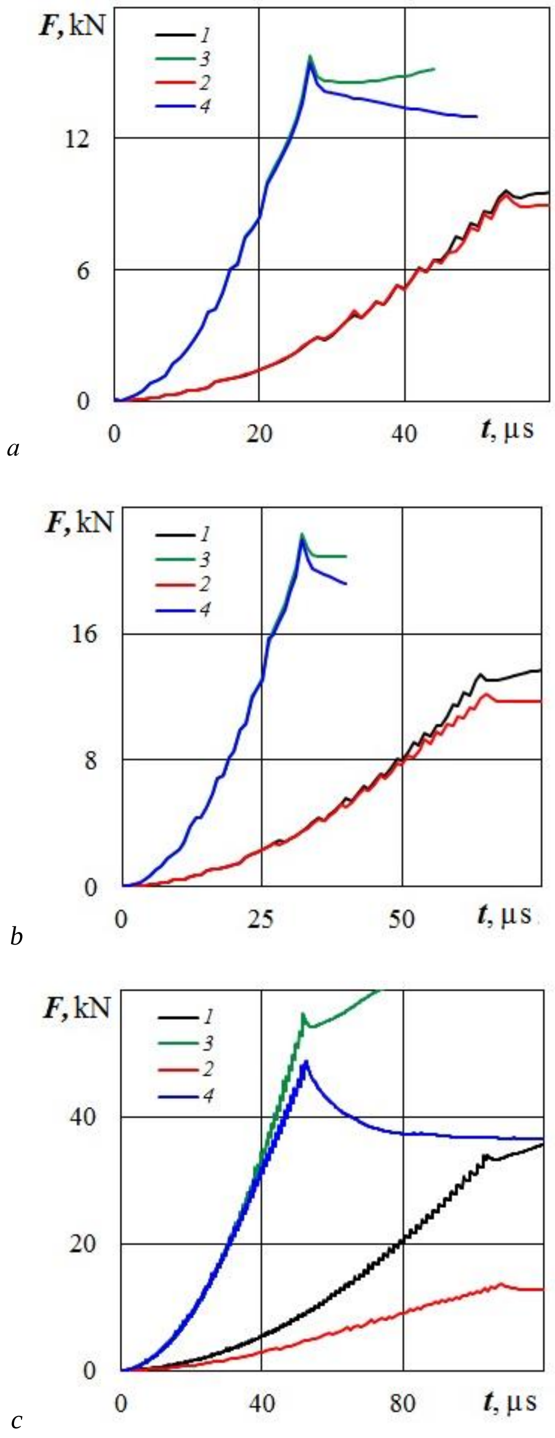

Fig. 2. The forces resisting to penetration of a conical striker with basis diameters of *d*=10 (*a*), 12 (*b*) and 20 mm (*c*) into frozen soil at velocities of 150 m/s (curves *1*, *2*) and 300 m/s (curves *3*, *4*).

Fig. 2 presents the forces resisting to penetration of a conical striker with basis diameters of d =10 (a), 12 (б) and 20 mm (в) into frozen soil at velocities of 150 m/s (curves 1, 2) and 300 m/s (curves 3, 4). Curves 1, 3 show the results, obtained in computations using the boundary condition 1 modeling the effect of a rigid container, whereas curves 2, 4 show the results of computations without a container (boundary condition 2).

Let us consider the value of the resistance force at the moment of penetration of a conical part of the striker $t^* = \frac{\sqrt{3}}{2}\frac{d}{V_0}$. Further, the growth of the contact surface area does not occur, and the observed changes in the resistance force to penetration are associated with the action of the boundary conditions caused by compressional-dilatational waves reflected from the borders of the region (container walls). The value of the resistance force at the moment of t^* is considered the maximal value of the force resisting to penetration.

It can be seen from Fig. 2, б that the influence of the boundary conditions on the maximal value of the force resisting penetration of a striker with a d =12mm basis does not exceed 10% at penetration velocities of 150m/s and then decreases with the increasing velocity. The force resisting penetration of a striker with a d =10 mm basis is practically independent of the type of the boundary conditions until the $t < t^*$. The boundary conditions have a significant effect on the force resisting penetration of a striker with a basis diameter of d =20 mm: when penetration velocities are varied from 150 m/s to 300 m/s the difference in maximal values decreases frome 60% to 15%.

The problems of penetration of a striker into frozen soil at a penetration velocity of 300 m/s, within the time interval of $0 < t < 1.5t^*$, equivalent to the problems of penetration into a half-space, were also considered. Fig.3 presents the results of computations in the form of time history of the force resisting penetration. Curves 1, 2 and 3 show the computational results of penetration into frozen soil of cones with basis diameters d =10, 12 and 20 mm. Practically constant (quasi-stationary) level of the force resisting penetration is observed upon reaching its maximal value. It is to be noted that, the maximal value practically coincides with the value, obtained in computations using boundary condition 1, which simulates an absolutely rigid container (see also Fig. 2).

Conclusion

It is shown that, in problems of penetration of conical strikers into frozen and water-saturated soils a fairly good agreement between the experimental data and numerical results can be achieved using Grigoryan's model of elastoplastic soil medium, accounting for the dependence of the yield criterion on pressure (the Mohr-Coulomb Tresca limit yield criterion).

The error in determining the force resisting penetration of a conical striker into frozen soil in the inverse experiment due to the effect of the waves, reflected from the container walls, was analyzed. The difference between maximal values of the force resisting penetration, obtained in the numerical calculations with two versions of the boundary conditions, was used as a measure of the effect.

It is shown that, for a striker with 20mm-dia basis, the error amounts 15% at velocities over 300 m/s and then decreases with the increasing velocity. For conical strikers with 10 and 12mm-dia bases, at impact velocities over 150 m/s, the effect of the container walls can be neglected.

This work was supported by a grant from the Government of the Russian Federation (contract No. 14.Y26.31.0031).

References

1. M.J. Forrestal, D.E. Grady. Int. J. Solids Struct. 1, 18 (1982)
2. M.J. Forrestal, L.M. Lee, B.D. Jenrette. J. Appl. Mech. 53, 2 (1986)
3. Vl.V. Balandin, Vl.Vl. Balandin, A.M. Bragov, V.L. Kotov. Tech. Phys. 61, 6 (2016)
4. V.G. Bazhenov, A.M. Bragov, V.L. Kotov, A.V. Kochetkov. J. Appl. Math. Mech. 67, 4 (2003)
5. V.V. Balandin, A.M. Bragov, L.A. Igumnov, A.Yu. Konstantinov, V.L. Kotov, A.K. Lomunov. Mech. of Solids 50, 3 (2015)
6. V.L. Kotov, V.V. Balandin, A.M. Bragov, Vl.Vl. Balandin. Tech. Phys. Let. 43, 9 (2017)
7. A.M. Bragov, Vl.V. Balandin, V.L. Kotov, Vl.Vl. Balandin. Tech. Phys. 63, 4 (2018).
8. V.G. Bazhenov, V.L. Kotov, S.V. Krylov, V.V. Balandin, A.M. Bragov, and E.V. Tsvetkova. J. Appl. Mech. Tech. Phys. 6, 42 (2001)
9. S.S. Grigoryan. J. Appl. Math. Mech. 24, 6 (1960)
10. M. Abouziarov, V.G. Bazhenov, V.L. Kotov, A.V. Kochetkov, S.V. Krylov, V.R. Fel'dgun, Comput. Math. Math. Phys. 40, 6 (2000)
11. V.G. Bazhenov, S.V. Zefirov, A.V. Kochetkov, S.V. Krylov, V.R. Feldgun. Matem. Mod. 12, 6 (2000)
12. V.L. Kotov, Vl.V. Balandin, Vl.Vl. Balandin, et al. Problems of Strength and Plasticity 79, 2 (2017) [In Russian]
13. D. Haimin, M. Wei, Z. Shujuan, Z. Zhiwei, L. Enlong. Cold Reg. Sci. Technol. 123, (2016)
14. M. Qin-Yong. J. Appl. Mech. Tech. Phys. 51, 3 (2010)
15. X. Qijun, Z. Zhiwu, K. Guozheng. Cold Reg. Sci. Technol. 106-107, (2014)
16. A.M. Bragov, V.V. Balandin, L.A. Igumnov, V.L. Kotov, L. Kruszka, A.K. Lomunov. Int. J. Impact Eng. 122, (2018)

DYMAT2019 P03

Analyzing resistance to penetration of a conical striker into sand at positive and negative temperatures, based on the results of inverse experiments

Anatoliy Bragov[1], *Vladimir V.* Balandin[1], *Vladimir Vl.* Balandin[1], *Vasiliy* Kotov[1,*], *Svetlana* Litvinchuk[1]

[1]Research Institute of Mechanics, National Research Lobachevsky State University of Nizhny Novgorod, 603950, Nizhny Novgorod, Russian Federation

Abstract. The laws of contact interaction between rigid and deformable strikers with dry and water-saturated soils in a wide range of temperatures were studied experimentally. Studies of the processes of impact and penetration of a steel conical striker into frozen sandy soil were carried out on the basis of the inverse experiment employing methodology of measuring bars. The dependences of the maximal values of the resistance force to penetration into soil of cones as a function of impact velocity ranging from 100 to 400 m/s are presented. The condition of sandy soil samples before freezing at a temperature of - 18°C is characterized by almost complete water saturation. A comparative analysis of the forces resisting to penetration of a striker into compacted dry, water-saturated and frozen sandy soil has been carried out. The resistance of frozen soil to penetration at low impact velocities significantly exceeds the resistance of dry and water-saturated soils. According to the results of the present experiments, at impact velocities over 300 m/s, the resistance curves of frozen and water-saturated soil tend to approach each other.

1 Introduction

The behavior of frozen soil is well enough studied in the experiments on uniaxial and triaxial compression at pressures up to 20 MPa and strain rates up to 10^{-2} s^{-1} [1-3]. Higher strain rates of the order of 10^2 - 10^3 s^{-1} were realized in the experiments using the SHPB system [4, 5], in which the deformation diagrams of frozen sand were obtained at a temperature of -28 ° C. The experimental data are used to equip mathematical models of the elastoplastic behavior of soil with various approximations of yield and failure surfaces [1–5]. More complex models explicitly take into account the dependence on temperature [6] or the influence of incompletely frozen water [7]. The elastic properties of frozen sand, characterized by the velocities of propagation of compression and shear waves, were determined in [8–10]. It was found that the velocity of a longitudinal wave in a water-saturated frozen soil at temperatures below -10°C could amount to 3-4 km/s.

An experimental complex for determining the main parameters of the process of impact and penetration of solid deformable bodies into soft soil media, based on the methodology of the inverse experiment with a measuring bar, was presented earlier in [11–16]. The forces resisting penetration of flat-ended strikers with hemispherical heads into compacted dry sandy soil are determined. Peculiar features of determining the maximal resistance force and the force values at quasi-stationary state of penetration of a flat-ended striker into a water-saturated soil, associated with dispersion during the propagation of short pulses of force in a measuring bar, were demonstrated. The maximal values of the force resisting to penetration of a hemispherical striker into dry, wet and water-saturated sandy soils were determined.

However, the results of impact experiments with frozen soil are not presented well enough in the available literature, though they could be used for numerical verification of mathematical models. The paper presents new results of inverse experiments, in which time histories of the resistance force and the dependences of the maximum values of the resistance to penetration of a conical striker into frozen sand were determined.

2 Measuring bars methodology in inverse experiment

Measuring bars methodology in inverse experiment was used to determine the resistance forces acting on heads during penetration into frozen sand.

In the inverse experiment, a resistance force was measured at an initial stage of penetration. The technique of measuring the force resisting the penetration of a striker into the sand using a measuring bar is as follows [12]. A container filled with sand is accelerated up to the required velocities and impacted against a stationary striker fixed on a measuring bar. The impact velocity and material properties of the bar are to be such that no plastic strains should occur in the bar. In this case, an elastic strain pulse ε (t) is formed in the bar. Registering this pulse makes it possible to determine force F, acting on the striker upon its interaction with the medium, according to the well-known relation $F(t) = E\varepsilon(t) S$, where E is elastic modulus of the bar, S is its cross section area. Thus, in this method, the task of measuring forces is greatly simplified and reduced to registering an elastic strain pulse in the bar, using strain gages. The setup implementing this method is schematically depicted in Fig.1. In the present version of the inverse experiment, a soil container is accelerated using a 57 mm – caliber gas-gun with a two-diaphragm breech mechanism (2), which makes it possible to provide stable and easily controlled impact velocities in the range of 50 -500 m/s.

The container is a thin-walled cartridge, made of D16-T aluminum alloy (3), filled with soil medium (4). To prevent soil from spilling in the process of preparation of the experiment and during the acceleration of the container, the front part of the container is sealed with 0.01 mm-thick lavsan film (5). The film is fixed and secured against the soil surface with a vinyl-plastic ring (6).

The impact velocity of the container was determined using two electric-contact transducers (7) located in the orifices of the barrel drilled in front of its muzzle. A 1.5 m-long and 20 mm-dia steel rod with a yield strength of over 2000 MPa was used as a measuring bar (8). One of the ends of the measuring bar has a threaded orifice (M10) housing a cylindrical striker with a head of appropriate geometry (9). The bar is located at a certain distance from the barrel muzzle, so that the impact occurs immediately after the container entirely leaves the barrel. The stand, on which the bar is located, has adjusting supports (10), which ensure the axisymmetric nature of the interaction. The rear end of the bar rests against a special damper (11), preventing it from displacement and damping the impact energy. Impact takes place inside the vacuum chamber (12), to which the gun barrel (13) is connected and into which the measuring bar (8) with the striker (9) is inserted. The cylindrical parts of the striker heads were 19.8 mm in diameter, with a hemisphere radius of 10 mm and were made of 45 steel ($\sigma \geq 600$ MPa) and EP638 steel ($\sigma \geq 1800$ MPa).

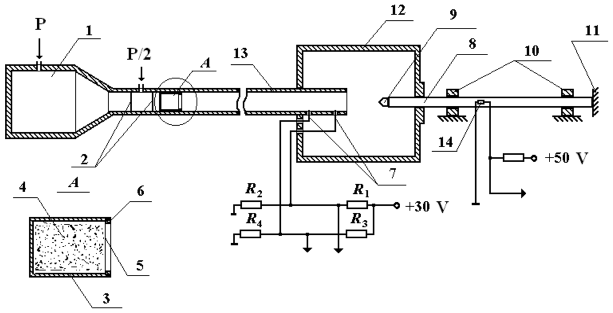

Fig.1. Schematic representation of the setup for measuring forces resisting to penetration in the inverse experiment.

The measuring bar was made of 03N18K9M5T steel with the density of 8050 kg/m^3, Young modulus of 186 GPa and yield strength of 2 GPa. The bar was 20.5 mm in diameter and 1.5 m in length. At one end, the bar had a threaded orifice (M10) for screwing in heads of required geometries. The conical heads with a cone angle of 60 ° were used in the experiments. Two types of the heads with a base diameter of 19.8 mm and 10 mm were used. The heads were made of 03N18K9M5T steel.

Besides, the effect on the experimental results of the threaded connections and joints between the head and the bar was evaluated using a 12 mm-dia 30HGSA steel with a yield strength of 700 MPa. One of the ends of the bar was in the form of a cone with an angle of 60 ° (Fig. 2).

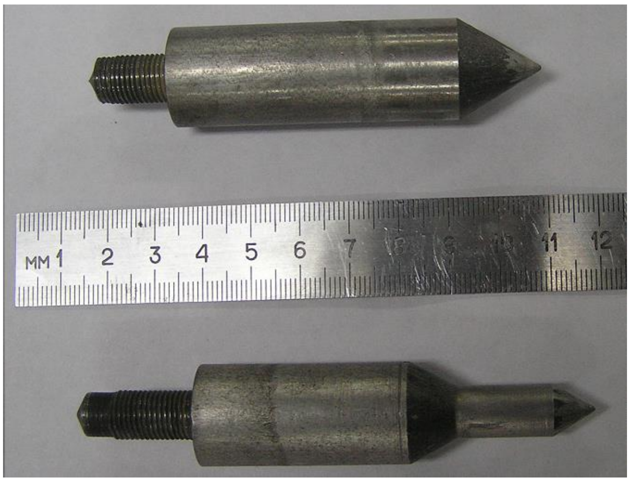

Fig.2. The heads of measuring bars used in the inverse experiments**.**

The experiments were carried out with a sand mixture of natural composition, from which particles larger than 1 mm and smaller than 0.1 mm had been removed. The accelerated containers were filled with dry sand, which was then compacted to an average density of about 1,750 kg/m^3. The containers were made of D16T alloy in the form of a thin-walled 70 mm high cylindrical cartridge with a wall thickness of 1.4 mm, an outer diameter of 56.8 mm and a bottom thickness of 2 mm. The containers were weighed to find the mass and density of the dry sand, and then gradually filled with water until the sand was fully saturated. Further humidification resulted in the formation a water layer over the surface of the sand, so the excess water was poured off. The containers were weighed again to determine the density of the water-saturated sand and its moisture content relative to its initial density. The average density of the water-saturated natural mixture was respectively 2090± 2050 kg/m^3. Since sand is mainly consists of quartz particles, the density of which is 2650 kg/m^3, thus, the porosity of sand is 0.34. When all the cavities are completely filled with water, the density of the humid sand should increase by 340 kg/m^3, and the density of the water-saturated sand should be equal to 2090 kg/m^3, which actually was the case during the preparation of the experiments. The moisture content of water-saturated sand was 18–19%. Then the container with water-saturated soil was frozen at -18 ° C in a freezer for at least 2 days.

When freezing, some of the water was displaced from the sand (since the density of ice is somewhat lower than that of water). The surface of the container got covered with a layer of ice which was removed before the experiment. After that, the container was weighed to find the density of the frozen sand. The average density of the frozen sand was 2050±50 kg/m^3.

3 Formulating the problem in numerical modeling

To get a better insight into the processes taking place during the impact of solid bodies against soil and to choose the conditions for inverse experiments, numerical methods evaluating the influence of geometric dimensions of the containers on the integral loads at the initial, nonstationary state of penetration into frozen soil were used in the present study. The computations were done using Grigoryan’s model of soil media, which contains a system of differential equations expressing laws of conservation of mass, pulse and constant maximal attained in the process of actively loading the soil, as well as equations of the theory of plastic flow with plasticity condition of Mises-Schleicher. The system of differential equations is closed with finite relations determining pressure and a fractional- rational function in the condition of plasticity of the soil medium. The applied Grigoriyan’s model of soil media describes failure of the structure of frozen soil under compression and the increase in shear resistance with increasing pressure [15, 16].

The system of equations of soil dynamics is complemented by initial and boundary conditions. A contact algorithm of "impermeability" along the normal line with "sliding along the tangent with dry friction" is used on the head of a conical striker contacting with soil medium, in accordance with Coulomb’s friction model with a constant friction coefficient. The normal and shear stresses on the free surfaces of the soil and the striker were set equal to zero. The outer boundaries of the computed soil region correspond to the geometric dimensions of the container used in the inverse experiment. The deformation of the container is not accounted for, the effect of the container walls is modeled by two versions of imposing the boundary conditions: “impermeability” along the normal and free sliding in the tangential direction and “free surface”, corresponding to the absence of any walls. Stresses and velocity of the soil particles are equal to zero at an initial time. The striker is assumed to be rigid, moving at a constant speed equal to the impact velocity.

4 The results of experiments

Fig. 3 presents the pulses of resistance force obtained in inverse experiments acting on the cones with different basis diameters: 10 mm, 12 mm and 20 mm, at impact velocities of 356 m/s, 354 m/s and 339 m/s, respectively. The maximum is reached when the cone is completely immersed into the soil. Until the maximum is reached, a time interval is noted, which is characterized by an increase in force close to a parabolic one and practically coincides for all used strikers. No signs of the effect of the joints on the pulse shape were revealed on the dependences of the force on time.

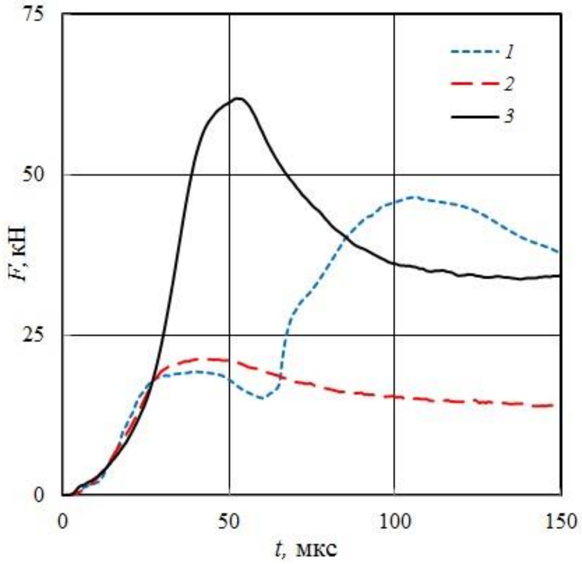

Fig. 3. The dependences of the force resisting to the penetration of 10, 12 and 20mm-dia cones into frozen soil, obtained during inverse experiments at impact velocities of 356, 354 and 339 m/s respectively.

Fig. 4 presents dimensionless dependences of the maximal values of the force resisting penetration of cones with a base diameter of *d*=10 (a) and 12 (b) as a function of impact velocity. The data presented in Fig.4 were obtained in inverse experiments (dark triangles), the solid and dashed lines correspond to the results of numerical calculations with boundary conditions that simulate absolutely rigid and compliance containers. Good agreement between the experimental data and numerical results is evident. The containers in the experiments were assumed to be absolutely compliant for all considered diameters of conical strikers. The proximity (taking into account the variability of experimental data) of the maximal values of the forces resisting penetration of conical strikers of 10 and 12 mm in diameter at impact velocities of more than 150 m/s, is to be noted. All dimensionless resistance forces exhibit a similar change from 3 to 1.5 at velocities from 200 to 400 m/s.

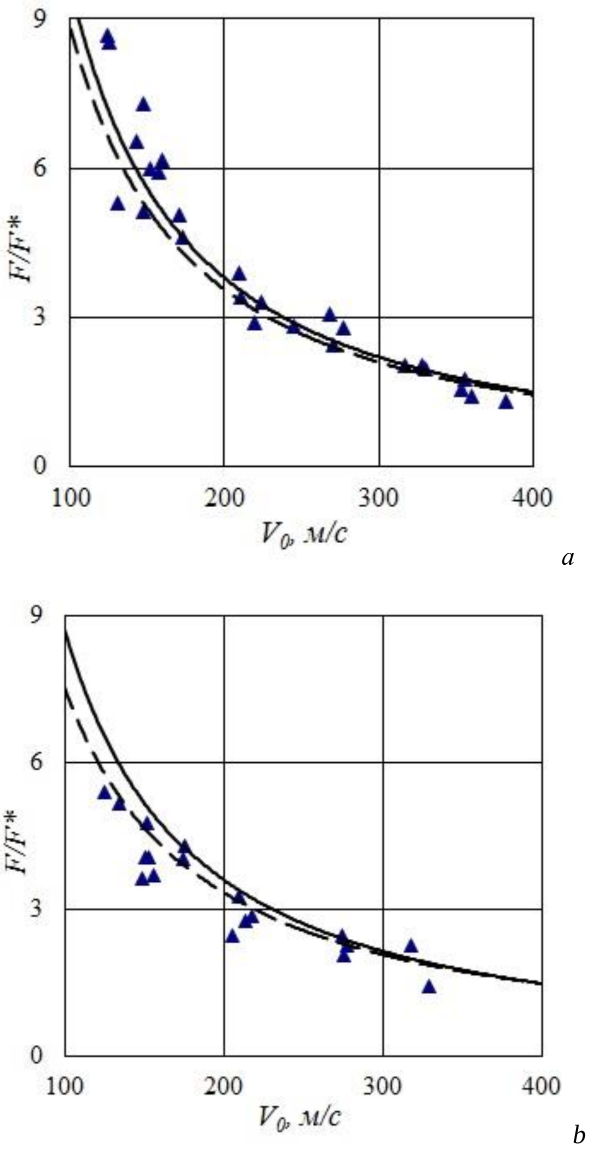

a

b

Fig. 4. Dimensionless dependences of the maximal values of the force resisting penetration of cones with a base diameter of d =10 (a) and 12 (b) as a function of impact velocity, obtained in inverse experiments and numerical results.

Fig.5 shows the dimensionless dependences of the maximal values of the force resisting penetration of the cone into the frozen (dark triangles and solid line), compacted dry (oblique crosses and dashed lines) and water-saturated soil (light triangles and dash-dotted lines). The markers correspond to the data of the inverse experiment, the lines show the results of axisymmetric numerical computations of the cone penetration into half-space of the soil.

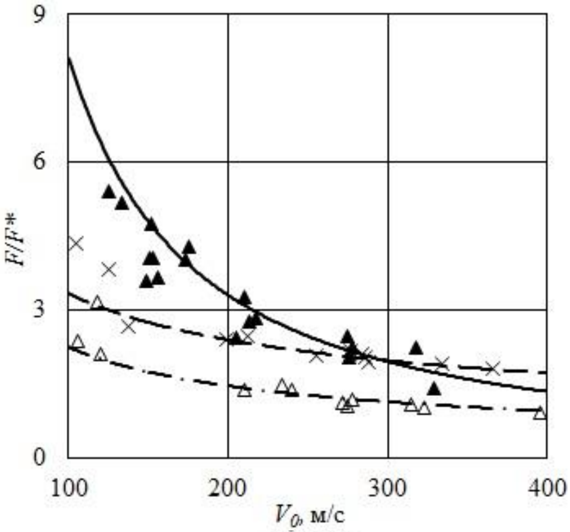

б

Fig. 5. Dimensionless dependences of the maximal values of the force resisting penetration of cones into frozen, dry and water-saturated soil as a function of impact velocity, obtained in inverse experiments and numerical results

Conclusion

For the problems of penetration of conical strikers into frozen and water-saturated soil, a fairly good agreement between experimental data and numerical results can be obtained with the help of Grigoryan’s model accounting for the pressure-dependent parameters. No significant effect of the threaded connection and joints between the head and the bar on the experimental results was found. This widens the scope of the inverse experiment methodology and the measuring bars technique by way of using changeable heads of required geometries. Resistance of frozen soil to penetration at low impact velocities is significantly higher than that of dry and especially water-saturated soils. According to the present experimental results, at impact velocities over 300 m/s, the resistance diagrams for the frozen and water-saturated soils tend to approach each other.

The work is financially supported by the Federal Targeted Program for Research and Development in Priority Areas of Development of the Russian Scientific and Technological Complex for 2014-2020 under the contract No. 14.578.21.0246 (unique identifier RFMEFI57817X0246) in part of modeling and by the Russian Science Foundation (Grant No. 16-19-10237-П) in part of experiments

References

1. Z. Shujuan, L. Yuanming, S. Zhizhong, G. Zhihua. Cold Reg. Sci. Technol. 47, (2007)
2. L. Yuanming, J. Long, C. Xiaoxiao. Int. J. Plast. 25, (2009).
3. Y. Yugui, L. Yuanming, L. Jingbo. Cold Reg. Sci. Technol. 60, (2010).
4. D. Haimin, M. Wei, Z. Shujuan, Z. Zhiwei, L. Enlong. Cold Reg. Sci. Technol. 123, (2016)

5. M. Qin-Yong. J. Appl. Mech. Tech. Phys. 51, 3 (2010)
6. X. Qijun, Z. Zhiwu, K. Guozheng. Cold Reg. Sci. Technol. 106-107, (2014)
7. R. Yang, E. Lemarchand, T. Fen-Chong, A. Azouni. Int. J. Solids Struct. 75-76, (2015)
8. Z. Zhiwu, K. Guozheng, M. Yue, X. Qijun, Z. Dan, N. Jianguo. Mech. Mat. 102, (2016)
9. M. Christ, J. Park. Cold Reg. Sci. Technol. 58, (2009)
10. J. Park, J. Lee. Cold Reg. Sci. Technol. 9, (2014)
11. X.Z. Ling, F. Zhang, Q.L. Li, L.S. An, J.H. Wang. Soil Dyn. Earthq. Eng. 76, (2015)
12. V.V. Balandin, A.M. Bragov, L.A. Igumnov, A.Yu. Konstantinov, V.L. Kotov, A.K. Lomunov. Mech. of Solids 50, 3, (2015)
13. Vl.V. Balandin, Vl.Vl. Balandin, A.M. Bragov, V.L. Kotov. Tech. Phys. 61, 6, (2016)
14. V.L. Kotov, V.V. Balandin, A.M. Bragov, Vl.Vl. Balandin. Tech. Phys. Let. 43, 9, (2017)
15. V.L. Kotov, Vl.V. Balandin, Vl.Vl. Balandin, et al. Problems of Strength and Plasticity 79, 2, (2017) [In Russian]
16. A.M. Bragov, Vl.V. Balandin, V.L. Kotov, Vl.Vl. Balandin. Tech. Phys. 63, 4, (2018)
17. A.M. Bragov, V.V. Balandin, L.A. Igumnov, V.L. Kotov, L. Kruszka, A.K. Lomunov. Int. J. Impact Eng. 122, (2018)

Thermal effects on the dynamic damage and fracture of a dual phase automotive steel

Sarath Chandran[1,*], *Wenqi* Liu[2], *Junhe* Lian[3], *Sebastian* Münstermann[2], *Patricia* Verleysen[1]

[1]MST-DyMaLab, Department of Electromechanical Systems and Materials, Ghent University,Technologiepark 46, 9052, Gent, Belgium
[2]Steel Institute, RWTH Aachen University, Intzestraße 1, 52072, Aachen, Germany
[3]Advanced Steel and Applications, Department of Mechanical Engineering, Puumiehenkuja 3, PL 14200, Espoo, Finland

Abstract. The effect of temperature and strain rate on the plastic deformation, damage and fracture of a commercial dual phase steel (DP1000) has been investigated experimentally by uniaxial and fracture tensile tests. In the study, temperatures of -40 to 300 °C and strain rates of 0.0001 to 1000 s^{-1} are covered, thus encompassing conditions experienced in automotive crash scenarios. Material properties including yield and ultimate tensile strength, uniform elongation, strain rate sensitivity and fracture area reduction, together with their dependence on temperature, have been systematically determined and discussed. The steel is found to be susceptible to dynamic strain aging (DSA) primarily at higher temperatures and lower strain rates. This phenomenon controls the deformation between 200 and 300 °C. The material experiences a significant drop in uniform and total ductility in the DSA range with negative strain rate sensitivity, thus indicating poor formability at these conditions. Increased strain rates and multiaxial stress states delays or diminishes the occurrence of DSA. The comprehensive experimental series allowed to better understand the complex relationship between strain rate and temperature, and the effect these conditions have on damage properties of the dual phase steel under study.

1 Introduction

The application of the advanced high strength steel alloys (AHSS) has been increasing in the automotive industry for weight reduction and collision safe performance. Among the AHSS, dual phase steel has gained reasonable popularity due to its high strength and relatively good formability. However, the temperature of the dual phase steel is observed to increase significantly during plastic deformation [1], which inevitably affects the plastic flow and formability of the material [2]. It is also reported that the temperature and strain rate affect a large group of mechanical properties with its significant impact on the stress-strain relationship and therefore influencing the forming properties [3-5].

The description of the flow stress considering the effects of temperature and strain rate is important in effective material design beside the microstructure. As the final application of the dual phase steel is mainly in the automotive sector, crash performance has been vastly studied under room temperature and high strain rates [3,6-10]. An increase in both the yield and ultimate strength and loss of ductility at dynamic strain rates are the common conclusions from the research. Deformation parameters become crucial during the forming of the dual phase steel parts into various complex shapes utilized in automotive applications. In sheet metal forming, strain rate and temperature significantly vary over a wide range. Local temperatures may even rise upto 220 °C due to deformation heating at high strain rates. Only a limited number of studies in the literature partially cover these thermomechanical conditions and even then a comprehensive overview of the material behavior accounting for the combined influence of temperature and strain rate is still lacking. Moreover, relevant studies are primarily targeted towards plastic deformation. Indeed, the impact of these interdependent parameters on the material damage and fracture has not been evaluated conclusively.

In crash situations, the mechanical response of the car body at actual local temperatures, stress states and strain rates determines the energy absorption and is thus of great importance for the structural integrity. In addition, structural analyses and safety assessments require constitutive relations between strain and flow stress which again contain temperature, strain rate and stress state as important parameters. In this study, uniaxial and fracture tensile tests have been performed on the commercial dual phase steel DP-K1000 covering applicable temperatures, strain rates and stress states experienced in automotive crash situations. The study thus provides an insight into the complicated effect of temperature, strain rate and stress state on the mechanical behaviour. The paper provides experimental data followed by an in-depth analysis and interpretative discussion.

2 Material and Methods

A commercial dual phase steel (DP-K1000) supplied in the form of rolled sheet with a thickness of 1.5 mm is used in this investigation. The microstructure consists of a mixture of ferrite grains (55%) and martensite islands (45%) along the rolling direction. The average grain size in the ferrite is less than 2μm.With such a microstructure, soft ferrite takes up major part of the plastic straining while the role of the

---

[*] Corresponding author: Sarath.Chandran@UGent.be

mainly elastically loaded martensite islands is to enhance the global hardening and formability of the material.

A comprehensive experimental program considering the material plasticity and fracture behaviour under variable temperatures and loading conditions experienced in automotive crash situations is designed and carried out. To determine the intrinsic mechanical properties of the DP1000 steel, tests are performed at wide range of loading speeds thereby covering the quasistatic and dynamic strain rates (0.0001 to 1000 s^{-1}) and temperatures (-40 to 300 °C). Uniaxial tensile tests are performed on dogbone shaped specimen to extract information on material plasticity and specially designed notched tensile specimens are used to assess the material damage and fracture properties. The uniaxial tensile specimen has a gauge length of 6 mm and the corresponding width is 3mm. Purpose-based samples with a notched radii of 4.5, 1.8 and 0.4 mm are employed to target specific range of stress triaxialities (0.39 to 0.52). Readers are directed to [11] for detailed analysis on the design optimization of the specimen geometries.

An Instron material testing machine (Model 5569) is used to conduct experiments at static rates of loading whereas a Split-Hopkinson bar tensile setup of DyMalab at Ghent University is used for the high strain rate tests. Various cross-head and impactor velocities are imposed as corresponding test inputs on static and dynamic testing machines aiming at targeted strain rates in the central gauge or notched section of the specimens. Force history of the respective specimens are derived from the test equipment. A full field local deformation measurement based on high speed imaging and digital image correlation (DIC, MatchID software) is used to monitor the non-homogenous strain fields and to compensate for the overestimation of the strain measurements from the test machine data. A system comprising of a hot air furnace (open top) with a heating element of 2KW and temperature controller is used to reach high temperatures at rapid heating rates. Heat transfer between hot air and specimen is improved by the use of a fan for fast circulation of hot air through the furnace. A Julabo FP50-HL cooling system is used on the other hand to obtain low temperature in the specimen.

3 Results and discussion

3.1 Uniaxial tensile tests

Uniaxial tensile tests are performed on smooth dogbone specimens at variable temperatures (-40, 25, 100, 200 and 300 °C) under different loading rates from quasi static to dynamic range (0.0001, 0.001, 0.01, 500, 800 and 1000/s) to evaluate the temperature dependence on plastic deformation. The work hardening flow strength of DP1000 is found to increase from static to dynamic strain rates which revealed noticeable positive strain rate hardening effect at room temperature [12]. However, deformation at high strain rates mainly occurs under adiabatic conditions. Temperature as high as 150 °C is reached immediately before failure in a region with maximum equivalent plastic strain for a uniaxial tensile specimen at 800 s^{-1}, see Fig 1 whereas negligible temperature rise is observed at 0.0001/s thus exhibiting isothermal conditions. As such, this thermal softening on the flow stress behavior due to adiabatic heating effects at higher strain rates has to be taken into account and a correction procedure has to be introduced for effective comparison across strain rates.

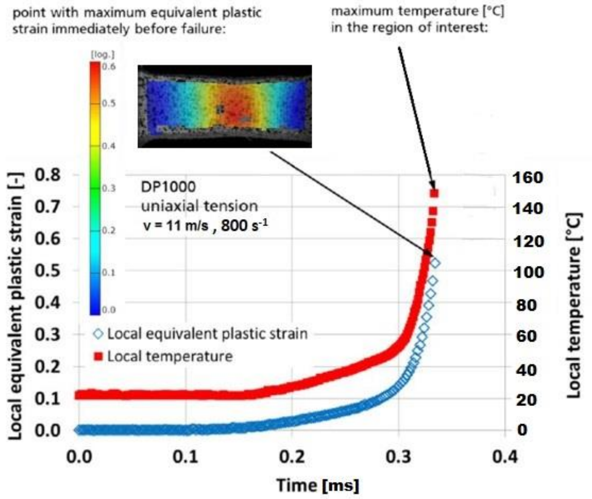

Fig. 1. Temperature and plastic strain evolution on uniaxial tensile specimen at 800 s^{-1}

Under truly adiabatic conditions, temperature increase depends on the strain level and is given by

$$\Delta T = \frac{\beta}{\rho C_p} \int_0^{\mathcal{E}} \sigma_{iso} \, . d\mathcal{E} \qquad (1)$$

Where ρ is the density of the material (8050 kg/m^3), C_p is the thermal capacity (465 J/kg/k) and β is the mechanical energy transformed into heat fraction. Temperature rise ΔT within the specimen is acquired based on the readings from the thermocouple attached to the bottom face. The fraction of plastic work converted into heat is estimated as 0.88 and is used for compensation of the flow stresses. Additionally, the temperature dependence function f(t) for DP1000 steel is determined based on the flow stress ratio between test temperature and reference temperature at different strain levels across various temperatures. Fig 2(a) displays the true stress values at -40, 25 and 100 °C for 1% strain and Fig 2(b) shows the resultant temperature dependent function. The adiabatic heating correction is achieved on the isothermal flow curves based on the value of β and f(t) at various strain rates according to the equation mentioned below :

$$\sigma_{adi} = f(t) . \sigma_{iso} \qquad (2)$$

The resultant isothermal stress-strain curves for DP1000 steel at strain rates of 0.0001, 0.01 and 500 s^{-1} can be observed in Fig 3. It is evident that adiabatic heating induces significant softening effect on the material flow stress and this phenomenon gets aggravated with increase in strain rate owing to the drastic rise in temperature within the specimen with increasing deformation.

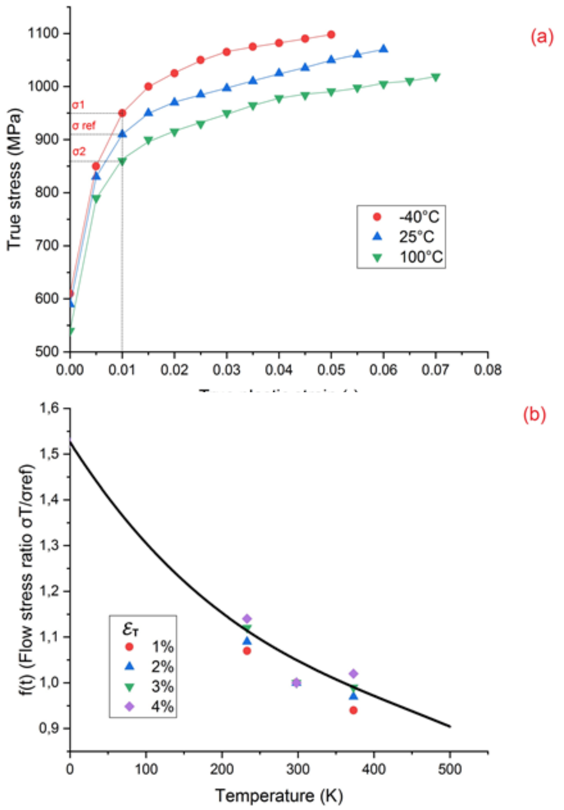

Fig. 2. (a) True stress – plastic strain curves of tensile specimen at -40, 25 and 100 °C (b) Temperature dependence function f(t)

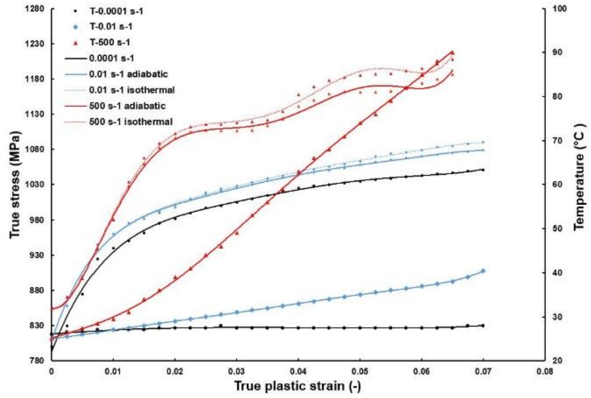

Fig. 3. Thermal softening effect on the stress-strain curve at various strain rates (0.01 and 500 s^{-1})

The influence of strain rate and temperature on the flow stress as a function of plastic strain is depicted in Fig 4. An increase in flow stress is generally observed at higher strain rates and decreased temperatures (see Fig 2a). An exception is found when the deformation takes place at temperatures of 200 and 300 °C. A significant shift from positive to negative strain rate sensitivity can be seen with increasing strain. Fig 4b gives an example of this phenomenon at 300 °C. In addition, a transition from the normal thermal softening behavior on the material strength is observed in these temperature ranges as opposed to general behavior observed in Fig 4a. Higher flow stresses are achieved at higher temperatures, see Fig 4c and d, especially at 300 °C and static strain rates. Besides, minor serrations are also observed at lowest strain rate when the material deforms at a temperature of 300 °C as shown in Fig 4b.

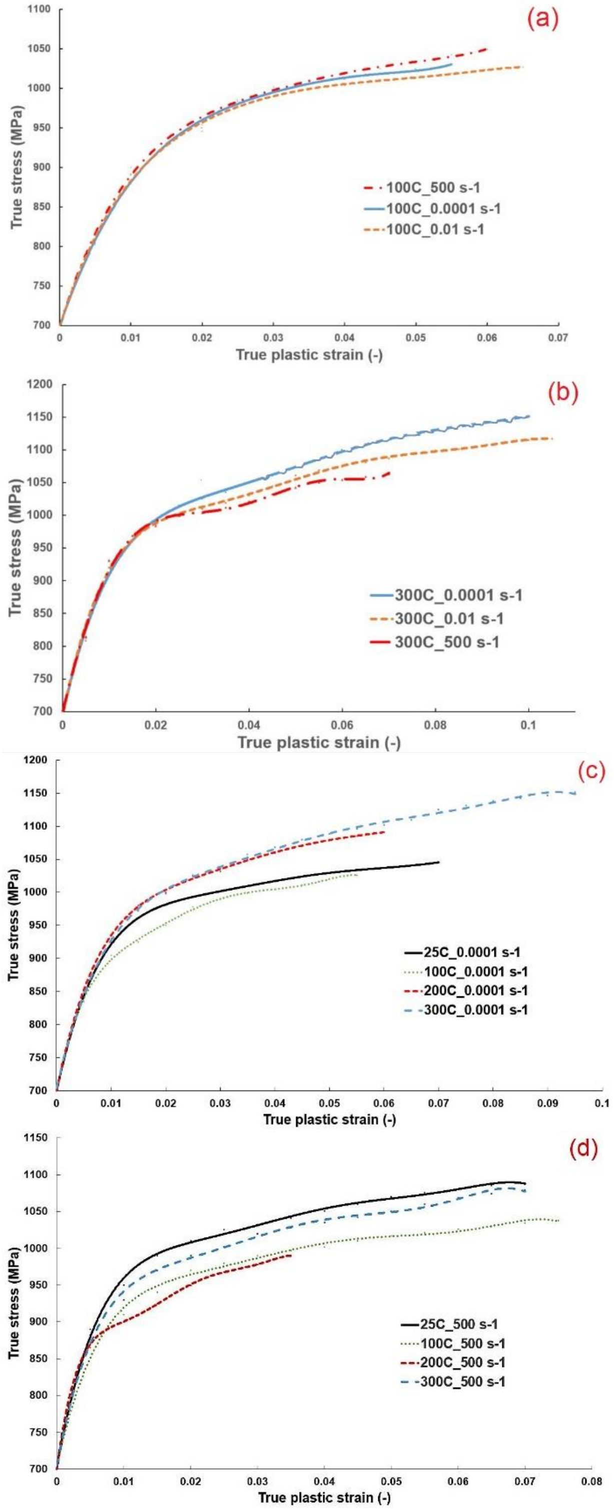

Fig. 4. Temperature and strain rate effects on the plastic deformation of DP1000 at a) temperature = 100 °C, b) temperature = 300 °C, c) strain rate = 0.0001 s^{-1} and d) strain rate = 500 s^{-1}

To have an in-depth quantitative analysis of the influence of temperature on material plasticity, yield and tensile strength of the DP1000 steel is extracted and plotted as a function of both strain rate and temperature. Fig 5 gives the yield and ultimate tensile strength under various deformation conditions. The material exhibits continuous yielding behaviour and pronounced strain hardening at all conditions. Large strain hardening ratios are observed which slightly decreases with increase in strain rate. Significant strain hardening exhibited by this material could be due to the presence of unlocked mobile dislocations which are introduced into the ferrite by the stresses induced by the formation of martensite. Local internal stresses developed during martensite formation could potentially help the initial yielding and allow for plastic flow in different zones throughout the material which in turn could be a reason for high strain hardening.

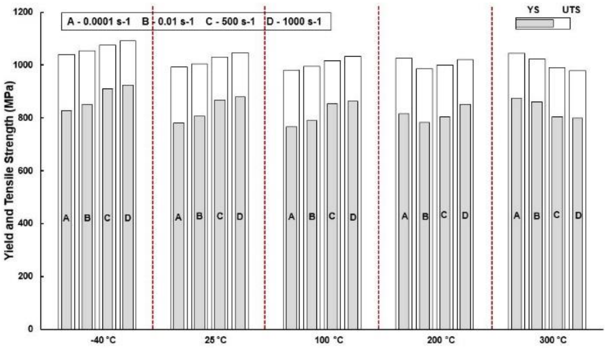

Fig. 5. Yield and ultimate tensile strength as a function of strain rate and temperature

As expected, higher yield and tensile strength is attained at -40 °C, however, at the expense of deformation capacity. Looking closely into Fig 5, the notion of the abnormal strain rate hardening effect at 200 and 300 °C is confirmed. Positive effect of the temperature on the strength is also seen especially at 300 °C. The peculiar phenomena, such as abnormal negative strain rate hardening, serrations and unusual positive temperature effect, are characteristic features of the dynamic strain aging (DSA) effect. DSA is caused by the Cottrell cloud i.e. the interaction between dislocation and interstitial dissolved foreign atoms like carbon. It can be explained as follows. Ferrite in the dual phase steel after quenching is expected to be supersaturated with carbon. Dislocations created during the deformation of ferrite can act as effective nucleation sites for precipitates. At the microscopic level, when the interstitial dissolved foreign atom's diffusion rate is equally close to the dislocation mobility speed, dislocations adhere to the foreign atoms, thereby restricting their movement, thus resulting in the formation of a Cottrell cloud. Accordingly, the externally applied stress is required to free the dislocations and produce further plastic deformation. The dissolved atoms diffusion rate is highly increased by the rising temperature and the dislocation mobility is mainly controlled by the plastic deformation rate i.e. the external loading strain rate.

Comparing Fig 4 c and d, it can be noticed that DSA effect i.e the negative strain rate hardening at a strain rate of 0.0001 s^{-1} and 200 °C is no longer observed in the dynamic strain rate range of 500 s^{-1}. Moreover, dynamic loading rates paved the way to a regular thermal softening at 200 °C. This phenomenon is also detected in Fig 5. Increase in the plastic deformation strain rate or the dislocation mobility rate will lead to shorter time of deformation and the precipitation which is mainly a time dependent process involving both nucleation and growth is suppressed at high strain rates and thereby requires higher temperature for the precipitation to occur again. On the other hand, at low strain rates, increased flow stress due to hardening by solute cluster formation and precipitation is expected beyond a certain strain level, yielding an increase in the ultimate tensile strength. DSA is thus sensitive to both temperature and strain rate. Consequently, in a steel with a specific carbon content, at a certain temperature and strain rate range, the repeated interaction between dislocation and dissolved carbon atoms becomes significant in the whole plastic deformation process resulting in serrations. Meanwhile, the required external stress leads to abnormal negative strain rate hardening and positive temperature effect on the flow stress at this DSA range. Furthermore, the increase of strain rate will raise the active threshold of the DSA effect, which means postponed DSA effect occurrence temperature and this phenomenon is also verified by the experimental results. At the static strain rates, DSA effect is observed at higher temperatures, while at dynamic loading rates, only 300 °C exhibits this peculiar phenomenon.

Uniform elongation of the DP1000 steel under various test conditions is displayed in Fig 6. It is evident that uniform strain is sensitive to both strain rate and temperature. An increasing strain rate generally lowers the uniform elongation at room temperature and -40 °C which explains tradeoff between strength and ductility in this dual phase steel. Large uniform ductility is observed at -40 °C primarily at the lowest strain rate. This is possibly related to the strain induced transformation of retained austenite, which is metastable, to martensite by cold plastic deformation. However, this improvement is mainly observed at low strain rate as higher loading rates increase the stability of retained austenite. Major drop in uniform ductility with increasing strain rates is shown by the tensile tests at -40 and 25 °C whereas a rather moderate decline is observed with rise in test temperature. Fig 6 also displays the evolution of strain rate sensitivity with respect to temperature. It is clearly depicted that strain rate sensitivity is adversely affected by the rise in temperature which in effect confirms the presence of dynamic strain aging effect on this dual phase steel at higher temperatures.

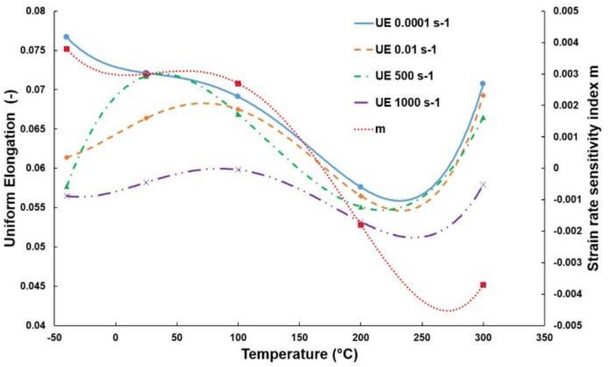

Fig. 6. Evolution of uniform elongation and strain rate sensitivity with temperature in DP1000 steel

Uniform elongation suffers simultaneously with increasing strain rates and temperatures. Combined with negative strain rate hardening, lower uniform strains at this

DSA range should result in poor formability of the DP1000 steel. The plastic instabilities in the form of local necks may start early in the deformation and the strain will accumulate in these instabilities due to the negative strain rate sensitivity. This phenomenon is predominantly observed at temperatures around 200 °C. This shorter uniform elongation noticed at this intermediate temperature range is referred to as blue brittleness effect especially since it leads to a reduction in the material toughness. Blue brittleness is further identified as a derivative of DSA effect. Therefore, temperatures between 200 and 300 °C should be avoided at any strain rate during forming operation on this dual phase steel grade, especially at dynamic rates, since prevalent adiabatic heating might aid the temperature in approaching the DSA range in this material.

According to Lou and Northwood model [13] the difference between the magnitude of work hardening rates at an elevated temperature and that at room temperature will help to show the dynamic strain aging effects (Δσ’) directly.

$$\Delta\sigma' = \Delta\sigma_T - \Delta\sigma_0 \qquad (3)$$

Fig 7 shows the effect of testing temperature on Δσ’. According to the figure, Δσ’ falls in the negative range up until around 150 °C for static loading rates and 250°C under dynamic loading conditions. Hence, DSA effects are dominant from 150 °C under static strain rates and from 250 °C under dynamic loading mode. Below these temperatures, softening effects are dominant in the respective loading regimes.

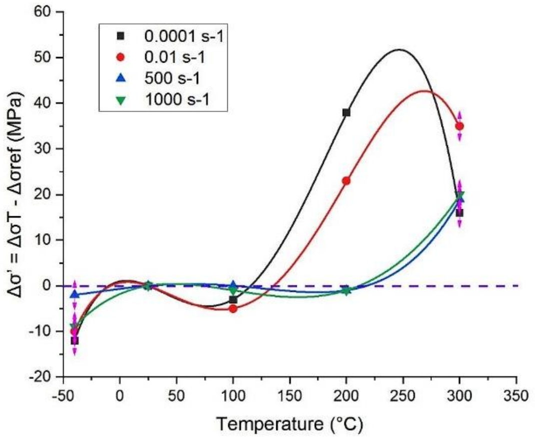

Fig. 7. Effect of deformation temperature on the dynamic strain aging effects

3.2 Fracture tensile tests

Tensile tests are carried out at different temperature and strain rate ranges on multiple specially designed notched specimen geometries with notched radii of 4.5, 1.8 and 0.4 respectively. These tests are then used to characterize the temperature and strain rate effect on the damage and fracture performance of the DP1000 steel. The specimen geometries were designed to achieve certain stress triaxialities in the assumed damage initiation point.

The effect of strain rate on material damage and fracture is studied in [12]. From the study, it is identified that strain rate has a positive effect on the material strength for all the notched tensile specimens primarily in the transition from static to dynamic rate of loading. This positive effect is also amplified by the increase in the stress triaxiality thereby establishing a complex interrelationship between stress state and strain rate on the material behaviour. Conversely, material ductility is negatively affected by the increase in stress state and is further degraded by the strain rate.

The influence of temperature on the material damage and fracture behaviour is the point of focus in the present investigation. Consistent with the results of uniaxial tensile tests, with the rise in test temperature, DSA effect also comes into existence in all fracture tests and shows similar temperature and strain rate trend as smooth tensile tests. Therefore, it could be argued that the effects of temperature and strain rate on the damage and fracture behaviour of DP1000 steel are mainly succeeded from their effects on plastic deformation.

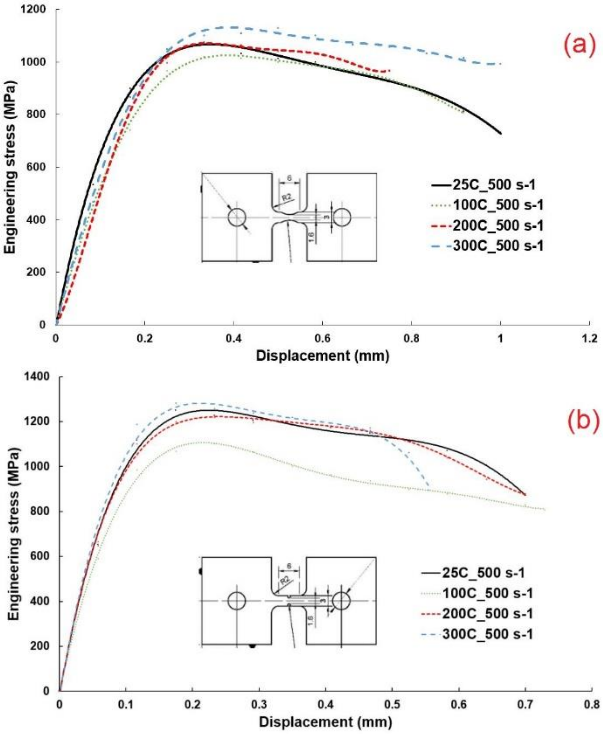

Fig. 8. Influence of temperature on the nominal stress-displacement curves at 500 s-1 for a) R4.5 tensile specimen and b) R0.4 tensile specimen

Fig 8 a and b shows the impact of temperature on the material response for notched tensile specimens R4.5 and R0.4 respectively at a strain rate of 500 s^{-1} as an example. Local displacements are extracted from the notched section of the sample using the digital image correlation method. Notched specimen R4.5 shows dynamic strain aging effects at temperatures 200 and 300 °C under both static and dynamic strain rates whereas this unusual positive hardening effect with temperature is found to diminish with increase in stress state for notched samples R1.8 and R0.4 as seen in Fig 8 b. Furthermore, DSA effect is effectively curtailed towards later-half of the material plastic deformation with increase in stress triaxiality. The obtained results rather highlight the presence of a complex influence of the stress state on the basic process of dynamic strain aging.

Further analysis and quantification of the impact of temperature on the material damage and fracture response is performed based on the comparison of absorbed energy and fracture area reduction ratio across various stress states under different temperatures and strain rates. Absorbed energy is calculated as the area under the force vs displacement curves for all the tensile tests executed whereas area reduction ratio is estimated based on the equation mentioned below :

$$AR = \frac{A_0 - A_f}{A_0} \qquad (4)$$

Where A_0 is the initial cross-sectional area in the critical zone of the test specimen and A_f is the final area based on the fracture surface measurements.

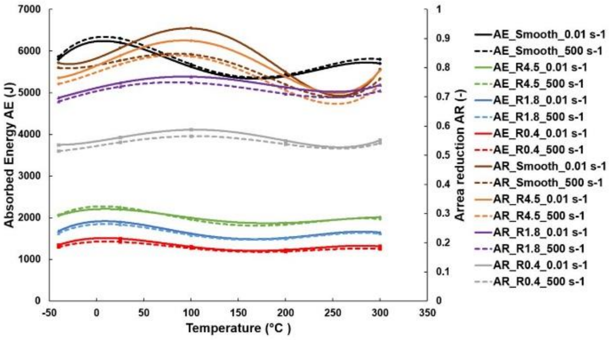

Fig. 9. Effect of temperature on the total absorbed energy and area reduction ratio for all the tensile specimen geometries at strain rates of 0.01 and 500 s-1

A drastic reduction is noticed for both absorbed energy and fracture area reduction ratio with changing stress state from uniaxial to notched tensile tests. This observation substantiates the detrimental effect of the stress triaxiality on the toughness of the material. As an example, absorbed energies and area reduction ratios of smooth and notched specimens are depicted at strain rates of 0.01 and 500 s^{-1} for the temperatures considered in this study, see Fig 9. Irrespective of the stress state within the specimen, lowest absorbed energy is observed around 200 °C which confirms the occurrence of blue brittleness in this temperature range. Moreover, absorbed energy decreases slightly in the DSA range for all the tensile specimens which indicates that the presence of dynamic strain aging in this dual phase steel might render it to be less effective option for crashworthiness in the automotive industry. However, this decline in the energy absorption under DSA is suppressed at higher stress states. Similar observation is also made in the case of area reduction ratios wherein decrease in ratio with rise in temperature and strain rate in the DSA range is constrained with increase in stress triaxiality from uniaxial stress state towards plane strain conditions.

Over hardening due to the solute drag effect on the dislocation is the main effect of DSA. However, as mentioned before, solute drag effect is also a function of strain rate. Difference in the mean strain rate distribution along the notch in addition to the probability of the activation of mobile dislocation sources by increasing the triaxiality of stretching and related surface morphology modifications could be a potential source for delayed and diminished effect of dynamic strain aging under high stress triaxiality conditions. These observations in the DP1000 steel calls for an improvement in the present plasticity and damage models considering the complex interrelationship between temperature, strain rate and stress state.

4 Conclusion

A critical relationship between temperature, strain state and stress state for the DP1000 steel is established from an extensive experimental campaign. DSA effect is dominant in the plastic deformation of the material primarily at high temperatures and low strain rates owing to the formation of Cottrell cloud. DSA has a positive impact on the strain hardening of the material whereas both strain rate sensitivity and material toughness are adversely affected by this phenomenon. Increasing the plastic deformation strain rate is found to raise the active threshold of DSA effect thereby diminishing the impact of dynamic strain aging at higher strain rates. Additionally, an increase in the stress state is found to suppress the effects of DSA. The influence of temperature and strain rate on the material damage and fracture behaviour is mainly succeeded from their effects on plastic deformation, however, the interdependency must be accounted for to ensure superior formability and absorption capacity.

The authors gratefully acknowledge the financial support of the Research Fund for Coal and Steel (RFCS) of the European Commission and the partners of the ‘Toolkit’ project for their technical support in this research. The authors also express their gratitude towards ThyssenKrupp Steel for supplying the steel sheets for the study.

References

1. A.Sachdev, J.Hunter, MTA.**13**, 1063 (1982)
2. D.Li,A.K.Ghosh,J.Mater.Process.Technol.**145**,281 (2004)
3. H.Huh,S.B.Kim,J.H.Song,J.H.Lim,Int.J.Mech.Sci. **50**, 918-31 (2008)
4. W.Wang,L.Huang,K.Tao,S.Chen,X.Wei,Mater. Des.**87**,835-44 (2015)
5. D.R.Satish,F.Feyissa,D.R.Kumar,Mater.Manuf.process.**010426914.2017.1317352** (2017)
6. N.D.Beynon,S.Oliver,B.T.Jones,G.Fourlaris, Mater.Sci.Technol.**21**,771-778 (2005)
7. A.Das,M.Ghosh,S.Tarafder,S.Sivaprasad,D.Chakrabarti, Mater.Sci.Eng.A.**680**, 259-268 (2017)
8. H.Takechi,M.Takahashi,K.Ito,T.Endo,Y.Tomota J.Iron Steel Inst.Jpn.**88**, 703-714 (2012)
9. H.Yu,Y.Guo,K.Zhang,X.Lai,Comput.Mater.Sci. **45**, 36-41 (2009)
10. S.Curtze,V.T.Kuokkala,M.Hokka,P.Peura, Mater.Sci.Eng.**A507**, 124-131 (2009)
11. S.Chandran,P.Verleysen,J.Lian,W.Liu,S.Münstermann, Proc.Eng.**197**, 204-213(2017)
12. S.Chandran,P.Verleysen,J.Lian,W.Liu,S.Münstermann , EPJ Web Conf.**183**, 02047(2018)
13. S. Lou, D.O. Northwood, Mater.Forum.**17,**153 (1993)

DYMAT2019 P05

Influence of Strain Rate on Fracture Behaviour of Ultra-High Strength Steel Sheet

Armin Abedini[*], *Cliff* Butcher, *Michael* Worswick

University of Waterloo, Department of Mechanical and Mechatronics Engineering, Waterloo, N2L 3G1, Canada

Abstract. In the present work the effect of strain rate on the constitutive and fracture response of two hot stamped, ultra-high strength steel sheet alloys Usibor®1500-AS and Ductibor®1000-AS is examined. These alloys have a nominal strength of 1,500 MPa and a minimum strength of 1,000 MPa, respectively. Miniature plane strain notch tension experiments are performed to study the influence of strain rate on the stress-strain response and strains to fracture under dynamic rates. A high-speed infrared (IR) camera was employed to measure temperature rise during deformation. In addition, high-speed digital image correlation (DIC) measurements were utilized for full-field strain measurement from the onset of deformation until fracture. Moreover, thickness strains of post-mortem specimens were measured under an optical microscope, the results of which were compared with the DIC data. The higher strength alloy is shown to exhibit higher temperature increase resulting in strong thermal softening and earlier localization of deformation at elevated strain rates. As a result, at the macro-scale (using DIC measurements), the strain to fracture was observed to decrease with increase in strain rate. In contrast, the local strain to fracture based on the reduction in thickness at the minimum cross-section showed similar values in quasi-static and elevated rates.

1 Introduction

Ultra-high strength steels (UHSS) processed through hot stamping, such as Usibor®1500-AS and Ductibor®1000-AS, are seeing extensive adoption within automotive structural applications, particularly within intrusion-resistant crash components such as b-pillars, roof rails and side sills, for example. Currently, the majority of research addressing the fracture resistance of such alloys utilizes experiments performed under quasi-static loading (*e.g.* Golling *et al.*, 2016; Ostlund *et al.*, 2016; Samadian *et al.*, 2019). Given the high rates of strain encountered during automotive crash events, it is important to understand the role of strain rate and temperature rise on the fracture response of automotive structural materials. The fracture behaviour of these materials under quasi-static conditions is relatively well understood, with the fracture strain often expressed as a function of the stress triaxiality and Lode parameter.

However, it is not clear whether the fracture strain increases or decreases at elevated strain rates under a constant stress state. In addition, under dynamic rates, the plastic work that is converted to heat does not have sufficient time to fully dissipate from the deforming area. This may cause a significant local temperature rise leading to temperature-induced softening and localization. Although it is well known that material ductility is enhanced at elevated temperatures, the earlier onset of localization associated with a temperature rise can lead to lower failure strains in terms of global measures such as the displacement to failure. However, a positive rate sensitivity is widely accepted to delay the onset of localization and strain rate sensitivity tends to increase with temperature for many materials. Consequently, the influence of elevated strain rate and the resulting temperature rise and thermal softening on the fracture response of UHSS is complex and not yet well understood.

The ductile fracture of high-strength steel sheets under quasi-static conditions is an active area of research (see for instance, Li *et al.*, 2010; Gruben *et al.*, 2011; Roth and Mohr, 2016; Deole *et al.*, 2018). However, when it comes to the effect of strain rate on fracture, the literature is scarce and the published data is contradictory in some respects. It was shown by Huh *et al.* (2008) that elongation to fracture increased at elevated strain rates in tensile tests on a TRIP600 steel sheet while elongation to fracture remained the same for TRIP800 and DP800. Winkler *et al.* (2008) found that both elongation and reduction in area increased in DP600 and DP780 steels. Interestingly, they also reported that elongation decreased with an increase in testing temperature while reduction in area increased. More recent studies by Roth and Mohr (2014) and Erice *et al.* (2018) on a range of high-strength steel alloys including DP590, TRIP780, DP980, CP980, and CP1180 revealed that the local fracture strain increased at high strain rates but with different degrees of rate sensitivity depending on the material. Rahmaan *et al.* (2017) highlighted the importance of length scale when reporting dynamic fracture strains of DP600 under shear loading. They discussed that although the macroscopic fracture strains measured by means of digital image correlation (DIC) techniques exhibited negative rate sensitivity, local fracture strains obtained by means of a grain boundary rotation technique increased by raising the strain rate.

The present paper further examines the effect of strain rate on the fracture behaviour of hot-stamped steels. In particular, the current work considers the

---

[*] Corresponding author: aabedini@uwaterloo.ca

dynamic fracture response of hot stamped Usibor®1500-AS and Ductibor®1000-AS using a miniature plane strain notch specimen. *In situ* DIC techniques are applied with high speed optical imaging to measure fracture strain, while high speed thermal (IR) measurements are used to characterize temperature rise during elevated rate testing. To study length scale effects, fracture strains of post-mortem samples were determined using an optical microscope and compared with the DIC measurements.

2 Materials and Experiments

The materials considered in this study include Usibor®1500-AS and Ductibor®1000-AS sheet with a nominal thickness of 1.2 mm. The materials were austenitized at 930 °C for 6.5 minutes and then quenched for 15 seconds in a die using a 900-ton hydraulic press. In addition, to produce a softer material, blanks of Usibor®1500-AS were cooled in still air to room temperature after the austenization process. This treatment results in a bainitic microstructure, while the die quenched condition leads to a martensitic microstructure for both materials. The Ductibor®1000-AS alloy has a lower carbon content which results in a lower martensite strength and hardness. The Vickers microhardness of the materials was measured using a 500 gf indenter force, the results of which are presented in Table 1. In addition, ultimate tensile strengths (UTS) in uniaxial tension along the transverse direction (TD) of the sheet materials are reported in Table 1.

Miniature coupon-level plane strain notch tensile specimens, with the geometry depicted in Figure 1, were fabricated along the TD of the as-quenched sheets.

Table 1. Vickers hardness and UTS of the materials. The data for Usibor® 1500-AS was obtained from ten Kortenaar (2016).

Material	Quench Condition	Vickers Hardness (HV)	UTS (MPa)
Usibor®1500-AS	Die Quenched (DQ)	486±8	1571±12
Usibor®1500-AS	Air Cooled (AC)	232±10	762±22
Ductibor®1000-AS	Die Quenched (DQ)	370±4	1122±9

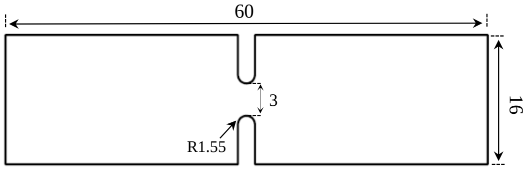

Fig. 1. Geometry of the notch specimen. All dimensions are in millimetres.

In order to study the role of strain rate on fracture, two different test velocities were considered: a quasi-static condition with a cross-head velocity of 0.004 mm/s and a dynamic state with a cross-head velocity of 125 mm/s. The quasi-static tests were conducted using a 100kN MTS model 45 servo-electric tensile frame whereas the elevated rate tests were performed using a hydraulic intermediate strain rate (HISR) apparatus, as can be seen in Figure 2. Stereo DIC was used for full-field strain measurements with Point Grey® 4.1 MP cameras with 180 mm Tamron® lenses with a frequency of two frames per second for the low rate tests. For the dynamic tests, high-speed Photron SA5 cameras were employed with 180 mm Tamron® lenses at a frame rate of 17,500 frames per second. All of the DIC analyses in this study were performed with a consistent virtual strain gauge length (VSGL) of 0.5 mm.

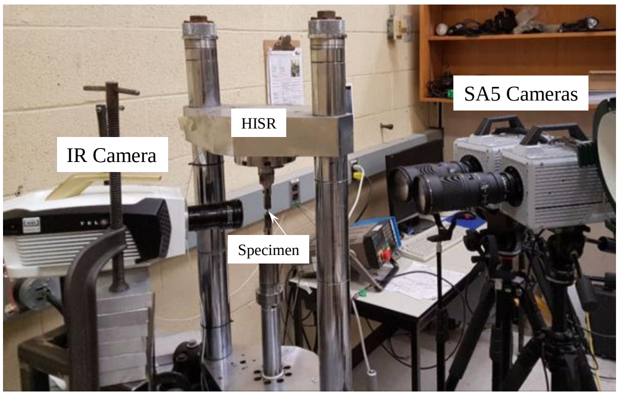

Fig. 2. Test setup for the dynamic test.

For the elevated rate tests, an infrared (IR) Telops FAST-IR 2K camera was utilized to measure the temperature on surface of the specimen with a frequency of 4,375 frames per second. To ensure repeatability, at least four samples were tested for each condition while representative data are reported in this paper.

Prior to each test, one surface of the sample was painted with a thin layer of white paint followed by applying black speckles to provide a speckle pattern for DIC measurements. The opposite surface of the sample (viewed by the IR camera) was painted black to improve emissivity and to minimize infrared reflections. Consequently, the temperature values measured by the IR camera were estimated as the actual surface temperature of the sample. A more sophisticated correction for temperature measurements can be done by emissivity characterization as done by Rahmaan *et al.* (2018) for aluminium alloys and will be addressed in future work. Note that the materials studied in this paper were coated with a thin layer of Al-Si to avoid corrosion; however, the coating may peel off from the base metal during deformation causing a false reading for the DIC and IR measurements. Therefore, the coating layer was carefully removed by sanding both sides of the specimen before painting.

3 Results and Discussion

The evolution of local strain rates as a function of major strain is shown in Figure 3 for Usibor®1500-AS in the air cooled condition. The local values were determined using a DIC circle inspector with a radius of 0.2 mm at the center of the gauge area. It can be seen that the strain rates increase with deformation; nevertheless, they remain within a range of 0.001 s^{-1} to 0.01 s^{-1} for the quasi-static and 10 s^{-1} to 190 s^{-1} for the dynamic tests. For brevity, only the results of Usibor®1500-AS in the air cooled condition are presented since this condition has the highest ductility and consequently the highest variation in the strain rate with deformation. It is worth mentioning that having a non-constant strain rate from the onset of deformation is a general feature of notch tensile tests and is difficult to eliminate when a constant cross-head velocity is employed.

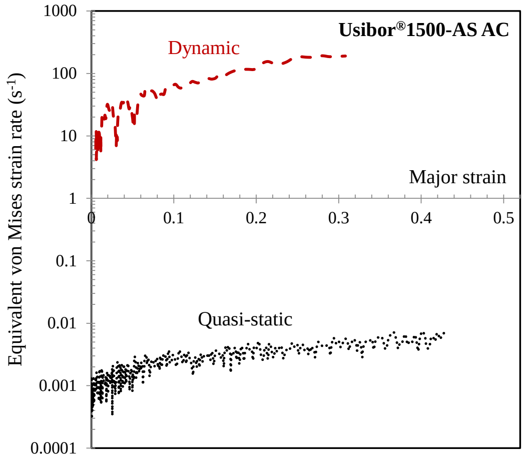

Fig. 3. Evolution of strain rates with deformation for air cooled (AC) Usibor®1500-AS.

The measured engineering stress-strain curves of the materials are shown in Figures 4 and 5 for Usibor®1500-AS and Ductibor®1000-AS, respectively. The far-field engineering strains were determined using a virtual DIC extensometer with an initial gauge length of 4.5 mm. At low strains, it can be seen that all the materials exhibit positive rate sensitivity. The degree of rate sensitivity is the highest for Usibor®1500-AS in the air cooled (bainitic) condition while the martensitic microstructures associated with fully quenched Usibor®1500-AS and Ductibor®1000-AS display lower rate sensitivity.

Also, it can be seen from Figures 4 and 5 that the measured maximum temperature rise is in the range of 50°C-70°C depending on the material. Although this level of temperature increase may not seem significant, it can trigger earlier localization and stronger softening at the dynamic rates due to thermal localization. It should be taken into consideration that these temperature measurements were conducted on the surface of the specimen while the temperature rise is expected to be higher through-thickness of the sample in the mid-plane. From the perspective of macroscopic (far-field) strains to fracture, it can be seen from Figures 4 and 5 that increasing the test velocity results in a lower engineering strain to fracture. In other words, compared to the quasi-static condition, the materials have a lower elongation to fracture under the dynamic rate. The local fracture behaviour of the materials was also studied as described below.

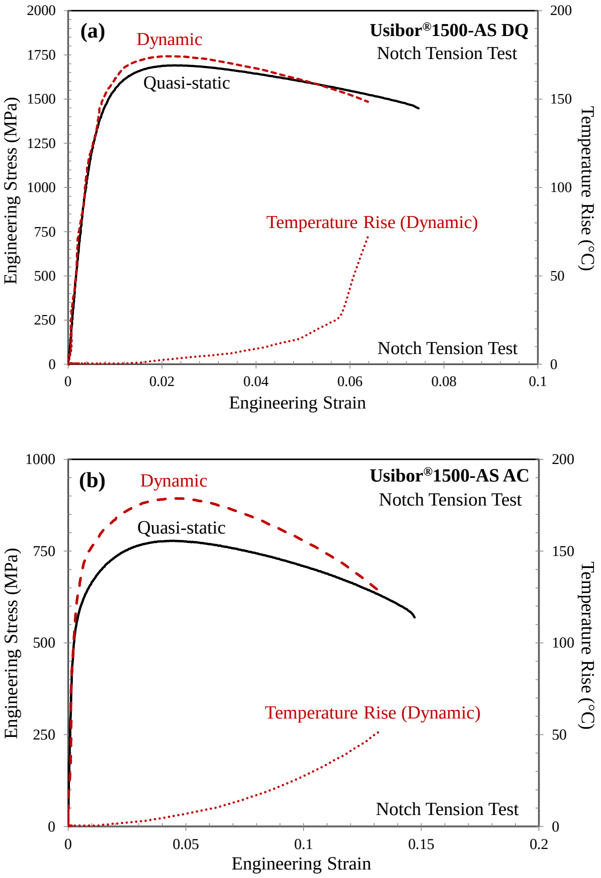

Fig. 4. Engineering stress-strain response of Usibor®1500-AS in (a) die quenched (DQ), and (b) air cooled (AC) conditions.

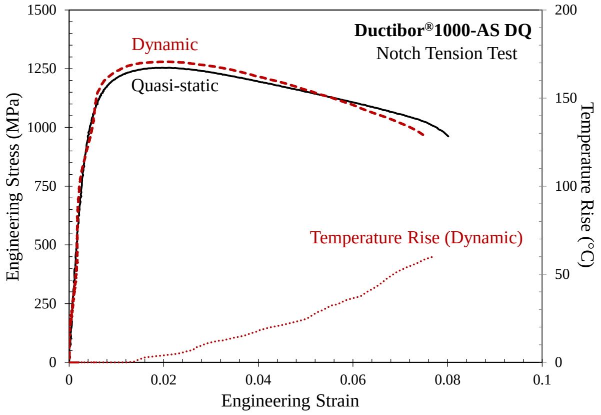

Fig. 5. Engineering stress-strain response of Ductibor®1000-AS in the die quenched (DQ) condition.

The major *versus* minor strain histories to fracture measured at the center of the specimen using the 0.2 mm DIC circle inspector are shown in Figures 6 and 7 for Usibor®1500-AS and Ductibor®1000-AS, respectively. The strain path data shows that the minor strain remains below 0.02 and therefore can be considered relatively negligible compared to the major strain, in accordance with the targeted plane strain condition. For reference, results of a quasi-static v-bend test that has a perfect plane strain path are also depicted in Figures 6 and 7. Note that v-bend data was not available for Usibor®1500-AS in the air cooled condition. It can be seen from the results of the notch tests that the local strains measured by the DIC system follow the same trend as the far-field strains seen in Figures 4 and 5, *i.e.* by increasing the strain rate, lower fracture strains are measured using the DIC system.

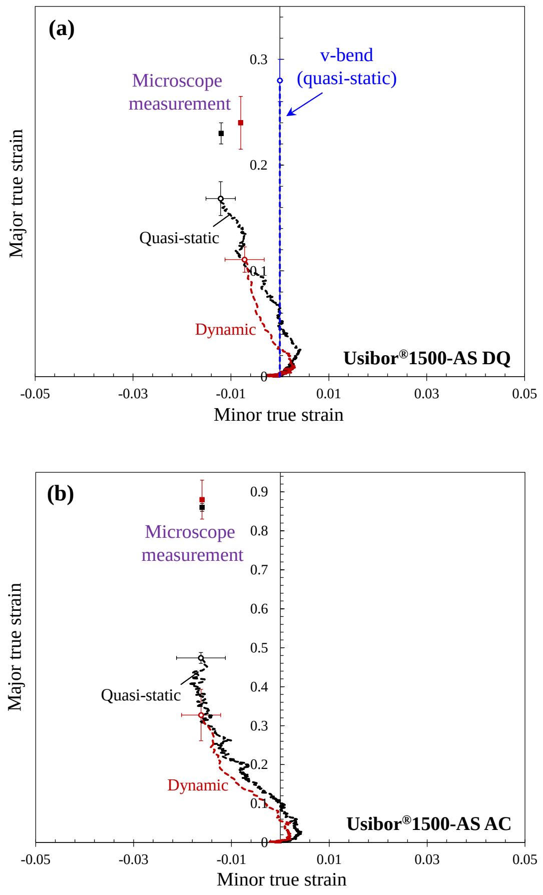

Fig. 6. Strain paths to fracture for Usibor®1500-AS in (a) die quenched, and (b) air cooled conditions.

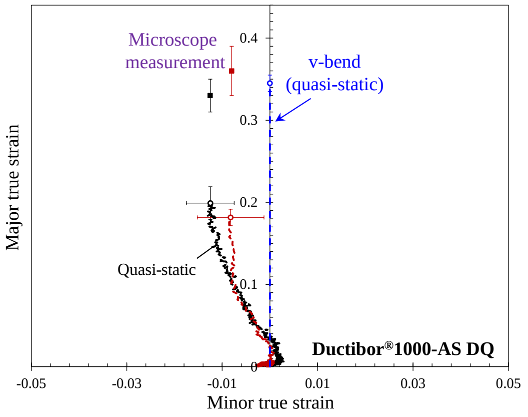

Fig. 7. Strain paths to fracture for Ductibor®1000-AS in the die quenched condition.

To further explore the local fracture behaviour, the thickness of post-mortem samples was carefully measured under an optical microscope (see Figure 8) to compute the thickness strain and corresponding in-plane major strain for comparison with the results of the DIC measurements. The strain data calculated using the microscope was added to Figures 6 and 7 (symbols) from which it can be seen that the strains measured by the DIC system are lower than those from the microscope measurements. The lower DIC strains can be attributed to the inherent gauge length of the DIC analysis which is not capable of capturing the localization and large strain gradients within the necking region. It should be noted that the severity of localization is more pronounced at elevated rates and is evident from the hardening rates in Figures 4 and 5. The stronger degree of localization in the dynamic tests is caused by the thermal softening effect. Accordingly, the more severe localization at dynamic rates leads to lower global elongation to fracture than quasi-static condition. A similar localization effect in DIC strain measurements was also observed by Abedini *et al.* (2017) and Rahmaan *et al.* (2017) in dynamic shear response of magnesium and DP600 sheets, respectively.

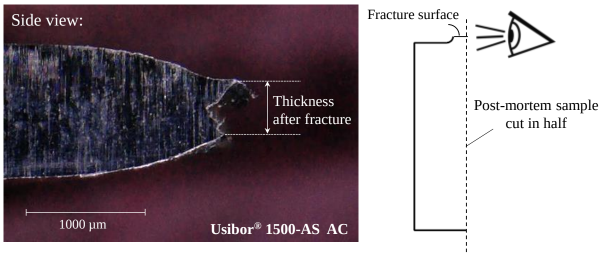

Fig. 8. Thickness of post-mortem samples was measured under an optical microscope.

In addition, it can be seen from Figures 6 and 7 that there is not a significant difference between fracture strains for the two rates once the strains are corrected using a microscope. Therefore, the local fracture behaviour of the materials does not seem to be significantly influenced by the strain rate for the test velocities considered in this study. However, at higher strain rates, for which the impact of temperature rise is more crucial, a more ductile condition might be expected, in accordance with the results reported by Roth and Mohr (2014) and Erice *et al.* (2018).

It is worth mentioning that there exists significant strain gradients through the thickness of the notch specimen prior to fracture and the strain measurement technique by means of microscope can only provide thickness strains in an average sense. However, such measurements can still serve as a good assessment method to capture overall behaviour of materials. Using this technique, the through-thickness strain gradient at the center of the notch is homogenized to a single strain measure that is convenient from an experimental perspective. The local sheet thickness can be readily measured in the press shop or from failed components. Detailed finite element analysis would be required to determine the severity of the strain gradient and it is expected that the failure strain would be higher at the center of the notch and be dependent upon the material and length scale.

Also, as demonstrated in Figures 6(a) and 7, the corrected fracture strains attained using the notch specimen are in better agreement with the v-bend data for the die quenched Usibor®1500-AS and Ductibor®1000-AS. Although the two test methods can be used for plane strain fracture characterization, there are notable differences between them. The outer radius of bend in a v-bend test is in simultaneous plane stress and plane stress states and fracture initiates from this point. In contrast to the v-bend, the plane strain notch sample experiences a triaxial plane strain state with the highest strains occurring through-thickness in the mid-plane.

4 Conclusions

Quasi-static and dynamic plane strain notch tests were conducted on hot stamped Usibor®1500-AS and Ductibor®1000-AS sheets. It was demonstrated that the materials show a positive strain rate sensitivity at low strains in terms of strength, while elongation to fracture decreased by increasing the test velocity due to thermal softening effects. In addition, local DIC strain data exhibited lower fracture strains at the dynamic rate which was in line with the reduced global elongation to fracture. However, a more detailed investigation into fracture strains using strain correction with an optical microscope revealed that the average strains are similar for the two test velocities considered in this study. Tests at higher rates (~1000 s^{-1}) will likely magnify the thermal effects and will be considered in future contribution.

Support for this work from Honda R&D Americas Inc., Promatek Research Centre, ArcelorMittal, the Natural Sciences and Engineering Research Council (NSERC) of Canada, the Ontario Advanced Manufacturing Consortium, the Ontario Research Fund, Canada Foundation for Innovation, and Ontario Centres of Excellence is gratefully acknowledged.

References

1. S. Golling, R. Ostlund, M. Oldenburg, Mater. Sci. Eng. A. 658, 427-483 (2016)
2. R. Ostlund, S. Golling, M. Oldenburg, Comput. Methods. Appl. Mech. Eng. 302, 90-108 (2016)
3. P. Samadian, C. Butcher, M.J. Worswick, Proceedings of CHS2 Conference (2019).
4. Y. Li, M. Luo, J. Gerlach, T. Wierzbicki, J. Mater. Process. Technol. 210, 1858-1869 (2010)
5. G. Gruben, E. Fagerholt, O.S. Hopperstad, T. Borvik, Eur. J. Mech. A Solid, 30, 204-218 (2011)
6. C.C. Roth, D. Mohr, Int. J. Plast. 79, 328-354 (2016).
7. A.D. Deole, M.R. Barnett, M. Weiss, Int. J. Solids Struct. 144-145, 20-31 (2018)
8. H. Huh, S. Kim, J. Song, J. Lim, Int. J. Mech. Sci. 50, 918-931 (2008)
9. S. Winkler, A. Thompson, C. Salisbury, M.J. Worswick, I. van Riemsdijk, R. Mayer, Metall. Mater. Trans A. 39, 1350-1358 (2008).
10. C.C. Roth, D. Mohr, Int. J. Plast. 56, 19-44 (2014)
11. B. Erice, C.C. Roth, D. Mohr, Mech. Mater. 116, 11-32 (2018)
12. T. Rahmaan, A. Abedini, C. Butcher, N. Pathak, M.J. Worswick, Int. J. Impact Eng. 108, 303-321 (2017)
13. L. ten Kortenaar, M.Sc. Thesis, University of Waterloo (2016)
14. T. Rahmaan, P. Zhou, C. Butcher, M.J. Worswick, Proceedings of DYMAT Conference (2018)
15. A. Abedini, C. Butcher, M.J. Nemcko, S. Kurukuri, M.J. Worswick, Int. J. Mech. Sci, 128-129, 54-60 (2017)

The temperature effect of pulse pressing on structure and mechanical properties of compacts

Anatoly Bragov[1], *Alexander* Konstantinov[1], *Svetlana* Litvinchuk[1], *Andrey* Lomunov[1,*], *Eugeny* Rusin[2]

[1]Research Institute for Mechanics, Lobachevsky State University of Nizhny Novgorod, 603950, Russia
[2]Mechanical Engineering Research Institute of RAS, Nizhny Novgorod, 603024,Russia

Abstract. The paper presents the results of the study of temperature effect on structure and properties of compacts, made from reduced iron fine powder (the average particle size of 3-5 μm) with Wolfram carbide nanopowder with average particle size of 25-30 nm, exposed to pulse pressing. The mass fraction of wolfram carbide in the powder composition was 5% of the total mass. Pulse pressing was carried out using the modified Kolsky method (under uniaxial deformation conditions) at temperatures ranging from 20°C to 300°C. Compacts with a relative density over 90% were obtained as a result of the experiments. Metallographic studies have shown that the obtained compacts have a fairly homogeneous fine-grained structure, the pore-size distribution is uniform and pore shape is generally close to spherical.

It is shown that an increase in pressing temperature leads to an increase in quality of the compacts obtained, formation of a perfect fine-grained structure, and an increase in density and micro-hardness values. The electrical conductivity of the obtained compacts was measured. It has been found that the electrical conductivity increases with increasing preheat temperature.

1 Introduction

The most important stage of manufacturing technology of compact materials is the molding of high-quality compacts of a given shape from powders of various particle size distribution - coarse powders, nanopowders and their compositions. Many powder compositions, including nanopowders, have unique physical and mechanical properties and functional characteristics. The presence of nanometer and submicron structural elements in the coarse-grained powder can lead to an increase in crack resistance, toughness, wear resistance, strength and hardness of the material. In the compaction process, a uniform density distribution should be ensured in order to manufacture high-quality products with desired properties. Besides, it is necessary to ensure the chemical purity and the required phase composition of final products. It should be noted that the compaction of hard-to-deform powders and nanopowders, using the known static methods, is hard if not impossible. Therefore, the applied dynamic compaction methods are distinguished by the complexity and variety of physical processes that affect the deformation of powder particles and consolidation of the porous billet as a whole [1-2]. The contribution of a particular mechanism in the compaction process may be different, depending on the pressed powder material, the size and shape of its particles, amplitude, duration of the pressure pulse and pressing temperature.

The strength of compact materials fabricated by any pressing method is directly dependent on the degree of consolidation in the interparticle contact areas. Pulse loading of porous and powder systems is accompanied by a severe plastic deformation and local heating of particles. In the case of metal powders, renewed surfaces of pure metal (juvenile surfaces) are formed due to the failure of particle surface layers during their deformation. High temperatures contribute to the activation of juvenile surfaces and metallic bonding formation in the contact zone. The degree of consolidation of powder particles is determined by the compaction temperature and a number of mechanical characteristics of the material, such as elastic constants.

Wolfram carbide (WC) is widely used in fabrication of hard alloys that make up the bulk of all tool materials. WC powder is a hard-to-deform powder even under conditions of dynamic pressing. Therefore, highly elastic reduced iron powder is used as a matrix. In the present paper, we investigate the possibility of adding WC nanopowder as a component for increasing the strength, hardness and wear resistance of basic powder material, a compact of which can be later used to manufacture parts, working under dry friction conditions in various micromechanisms and devices.

The present paper is aimed at studying the effect of compaction temperature on structure and mechanical properties of compacts under fixed kinematic loading parameters.

---

[*] Corresponding author: lomunov@mech.unn.ru

Table 1. Parameters of specimen testing and obtaining results

Specimen No	Heating temperature, °C	Specimen mass, g	Specimen height, mm	Specimen volume, mm^3	Density, kg/m^3	Relative density, %	Strain, %
1	20	0.95	4.89	188.19	5048	85.04	28.22
			3.51	135.08	7033		
2	20	0.85	4.21	162.02	5246	86.43	26.60
			3.09	118.92	7148		
3	100	0.86	4.29	165.10	5209	87.73	28.20
			3.08	118.53	7255		
4	100	0.91	4.51	173.57	5243	89.07	28.82
			3.21	123.54	7366		
5	200	0.82	4.26	163.94	5002	92.34	34.50
			2.79	107.37	7637		
6	200	0.83	4.07	156.63	5299	93.14	31.20
			2.8	107.76	7703		
7	300	0.96	4.66	179.34	5353	94.26	31.33
			3.2	123.15	7795		
8	300	0.79	3.91	150.47	5250	95.47	33.50
			2.6	100.06	7895		

2 Materials under study

Reduced iron powder (average particle size 8–10 µm, density ≈7.874 g/cm³) with addition of wolfram carbide (WC) nanopowder with an average particle size of 25–30 nm and density ≈15.8 g/cm³ was used for study. The mass fraction of wolfram carbide was 5% of the total mass, the theoretical density of the powder mixture was ≈8.27 g/cm³. Powder mixing was carried out as follows: ≈80 g of chemically pure acetone was added to a mixture of powders (≈40-50 g) and the suspension was treated in an ultrasonic bath for 20 minutes. Then acetone was evaporated in a drying oven at 60°C. Table 1 shows the values of the initial density and density of compacts after dynamic pressing. The density was determined by measuring the mass and volume of the specimen (compact). The volume was calculated by hydrostatic weighing.

The relative density of the compact was determined by dividing the actual density by the theoretical density of the powder mixture (8.27 g/cm³). Table 1 shows the values of height, volume and actual density in the initial state (in the numerator) and after pressing (in the denominator) for each specimen.

Before pulsed compaction, the powder material was subjected to preliminary static compression.

3 Testing technique

A modification of the Kolsky method was used for compacting powder materials [3].

The experiments were carried out on the setup that includes a loading device (gas gun of 20 mm caliber), two measuring bar with a diameter of 20 mm each and a complex of recording and synchronizing equipment (Fig. 1).

The compression pulse was excited by the impact of the striker against the loading bar. Variation of striker length and velocity enables to set the required compaction modes of powder materials: the duration of the loading pulses in the range of 100–400 µs, the pressure amplitude up to 2000 MPa. Measurement of deformations was carried out using strain gauges glued on the side surface of the bars. Signals from strain gauges were recorded with a digital oscilloscope.

Using the registration data of elastic deformation pulses in both bars, one can determine the development processes with time of stress, strain and strain rate in a specimen of powder material during compaction:

$$\sigma_s(t) = \frac{EA}{A_S^0}\varepsilon^T(t), \quad \varepsilon_s(t) = -\frac{2C}{L_0}\int_0^t \varepsilon^R(t)\cdot dt, \quad \dot{\varepsilon}_s(t) = -\frac{2C}{L_0}\cdot\varepsilon^R(t),$$

and then plot a dynamic compaction diagram in the axes σ–ε, where $\varepsilon^I(t)$, $\varepsilon^R(t)$ and $\varepsilon^T(t)$ are respectively, incident, reflected and transmitted deformation pulses in measuring bars, C is the velocity of elastic waves in the bars, E and A are the Young's modulus and the cross-sectional area of the measuring bars, L_0 is the initial specimen length.

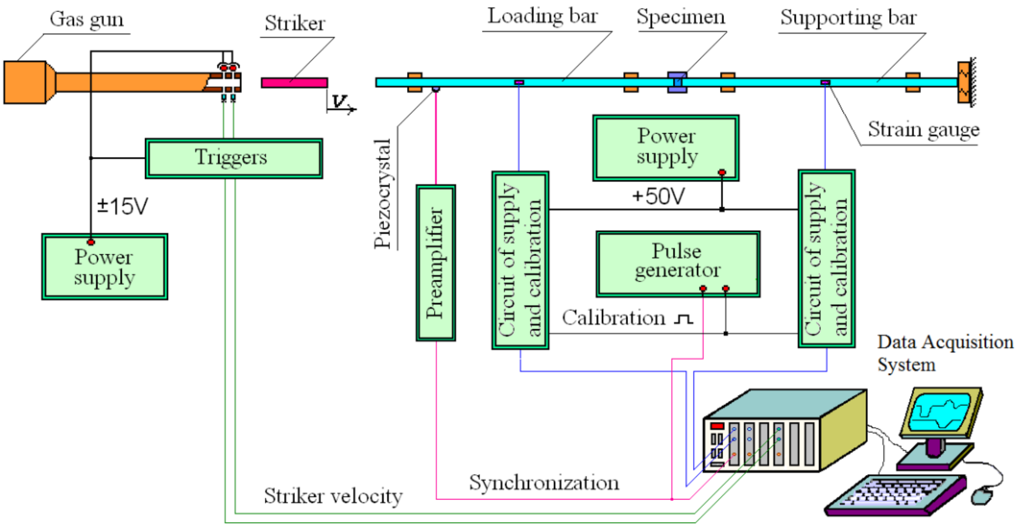

Fig.1. Scheme of experimental setup for pulse pressing powder materials

By varying the specimen height $h_s(t) = C\int_0^t \left[\varepsilon^I(t) - \varepsilon^R(t) - \varepsilon^T(t)\right]\cdot dt$ we can plot a curve of density change of the compact during the pressing process $\rho(t) = \rho_0 + \dfrac{m4h_s(t)}{\pi d^2}$, where *m* is initial specimen mass, *d* is its diameter.

The pressed powder mixture was placed in a high-strength steel jacket sandwiched between the measuring bars ends. The inner diameter of the jacket was 7 mm.

To assess the quality of the obtained compacts, metallographic studies of microsurface and cross-sections of the compacts were carried out using scanning electron microscopy by an electron microscope TESCAN VEGA II.

Microhardness measurement of compacts was carried out on a standard microhardness tester.

4 Results of testing

A series of experiments was carried out on dynamic pressing of the powder mixture Fe+5%WC at temperatures of 20, 100, 200 and 300°C under the same loading conditions: a pressure pulse duration of ~350 µs, an amplitude of ~1500 MPa. To create such parameters, a 400 mm long steel striker, accelerated up to a velocity of ~21 m/s, was used.

Two experiments were carried out for each temperature regime. In each experiment the loading rate and temperature were recorded, as well as strain pulses in the measuring bars, which were used to construct the dynamic pressing diagrams of the powder under study (Fig. 2).

The obtained compacts exhibit a fairly homogeneous fine-grained structure. Pore distribution is uniform and the shape of the pores, as a rule, is close to spherical.

A metallographic analysis of the obtained compacts showed that the structure of compacts contains zones with local elevated temperatures, located along the boundaries of the particles, at the places of pore wicking.

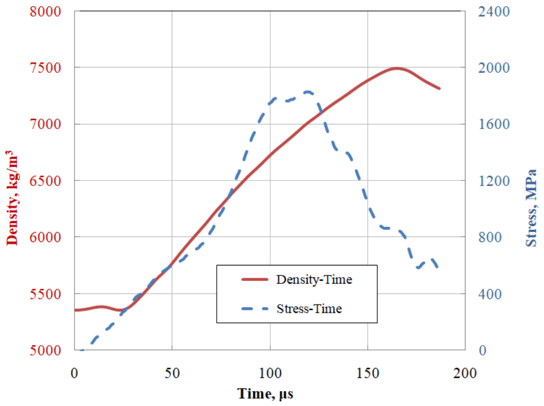

Fig.2. A compacting diagram (density, stress) as a function of time

Pictures of the compact surfaces obtained at different pressing temperatures, with a 10000-fold increase, are shown in Fig. 3.

The structure analysis of the obtained compacts showed that preheating the powder material leads to a more homogeneous release of energy over the particle surface. The pressing process of the powder mixture starts with initial repacking of particles - mutual displacement of particles and filling the spaces between large particles with smaller ones. Then the particles are compacted due to their plastic deformation up to the exhaustion of the plasticity of the particles of powder materials. Regardless of the further growth of applied load, the density threshold of the powder body is reached, the subsequent increase of which is impossible without changing the physical properties of particle material of the formed medium. Preheating the specimen before compaction ensures an additional increase in density due to further movement of particles.

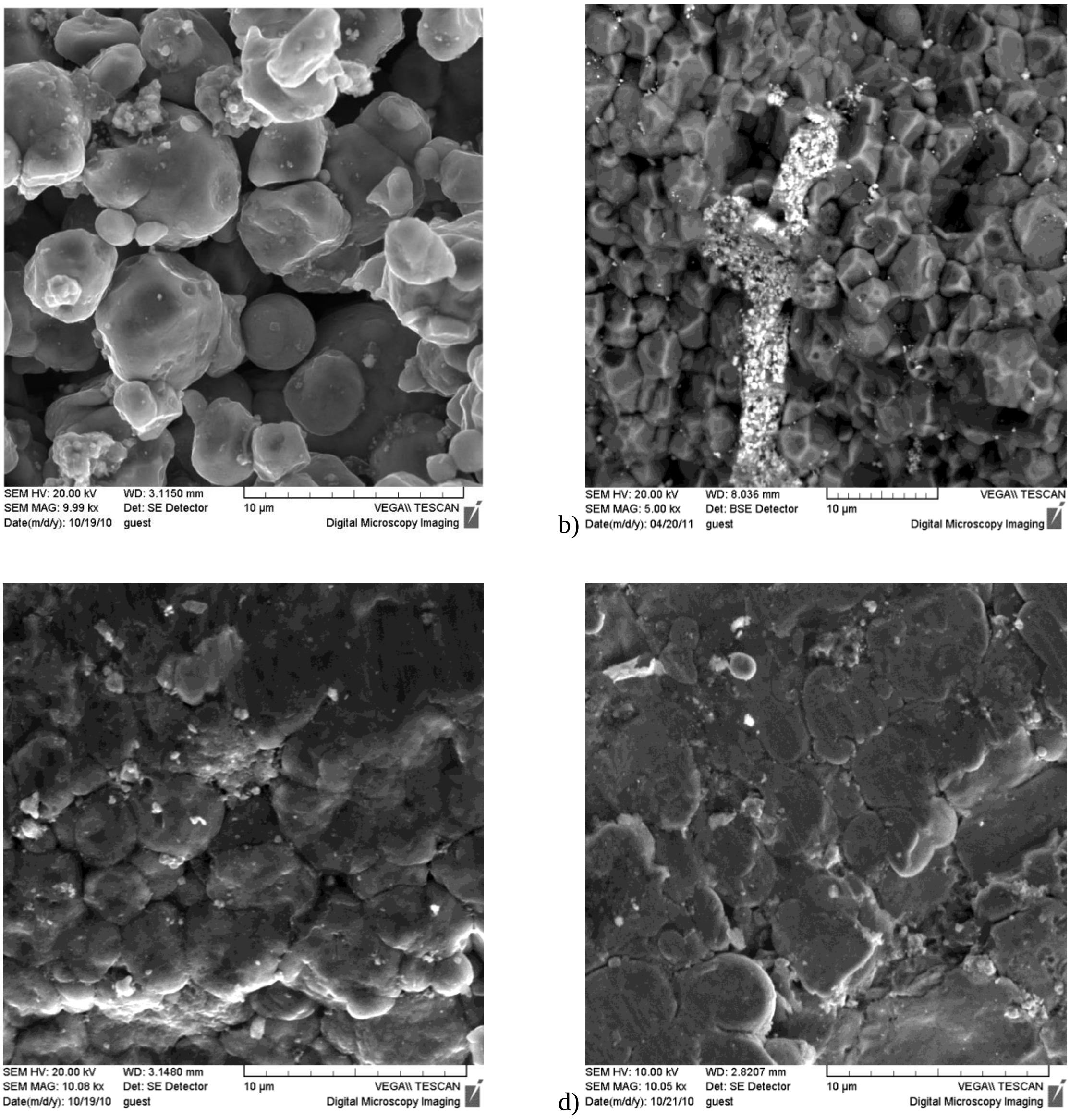
SEM HV: 20.00 kV
SEM MAG: 9.99 kx
Date(m/d/y): 10/19/10
WD: 3.1150 mm
Det: SE Detector
guest
10 µm
VEGA\\ TESCAN
Digital Microscopy Imaging
SEM HV: 20.00 kV
SEM MAG: 5.00 kx
Date(m/d/y): 04/20/11
WD: 8.036 mm
Det: BSE Detector
guest
10 µm
VEGA\\ TESCAN
Digital Microscopy Imaging
SEM HV: 20.00 kV
SEM MAG: 10.08 kx
Date(m/d/y): 10/19/10
WD: 3.1480 mm
Det: SE Detector
guest
10 µm
VEGA\\ TESCAN
Digital Microscopy Imaging
SEM HV: 10.00 kV
SEM MAG: 10.05 kx
Date(m/d/y): 10/21/10
WD: 2.8207 mm
Det: SE Detector
guest
10 µm
VEGA\\ TESCAN
Digital Microscopy Imaging

a) b) c) d)

Fig.3. Surface structure of compacts, obtained at pressing temperatures 20°C (a), +100°C (b), +200°C (c), +300°C (d)

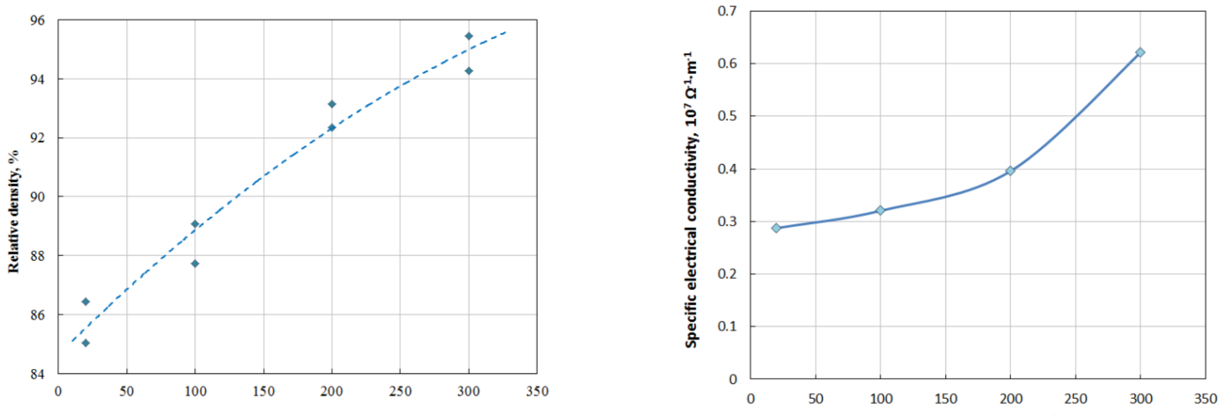

a) b)

Fig.4. The effect of pressing temperature on relative density of compacts (a) and their electrical conductivity (b)

The studies have also shown that an increase in pressing temperature leads to an increase in the density of compacts (Fig. 4a). The maximum compact density was ~95% at a pressing temperature of 300°C, and the minimum density of ~85% was observed for the compact obtained at a temperature of 20°C.

The electrical conductivity of compact materials is determined by the nature of powder material, size, structure and surface state of interparticle contacts. Variation of the surface properties of powder particles during the pressing process would affect the electrical conductivity of the compacts. The resistance of the specimens was measured with a digital micro-ohmmeter with an accuracy of 10^{-5} ohms, the material resistivity ρ and its electrical conductivity r' were calculated whereafter according to the known formulas:

$$\rho = R\frac{S}{l}, \qquad r' = \frac{1}{\rho},$$

where R is specimen resistivity; S is specimen cross-section area; l is specimen length.

Measurements of electrical conductivity of the obtained compacts were carried out. Measurements of the electrical resistance of compact materials made it possible to estimate the effect of pressing temperature on physicomechanical properties of compacts. It has been established that the specific electrical conductivity of the specimens increases with increasing pressing temperature (Fig.4b).

The microhardness of the compact surface was measured using a standard microhardness meter along the compact diameter with a 0.5 mm step. The results of measuring the microhardness of the compact surfaces obtained at different pressing temperatures are shown in Fig.5. The studies have shown that increasing pressing temperature leads to an increase in density of all obtained compacts and their microhardness (see Table 1).

It was revealed (Fig. 5) that the microhardness of compacts in the central region of the specimen is higher than that at the peripheral region, which is probably due to the presence of friction of the powder material against the wall of the jacket.

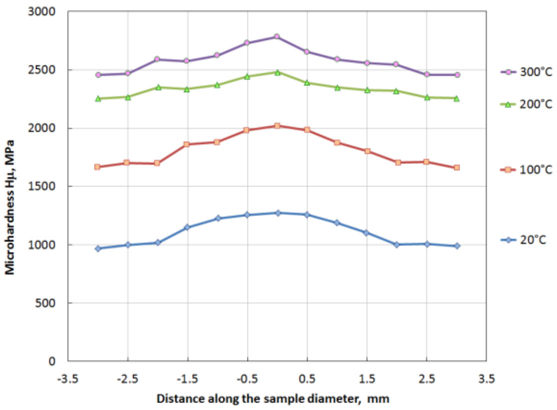

Fig.5. The effect of pressing temperature on compact microhardness

The present study has also shown that an increase in preheating temperature of the powder leads to microhardness growth. The stress gradients in the molding process lead to different deformations and changes in the density inside the pressed jacket, interparticle friction and pressing pressure. During pulsed pressing at temperatures of 20, 100, 200 and 300°C, the nature of the distribution of microhardness and density over the compact volume remains unchanged.

The results of the study of temperature effect of pulsed pressing on the structure and properties of compacts of reduced iron powder with the addition of wolfram carbide nanopowder are presented. It is shown that an increase in the pressing temperature leads to an increase in the quality of the compacts obtained, the formation of a perfect fine-grained structure, and an increase in the density and microhardness values.

The conducted metallographic studies of the structure of the obtained compacts showed that an increase in the preheating temperature leads to the formation of a more perfect fine-grained structure. This is due to an increase in the juvenile surface area and the formation of a metallic bond in the zone of contact of the powder particles.

Conclusion

For dynamic compacting of powder mixtures, a modified Kolsky technique was successfully used, which allow to control loading parameters, select compacting modes, and obtain homogeneous powder compacts of good quality under loading duration of 100-400 µs with amplitudes up to 2000 MPa.

As a result of the experiments, Fe-based compacts with the addition of 5% WC were obtained. The addition of WC nanopowder leads to an increase in the microhardness of compacts as compared to compacts from pure Fe.

It was established that heating the powder material with the same pressing parameters (pressure pulse duration ≈300 µs, amplitude ≈1500-1800 MPa) enables further increase in compact density (up to 95%).

The wear resistance of compacts obtained at a pressing temperature of 300°C exceeds by 1.85 and 2.09 times the wear resistance of the same compacts obtained at room pressing temperature.

The studies on pulsed pressing of powder materials were carried out under financial support of the Federal target research and development program in the priority areas of development of the Russian scientific and technological complex for 2014-2020 under the contract No. 14.578.21.0246 (unique identifier RFMEFI57817X0246). Studies on structure of the obtained compacts were carried out under partial financial support from the Russian National Science Foundation (grant 16-19-10237-P).

References

1. K. Kondo, S. Sawai, J.Amer.Ceram.Soc. **73(3)** 1983 (1990)
2. D. Raybould, Powder Metallurgy, **25(1)** 35 (1982)
3. A.M. Bragov, S.N. Rodionov, E.E. Rusin, Technical Physics Letters, **30(11)** 892 (2004)

Coupling of temperature, strain and strain rate effects on the flow stress of a stainless steel

Giuseppe Mirone[*], *Raffaele* Barbagallo

Università di Catania, Dipartimento di Ingegneria Civile e Architettura, Via S. Sofia 64, 95100 Catania, Italy

Abstract. The effects of strain rate and temperature on the stress-strain response of a stainless steel are analyzed for investigating whether they are coupled to each other and eventually dependent on the strain too.

Results of an experimental campaign are analyzed, including tensile tests at low strain rates and various temperatures together with dynamic tests, by Hopkinson bar and by hydraulic testing machine, where the initial room temperature increases due to fast adiabatic dissipation of plastic work.

Stress, strain and strain rate evaluations are based on optical measurements of current diameters of round specimens, ensuring the reliability of the experimental data also at large postnecking strains up to failure.

The coupling of temperature and strain at low rates is evidenced for softening function of the steel at hand, so a simple softening function including both variables is modelled. The coupling of strain and temperature variables within the softening function is confirmed by the large anticipation of necking onset promoted by increasing temperature. The dynamic amplification is then obtained from the high strain rate tests, revealing a more pronounced interaction of strain and strain rate within the function expressing the strain rate effect.

1 Introduction

Use A4 paper size (210 x 297 mm) and adjust the The effects of high strain rate and temperature on the hardening of metals are usually modelled by multiplying the static stress at room temperature, which is function of the strain, by a dynamic amplification depending on the strain rate and by a thermal softening depending on the temperature. For characterizing such two effects, the thermal softening must be firstly determined from static tests at high temperature and then the dynamic amplification can be derived from dynamic tests. High strain rates are accompanied by temperature increases, so the stress-strain curves from experiments are subjected to both thermal softening and dynamic amplification effects. Then for characterizing the latter effect, the former one must be eliminated from the experimental dynamic curves. This involves the calculation of temperature histories due to fast plastic dissipation. In Kapoor & Nemat-Nasser [7] and Walley et al. [20] it is demonstrated that the plastic work in tests of different metals is almost completely converted into heat, while Jovic et al. [6] and Rittel et al. [15] calculated that different fractions of plastic work can be converted into heat for the same material. Ruggiero et Al. [16] and Scapin et Al. [19] investigated strain rate and temperature effects on the material ductility. Concerning the equivalent stress-strain curve, necessary to estimate the temperature increase during a test, Peroni et al. [14] developed a new neck-profile-based procedure while Sasso et al. [18] studied a novel procedure for the FEM-based material curve calibration. The equivalent curve can also be obtained from the true curve without numerical iterations, by the Bridgman [2] method or by the more recent and simpler MLR method proposed by Mirone [9]. Such true curve can be obtained by means of optical measurements or with the material independent method able to obtain the true variables from engineering ones for cylindrical and rectangular specimens developed by Mirone et al. [12]. Rusinek et al. [17] and Osovski et al. [13] analyzed the multiple necking phenomenon while Besnard et al. [1] used stereocorrelation for accurate necking investigation. Mirone et Al. [10] and Mirone et Al. [11] investigated the interactions between the effective true strain rate and the dynamic amplification of flow stress. Here a stainless steel A270 is subjected to static tension at different temperatures up to 300 °C and to high strain rate tensile tests at different rates, by hydraulic machine and by Split Hopkinson Tension Bar (SHTB). All tests are supported by camera acquisitions for measuring the effective evolving neck sections; the experimental true stress-true strain curves are then processed for separating and extracting the functions of thermal softening and dynamic amplification.

2 Experimental campaign

2.1 Overview

The combined strain rate and temperature effects are investigated on a A2-70 stainless steel by static, dynamic and high temperature tensile tests on cylindrical specimens, according to the list in Table 1. The reference strain rate of each tests is the true strain rate at the moment of the necking inception. Round tensile specimens are machined with nominal 3 mm diameter and 9 mm length of the constant cross section segment. Static tensile tests are carried out by motor driven machines at static rate under different temperatures (around 20, 80, 140, 200 and 300 °C). Dynamic tests at different rates are carried out by a Instron 8501 hydraulic testing machine (nominal rates 1 and 10 s-1) and by the

---

[*] Corresponding author: gmirone@dii.unict.it

direct-tension split Hopkinson tension bar (SHTB) developed at the University of Catania (nominal rates 900 and 1800 s-1).

Table 1. Summary of the A2-70 Experimental Campaign

Test Series		Test Name	Reference True Strain Rate [s-1]	Test Temp. [°C]
Static TROOM	Motor driven	S-TROOM-01	0.003	19
		S-TROOM-02	0.003	22
		S-TROOM-03	0.003	22
Static T80		S-T80-01	0.003	80
		S-T80-02	0.003	80
Static T140		S-T140-01	0.003	140
		S-T140-02	0.003	140
Static T200		S-T200-01	0.003	200
		S-T200-02	0.003	200
Static T300		S-T300-01	0.003	300
		S-T300-02	0.003	300
		S-T300-03	0.003	300
Dynamic TROOM	Hydraul.	D1-01	1	22
		D1-02	1	22
		D10-01	10	22
		D10-02	10	22
	SHTB	D800-01	700	20
		D800-02	890	20
		D1800-01	1800	20
		D1800-02	1850	20

From each test, the triplet of variables t, P and d (time, load and minimum cross section diameter) is determined. In static tests, simple camera acquisitions and testing machine recording provided the necessary information while, for SHTB tests, the load was derived from the transmitted wave and the diameter from a high-frame rate Phantom® camera acquisitions at about 200’000 fps.

The static and dynamic tests delivered discrete true stress-true strain points plus the time derivative of the best fit function $\varepsilon_{True}(t)$, delivering the strain rate, according to eqs. (1), (2) and (3):

$$\sigma_{True} = \frac{F}{\pi/4 \cdot d^2} \tag{1}$$

$$\varepsilon_{True} = 2 \cdot Ln\left(\frac{d_0}{d}\right) \tag{2}$$

$$\dot{\varepsilon}_{True} = \frac{\partial \varepsilon_{True}(t)}{\partial t} \tag{3}$$

2.2 Thermal softening at quasistatic rate

Firstly, the true stress-true strain curves shown in Fig. ***1*** are obtained from the static tests at different temperatures, together with the corresponding values of the yield stresses and the static necking strains ε_{N-S} for each temperature, listed in Table 2.

Table 2. Yield Stress and Necking Strain for static temperature tests

	S-TROOM (20)	S-T80	S-T140	S-T200	S-T300
$\sigma_{yield}\,[MPa]$	447.5	460	420	420	400
ε_{N-S}	0.44	0.35	0.19	0.18	0.18

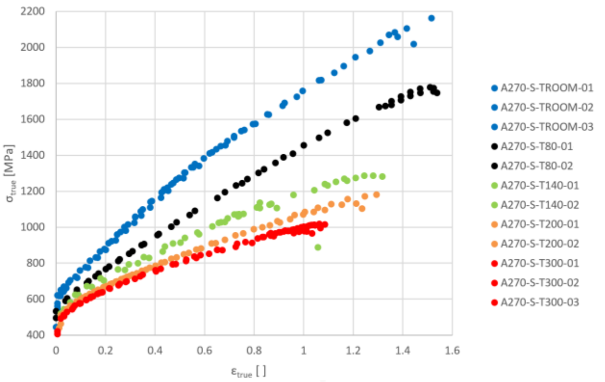

Fig. 1. Experimental true stress-true strain data of the static tests at different temperature

From such data, it is already possible to evidence that the thermal softening has a great effect on the necking inception strain, in fact the necking onset is anticipated from 0.44 at 20 °C to 0.18 at 300 °C.

Then the experimental true curves are corrected in the postnecking phase for determining the equivalent Mises stress-strain curves, by the MLR correction (Mirone [9]).

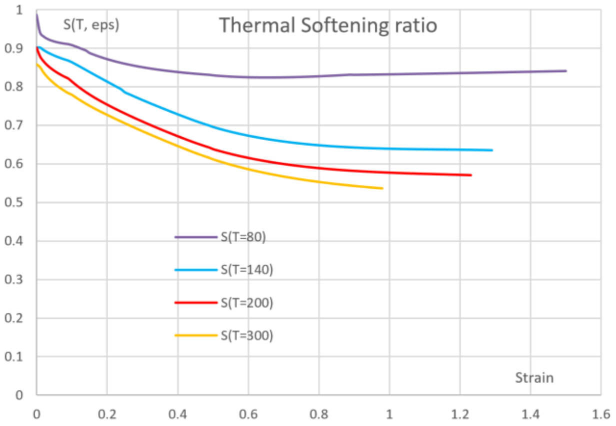

Fig. 2. Thermal softening

The ratio $S(T) = \sigma_{Eq}(T)/\sigma_{Eq}(T_{Room})$ is calculated for the tests at 80, 140, 200 and 300 °C at each strain level, as shown in **Errore. L'origine riferimento non è stata trovata.**. The experimental softening curves clearly demonstrate that the thermal softening at each given temperature is remarkably strain-dependent, which opposes the usual assumption of uncoupling between temperature and strain effects. Therefore a two variables best fitting function $S(T,\varepsilon)$ is calculated for modeling the thermal softening, instead of the usual single-variable function $S(T)$. This is in perfect agreement with the large necking anticipation found by experiments as temperature increases: in fact, if S was independent of ε, then the stress-strain curves at different temperatures would be scaled each other by a constant, then the condition $\sigma_{Eq} = \frac{\partial \sigma_{Eq}}{\partial \varepsilon_{True}}$ would occur at the same strain for all tests and the necking onset would be independent of the temperature.

2.3 Combined Strain Rate and Temperature Effect

In this section, the combined strain rate and temperature effects on the material behavior are analyzed. The true stress-true strain data from the dynamic tests are shown in **Errore. L'origine riferimento non è stata trovata.** together with the static true stress – true strain curve at room temperature. The dynamic curves obviously include the thermal softening due to the spontaneous adiabatic heating at such rates.

At low strains the temperature are still close to the room temperature, then the dynamic effect is not counterbalanced and the dynamic curves are higher than the static reference one. At later stages the thermal softening progressively increases, thus the dynamic curves are gradually pushed down until they become lower than the static curve. The dynamic curves at larger strain rates are greater than those at lower rates, evidencing the strain rate effect. For completing the insight on these experiments, the true strain rate vs. true strain relationship is obtained according to eqs. (2) and (3); the evolving strain rates are reported in

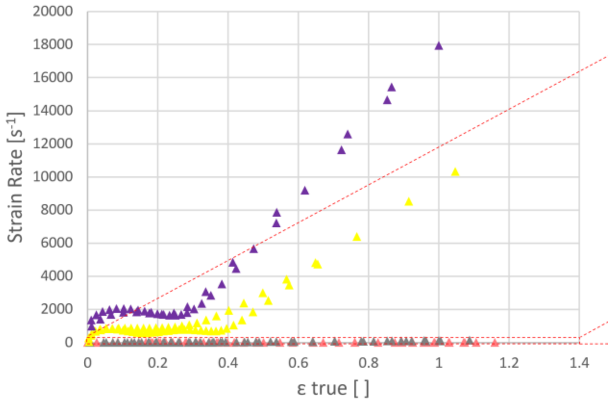

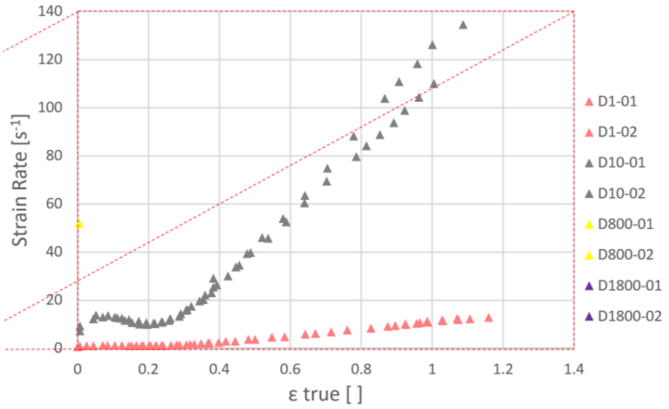

.

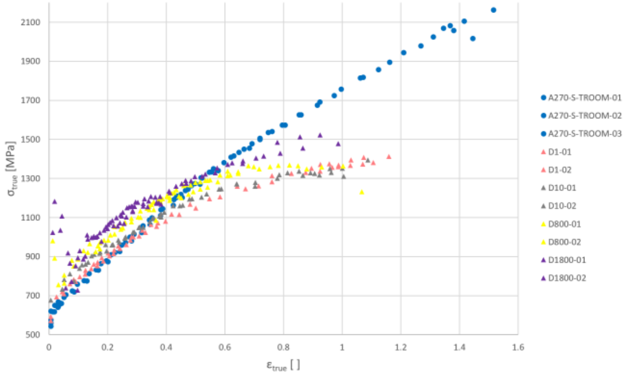

Fig. 3. Experimental True Stress-True strain Dynamic Curves from Dynamic tests

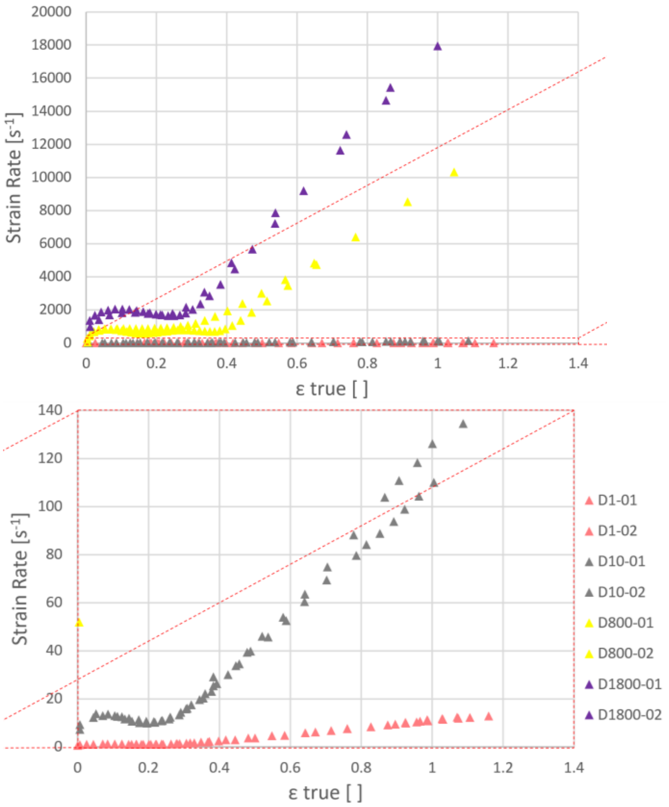

Fig. 4. True strain rate vs. true strain Curves from Dynamic tests

In order to evaluate the temperature evolution during the dynamic tests, the dynamic true curves are firstly corrected by the post-necking function MLR for obtaining the dynamic Mises stress-strain curves. Then the latter curves are integrated to calculate, via the Taylor-Quinney coefficient (TQC), the temperature istory during each dynamic test. According to the findings by Kapoor & Nemat-Nasser [7], the TQC has been considered equal to one. The temperature evolution during each test is shown in Figure 5, showing that the temperature evolution is nearly independent of the strain rate, due to the modest difference between the dynamic curves at different strain rates.

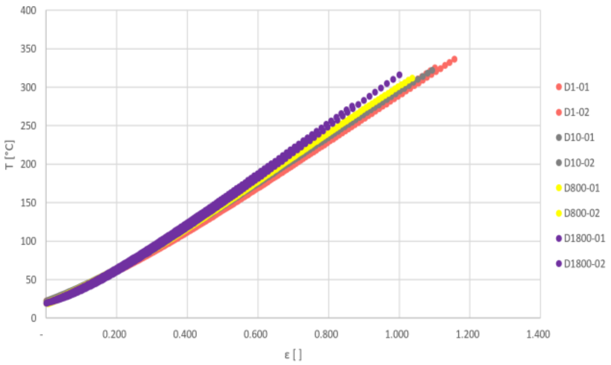

Fig. 5. Evolution of the material temperature during each dynamic test

Now the temperature histories of dynamic tests from **Errore. L'origine riferimento non è stata trovata.** are introduced in the best fit functions $S(T,\varepsilon)$ derived from static tests, and the resulting softening history is eliminated from the dynamic curves dividing the latter by the softening history,

$$\sigma_{Eq}(\varepsilon_{True},\dot{\varepsilon}_{True},T_{Room}) = \sigma_{Eq}(\varepsilon_{True},\dot{\varepsilon}_{True},T)/S(T,\varepsilon)$$

For the sake of brevity, we say that the Mises curves are mathematically "cooled down" to the room temperature, and this calculation is legit as far as the uncoupling of strain rate and temperature effects applies. Finally, the "cooled" dynamic Mises curves, only affected by the dynamic amplification, deliver the strain rate sensitivity function R of the A270 steel, simply dividing them by the static curve at room temperature:

$$R(\dot{\varepsilon}) = \sigma_{Eq}(\varepsilon_{True},\dot{\varepsilon}_{True},T_{Room})/\sigma_{St}(\varepsilon_{True},T_{Room})$$

Such strain rate sensitivity functions are plotted for every test in and **Errore. L'origine riferimento non è stata trovata.**, by respectively taking as the common variable $\dot{\varepsilon}_{True}$ and ε_{True}.

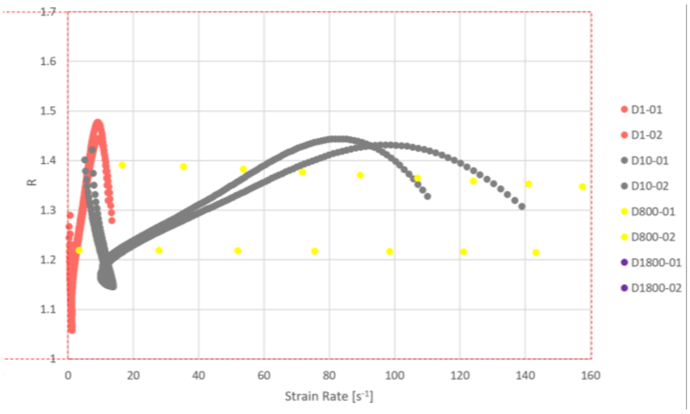

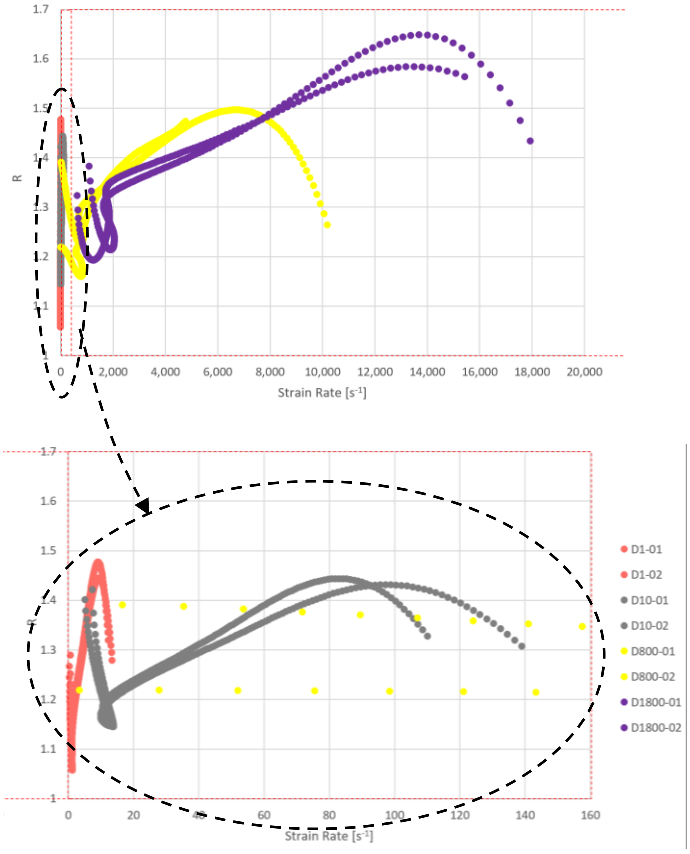

Fig. 6. Dynamic amplification of the stress, R vs $\dot{\varepsilon}_{True}$ plot, from all dynamic tests (left) and enlargement of the moderately high strain rate part of the same plot (right)

It is essential to underline that in

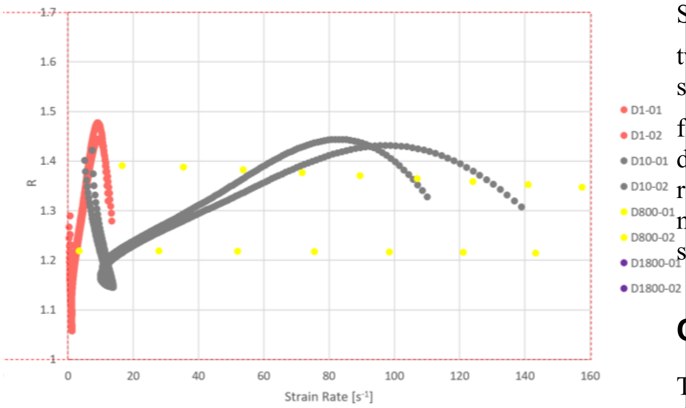

, a given strain rate corresponds to very different strain rates for different tests, while in **Errore. L'origine riferimento non è stata trovata.** a given strain corresponds to very different strain rates for te different tests.

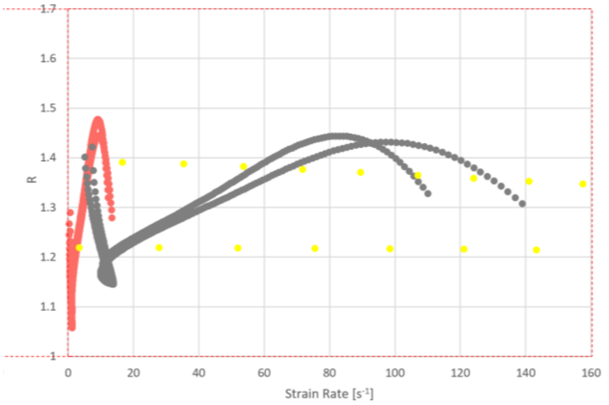

shows that the dynamic amplification functions plotted against $\dot{\varepsilon}_{True}$ are very different one from another, suggesting that R also depends on ε_{True} instead of depending on $\dot{\varepsilon}_{True}$ alone. The right plot of such Figure is an enlargement of the moderately high strain rate part of the left one in order to better analyze the moderately high strain rate tests curves. **Errore. L'origine riferimento non è stata trovata.** confirms such finding and also shows that the dependence of R on ε_{True} is quite greater than the dependence on $\dot{\varepsilon}_{True}$.

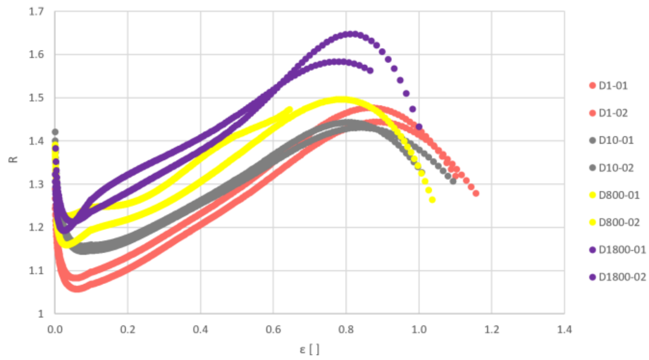

Fig. 7. Dynamic amplification of the stress, R vs ε_{True}, from all dynamic tests

Similarly to the thermal softening, which is found to be a two-variable function $S(T,\varepsilon)$ including the plastic strain, also the dynamic amplification of the A270 is found to be a two-variable function $R(\dot{\varepsilon},\varepsilon)$. This demonstrates that the typical uncoupling of strain, strain rate and temperature effects, typically implemented in many literature models, is not suitable for describing a structural metal like the A270 steel at hand.

Conclusions

The combined strain rate and temperature effects on an A270 steel were analyzed in this work, by means of an experimental campaign including static and dynamic tests at room and high temperature.

The static experimental true curves were translated into Mises curves via post-necking correction, for determining the thermal softening function of the A270 steel.

Such function resulted to be a two-variables function of both temperature and plastic strain. The large anticipations of the necking onset at high temperatures in static tests delivered one more strong evidence confirming that plastic strain and temperature are coupled within the thermal softening function.

In addition, the true curves from dynamic experiments were translated into Mises curves, for determining the temperature histories via a unit Taylor-Quinney parameter and, in turn, determining the history of thermal softening. Then, the dynamic stress-strain curves depurated of such thermal softening delivered the dynamic amplification.

Also the strain rate effect resulted to depend on both plastic strain and strain rate, to the extent that the dependence on ε_{True} was clearly larger than that on $\dot{\varepsilon}_{True}$.

These findings suggest the implementation of remarkable changes in many material models, for taking into account the frequently neglected coupling between strain, strain rate and temperature variables.

References

1. Besnard G., Hild F., Lagrange J. M. , Martinuzzi P., Roux S., (2012); Analysis of necking in high speed experiments by stereocorrelation, International Journal of Impact Engineering. 49: 1353–1367.
2. Bridgman, P. W. (1952). Studies in large plastic flow and fracture (Vol. 177). New York: McGraw-Hill.
3. Ghosh, A. K. (1977). Tensile instability and necking in materials with strain hardening and strain-rate hardening. Acta Metallurgica, 25(12), 1413-1424.
4. Guan, Z. (2014). Quantitative analysis on the onset of necking in rate-dependent tension. Materials & Design (1980-2015), 56, 209-218.
5. Hart EW. (1967) Theory of the tensile test, Acta Metall;15:351–5.
6. Jovic, C., Wagner, D., Herve, P., Gary, G., & Lazzarotto, L. (2006, August). Mechanical behaviour and temperature measurement during dynamic

deformation on split Hopkinson bar of 304L stainless steel and 5754 aluminium alloy. In Journal de Physique IV (Proceedings) (Vol. 134, pp. 1279-1285). EDP sciences.

7. Kapoor, R., & Nemat-Nasser, S. (1998). Determination of temperature rise during high strain rate deformation. Mechanics of materials, 27(1), 1-12.
8. Lin, E. I. H. (1977). Plastic instability criteria for necking of bars and ballooning of tubes (No. CONF-770807-36). Argonne National Lab., Ill.(USA).
9. Mirone, G. (2004). Approximate model of the necking behaviour and application to the void growth prediction. International Journal of Damage Mechanics, 13(3), 241-261.
10. Mirone, G., Barbagallo, R., & Giudice, F. (2019). Locking of the strain rate effect in Hopkinson bar testing of a mild steel. International Journal of Impact Engineering, 130, 97-112.
11. Mirone, G., Barbagallo, R., Corallo, D., & Di Bella, S. (2016). Static and dynamic response of titanium alloy produced by electron beam melting. Procedia Structural Integrity, 2, 2355-2366.
12. Mirone, G., Verleysen, P., & Barbagallo, R. (2019). Tensile testing of metals: Relationship between macroscopic engineering data and hardening variables at the semi-local scale. International Journal of Mechanical Sciences, 150, 154-167.
13. Osovski, S., Rittel, D., Rodríguez-Martínez, J. A., & Zaera, R. (2013). Dynamic tensile necking: influence of specimen geometry and boundary conditions. Mechanics of materials, 62, 1-13.
14. Peroni L., Scapin M., Fichera C., (2015) An advanced identification procedure for material model parameters based on image analysis, 10th European LS-DYNA Conference 2015, Würzburg, Germany.
15. Rittel, D., Zhang, L. H., & Osovski, S. (2017). The dependence of the Taylor–Quinney coefficient on the dynamic loading mode. Journal of the Mechanics and Physics of Solids, 107, 96-114.
16. Ruggiero, A., Bonora, N., Gentile, D., Iannitti, G., Testa, G., Colliander, M. H., ... & Vettore, F. (2018, July). Strain rate effects on fracture behavior of austempered ductile irons. In AIP Conference Proceedings (Vol. 1979, No. 1, p. 070028). AIP Publishing.
17. Rusinek, A., Zaera, R., Klepaczko, J. R., & Cheriguene, R. (2005). Analysis of inertia and scale effects on dynamic neck formation during tension of sheet steel. Acta Materialia, 53(20), 5387-5400.
18. Sasso, M., Fardmoshiri, M., Mancini, E., Rossi, M., & Cortese, L. (2016). High speed imaging for material parameters calibration at high strain rate. The European Physical Journal Special Topics, 225(2), 295-309.
19. Scapin, M., Peroni, L., & Fichera, C. (2014). Investigation of dynamic behaviour of copper at high temperature. Materials at High Temperatures, 31(2), 131-140.
20. Walley, S. M., Proud, W. G., Rae, P. J., & Field, J. E. (2000). Comparison of two methods of measuring the rapid temperature rises in split Hopkinson bar specimens. Review of scientific instruments, 71(4), 1766-1771.

DYMAT2019 P08

Temperature evolution and consequences in adiabatic shear localization onset and development

Patrice Longère[1]

[1]Institut Clément Ader (CNRS 5312), Université de Toulouse, ISAE-SUPAERO, 10 avenue Edouard Belin, 31055 Toulouse, France

Abstract. Adiabatic shear banding (ASB) is a shear localization mechanism occurring in high strength materials under high strain rate and impact loading as the consequence of thermo-mechanical instability. The influence of the method used for evaluating the plastic dissipation induced temperature rise, of the competition between thermal softening and microstructure changes, and of the cooling during unloading are discussed in regards with ASB onset and post-loading state in materials and structures undergoing high strain rate and impact loading.

1 Introduction

Adiabatic shear banding (ASB) is a shear localization mechanism occurring in high strength materials under high strain rate and impact loading involving (quasi) adiabatic conditions as the consequence of thermo-mechanical instability. Temperature thus plays a major role in this mechanism favouring the ultimate structural failure.

During a long time, thermal softening has been considered as the predominant factor in ASB initiation. Self-heating is generally deduced from the inelastic heat fraction or Taylor-Quinney coefficient usually considered as having a constant value, which is a strong hypothesis experimentally disproved, see e.g. [1]. Indeed, experimental investigations have evidenced the dependence of the quantity in question on strain, strain rate and temperature, see [1-4]. The hypothesis consisting in considering the inelastic heat fraction as independent on the loading path is now recognized as highly unrealistic. When searching for the conditions for ASB and further failure onset, an accurate evaluation of the plastic dissipation induced temperature rise during any transient transformations is thus required.

From their pioneering experimental works, Zener and Hollomon, see [5], have shown that the temperature rise and resulting thermal softening induced by the plastic dissipation (under adiabatic conditions) is responsible for the mechanism of strain localisation known as adiabatic shear banding, at least in high strength steels. More recently, some experimental investigations of ASB susceptibility of titanium alloys have evidenced recrystallization in the post-mortem band material, see [6-7]. On the other hand, according to a microstructural investigation of ASB in the Ti-6Al-4V alloy, Rittel and co-workers, see e.g. [8-9], state that dynamic recrystallization (DRX) is not the consequence of ASB but is at its origin, and that thermal softening actually plays at best a secondary role, even no role at all. So, depending on the material, e.g. high strength steel vs. high strength titanium alloy ASB onset may be triggered by thermal softening, see [5], or by microstructural changes (e.g. dynamic recrystallization, DRX), see [8], or by their combination.

At last, after unloading, the hot adiabatic shear bands are subject to a fast quenching by the cooler surrounding matrix and are accordingly the siege of microstructural transformations, see [10].

The influence of the method used for evaluating the plastic dissipation induced temperature rise, see Section 2, of the competition between thermal softening and microstructure changes, see Section 3, and of the cooling during unloading, see Section 4, are discussed in regards with ASB onset and post-loading state in structures undergoing high strain rate and impact loading.

2 Evaluation of the plastic dissipation induced temperature rise and its consequence on ASB onset

In this section, we are studying the consequences on the ASB initiation conditions of the simplifications made for evaluating the plastic dissipation induced temperature rise during any adiabatic processes.

2.1 Theoretical and modelling framework

We are here considering a rate and temperature dependent material with isotropic strain hardening whose yield function F is assumed of the form

$$\begin{aligned} F\left(\underline{\underline{\tau}}, R\right) &= \sigma_{eq}\left(\underline{\underline{\tau}}\right) - \left[R_0\left(T\right) + R\left(\kappa, T\right)\right] \\ &= \sigma_v\left(\dot{\kappa}\right) \geq 0 \end{aligned} \qquad (1)$$

where $\sigma_{eq}\left(\underline{\underline{\tau}}\right)$ represents the equivalent stress, $\underline{\underline{\tau}}$ the Kirchhoff stress tensor, $R_0\left(T\right)$ and $R\left(\kappa, T\right)$ the temperature dependent, initial radius of the Huber-Mises yield function and strain hardening force, respectively, and $\sigma_v\left(\dot{\kappa}\right)$ the viscous stress. T is the absolute temperature and κ the cumulated plastic strain.

---

* Corresponding author: patrice.longere@isae.fr

The stress-related quantities in (1) are expressed as

$$\begin{cases} R_0\left(T\right)=R_i f\left(T\right) \\ R\left(\kappa,T\right)=h'\left(\kappa\right)f\left(T\right) \\ \sigma_v\left(\dot{\kappa}\right)=B\dot{\kappa}^{1n} \end{cases} \tag{2}$$

where R_i, B, n are constants and where $h\left(\kappa\right)$ represents the stored energy of cold work and $f\left(T\right)$ the thermal softening function. In the following, the arguments of the functions are not necessarily specified.

Under high strain rate loading involving adiabatic conditions, heat equation reduces to

$$\begin{cases} \rho c\dot{T}=D+T\dfrac{\partial\underline{\underline{\tau}}}{\partial T}:\underline{\underline{d}}^{e}+T\dfrac{\partial R}{\partial T}\dot{\kappa} \\ D=\underline{\underline{\tau}}:\underline{\underline{d}}^{p}-R\dot{\kappa}=\left(\sigma_{eq}-R\right)\dot{\kappa}\geq 0 \end{cases} \tag{3}$$

where ρ, c are the mass density and specific heat, $\underline{\underline{d}}^{e}, \underline{\underline{d}}^{p}$ the elastic and plastic strain rate tensors contributions. In (2) the quantity D represents the unrecoverable energy rate dissipated by heating, the mechanical dissipation, where $\underline{\underline{\tau}}:\underline{\underline{d}}^{p}=\sigma_{eq}\dot{\kappa}$ is the plastic work rate and $R\dot{\kappa}$ the stored energy rate ; $T\dfrac{\partial\underline{\underline{\tau}}}{\partial T}:\underline{\underline{d}}^{e}$ represents the thermo-elastic coupling contribution which describes cooling during any tension loading and heating during any compressive one, and $T\dfrac{\partial R}{\partial T}\dot{\kappa}$ the thermo-plastic coupling contribution which expresses the stored energy release rate during the temperature rise. The thermo-elastic coupling contribution is actually significant in problems involving very high velocity impact and/or high pressure shock loading. In the context of this work, velocity and pressure are considered moderate and thermo-elastic coupling is neglected. We are now defining the inelastic heat fraction $\beta=\rho c\dot{T}/\underline{\underline{\tau}}:\underline{\underline{d}}^{p}$. Accordingly, combining (1) and (3) yields

$$\begin{cases} \dot{T}=\dfrac{1}{\rho c}\left[\sigma_{eq}-\left(R-T\dfrac{\partial R}{\partial T}\right)\right]\dot{\kappa} \\ \beta=1-\dfrac{R-T\dfrac{\partial R}{\partial T}}{\sigma_{eq}} \end{cases} \tag{4}$$

According to (4), the inelastic heat fraction β is inherently a function of plastic strain, plastic strain rate and temperature, see also [11-12].

2.2 Application to shear loading

The description of the post-critical response is not the purpose of the present study. Yet, in order to visualize the drop in stress provoked by adiabatic shear banding, the ASB deterioration model developed in the large scale postulate framework by Longère and co-workers, [13-15] is used. In the following application, functions $h'\left(\kappa\right)$ and $f\left(T\right)$ in (2) are expressed as

$$\begin{cases} h'\left(\kappa\right)=\tau_s\left[1-\exp\left(-b\kappa\right)\right] \\ f\left(T\right)=1-aT \end{cases} \tag{5}$$

where τ_s represents the saturation stress (Voce law) and a, b are constants.

We are now considering the high strain rate shear loading of a representative volume (RVE) with four evaluations for the inelastic heat fraction β :

- quasi complete evaluation with Eq.(4)
- simplified evaluation with $\beta=1-R/\sigma_{eq}$
- basic evaluation with $\beta=0.8$
- basic evaluation with $\beta=1$.

In the second evaluation, the thermo-plastic coupling contribution has been neglected. The evolution of the 'regular' temperature (temperature of the bulk material, outside the band) and of the shear resistance are plotted versus the shear strain in Figs.1-2. According to Fig.1, the 'regular' temperature is increasing until ASB onset and then saturates – when the plastic dissipation concentrates inside the band and makes the 'singular' temperature (the temperature inside the band) increase, see Fig.1. ASB onset is the point at which the shear stress starts to drop, see Fig.2.

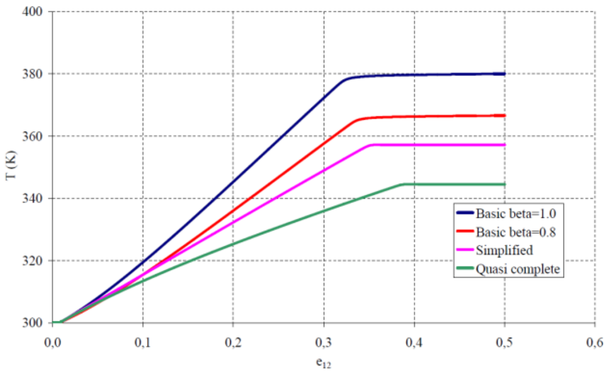

Fig. 1. Influence of the method used to estimate the plastic dissipation induced temperature rise. Temperature evolution.

According to Figs.1-2, assuming a high constant value for β leads to an overestimate of the temperature rise and, accordingly, an early ASB onset. Depending on the application, the error done may be conservative or not.

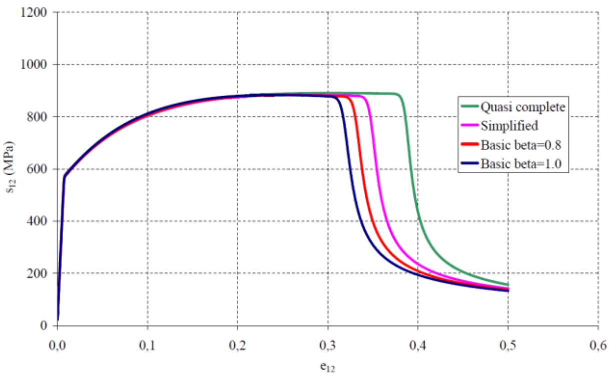

Fig. 2. Influence of the method used to estimate the plastic dissipation induced temperature rise. Shear stress evolution.

3 Thermal softening vs. DRX as predominant mechanism triggering ASB onset

In this section, we are studying the competition between thermal softening and dynamic recrystallization (DRX) in adiabatic shear banding (ASB) onset in a high strength titanium alloy like material.

3.1 Modelling framework

In this study, strain hardening phenomenologically accounts for the combined effects of dislocation production and accumulation (positive hardening) on one hand and dynamic recovery (DRC) and DRX (negative hardening, or equivalently softening) on the other hand via the expression of the following expression for $h'(\kappa)$ in (2)

$$\begin{cases} h'(\kappa)=\tau_s\left(Y(\kappa)\right)\left[1-\exp\left(-\dfrac{Y(\kappa)}{2}\kappa\right)\right] \\ \tau_s\left(Y(\kappa)\right)=\dfrac{\eta}{Y(\kappa)} \end{cases} \tag{6}$$

where η is a constant. The quantity Y is the sum of DRC and DRX contributions, i.e. $Y=Y_{DRC}+Y_{DRX}$, with

$$\begin{cases} Y_{DRC}=Y_0 \\ Y_{DRX}=Y_{\max}\left[1-\exp\left(-\dfrac{\langle\kappa-\kappa_c\rangle}{\Delta\kappa_r}\right)\right] \end{cases} \tag{7}$$

where Y_0 is a constant, $Y_{\max}$ is the saturation value of Y_{DRX}, κ_c the plastic strain at DRX onset and $\Delta\kappa_r$ a constant. $\langle . \rangle$ are Macauley brackets, i.e. $\langle x\rangle=\mathrm{Max}(0,x)$. The thermal softening function $f(T)$ in (2) is now expressed as

$$f(T)=\left\langle 1-\left(\frac{T}{T_{ref}}\right)^m\right\rangle \tag{8}$$

Equations (6-8) allow for describing thermal softening and DRX-induced softening, independently or concomitantly.

3.2 Application to shear loading

We are once again using the approach developed by Longère and co-workers, see above. In the following graphs in Figs.3-5, the shear stress is plotted with respect to the shear strain considering four configurations:

(i) no thermal softening and no DRX (No TS & No DRX),

(ii) no thermal softening and with DRX (No TS & With DRX),

(iii) with thermal softening and no DRX (With TS & No DRX),

(iv) with thermal softening and with DRX (With TS & With DRX),

for different values of the DRX-related constants in (7).

According to Fig.3 considering late DRX onset, the curves With TS & No DRX and With TS & With DRX are perfectly superposed meaning that DRX has no effect on ASB occurrence in this case. ASB initiation is thus only triggered by thermal softening. On the opposite, according to Fig.4 considering early DRX onset, the drop in stress is (quasi) simultaneous for the curves No TS & With DRX and With TS & With DRX. Thermal softening has consequently no (significant) effect on ASB occurrence. ASB initiation is thus mainly controlled by DRX softening. In Fig.5, values given to DRX related constants have been chosen so that the drop in stress is simultaneous for thermal softening-controlled ASB initiation (With TS & No DRX) and DRX-controlled ASB initiation (No TS & With DRX). According to Fig.5, when both activated (see curve With TS & With DRX), DRX and thermal softening act together for making ASB initiate earlier, see also [16].

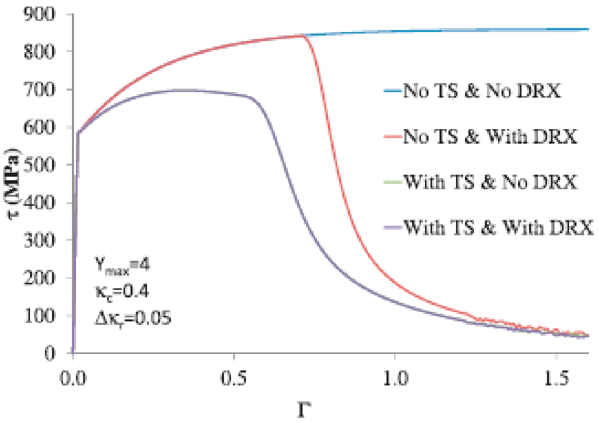

Fig. 3. Competition between thermal softening and DRX in ASB onset. Late DRX onset.

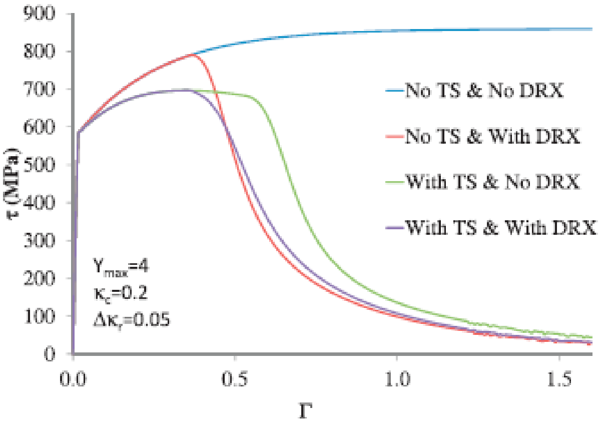

Fig. 4. Competition between thermal softening and DRX in ASB onset. Early DRX onset.

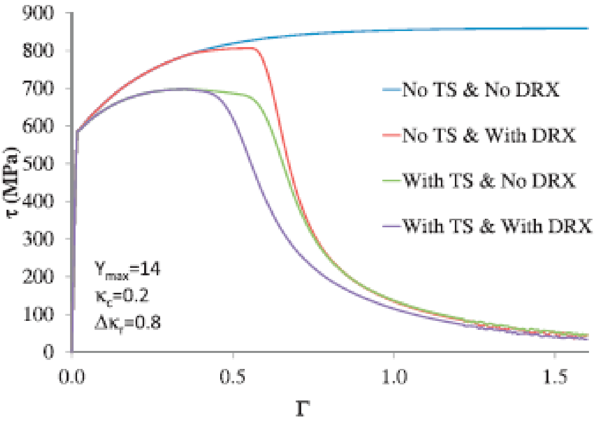

Fig. 5. Competition between thermal softening and DRX in ASB onset. Concomitant thermal softening and DRX.

4 Effect of cooling in the post-loading stage

Adiabatic shear banding is a strong localisation mechanism which may be the siege of significant microstructural transformations while preserving matter cohesion. At a more or less advanced stage of the ASB process, micro-voids may nucleate, grow and coalescence in the band wake leading to the formation of a crack and further failure of the structure, see e.g. [17-18]. Depending on the loading conditions (intensity, duration, etc), the post-loaded structure may contain ASB-affected zones (covering an area A_{ASB}) which are partly damaged by micro-voiding/cracking (covering an area A_{MV}), see Figs.6-7 after [19]. The damaged parts (covering an area A_{MV}) of ASB are irreversibly deteriorated, and may accordingly be no longer able to carry stresses, whereas the parts of ASB with matter cohesion (covering an area $A_{ASB} - A_{MV}$) have been submitted to cooling induced micro-structural changes during post-loading, and are accordingly still able to carry stresses. For this reason, ASB onset cannot be considered as a failure criterion.

The microstructural state of the undamaged parts of ASB strongly depends on the thermo-mechanical history and on the material itself.

For example in high-strength steels, during loading the temperature inside the band may be so high that the material is austenitized and even partly liquid, see [4]. The band being hot and the surrounding matrix being cooler, the unloading provokes a fast quenching of the band material which results in a martensitic transformation induced hardening of the band material at room temperature. After polishing and etching, the band is white and we speak of ‘transformed’ band. Upstream from the transformed part of the band, the band may be only deformed, we accordingly speak of ‘deformed’ band. The ‘transformed’ band material has thus recovered mechanical properties that can even be higher (at least in terms of strength) than the properties of the surrounding matrix, see [20].

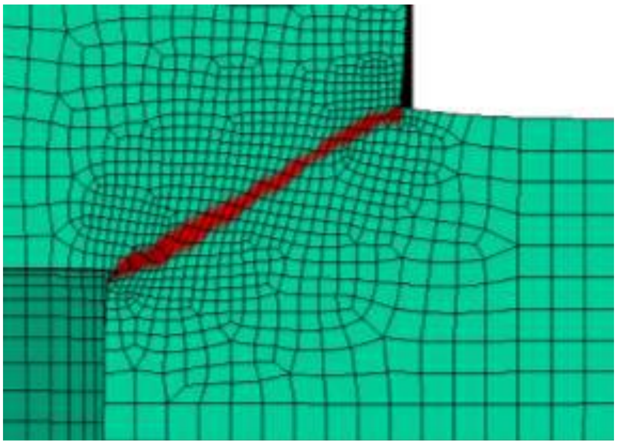

Fig. 6. High strain rate shear-compression loading of a hat shaped specimen. ASB indicator map in red.

For titanium alloys, the temperature inside the band during the loading is not very high and the material of the band is mostly subject to dynamic recrystallization (DRX), see [6]. It is noteworthy that the stored energy at recrystallization onset depends on temperature. The fast cooling during unloading freezes the microstructure. The deformed band has generally mechanical properties lower than those of the surrounding matrix.

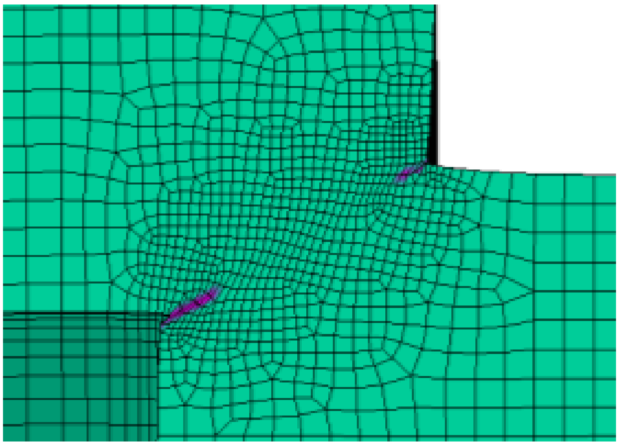

Fig. 7. High strain rate shear-compression loading of a hat shaped specimen. MV indicator map in purple.

Conclusion

When addressing problems involving dynamic plasticity, a particular attention must be paid to the evaluation of the plastic dissipation induced temperature rise. Indeed, the temperature magnitude and history have a direct consequence on the potential thermomechanical instability (adiabatic shear banding) onset and on the microstructural state of the post-loaded structure.

References

1. Mason J.J., Rosakis A.J. and Ravichandran G., On the strain and strain rate dependence of the fraction of plastic work converted to heat: an experimental study using high speed infrared detectors and the Kolsky bar, Mech. Mat., 17, pp.135-145 (1994).
2. Chrysochoos A., Maisonneuve O., Martin G., Caumon H. and Chezeaux J.C., Plastic and dissipated work and stored energy, Nucl. Eng. and Design, 114, pp.323-333 (1989).
3. Kapoor R. and Nemat-Nasser S., Determination of temperature rise during high strain rate deformation, Mech. Mat., 27, pp.1-12 (1998).
4. Oliferuk W., Maj M. and Raniecki B., Experimental analysis of energy storage rate components during tensile deformation of polycrystals, Mat. Sci. Eng., A 374, pp.77-81 (2004).
5. Zener C., Hollomon J.H., Effect of strain rate upon plastic flow steel, J. Appl. Phys., 15, pp.22-32 (1944).
6. Meyers M.A., Nesterenko V.F., LaSalvia J.C., Xue Q., Shear localization in dynamic deformation of materials: microstructural evolution and self-organization, Mat. Sci. Eng. A317 204–225 (2001)
7. Wang B., Li J., Sun J., Wang X., Liu Z., Shear localization and its related microstructural evolution in the ultrafine grained titanium processed by multi-axial compression, Mat. Sci. Eng. A 612, 227–235 (2014)
8. Rittel D., Landau P., Venkert A., Dynamic recrystallization as a potential cause for adiabatic shear failure, Phys. Rev. Lett. 101, 165501 (2008)
9. Landau P., Osovski S., Venkert A., Gärtnerová V., Rittel D., The genesis of adiabatic shear bands, Nature, Scientific Reports 37226, pp.1-6 (2016)
10. Derep J-L., Microstructure transformation induced by adiabatic shearing in armour steel, Acta Metal., 35-6, pp.1245-1249 (1987)
11. Longère P., Dragon A., Evaluation of the inelastic heat fraction in the context of microstructure-supported dynamic plasticity modelling, Int. J. Impact Eng. 35 992–999 (2008)
12. Longère P., Dragon A., Inelastic heat fraction evaluation for engineering problems involving dynamic plastic localization phenomena, J. Mech. Mat. Struct., 4-2, 319-349 (2009)
13. Longère P., Dragon A., Trumel H., de Resseguier T., Deprince X. and Petitpas E., Modelling adiabatic shear banding via damage mechanics approach, Arch. Mech., 55, pp.3-38 (2003)
14. Longère P., Dragon A., Trumel H. and Deprince X., Adiabatic shear banding induced degradation in a thermo-elastic/viscoplastic material under dynamic loading, Int. J. Impact Eng, 32, pp.285-320 (2005)
15. Longère P., Dragon A., Deprince X., Numerical study of impact penetration shearing employing finite strain viscoplasticity model incorporating adiabatic shear banding, J. Eng. Mat. Tech., ASME, 131, pp.011105.1-14 (2009)
16. Longère P., Respective/combined roles of thermal softening and dynamic recrystallization in adiabatic shear banding initiation, Mech. Mat., 117, pp.81-90 (2018)
17. Longère P. and Dragon A., Dynamic vs. quasi-static shear failure of high strength metallic alloys: Experimental issues, Eng. Fract. Mech., 80, pp.203-218 (2015)
18. Xue Q., Meyers M.A. and Nesterenko V.F., Self-organization of shear bands in titanium and Ti-6Al-4V alloy, Acta Mater., 50-3, pp.575-596 (2002)
19. Dorothy H.L., Longère P. and Dragon A., Coupled ASB-and-microvoiding assisted dynamic ductile failure, Proc. Eng., 197, 60-68 (2017)
20. Rogers H.C. and Shastry C.V., Material factors in adiabatic shearing in steels, [in] Shock waves and high strain rate phenomena in metals –

Concepts and applications, Plenum Press, M.A Meyers and L.E. Murr Eds, pp.285-298 (1981)

DYMAT2019 P09

The thermal softening response of soda-lime glass inferred from plate-impact experiments, ballistic tests, and computational analysis

Timothy Holmquist[*]

Southwest Research Institute, 5353 Wayzata Blvd., Minneapolis, MN, USA

Abstract. This work presents the high-strain-rate thermal softening response of soda-lime glass inferred from plate-impact experiments, ballistic impact tests, and computational analysis. Over the past 25 years several researchers have presented plate-impact experiments on soda-lime glasses that identified several interesting features: a softening of the bulk modulus for volumetric strains up to 0.23, a significantly stiffer bulk modulus for volumetric strains greater than 0.23, and a dramatic softening of the net stress (Hugoniot stress) for volumetric strains between 0.13 and 0.23. This dramatic softening has been the topic of discussion where explanations have included glass failure (damage softening), softening of the bulk modulus, and/or permanent densification. The work presented herein provides a third possibility, high-strain-rate thermal softening. Computed results that incorporate thermal softening are able to reproduce both the plate-impact softening characteristics, and the ballistic impact experiments that produce interface defeat; computed results that include only damage softening, or bulk modulus softening with permanent densification, cannot. These results suggest the dramatic softening observed in the plate-impact experiments is a result of thermal softening.

1 Introduction

The high-strain-rate behavior of glass is of interest because it is used in protective structures and other ballistic applications. Because of its wide use and unique behavior, it has been extensively studied, particularly in the plate-impact configuration. Plate-impact experiments have identified a unique response where the Hugoniot stress decreases (softens) as the volumetric strain increases. This softening is dramatic and has been the topic of discussion for many years. Explanations have included damage softening, time-dependent softening, and bulk modulus softening with permanent densification, but there has been no conclusive evidence for these hypotheses. The work presented herein will present a strong argument for high-strain-rate thermal softening. Although computations that include either damage softening or thermal softening can reproduce the plate-impact responses, the same damage softening behavior used to reproduce the plate-impact tests cannot reproduce ballistic impact experiments. The following sections will review the plate-impact experiments and present computed results that are in good agreement with both the plate-impact experiments and ballistic impact tests suggesting that the softening observed in the plate-impact experiments is due to thermal effects.

2 Plate-impact experiments

Figure 1 presents data from plate-impact experiments, for soda-lime glass, for volumetric strains up to $\mu = 0.35$. The test data are provided by Alexander et al. [1], Grady and Chhabildas [2], Simha and Gupta [3], and Dandekar [4] with all using similar forms of soda-lime glass (0.71-0.74 SiO_2, 0.11-0.15 Na_2O, 0.09-0.10 CaO). The softening behavior is clearly observed starting at approximately $\mu = 0.13$ and concluding at $\mu = 0.23$. What is unusual is the net stress actually decreases over this “softening zone” peaking at approximately 8 GPa at $\mu = 0.13$ and reducing to approximately 6.5 GPa at $\mu = 0.23$. The author is not aware of any material that exhibits this type of response. Because of this unusual behavior it is natural to question the accuracy of the data, but because two different researchers performed the experiments [1, 2], using two different plate impact techniques (standard and reverberation), there is strong evidence that this is the actual material behavior and not an experimental artifact (see Fig 1 tests AT-2, AT-8 and SODA-1). Figure 2 presents the plate impact data in terms of equivalent stress and pressure (the hydrostat presented in Fig. 1 is used to determine the pressure and equivalent stress), also included are data from Bourne and Rosenberg [5] and Brar et al. [6]. The softening is also clearly shown in Fig. 2 where the loading is initially elastic until the yield surface is reached (at approximately 4 GPa), maintained until the pressure reaches 5 GPa, and dramatically softened at pressures above 5 GPa. Grady and Chhabildas [2] suggested that this softening could possibly be a result of brittle shear fracture (damage softening) and/or permanent densification. Simha and Gupta [3] suggested time-dependent damage softening. The work presented herein will investigate the possibility of three separate softening responses: damage softening, thermal softening, and bulk modulus softening with permanent densification.

---

[*] Corresponding author: tholmquist@swri.org

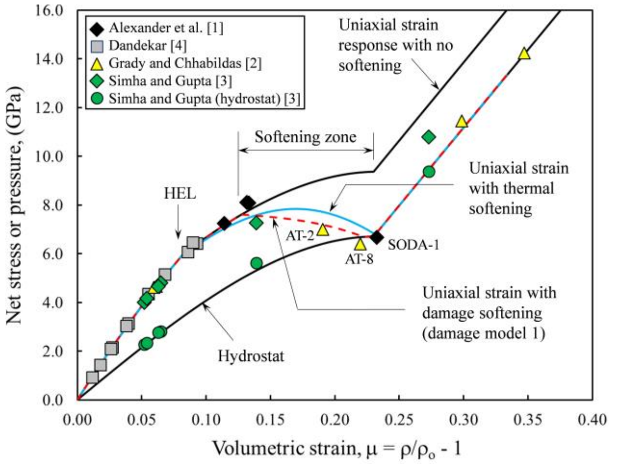

Fig. 1. The net stress and pressure as a function of volumetric strain for plate-impact experiments from several different researchers. Dramatic softening occurs over the "softening zone".

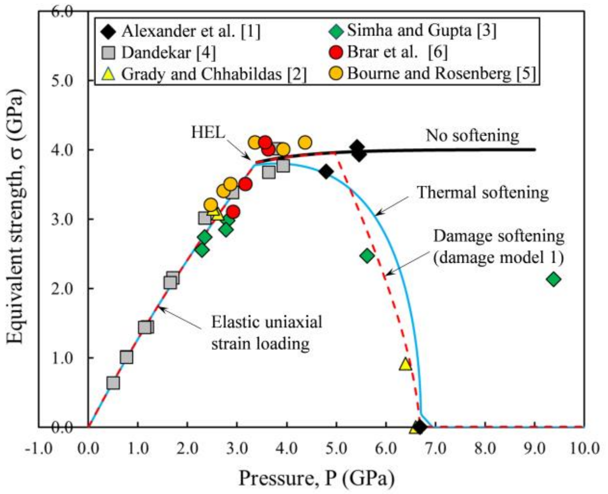

Fig. 2. The equivalent stress as a function of pressure for plate-impact experiments from several different researchers. Dramatic softening occurs when the pressure reaches approximately 5 GPa.

3 Computational analysis

In 2016 Holmquist, Johnson, and Gerlach (HJG) presented a revised glass model [7] and this will be the model used herein for the computational analysis. The model has an intact strength and failed strength; a pressure-volume response that includes bulking and permanent densification; a damage model to transition the strength from intact to failed, and thermal softening (a more in-depth description of the model is presented in reference 7).

There are at least three possibilities that could produce the softening response observed in Figs. 1 and 2: softening of the hydrostat with permanent densification; thermal softening; or damage softening. Each of these possibilities will be evaluated in turn.

The first possibility evaluated is hydrostat softening including permanent densification. The hydrostatic response of glasses is difficult to determine because they are amorphous and not well suited for test techniques that include x-ray diffraction (such as diamond anvil cell). Although difficult, there are other test techniques that can be used. Simha and Gupta [3] presented the hydrostatic response of soda-lime glass using plate-impact tests that included lateral gauges. The use of lateral and axial gauges allows for the direct determination of points along the hydrostat. They performed six experiments, reproduced in Fig. 1 by the circles. Also shown in Fig. 1 is the assumed hydrostat that goes through the data of Simha and Gupta, including consistency with the Hugoniot (net stress) data which must not fall below the hydrostat (note that test AT-8 does fall slightly below the hydrostat, but it is considered to be within the scatter of the data and taken herein to be on the hydrostat). Another important characteristic of soda-lime glass is that it exhibits 6% permanent densification when compressed to elevated pressures as presented by Ji et al. [8]. Permanent densification begins when the pressure exceeds 5 GPa and concludes when the pressure reaches 20 GPa. Using the HJG glass model with the hydrostat shown in Fig. 1, a permanent densification of 6%, and a constant flow strength (shown as the "no softening" response in Fig. 2) produces the uniaxial strain (no softening) response presented in Fig. 1 which is clearly not in agreement with the test data. This result suggests that softening of the hydrostat, including permanent densification, is not solely responsible for the softening observed in the plate-impact experiments.

The second possibility is thermal softening. Soda-lime glass has a low glass transition temperature, $T_g = 823K$ [8], at which temperature glass has very little strength (it becomes soft and rubbery). The glass model incorporates thermal softening in the same manner as the Johnson-Cook model [9]. The strength is given by $\sigma = \sigma_i\,[K_T]$ where σ_i is the intact strength and K_T is the thermal softening fraction. The thermal softening response for soda-lime glass is approximated from indentation data provided by Le Bourhis and Rouxel [10] and Watanabe et al. [11] as shown in Fig. 3 (here it is assumed that indentation softening represents strength softening) where K_T is presented as a function of the homologous temperature T^*. The homologous temperature is defined as $T^* = (T - T_r) / (T_g - T_r)$ where T is the actual temperature, T_r is the room temperature, and T_g is the glass transition temperature. Using the thermal softening response presented in Fig. 3 produces the uniaxial strain responses shown in Figs 1 and 2 (labeled as thermal softening) in good agreement with the test data. It appears that thermal softening is a possible explanation.

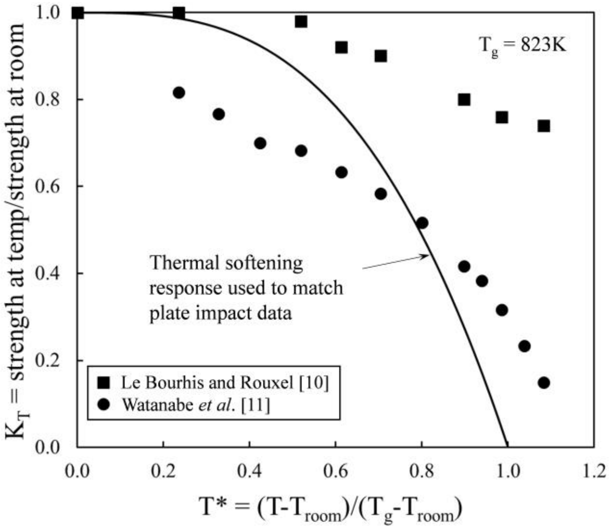

Fig. 3. Thermal softening of soda-lime glass as a function of the homologous temperature. Both experimental data and the model are presented.

The third possibility is damage softening, a characteristic of brittle materials. The glass model has the capability to gradually transition from the intact to failed strength as a function of damage (damage softening). Damage, D, is defined as $D = \Sigma(\Delta\varepsilon_p/\varepsilon_p^f)$ where $\Delta\varepsilon_p$ is the incremental equivalent plastic strain which occurs during an integration cycle, and ε_p^f is the equivalent plastic strain to fracture. The strain to fracture is given by $\varepsilon_p^f = D1(t^*+P^*)$ where t^* is the normalized tensile strength, P^* is the normalized pressure (both are normalized to the intact strength), and D1 is a constant. There is also the ability to delay softening until the damage reaches a critical value and then gradually (linearly) approaches the failed strength, reaching the failed strength when the damage equals 1.0. For this analysis the intact strength is 4 GPa and the failed strength is zero. The best correlation to the experimental data is shown in Figs. 1 and 2 (dashed line) using damage model 1 presented in Fig. 4. The model response also includes a delay in softening (softening does not begin until damage exceeds D = 0.4), evident in the uniaxial strain response in Fig. 2 as it initially follows the plastic response (no softening) before softening begins at P = 5 GPa. Damage softening using model 1 and a 40% delay produces results that are in good agreement with the test data. It appears that damage softening is also a possible explanation.

From the computed results it appears that the use of either damage softening or thermal softening is capable of reproducing the softening observed in the plate-impact experiments. However, there are ballistic tests that provide additional information, and clarity, into what response is most probable. Recently Southwest Research Institute (SwRI) performed reverse ballistic experiments where soda-lime glass cylinders impacted stationary gold rods. The objective of these tests was to determine the dwell-penetration-transition velocity, V_{dpt}. (When the impact velocity is below V_{dpt} interface defeat occurs where there is no penetration into the glass cylinder, when the impact velocity is above V_{dpt} penetration occurs.) This type of test has been performed on several other brittle materials and the reader is referred to references 12 and 13 for a more in-depth discussion. Fourteen experiments were performed on soda-lime glass and the dwell-penetration-transition velocity was determined to be V_{dpt} = 440 m/s +-22 m/s. Figure 5 presents the experimental result for an impact velocity of V = 417 m/s which produced interface defeat (no penetration into the glass cylinder). When the impact velocity was increased to V = 500 m/s there was prompt penetration. These experiments provide information regarding damage softening because there is very little thermal softening that occurs prior to penetration: the transition from dwell to penetration is primarily a result of damage softening. Figures 6 and 7 present the computed results for a gold rod impacting a soda-lime glass cylinder at V = 400 m/s using damage model 1 and damage model 2. The result using damage model 1 produces prompt penetration, in disagreement with the experiment. Damage model 2 is required to reproduce the experimental result of interface defeat and is nearly an order of magnitude more ductile than damage model 1. The uniaxial strain response using damage model 2 is identical to the response with no softening in Figs. 1 and 2 (because D < 0.4, the onset of softening) and clearly is too strong, in disagreement with the test data. Computed results that include both the thermal softening response shown in Fig. 3 *and* damage model 2 shown in Fig. 4, produce results that are in agreement with the softening response exhibited by the plate-impact experiments and the dwell-penetration-transition ballistic tests. Thermal softening dominates in the plate-impact experiments (because D << 1.0 due to high pressures and greater ductility at those pressures) and damage softening dominates in the interface-defeat (dwell) ballistic tests (because T^* << 1.0 due to low levels of plastic strain). These results provide strong

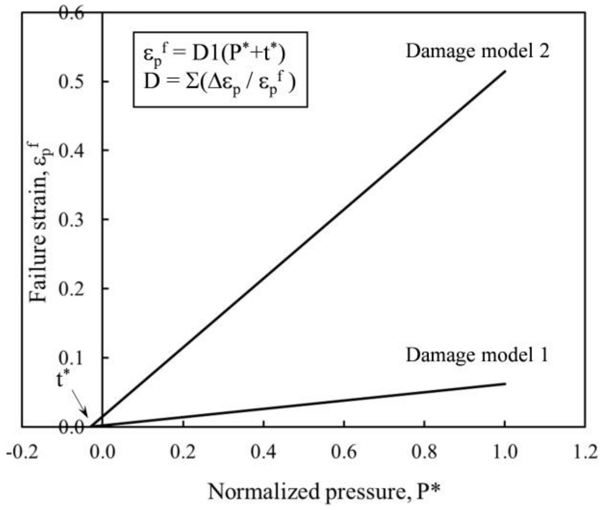

Fig. 4. Failure strain as a function of normalized pressure. Two damage models are shown; damage model 1 is required to produce computed results in agreement with the plate-impact experiments, damage model 2 is required to produce interface defeat at V = 400 m/s.

evidence that the softening observed in the plate-impact experiments is due to high-strain-rate thermal softening.

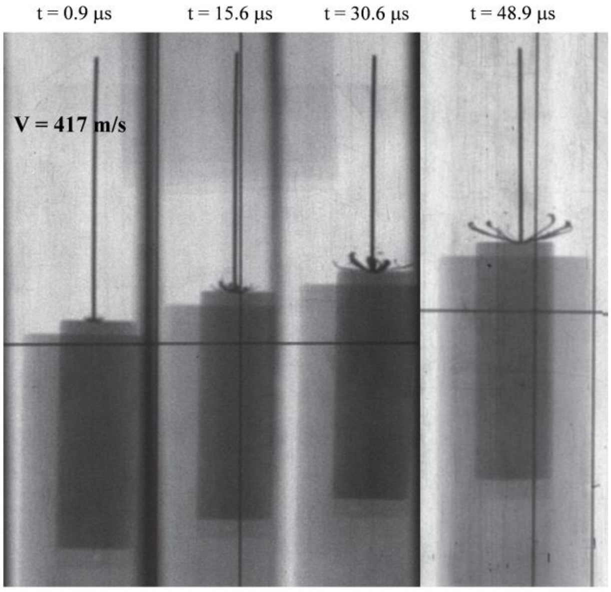
t = 0.9 µs
t = 15.6 µs
t = 30.6 µs
t = 48.9 µs
V = 417 m/s

Fig. 5. Experimental result for a soda-lime glass cylinder impacting a stationary gold rod at V = 417 m/s. The results are presented at t = 0.9, 15.6, 30.6, and 48.9 µs after impact. No penetration into the glass cylinder occurs.

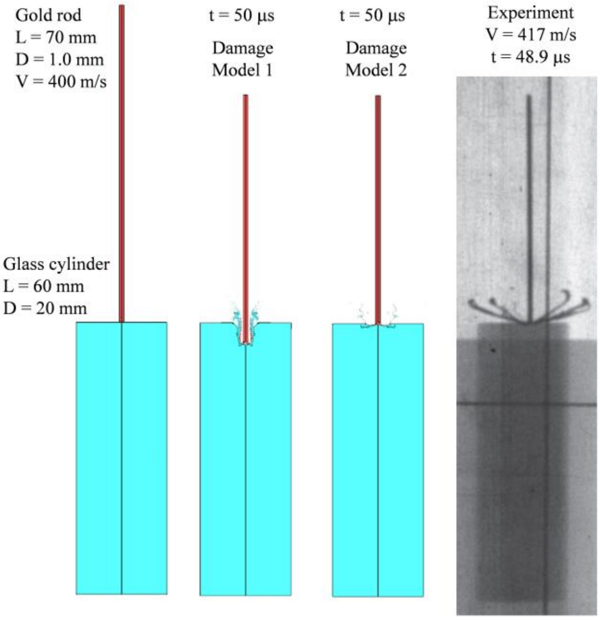
Gold rod
L = 70 mm
D = 1.0 mm
V = 400 m/s
t = 50 µs
Damage Model 1
t = 50 µs
Damage Model 2
Experiment
V = 417 m/s
t = 48.9 µs
Glass cylinder
L = 60 mm
D = 20 mm

Fig. 6. The left shows the initial geometry and the computed results at 50 µs after impact using damage model 1 and damage model 2. The far right presents the experimental result at t = 48.9 µs. When damage model 1 is used there is significant penetration into the glass cylinder, when damage model 2 is used there is no penetration into the glass cylinder, consistent with the experimental result.

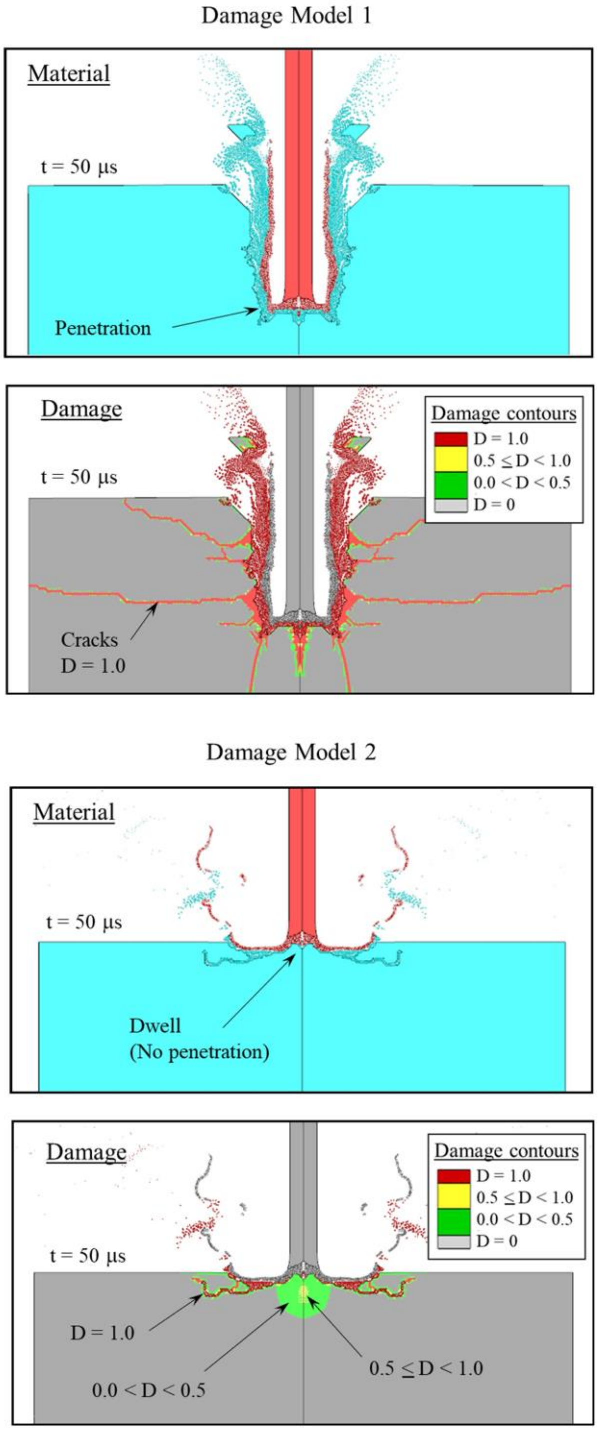
Damage Model 1
Material
t = 50 µs
Penetration
Damage
t = 50 µs
Damage contours
D = 1.0
0.5 ≤ D < 1.0
0.0 < D < 0.5
D = 0
Cracks
D = 1.0
Damage Model 2
Material
t = 50 µs
Dwell
(No penetration)
Damage
Damage contours
D = 1.0
0.5 ≤ D < 1.0
0.0 < D < 0.5
D = 0
t = 50 µs
D = 1.0
0.0 < D < 0.5
0.5 ≤ D < 1.0

Fig. 7. Computed results using damage model 1 and damage model 2. The top portion presents the computed results using damage model 1 showing material and damage. The bottom portion presents the computed results using damage model 2 showing material and damage. When damage model 1 is used there is immediate penetration into the glass cylinder, when damage model 2 is used there is no penetration.

Conclusions

This work has used plate-impact experiments, ballistic impact tests, and computational analysis to infer that the dramatic softening observed in soda-lime glass plate-impact experiments is most probably due to high-strain-rate thermal softening. A glass model that includes both thermal softening (estimated from indentation experiments) and damage softening (estimated from ballistic data) was used to reproduce plate-impact data and ballistic experiments providing the evidence used to make this conclusion.

The author acknowledges the financial support of the US Army Combat Capabilities Development Command Ground Vehicle Systems Center, (CCDC GVSC), Warren, MI that funded this work through NAMC Agreement Number 69-201501. The author would like to thank T. Talladay (US Army CCDC GVSC) for his support throughout this effort; to C. Anderson, Jr. (CEA Consulting), and D. Grosch (SwRI) for providing dwell-penetration-transition velocity ballistic data; and to S. Alexander (Sandia National Laboratory) for providing additional data and discussions regarding the plate-impact experiments.

References

1. S. Alexander, L. Chhabildas, W. Reinhart, and D. Templeton, Int. J. Impact Eng. **35** (2008)
2. D. Grady and L. Chhabildas, *Proceedings of the 14th U.S. Army Symposium on Solid Mechanics* (Myrtle Beach, South Carolina, 1996)
3. C. Simha and Y. Gupta, J. of Appl. Phys. **96** (2004)
4. D. Dandekar, J. of Appl. Phys. **84** (1998)
5. N. Bourne and Z. Rosenberg, *Proceedings of Shock Compression of Condensed Matter* (1996)
6. N. Brar, S. Bless, and Z. Rosenberg, Appl. Phys. Letters **59** (1991)
7. T. Holmquist, G. Johnson, and C. Gerlach, Phil. Trans. A, Royal Society, (2016)
8. H. Ji, V. Keryvin, R. Rouxel, and T. Hammouda, Scripta Materialia **55** (2006)
9. G. Johnson and W. Cook, *Proceedings of the Seventh International Symposium on Ballistics* (The Hague, Netherlands, 1983)
10. E. Le Bourhis and T. Rouxel, J. Non-Cry. Solids **316** (2003)
11. T. Watanabe, K. Puratsubaki, Y. Benino, H. Saitoh, T. Komatsu, J. Mat. Science **36** (2001)
12. T. Holmquist, C. Anderson, Jr., T. Behner, and D. Orphal, Adv. in Appl. Ceramics **109** (2010)
13. C. Anderson, Jr., T. Holmquist, D. Orphal, and T. Behner, Int. J. Appl. Ceramic Technol., **7** (2010)

DYMAT2019 P10

Hybrid Polymer-Nickel Auxetic Structures: Testing Using Open Hopkinson Bar, Digital Image Correlation and High-speed Thermography

Tomáš Fíla[1,*], *Jan* Falta[1], *Stefan* Bronder[2], *Petr* Koudelka[1], *Petr* Zlámal[1], *Marcel* Adorna[1], *Ondřej* Jiroušek[1], *Anne* Jung[2]

[1]Czech Technical University in Prague, Faculty of Transportation Sciences, Department of Mechanics and Materials, Konviktská 20, 110 00 Prague 1, Czech Republic
[2]Saarland University, Applied Mechanics, Campus A4.2, 661 23 Saarbruecken, Germany

Abstract. Two types of the hybrid polymer-nickel auxetic specimens were subjected to the quasi-static compression and compressive impact loading using Open Hopkinson Pressure Bar. Two variants of the 3D re-entrant auxetic lattice were used: i) structures with rectangular struts and ii) structure with rounded struts. The specimens were numerically optimized, prepared using computer aided design, and the base constructs were 3D printed from VisiJet EX200 polymer. The constructs were then coated using the electrodeposition of the nanocrystalline nickel in two nominal thicknesses of the coating (60 μm and 120 μm). After the coating process, the core part of the constructs was removed by the burning-out of the polymer at elevated temperature. The structures were subjected to the quasi-static compression and simultaneously inspected using an CCD camera, while Hopkinson bar was used for the impact loading of the specimens at two different impact velocities (ca. 5 m/s and 26 m/s). Dynamic experiments were observed with a pair of high-speed cameras and an infrared camera. The high-speed camera images were processed using a custom digital image correlation algorithm. Mechanical as well as thermal behavior of the hybrid auxetic structures subjected to the different loading conditions was analyzed and summarized in this paper.

1 Introduction

Auxetic structures are meta-materials exhibiting negative Poisson's ratio [1] that are therefore very promising for energy absorption applications [2]. Nowadays, the auxetics are usually porous structures created using 3D printing, additive manufacturing or other advanced manufacturing methods [3].

In this work, electrolytic coating deposition of a nanocrystalline metal layer on a base auxetic material (polymeric or metal additively manufactured constructs), was used. Two types of hybrid auxetic structures with a polymeric core and a nickel coating were tested using both quasi-static and dynamic compression. Nickel coating layer was deposited on the base structure produced by 3D printing of polymer. Three types of specimens were prepared: base structure specimens without coating, specimens with 60 μm coating layer thickness, and with 120 μm coating layer thickness. Complex experimental investigation was performed for evaluation of material properties, deformation mechanisms, energy dissipation and heat transfer effects at different strain rates. The specimens were tested quasi-statically in compression using electromechanical testing device and analyzed using digital image correlation (DIC) and thermography. For dynamic experiments, an Open Hopkinson Pressure Bar (OHPB) apparatus was used for compression of the specimens at two different strain-rates. Dynamic compression was observed using two high-speed cameras and a high-speed thermal imaging camera.

2 Materials and Methods

2.1. Specimens

The geometry of the samples was based on a periodical assembly of 3 × 3 × 3 re-entrant honeycomb auxetic unit cells. Two different types of structures with 25 samples per structure were manufactured. The first structure consisted of struts with circular cross section (referred as AuxR in the following text), and the second structure had struts with rectangular cross-section (referred as Aux3 in the following text). The 3D renders of both types of the specimens are shown in Fig. 1. The specimens were printed using the Pro Jet HD3000 3D printer (3D Systems, Rock Hill, USA) from the UV-curable polymer VisiJet EX200 with the highest resolution (656 × 656 × 800 DPI). The overall sample dimensions of the rectangular specimens were approximately 12.5 × 12.5 × 18.4 mm and of the circular specimens approximately 13.7 × 13.7 × 19.5 mm. Selected polymeric samples were electrochemically coated with 60 μm and 120 μm thick layer of nickel, respectively. Therefore, the polymer samples had to be made electrically conductive. This was achieved via dip-coating with a graphite lacquer. To connect the sample with the galvanostat, the sample was contacted with copper wires and positioned centrally in the deposition cell. A double-walled hollow cube with PVDF edges and titanium expanded metal side walls were used as anodic cage. The walls were filled with small nickel pellets as sacrificial anode and each wall was connected to the galvanostat. Further information on the coating process can be found in Jung et al. [4]. For the coating, a current density of 1.35 mA/cm^2 for the 120 µm nickel coating and a current density of 1.7 mA/cm^2 for the 60 µm nickel coating was applied. A commercial nickel sulfamat electrolyte (110 g/l Ni, Enthone GmbH, Langenfeld, Germany) was used at a constant temperature of 50 °C. Afterwards, the polymer was molten out via pyrolysis at about 1000 °C.

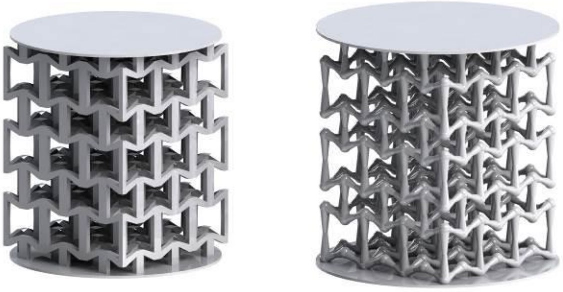

Fig. 1. 3D renders of the tested specimens: 3D re-entrant with rectangular cross-section of the struts – Aux3 (left), 3D re-entrant with circular cross-section of the struts – AuxR (right).

2.2 Quasi-static experiments

The quasi-static experiments were performed using electro-mechanical loading device 3382 (Instron, USA) with the loading velocity of 0.05 mm/s. The deformation was observed by a 5 Mpx monochromatic CCD camera G504b (AVT, Germany) attached to a bi-telecentric zoom revolver TCZR072 (Opto Engineering, Italy) for DIC and a thermal imaging camera SC7600 (FLIR, USA) operated in high-resolution mode. The experiments were performed in order to evaluate quasi-static compressive response of the investigated samples where strains were obtained using DIC, together with the inspection of their thermal response at low strain-rate. The quasi-static experimental setup is shown in Fig. 2.

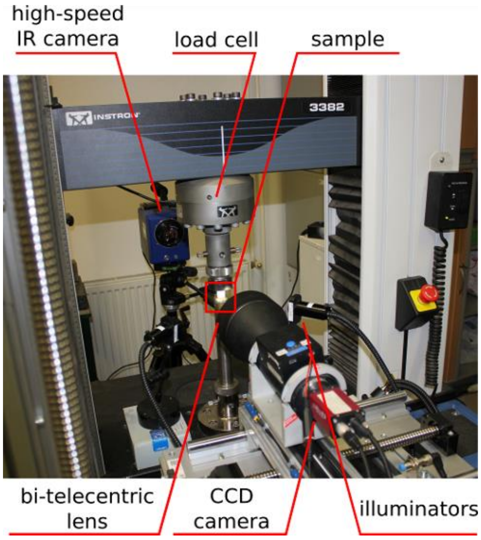

Fig. 2. Quasi-static experimental setup.

2.3 OHPB setup and experiments

Dynamic testing of the auxetic structures was performed using the OHPB setup [5]. OHPB method does not use a striker bar as the conventional Split Hopkinson Pressure Bar (SHPB). Instead, the instrumented incident bar is accelerated directly using a gas-gun system and impacts the specimen mounted on the transmission bar. In our setup, the incident bar is guided by the gas-gun barrel and by the low friction linear guidance system. Key advantages of the OHPB system are high strain reached in the specimen (comparing to the standard SHPB), measurement of the direct response of the specimen at both sides, no noise oscillations in the incident bar signals and easier evaluation of the results. Disadvantages of the method are lower maximum reachable strain-rate in the specimen (compared to the standard SHPB) and higher complexity of the system. The principle of the method is shown in Fig. 3.

Due to low mechanical impedance of the samples, the polymethyl-methacrylate (PMMA) bars with diameter of 20 mm were used. Length of both bars was 1750 mm. One measurement point (MP) was created on the incident bar, two MPs were created on the transmission bar. Each MP consists of two pairs of strain gauges in Wheatstone half-bridge arrangement. The first pair was equipped with foil strain gauges 3/120 LY61 (HBM, Germany) with 3 mm active length, whereas the second pair was equipped with semiconductor strain gauges AFP-500-090 (Kulite, USA) with 2.29 mm active length. The incident bar was guided by the linear guidance system consisting of the rail and the carriage drylinT (IGUS, Germany). Length of the track was 1200 mm. The transmission bar was supported by four linear bushings drylin (TJUM, IGUS, Germany). Wave dispersion effects in the PMMA bars were corrected using a conventional method based on the transfer function and experimentally measured wave propagation function [6]. Prior to the experimental campaign, quasi-static force calibration of the strain-gauges and experimental investigation of the dispersion effects was performed. The experiments were simultaneously observed by a synchronized pair of high-speed cameras Fastcam SA-Z (Photron, Japan) and by the same thermal imaging camera operated in the case of quasi-statics experiments in the high-speed mode. The OHPB experimental setup is shown in Fig. 4.

The hybrid auxetic specimens were tested at two nominal strain-rates corresponding approximately to 400 1/s (referred as low-rate in the following text) and 800 1/s (referred as high-rate in the following text). Reaching the identical nominal strain-rate in all the experiments required different impact velocity for each type of the coating of the samples. Thus, impact velocities from approx. 5 m/s to approx. 26 m/s were used in the experiments. The experiments were observed by the high-speed cameras with resolution of 256 × 168 px at approx. 250 kfps. Thermal response of the samples during the impact, heat transfer, and heat dissipation effects were observed using the thermal imaging camera at the resolution of 96 × 44 px at approx. 2 kfps.

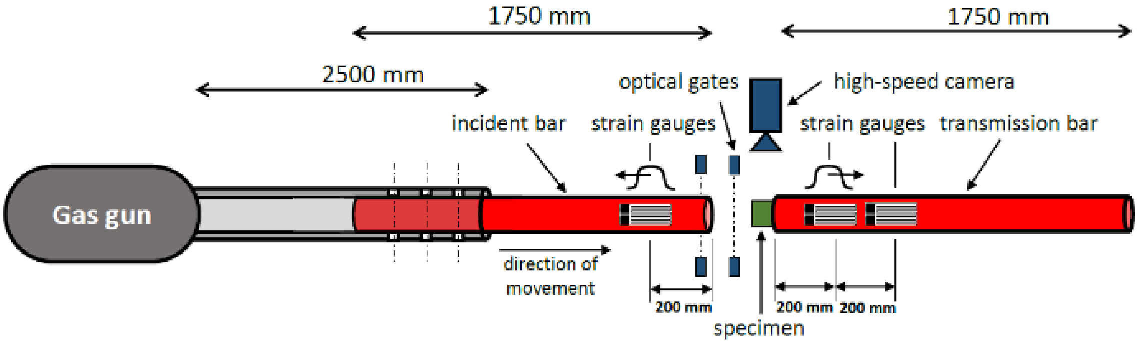

Fig. 3. Principle and scheme of the OHPB method

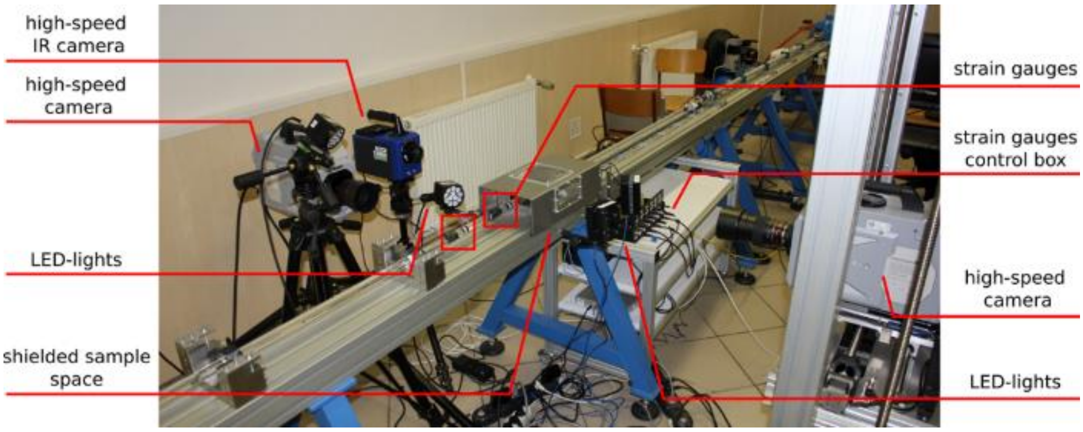

Fig. 4. OHPB experimental setup

3 Results

3.1 Quasi-static results

The quasi-static experiments were used for the evaluation of the material properties at strain-rate close to zero. Significantly different deformation behavior of the coated and uncoated structures was observed. Also thickness of the coating layer has a significant effect on the mechanical properties, particularly the stress-level at the plateau region. No heat transfer and heat dissipation effects were identified in the quasi-static experiments for both coated and uncoated specimens.

3.2 OHPB results – strain-gauges

In the dynamic experiments, the materials exhibited similar trends as in the quasi-static compression. However, effects of strain-rate were substantial and significant changes in the deformation behavior were identified. Using the OHPB with the PMMA bars, it was possible to reliably measure forces lower than 100 N and precisely evaluate the behavior of the structures during dynamic compression. Uncoated specimens exhibited very brittle behavior and disintegrated instantly during the initial phase of the impact. Coated specimens exhibited ductile behavior and it was possible to measure relevant material properties up to densification of the structure.

However, not all the coated specimens reached perfect dynamic equilibrium. Two effects were identified as a factors causing this behavior. Firstly, wave propagation time in the specimen was relatively long because of the length of the specimens and their low mechanical impedance. Secondly, strong effect from imperfections of the coating layer was observed. Some specimens did not have uniform distribution of the coating material together with defects in the coating layer. Moreover, small distortions of the structures caused by the melting of the base polymer was observed at some specimens. Therefore, some of the specimens were undergoing dramatic dynamic effects causing slower convergence of the incident and transmission signals. However, all measured signals were of good quality and were relevant for the analysis of the deformation behavior.

Signals from the incident strain-gauges and signals from all the transmission strain-gauges were in very good agreement. However, semiconductor strain-gauges exhibited strong non-linearity above 500 με as well as the significantly reduced lifetime [7]. The signals from the semiconductors were not used for the evaluation of the results. The data from foil gauges were processed using a similar technique described by Govender [5]. As the impact velocity of the incident bar is a crucial quantity for the reliable evaluation of strain in the specimen, digital image correlation of the incident bar displacement right prior to the impact was used for the evaluation of the impact velocity [8]. Impact velocity calculated using the flight-time of the incident bar between two optical gates was found unreliable and exhibited an error of around 10%. As the visco-elastic PMMA bars were used in the experiments, dispersion correction procedure based on method published by Bacon [6] was used for the time-shifting of the strain-gauges signals. Interestingly, the effect of the dispersion correction procedure was minor and the time shifted signals were almost identical with the measured signals. It can be estimated that because of the short distance between impact faces and strain-gauges and because of low mechanical impedance of the specimen it is not necessary to correct the strain-gauges data for the wave dispersion effects. However, wave dispersion analysis according to the abovementioned procedure has to be performed to evaluate the exact dynamic material properties of the measurement bars and correct for the geometrical imperfections of the setup. The example of the recorded good quality dynamic equilibrium of the AuxR specimen is shown in Fig. 5. The example of the evaluated stress-strain and strain-rate-strain curves for AuxR at both strain-rates is shown in Fig. 6.

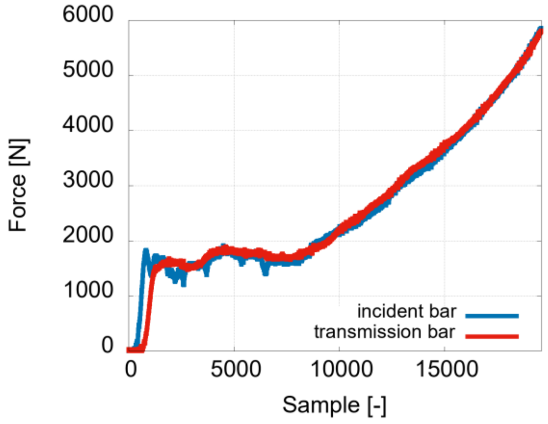

Fig. 5. Example of the dynamic equilibrium

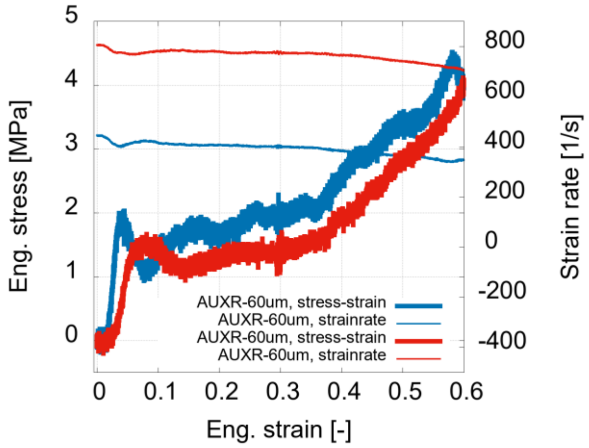

Fig. 6. Example of the recorded stress-strain and strain-rate-strain diagrams (raw curves – no filtration).

3.3 OHPB results – high-speed camera

High-speed camera images were used for the visual inspection of the experiment, for precise identification of the impact velocity, and for other processing using DIC. Image correlation techniques were successfully employed and it was possible to calculate displacement and strain fields of the coated and the uncoated specimens up to the plateau region of their deformation response. The Poisson's ratio was also evaluated in dynamic experiments using DIC. It was confirmed that the structures exhibit negative Poisson's ratio even in the dynamic compression. Results of the DIC were in a good agreement with the strain-gages results.

Typical results of the DIC are shown in Fig. 7 – 9. Comparison of the stress-strain diagrams evaluated from the strain-gauges and diagrams where strain was evaluated using DIC (stress was calculated from the strain-gauges signals) for AuxR structure with 60 µm coating is shown in Fig. 7. Diagrams calculated for both incident and transmission bar are shown in the picture. DIC strain was evaluated at the boundary between the bar and the specimen and is in very good agreement with the strain-gauges signals indicating that the strain-gauges were properly calibrated and produced reliable results.

Full-field DIC results of the longitudinal strain of the AuxR specimen with 60 µm coating at high-rate are shown in Fig. 8. As the unit cells of the structure were relatively large in comparison with the overall specimen's dimensions, it was possible to track the correlation points reliably to very high strain (up to ca. 40%).In the presented example, the strain was distributed evenly throughout the specimen. In some experiments, the deformation was more localized or lateral movements of the specimen during collapse of the individual cell layers was observed. Poisson's ratio to strain diagram evaluated using DIC from the points on the edges of the specimen and from the internal core of the structure is shown in Fig. 9. The specimen exhibited stable negative Poisson's ratio during the whole experiment.

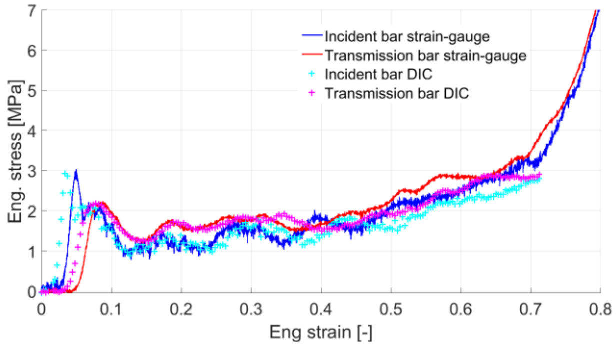

Fig. 7. Comparison of the incident and transmission stress-strain diagrams of the AuxR specimen with 60 µm coating evaluated using strain-gauges (solid lines) with diagrams where strain was evaluated using DIC (dotted lines).

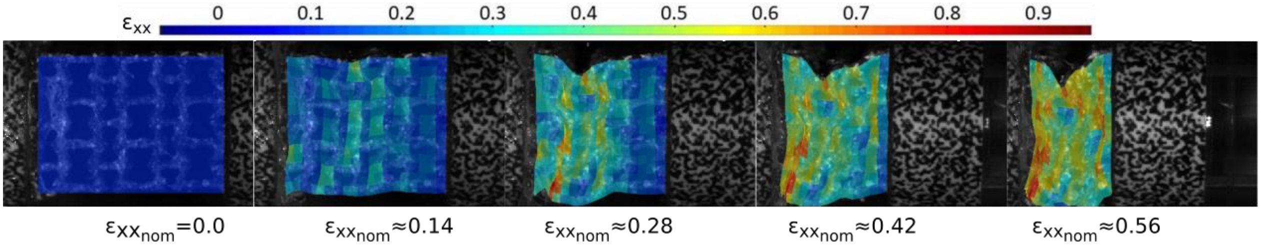

Fig. 8. Full-field DIC results of the longitudinal strain of the AuxR specimen with 60 µm at high-rate.

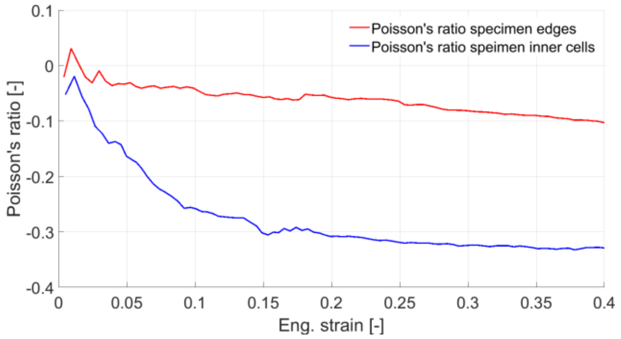

Fig. 9. Poisson’s ratio to strain diagram evaluated using simple DIC technique on the edges of the AuxR specimen with 60 µm at high-rate. Poisson’s ratio evaluated in the internal cells of the specimen (blue), Poisson’s ratio evaluated on the edges of the specimen (red).

3.4 OHPB results – thermal imaging

Changes in the heat transfer and heat dissipation effects were observed using the infrared camera. In all the experiments, it was possible to capture a limited number of the infrared images of a sample undergoing deformation. Heat-related effects were identified to be very different for all three types of the specimens,

particularly the maximum observed temperature and the heated area of the specimen. According to the obtained results, the thermograms can be successfully used for identification of the stress-concentration regions of the deforming structures as both heating of the individual struts and the joints was clearly apparent. This also open possibilities for analysis of friction-effects on the bar-specimen boundary that are crucial for numerical simulations of the experiments, where finding appropriate models and constants for frictional boundary effects is a very challenging task. In the following paragraph, representative results derived using infrared imaging are presented. Note, that only qualitative analysis of the heat distribution can be provided as the precision of the thermal imaging in this temperature range has inherent physical limitations because the photon counting detector was used for thermal imaging. Here, the quality of the images is affected by a limited amount of photons emitted by the specimens in spectral range of the detector, while the required maximum frame rate influences the necessary integration time yielding uncertainties and low signal-to-noise ratio in the observed temperature range.

The AuxR structures without coating exhibited averaged maximum temperature in the specimen approx. 44°C in the low-rate experiments and approx. 43°C in the high-rate experiments. The uncoated Aux3 specimens exhibited averaged maximum temperature approx. 41°C in the low-rate as well as in the high-rate experiments. The AuxR specimens with 60 µm coating exhibited 56°C in the low-rate experiments and 52°C in the high-rate experiments. The Aux3 specimens with 60 µm coating exhibited 54°C in the low-rate experiments and 56°C in the high-rate experiments. The AuxR specimens with 120 µm coating exhibited 61°C in the low-rate experiments and 65°C in the high-rate experiments. The Aux3 specimens with 120 µm coating exhibited 61°C in the low-rate experiments and 64°C in the high-rate experiments. Despite the temperature values are only estimated because of the thermal imaging precision, it can be concluded that no significant effect of the strain-rate in terms of the averaged absolute temperature for all types of the structures was observed. However, significant influence of the coating thickness on the averaged absolute temperature was identified. Moreover, the average temperature values in the individual specimen groups (based on the coating thickness) exhibited similar values.

Influence of the strain-rate on heat distribution in the Aux3 specimen with coating of 60 µm is shown in Fig. 10a. It can be seen, that despite the absolute values of the temperature were not significantly changed with the strain-rate, the heat distribution throughout the specimen was different. This trend was observed for the majority of the coated specimens. Influence of the coating layer thickness on the thermal properties of the Aux3 specimens is shown in Fig. 10b. It can be seen that thickness of the coating had the significant effect on both maximum temperature and heat distribution throughout the specimen.

4 Discussion

Based on the achieved results, some outcomes and findings can be summarized and discussed:

- OHPB method with PMMA bars was found to be suitable for testing of low impedance materials with good precision. Even results of the uncoated specimens, exhibiting fast disintegration after the initial phase of the impact, were found reliable and dynamic equilibrium prior to the disintegration was identified.

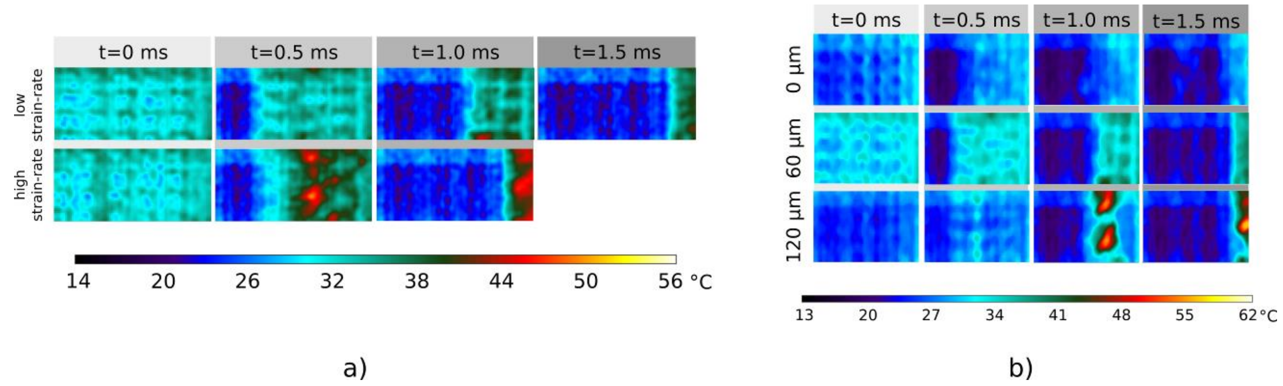

Fig. 10. Thermal imaging results: (a) influence of the strain-rate on heat distribution of the Aux3 specimens with 60 µm coating, (b) influence of the coating thickness on heat distribution of the AuxR specimens at low-rate.

- OHPB provided good quality data as the strain-gauges exhibited low noise and signals were not affected by the high amplitude oscillations. For some specimens, dynamic equilibrium was not achieved. However, it was found out that this behavior was not connected with the OHPB method but with the quality of the specimens.
- It was possible to test the specimens at strain-rates laying in the range between capabilities of drop-tower and conventional SHPB.
- Digital image correlation technique had to be employed for the evaluation of the incident bar impact velocity as the conventional evaluation using the flight-time between optical gates provided unreliable results with an error of approx. 10%. As the impact velocity is crucial for the correct evaluation of strain in the specimen in the OHPB method, it has to be evaluated with high precision.
- Because of the low impedance of the specimens, effectively filtering the high frequency oscillations, and short distance between strain-gauges and impact faces of the bars, wave dispersion effects in the visco-elastic PMMA bars were almost negligible. However, dispersion correction still had to be employed for the evaluation of the exact material properties of the bars at high strain-rate.
- Custom DIC tool was successfully employed for the evaluation of displacement and strain fields in the specimen at both low and high strain-rates.
- Results of DIC were in good agreement with the results of strain-gauges.
- High-speed thermal imaging was possible with the used infrared camera.
- As the recorded temperature of the specimens during the impact was relatively low, the results of the thermal imaging had to be considered qualitative with limited precision only. Nevertheless, the thermal imaging provided vital information about the heat distribution throughout the specimens with different coating.
- The manufacturing method of the specimens affected their quality in some cases (geometry distortion, imperfections of the coating etc.). Therefore, discrepancy in the deformation behavior of some specimens was observed. Thus, possible strain-rate related effects could not be identified as, if exist, they would be lower than the standard deviation throughout the OHPB experiments.
- OHPB together with DIC and thermal imaging was found to be vital experimental technique for the complex analysis of the mechanical behavior of the low impedance hybrid polymer-nickel auxetic specimens subjected to impact compression at moderate strain-rates.

5 Conclusion

Experimental campaign concerning an innovative hybrid auxetic structures was performed. Two types of auxetic structures produced by 3D printing were coated by the electrodeposition of the nickel at two different layer thicknesses. The specimens were tested in quasi-static and dynamic compression. OHPB was used as a method for dynamic compression at two different strain-rates. DIC and high-speed thermography were successfully used for the advanced analysis of the material behavior at both quasi-static and dynamic loading conditions.

The research was supported by the Czech Science Foundation (project no. 19-23675S) and the internal grants of the Czech Technical University in Prague (projects no. SGS18/153/OHK2/2T/16 and SGS18/154/OHK2/2T/16). All the financial support is gratefully acknowledged.

References

1. T. Li et al., Mater. Des. 142, 247 (2018).
2. N. Novak et al., Int. J. Impact Eng. 31, 122 (2018).
3. I. Gibson et al., Springer, New York, USA, (2010).
4. A. Jung et al., Adv. Eng. Mater. 18, 4 (2016).
5. R. A. Govender, R. J. Curry, J. dynamic behavior mater. 2, 43 (2016).
6. C. Bacon, Exp. Mech. 38, 242 (1998).
7. J. Falta et al., In: Engineering Mechanics 2019, 97-100, (2019).
8. M. Adorna et al., In: Engineering Mechanics 2019, 29-32, (2019).

DYMAT2019 P11

Behaviour of bio-based cellular materials under severe loadings Effect of temperature and strain rate

Louise Le Barbenchon*, *Philippe* Viot, *Jérémie* Girardot *Jean-Benoît* Kopp

Arts et Métiers ParisTech, CNRS, I2M Bordeaux, Esplanade des Arts et Métiers, F-33405 Talence Cedex, France

Abstract. The demand for bio-sourced materials is currently increasing. Cork material because of its unique properties (fire resistant, energy absorbing, ...) is then an excellent candidate for a large set of applications. This paper investigates the dependency of the mechanical behaviour from environmental conditions under a compressive loading. The material behavior has been determined as a function of the temperature and the mean strain rate. The microstructure was observed through scanning electronic microscopy. The characterisation of cork at different strain rates was then carried out. An electromechanical testing machine was used to apply an uniaxial compression at quasi-static strain rates. A fly-wheel was used for higher strain rates, up to 70 s^{-1}. Agglomerated cork was found to be temperature and strain-rate dependent. Its micro-structure reveals at complex composite material influencing strongly mechanical properties.

1 Introduction

Cellular materials are used in many different application domains such as transport, sport, food, health and energy. The main characteristics of these materials are a low density, an elastic rigidity, a capability to absorb noises and vibrations or to dissipate energy during an impact loading. Polymeric foams such as PVC, polypropylene and polystyrene foams are more particularly used in industry and their behaviour are largely commented in the literature [1]. These kinds of cellular materials do not support low or high temperatures and they cannot be used in aeronautic or spatial applications under severe conditions of loadings and temperatures. It can thus be interesting to investigate the behaviour of bio-based cellular materials that can with-stand extreme temperatures. Material like balsa [2], red-wood or cork which are in fact already used in passive safety applications, under severe conditions of temperature. For our study, an agglomerated cork has been chosen to evaluate its behaviour under quasi-static and high strain rates and low and high temperatures. Cork is naturally composed of microscopic prismatic cells shown in Fig. 1. The shape, orientation and organisation are anisotropic due to the growth of the tree. The main component of cork cell walls is suberin, a polymeric substance [3]. The other ones are lignin, cellulose and hemi-cellulose. Cork can be then considered as a multi-phased polymeric material. As expected from an organic material, cork and its by-products have a mechanical behaviour that is function of the environment like the humidity [4] and the temperature [5, 6] but also function of the loading conditions like the loading regime [7]. Previous studies demonstrated those dependancies on the structure behaviour. Yet the influence of the temperature and the mean strain rate on the deformation mechanisms is still not explicit. It is then important to investigate and try to explain the origin of these dependencies because several industrial applications can display a wide range of those conditions. The aim of this work is to study the mechanical behaviour of an agglomerated cork. It is a composite material made from a natural cellular material - the cork granules - bonded with a thermoset polymeric matrix. The strain rate and the temperature dependency of agglomerated cork products during compressive loadings are studied and described. Hypothesis concerning their origin is discussed taking into account the dependency of the cell wall constitutive material but also the specific structure of this material.

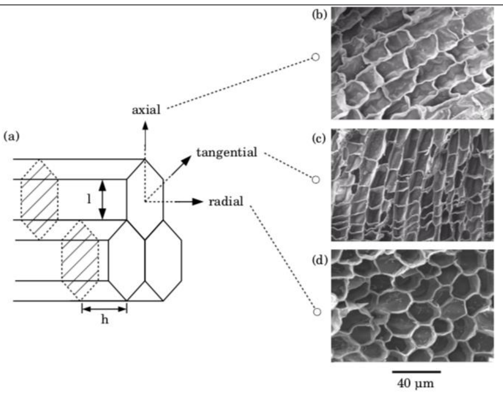

Figure 1. a) Oak trunk with the axis system of the tree. b) Cells disposition in a cork section. c) A corrugated cork cell, showing dimensions (schemes from [23]).

2 Material & Methods

2.1 Materials

To obtain agglomerated cork, small beads (∅ = 0.5/1 mm) were mixed together with a bio-sourced thermoset resin. This way, they are coated with resin. This mixture is uni-axially compressed into a mold to obtain a 1000 × 500 × 150 mm^3 block at a 0.42 density. During the

---

[*] Corresponding author: louise.le_barbenchon@ensam.eu

molding, the compression induces a preferential orientation of the beads already discussed in a previous article [8]. Fig. 2 shows the process with the two directions induced by the bead flattening: directions in the (Oxy) plane will be called in-plane directions (IP) and (Oz) direction will be called out-of-plane direction (OP). Giving the size of granulates, this material belongs to the micro-agglomerate category. The crossing was made in an autoclave at 130°C during 12 hours. Slab were then machined from the block.

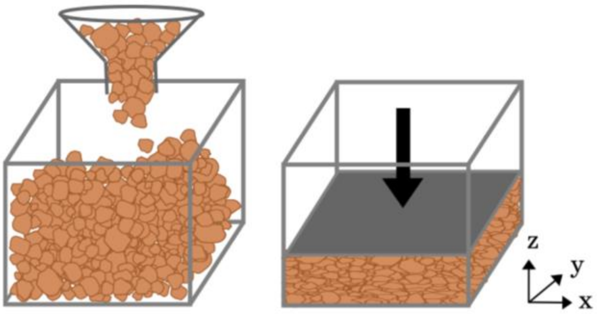

Figure 2. Manufacturing process. Cork beads coated with resin are poured inside a metallic mold then compressed uniaxially in the (Oz) direction.

2.2 Quasi-static regime

2.2.1 Tests at room temperature

20 × 20 × 20 mm^3 samples were cut from large slabs of agglomerated cork. They were conditioned at the 50% relative humidity (RH) for one month. An electromechanical traction/compression machine (Zwick Roell 250) with a load cell capacity of 250 kN was used. The imposed speed of the lower punch was set at 0.05, 5, 500 mm · min^{-1} corresponding to average strain rates of 4.2×10^{-5} s−1, 4.2×10^{-3} s^{-1} and 4.2×10^{-1} s^{-1}. Mechanical behaviour of the two main directions, in-plane and out-of-plane, were investigated.

2.2.1 Compression at different temperatures

At 4.2×10^{-3} s^{-1}, four temperature conditions were set: -30, -10, 100°C and the ambient temperature measured at 23°C. The heating/cooling was performed in a furnace equipped with a heater (for the 100°C temperature), a nitrogen cooling connector (for the temperatures of -30 and -10°C) and induced circulation to keep the temperature constant in the chamber during the tests. As cork is a thermal insulation material, samples were placed at least one hour beforehand in the furnace at the wanted temperature in order for them to reach a stabilized temperature. During room temperature tests, the heating chamber was removed. The temperature was verified using infrared temperature sensor before and after testing but also during testing for low mean strain rates.

2.3 Low dynamic compression regime

To reach higher levels of strain rates, cork samples were tested on a flywheel. It is an original device which allows to dynamically load specimens at intermediate strain rates (from 50 to 800 s^{-1}) This device, due to its high moment of inertia (77 kg·m2), enables the compression of specimens under constant velocity, since the specimen does not absorb enough energy to slow the wheel down. The operation of the wheel can be summarized as follows (see Fig. 3):
The heavy metallic wheel (1 m diameter, 617 kg) is set in motion and its rotation velocity is accurately controlled by an asynchronous motor. A hammer fixed on the wheel is the impactor of this machine which can impose tensile loadings on metallic or composite material and compressive loadings on cellular material according the associated apparatus being used [1].
To carry out compression tests on cork material, when the desired rotation velocity of the wheel is reached, a pneumatic jack pushes the anvil alongside the wheel. The anvil is then grabbed by the hammer inducing a rapid rotation of the crosspiece. This rotation imposes the displacement of the buckling bar BC and the lower power. The compression loading of the sample happens. Once the specimen is totally compressed or the compressive force reaches a threshold value, the bar BC buckles and interrupts further specimen compression. The unloading however is not controlled and is not operated at the same strain rate.
The compressive stress is measured by a piezoelectric force sensor and the compression displacement is determined by a dynamic laser sensor (Keyence LC 2100) [9]. Raw signals were used as they presented low noises.

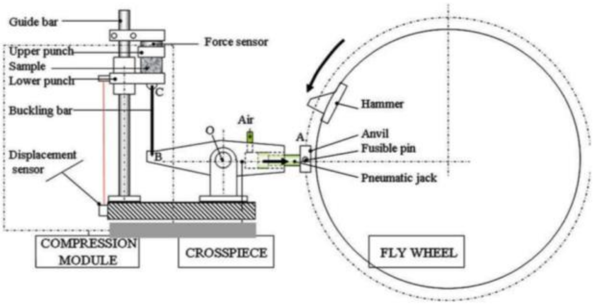

Figure 3. Scheme of the flywheel and compression device

2.4 Experimental compression curves post-treatment

From the force/displacement data, stress/strain curves were deducted by calculating nominal stress (σ = F/S0) and true strain ($\varepsilon = ln((l_0 - l)/l)$). Poisson's ratio of cork being close to 0 [10], the section did not change during the compression test.
The Young's modulus is calculated between a low strain ε_0 arbitrary fixed to 0.001 and the strain at the transition between linear and plateau response. To determine the

transition strain ε_r, the curve was fitted with a seven degree polynomial. The inflection point of the elastic part of the curve was found with its second derivative. The Young modulus is then calculated from the mean slope of the curve between the two strains ε_0 and ε_r.

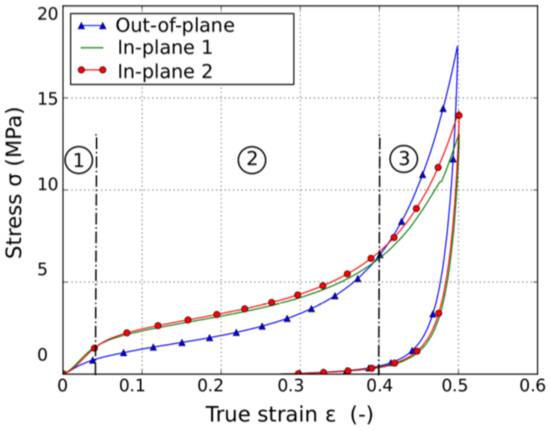

Figure 4. General aspect of a compressive curve for agglomerated cork in the Off-plane and In-plane directions.

3 Results & Discussion

3.1 General compression behaviour of agglomerated cork

Cork compressive behaviour is typical of foam-like materials [11]. A rather good repeatability was observed between samples tested in the same conditions, providing a preliminary conditionnement of the samples. Fig. 4 shows the mechanical behaviour of cork agglomerate under a compressive loading in both directions. First, for small strains (around 5 %) in (1), cork has an linear behaviour, that would be mainly due to cell walls bending [10]. A plateau in (2) follows where stress does not vary much until a 0.4 strain. During this phase, cells become more and more distorted. After that cell walls progressively collapse completely causing stress to increase strongly. This last stage is called the densification (3).

Because of the oriented structure of the cork beads due to the industrial process, the isotropy of the classical behaviour of cork agglomerates mentioned in several papers [7, 12, 13] is here questioned. In-plane direction proves to be stiffer which can be correlated with the geometrical aspects studied thank to x-ray tomography observations in a previous work [8]. Beads are initially more elongated in in-plane directions (during process) and thus harder to deform explaining this direction is more rigid.

Compressive tests demonstrate an anisotropic mechanical behaviour for cork agglomerates caused by an anisotropic geometry.

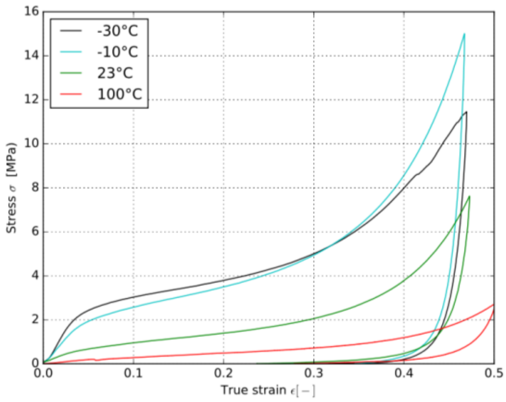

(a) Out-of-plane direction.

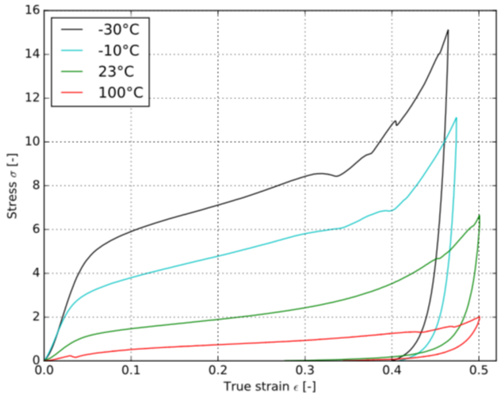

(b) In-plane direction.

Figure 5. Effect of the temperature on the mechanical compressive behaviour of cork agglomerate tested in the out-of-plane direction at a mean strain rate of $4.2 \times 10^{-3}\ s^{-1}$.

3.2 Effect of temperature

Fig.5 shows experimental stress/strain curves for quasi-static compression tests at several temperatures Fig.5 shows experimental stress/strain curves for quasi-static compression tests at several temperatures from - 30°C to around 100°C for cork agglomerates tested in both directions. As the temperature dependency is comparable the two directions, comments will only be on the out-of-plane direction in Fig. 5(a). At low temperatures (-30 and -10°C), the linear behaviour (first step) is clearly distinct. On the other side, for higher temperatures (23 and 100°C) this first phase is less visible and is hardly distinguishable from the plateau. Considering the linear and the plateau steps, for decreasing temperatures, increasing stresses are reached during the compression loading.

The temperature dependency of the mechanical behaviour of cork agglomerates, already reported in [14] is not surprising. Indeed, the whole material is a composite made of several polymeric materials. On one hand, there is the thermosetting resin, which is expected to have a linear dependency of its stiffness to the temperature on a wide range of temperature (glass transition temperature being high). On the other hand, there are beads of cork. And cork cells walls are made of several thermoplastic polymeric substances [15, 16].

When the temperature rises, molecular agitation increases. This agitation facilitates strain which is why the stress decreases.

It was possible in each case to measure the Young's modulus as reported in Fig.6. This figure shows the material stiffness in the out-of-plane and in-plane directions tested at 4.2×10^{-3} s^{-1} as a function of the temperature of the sample during the test. The material Young's modulus decreases quickly when the temperature rises from -30°C to 23°C. For higher temperatures the evolution is much less important. The difference between the stiffness at room temperature and high temperature is only of few MPa, for a temperature increase of 80°C. Thus the stiffness variation shows a rather non-linear behaviour with an inflection point around 10°C.

Recently temperature transition in the cork mechanical behaviour was studied [4]. A glass transition for cork equilibrated at 53 % relative humidity (RH) was identified around -6°C. It seems to depends a lot on the RH of the sample. The more dry the sample, the higher the glass temperature (from around 26.5°C for RH = 0 % to around -10 for RH = 97 %). Furthermore cork is a complex mixture of four main polymers (suberin, lignin, cellulose and hemi-cellulose). Their structure, bonding and molecular organization, which can actually have an impact on the water-dependance of T_g are not yet fully elucidated. The change in temperature dependency of the mechanical behaviour, here around 10°C, can then be associated to the near glass transition of one or several polymeric constituents of the cell walls of cork. It can be conclude that having a glass temperature right in the range of use and near ambient temperature, studies of the mechanical behaviour of cork-based material have to be very cautious regarding the environmental conditions, in relative humidity and in temperature.

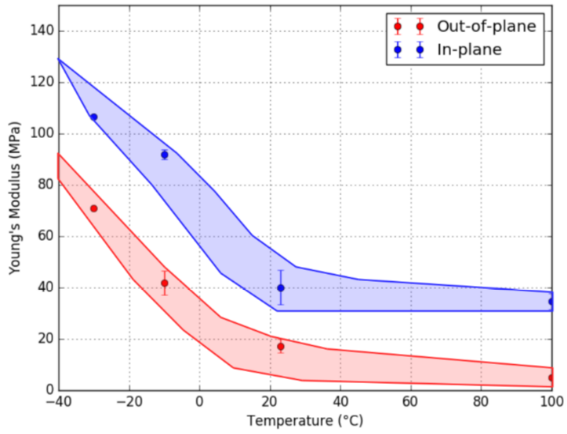

Figure 6. Effect of the temperature on the Young's modulus of cork agglomerate tested at a mean strain rate of $4.2 \times 10^{-3}\ s^{-1}$.

3.3 Effect of the mean strain rate

Because of the polymeric constitution of cork, cork-based materials are expected to be strongly strain-rate dependents. Besides cork agglomerate is considered for impact absorption. It is then important to characterize its mechanical behaviour at several loading rates and to understand the underlying mechanisms.

Fig.7 shows the experimental strain/stress curves of cork agglomerates tested in both directions at room temperature (23°C) at several mean strain rates, from the quasi-static regime to dynamic loadings. Once again a typical foam-like behaviour can be spotted on both figures. The bigger the mean-strain rate, the bigger stresses reached during the compression loading as already reported in [17].

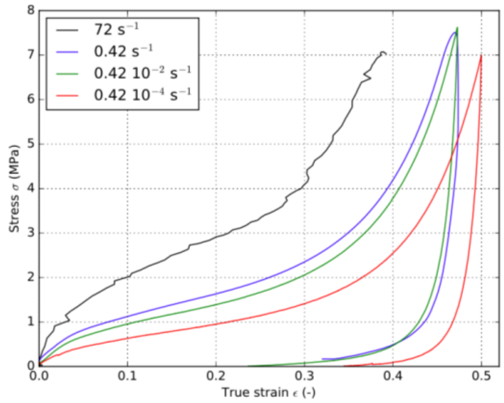

(a) Out-of-plane direction.

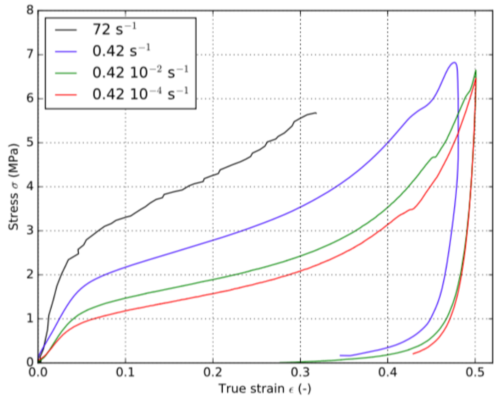

(b) In-plane direction.

Figure 7. Effect of the mean strain-rate on the mechanical compressive behaviour of cork agglomerate tested in the out-of-plane direction at room temperature (23°C).

This increase in stress comes partly from the fact that at the molecular scale, when the strain rate increases, the molecular chains have less time to deform. So it forces them to do more local movements. These movements are less effectives to produce strain and thus consume more energy. This is the exact same scenario as for the decrease for increasing temperature seen earlier. This typical behaviour of polymer is caused by the molecular movements that are thermally activated and is called the time/temperature equivalence [18, 19].

It is however only the dependency of constitutive material of the cell walls in the cork beads that is hereby considered. Other phenomena can also influence the strain-rate dependency. Gibson and Ashby report them in their book [11]. For high-strain rate loadings, special features of cellular solids influence the overall force-displacement response. Inertial energy contained in the rotations and asymmetric deflections associated with buckling modes of deformation can cause inertia at the microscopic scale, i.e. a delay in the buckling of cell wall. This delay leads to a deformation mode which can resist higher loads [20].

Moreover when a closed-cell foam, like cork, is deformed, the fluid within the cells is either compressed or expanded. For elastomeric foam, like cork, the effect of the gas on the rest of the stress-strain curve is very pronounced [21], even for reasonable ranges of strain rates (between 2×10^{-3} s^{-1} to 50 s^{-1}). For increasing strain rates, gas compression would then cause an increase in stress.

Depending on the cell wall material, the cell morphology and the material microstructure, these three possible causes to strain-rate dependency will not play the same role. To deconvoluate such effects, specific tests (like hydrostatic compression tests [22]) or modelisation and numerical simulation taking into account these parameters [23, 24] are needed.

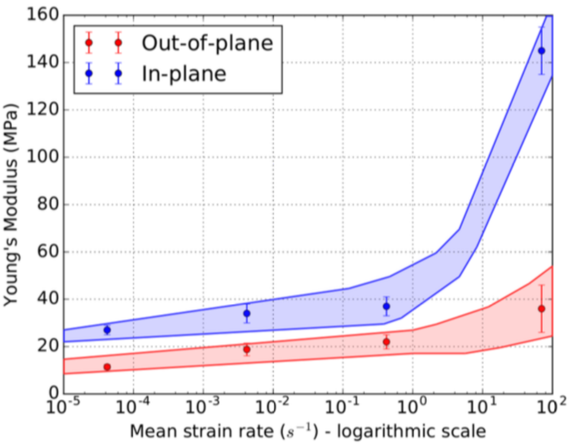

Figure 8. Effect of the mean strain rate on the Young's modulus of cork agglomerate tested at at room temperature (23°C).

The Young's modulus can also be plotted as a function of the mean strain rate with a logarithmic scale in Fig. 8. Whereas the evolution is quite linear in the quasi-static regime, a strong increase is noticed for the Young's modulus measured near 100 s^{-1}. As this step in the compression loading is only for small displacements without cell wall buckling. It would then be unlikely that either inertia in the microstructure nor gas compression in the closed cells have an effect on this material parameter. So the own dependency of the constitutive material seems to cause this non-linear increase of the Young's modulus for increasing strain-rate. By taking into account the time/temperature dependency, an analogy to the previous results can be made. The non-linearity in the Young's modulus evolution could also come from the fact that at 23°C for high strain rates, cooperative movements do not appear. Cell walls would then be no more into the rubbery state but in the glassy one. It would thus lead stress and the initial rigidity to increase much more rapidly than in the rubber state (for lower strain rates).

Conclusions

The aim of this work was to study the mechanical behaviour of an agglomerated cork and its dependencies to temperature and strain rate during a compressive loading. These two environmental conditions seemed to be intrinsically linked. It was indeed observed that either for increasing temperature and decreasing strain-rate, a drop of the stress could be observe on the macroscopic curves. A non-linear dependency was observed in the initial rigidity for both temperature and strain-rate.

Hypothesis concerning the origin of this dependency and its non-linearity was discussed taking into account the dependency of the cell wall constitutive material. A explanation at the molecular scale was then proposed. The specific structure of this material (closed-cells foam) was also mentioned as a possible influence for the strain rate dependency. Indeed inertia of the microstructure and compression of the enclosed gas could be potential causes of the increasing of stress for increasing strain-rates.

Perspectives of this work would be to study the mechanical behaviour of such material at several strain-rates in temperature in order to better describe the non-linear dependency. A thermal chamber for the fly wheel apparatus is being build. Modelisation of this behaviour will also be undertaken in order to try to deconvoluate what causes the strain-rate/temperature dependency.

Acknowledgements

This work was performed in the framework of the LIAMA project supported by Lieges HPK (Agnès de Montbrun), Safran Power Unit (Romain Quinton) and Région Nouvelle Aquitaine.

References

1. R. Bouix, P. Viot, J.L. Lataillade, International Journal of Impact Engineering 36, 329 (2009)
2. B. Toson, P. Viot, J. Pesqué, Engineering Structures 70, 36 (2014)
3. H. Pereira, Wood Science and Technology 26, 259 (1992)
4. A. Lagorce-Tachon, T. Karbowiak, D. Champion, R.D. Gougeon, J.P. Bellat, Materials and Design 82, 148 (2015)
5. M.E. Rosa, M. Fortes, Mater. Sci. Eng. A 111 100, 217 (1988)
6. M. Ptak, P. Kaczynski, F.A. Fernandes, R.J. de Sousa, International Journal of Impact Engineering 106, 238 (2017)
7. R. Jardin, F. Fernandes, A. Pereira, R. Alves de Sousa, Materials & Design 68, 121 (2015)
8. L. Le Barbenchon, J.B. Kopp, J. Girardot, P. Viot, Materialia (2019)
9. P. Viot, D. Bernard, 1, 2 (2005)
10. L.J. Gibson, K.E. Easterling, M.F. Ashby, Proceedings of the Royal Society A: Mathematical, Physical and Engineering Sciences 377, 99 (1981)

11. L.J. Gibson, M.F. Ashby, Cellular Solids: Structure and Properties, cambridge edn. (Cambridge University Press, Oxford, 1997)
12. P.T. Santos, S. Pinto, P.A. Marques, A.B. Pereira, R.J. Alves de Sousa, Composite Structures 178, 277 (2017)
13. R.A.S. Moreira, F.J.Q. De Melo, J.F. Dias Rodrigues, Journal of Materials Science 45, 3350 (2010)
14. P. Kaczynski, M. Ptak, J. Wilhelm, F.A.O. Fernandes, R.J.A. de Sousa, International Journal of Impact Engineering 126, 109 (2019)
15. H. Pereira, Wood Science and Technology (1988)
16. S.P. Silva, M.A. Sabino, E.M. Fernandes, V.M. Correlo, L.F. Boesel, R.L. Reis, International Materials Reviews 50, 345 (2005)
17. C.P. Gameiro, J. Cirne, G. Gary, Journal of Materials Science 42, 4316 (2007)
18. J.L. Halary, F. Lauprêtre, Mécanique des matériaux polymères (Humensis, 2015), ISBN 978-2-7011-8528-6
19. M.L. Williams, R.F. Landel, J.D. Ferry, Journal of the American Chemical Society 77, pp 3701 (1955)
20. Y. Sun, Q.M. Li, International Journal of Impact Engineering 112, 74 (2018)
21. J. Zhang, A. M.F., Tech. rep., Cambridge (1988)
22. P. Viot, International Journal of Impact Engineering 36, 975 (2009)
23. Y. Sun, Q.M. Li, International Journal of Solids and Structures (2015)
24. Y. Sun, B. Amirrasouli, S.B. Razavi, Q.M. Li, T. Lowe, P.J. Withers, Acta Materialia (2016)

DYMAT2019 P12

Using Full-Field Strain and Temperature Measurements to Determine the Taylor-Quinney Coefficient in Dynamic Tensile Tests

Jarrod L. Smith[1], *Jeremy D. Seidt*[1], *Amos Gilat*[*], *Veli-Tapani Kuokkala*[2]

[1]The Ohio State University, Department of Mechanical and Aerospace Engineering 201 W. 19th Ave., Columbus, OH, 43210, USA
[2]Tampere University of Technology, Department of Materials Science, Tampere, 33101, Finland

Abstract. Plastic deformation generates heat and the fraction of the plastic work that is dissipated by heat is given by the Taylor–Quinney coefficient (β). Temperature increase during plastic deformation softens the material and can offset the increase of stress due to strain hardening. Knowledge of the value of β is essential in numerical simulations of applications that involve dynamic loading since there is not sufficient time for the heat to dissipate and the temperature rise can be significant. A new test for determining the value of β is presented. In this test a material coupon specimen is loaded in tension at high strain rate. Full field measurements of deformation and temperature throughout the test (including in the necking region during the localization) are used for determining the value of β as a function of strain. Results from tests with specimens made of AISI 316L austenitic stainless steel show that the value of β increases with strain and reaches a plateau value of about 0.8 at strain of about 0.15.

1 Background

Plastic deformation generates heat and the Taylor-Quinney coefficient (β) is the ratio between the energy dissipated as heat and the overall work invested in producing the deformation. Knowing the value of the Taylor-Quinney coefficient is of great importance. It can provide insight into the microstructural evolution that occurs during the deformation, and it can play an important role in numerical simulations of applications that involve plastic deformation and failure. Accurate simulation of the temperature rise during the deformation is essential since a rise in temperature may offset the increase in stress due to strain hardening. This effect can be substantial when high strain rates and dynamic loading are involved where there is little or no time for the generated heat to dissipate and the temperature rise can be significant.

The fraction of plastic work that is converted to heat during deformation was first studied by Farren and Taylor [1] and Taylor and Quinney [2] during their experiments on the cold working of metals. In these experiments β was determined to be a constant 0.8-0.9 for all metals. These first tests, however, were performed quasi-statically at low levels of strain using complex calorimeter setups. Measurements of the Taylor-Quinney coefficient during high strain rate deformation have been mostly done in compression experiments conducted with the split Hopkinson bar (Kolsky) apparatus (SHB) [3-5]. In these tests the nominal stress and strain in the specimen during the tests were determined from the measured waves in the incident and transmitter bars assuming that the strain in the specimen is uniform. The temperature of the specimen was only measured at one, or a few, points using infrared (IR) detectors. McDougal and Harding [6] measured the temperature increase and calculated the Taylor-Quinney coefficient of Ti-6Al-4V using the torsional split Hopkinson bar technique. In a recent investigation [7] the Taylor-Quinney coefficient was determined in tensile SHB experiments. In this case the temperature was measured at only one point and the average strain was determined from the recorded waves in the incident and transmitter bars. Consequently, values of the Taylor-Quinney coefficient were obtained only for small strains since the average strain that is determined from the waves is valid only during uniform deformation before localization (necking) starts.

In the present paper the Taylor-Quinney coefficient is determined from tensile tests over a wide range of strain rates including high strain rates which are conducted in a tensile SHB apparatus. In these tests simultaneous full-field strain and full-field temperature measurements are made on the surface of the specimens. The strains are measured using the Digital Image Correlation (DIC) method with high-speed cameras, and the temperature is measured with a high-speed IR camera. Both, strain and temperature are measured throughout the test including in the necking region during the localization. By combining these measurements with the force determined from the wave in the transmitter bar, the Taylor-Quinney coefficient can be determined when the strain is uniform and in the necking region at large strains. Results from testing AISI 316L austenitic stainless steel show that the strain in the necking region can exceed 0.8 and the temperature rises by more than 300°C. The Taylor-Quinney coefficient increases with strain and reaches a plateau value of about 0.8 at strains above 0.15.

2 Experimental Setup

The Taylor Quinney coefficient was determined by conducting tensile tests at various strain rates (including dynamic tests) that included simultaneous measurements of full-field deformation and full-field temperature on the surface of the specimens during the tests. Tests at quasi-static stain rate were done using a servo-hydraulic load frame. Tests at a dynamic strain rate were done using a special intermediate strain rate apparatus [8], and high strain rate tests were done using a tensile split Hopkinson (Kolsky) bar (SHB) apparatus. The experimental setup is shown in Figure 1. The specimens are made of 316L austenitic stainless steel are flat and thin with dimensions shown in Fig. 2. The optical setup consists of a visual camera on one side of the specimen and a high speed IR camera on the other side.

---

[*] Corresponding author: gilat.1@osu.edu

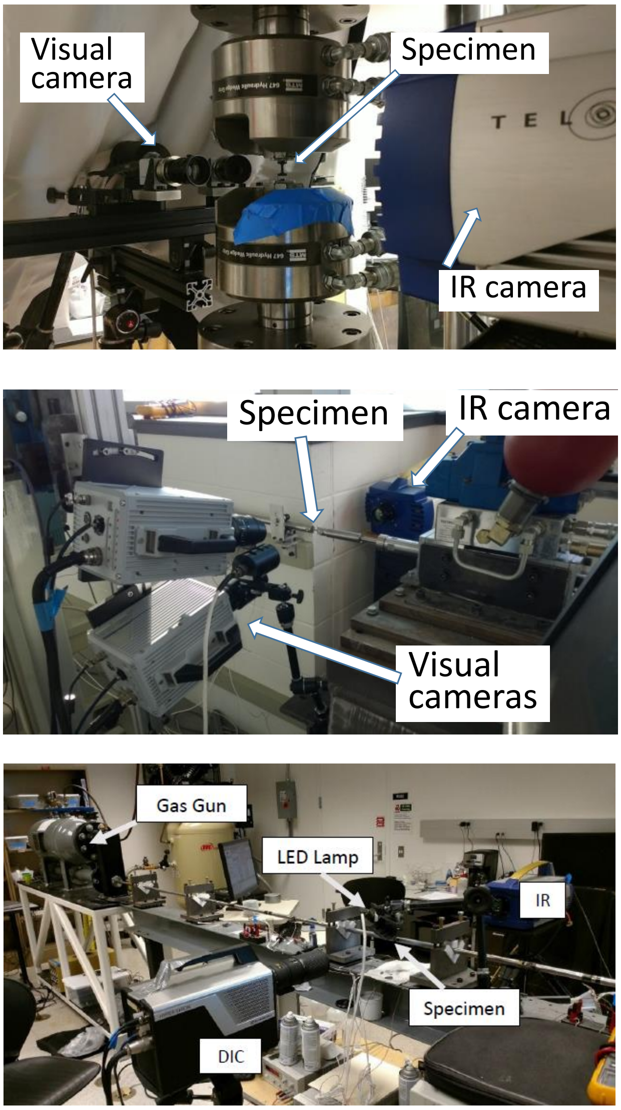

Fig. 1. Experimental setup; Low strain rate (top), intermediate strain rate (middle), high strain rate (bottom).

The quasi-static tests were done with the specimens deforming at a nominal strain rate of 1 s^{-1}. A Vision Research Phantom v7.3 camera was used for the DIC with a pixel resolution of 800x600 and frame rate of 500 fps. The temperature was measured with a Telops FAST-IR camera with a pixel resolution of 256x320 and frame rate of 500 fps. The dynamic tests were done with the specimens deforming at a nominal strain rate of 200 s^{-1} and 3,000 s^{-1}. In the 200 s^{-1} tests a Vision Research Phantom v7.3 camera was used for the DIC with a pixel resolution of 512x128 and frame rate of 20,000 fps. The temperature was measured with a Telops FAST-IR camera with pixel resolution of 64x128 and frame rate of 10,000 fps. In the 3,000 s^{-1} tests a Photron SA1.1 camera was used for the DIC with a pixel resolution of 384x128 and frame rate of 90,000 fps. The temperature was measured with a Telops FAST-IR camera with a pixel resolution of 24x64 and frame rate of 30,000 fps.

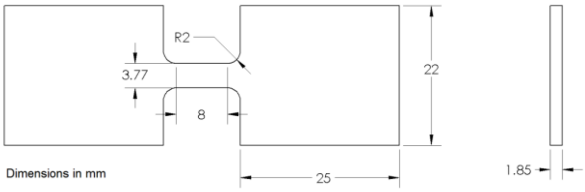

Fig. 2. Specimen geometry.

3 Results

Stress strain curves from testing 316L stainless steel specimens at different strain rates are shown in Figure 3. The figure shows significant strain rate sensitivity with increasing stress with increasing strain rate.

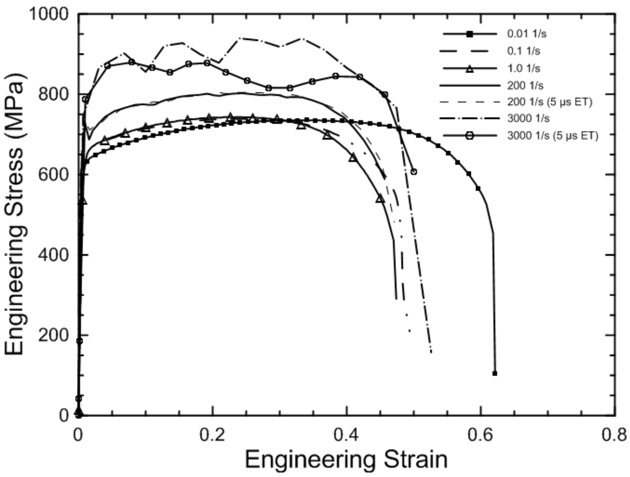

Fig. 3. Stress strain curves from testing 316L austenitic stainless steel at different strain rates.

Images of the deformation (DIC axial strain) and temperature recorded by the visual and IR cameras during tests at nominal strain rates of 1.0 s^{-1}, 200 s^{-1}, and 3,000 s^{-1} are shown in Figures 4-6.

The quantitative data from the images in Figures 4-6 are shown as waterfall plots in Figures 7-9. The figures show the distribution of the axial strain and the temperature along the center line of the specimen at different times during the test. Figures 7-9 show a nearly uniform deformation up to a strain of about 0.3 when necking starts to develop. Once the necking starts the deformation localizes quickly. The maximum strain at the necking region ranges from 0.5 at the high strain rate to 0.8 at the low strain rate. In the necking region the maximum temperature exceeds 240°C in the 1.0 s^{-1} strain rate test and reaches 320°C in the 200 s^{-1} and 3,000 s^{-1} strain rate tests.

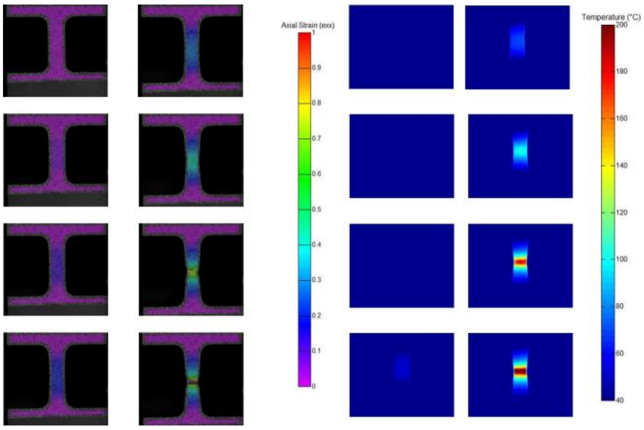

Fig. 4. Axial strain (DIC) and temperature measurements in a tension test at strain rate of 1 s^{-1}.

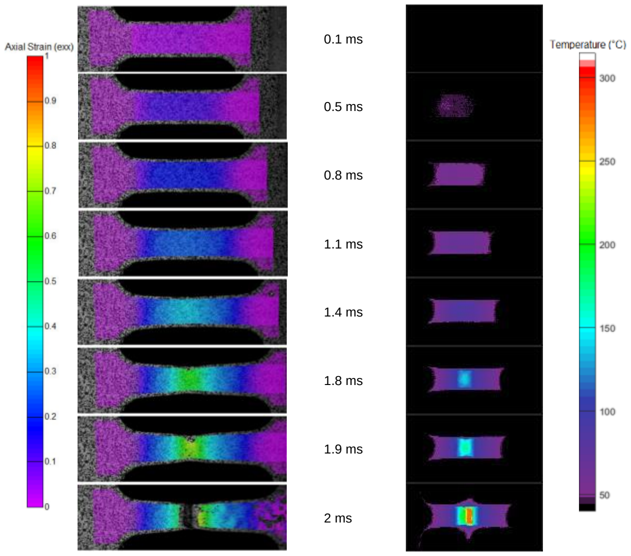

Fig. 5. Axial strain (DIC) and temperature measurements in a tension test at strain rate of 200 s^{-1}.

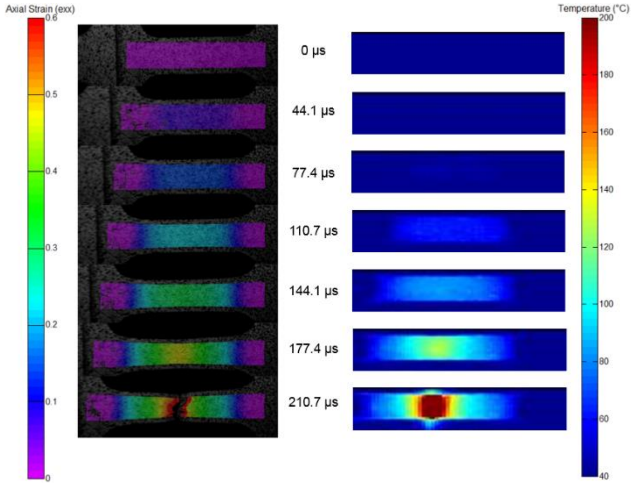

Fig. 6. Axial strain (DIC) and temperature measurements in a tension test at strain rate of 3000 s^{-1}.

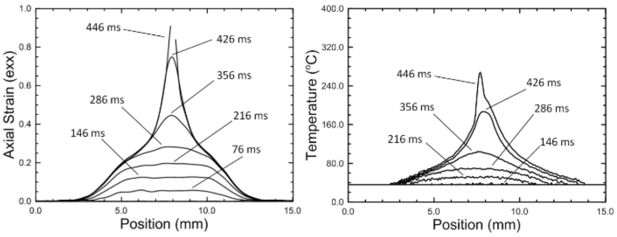

Fig. 7. Axial strain (DIC) and temperature measurements during a tension test at strain rate of 1 s^{-1}.

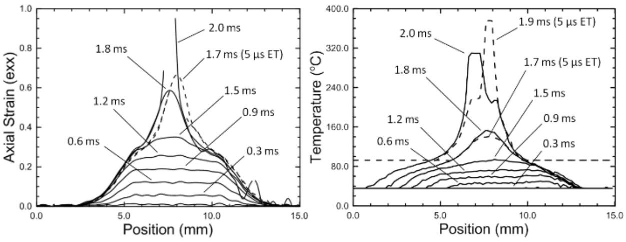

Fig. 8. Axial strain (DIC) and temperature measurements during a tension test at strain rate of 200 s^{-1}.

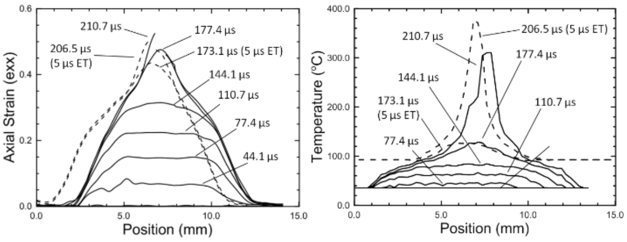

Fig. 9. Axial strain (DIC) and temperature measurements during a tension test at strain rate of 3,000 s^{-1}.

The Taylor-Quinney coefficient (β) is given by:

$$\beta = \frac{\rho c_p \Delta T}{\int_0^t W_p}$$

Where ρ is the density of the material, c_p is the specific heat of the material ΔT is the change in temperature, and $\int_0^t W_p$ is the plastic work. In the present paper the Taylor-Quinney coefficient is calculated at the point in the necking region where the maximum temperature is measured. The time history of the strain and temperature at that point for the tests at strain rates of 1.0 s^{-1}, 200 s^{-1} and 3,000 s^{-1} is shown in Figures 10-12, respectively. Each figure shows the engineering strain and the true strain. The engineering strain (change in length divided by undeformed length) is obtained from the DIC data by creating an virtual extensometer using two points outside the necking region such that the necking is between the points. The true strain at the point with the maximum temperature is obtained from the DIC software. In all three tests the engineering and true strains are nearly identical from the beginning of the test up to the time when the necking starts. The figures also show a moderate temperature increase during the uniform deformation that is followed by a significant increase due to the localization.

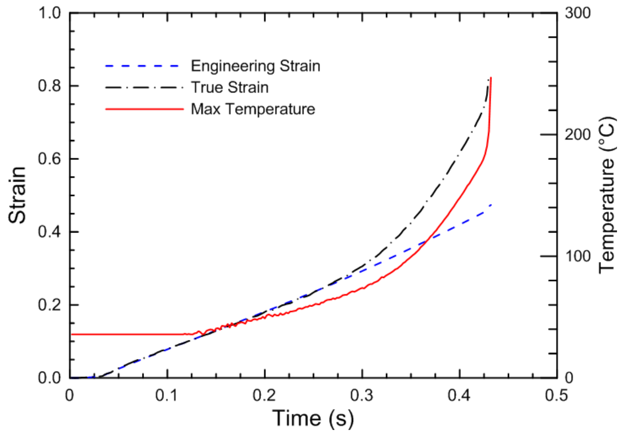

Fig. 10. History of strain and temperature at the point of maximum temperature in a tension test at strain rate of 1.0 s^{-1}.

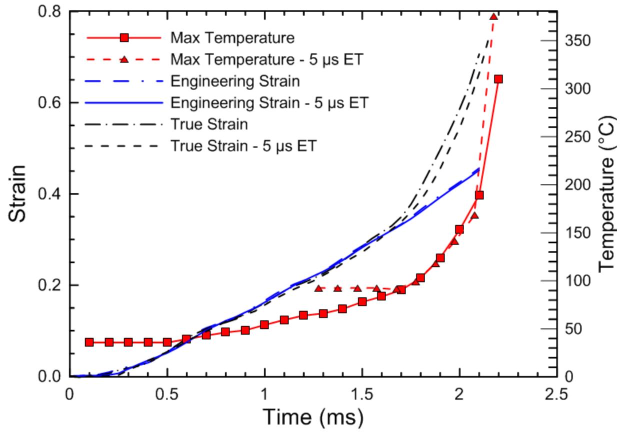

Fig. 11. History of strain and temperature at the point of maximum temperature in a tension test at strain rate of 200 s^{-1}.

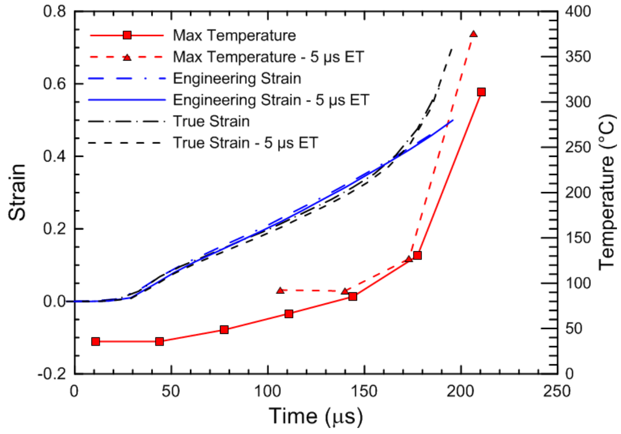

Fig. 12. History of strain and temperature at the point of maximum temperature in a tension test at strain rate of 3000 s^{-1}.

The calculated Taylor-Quinney coefficient (β) is displayed in Figure 13. The figure shows values that range between 0.75 and 0.82 at strains larger than 0.15. There is no significant difference between the tests at the different strain rates. It should be pointed out that at small strains (less than 0.15) the calculated values of β are less accurate due to a larger tolerance in the temperature measurement.

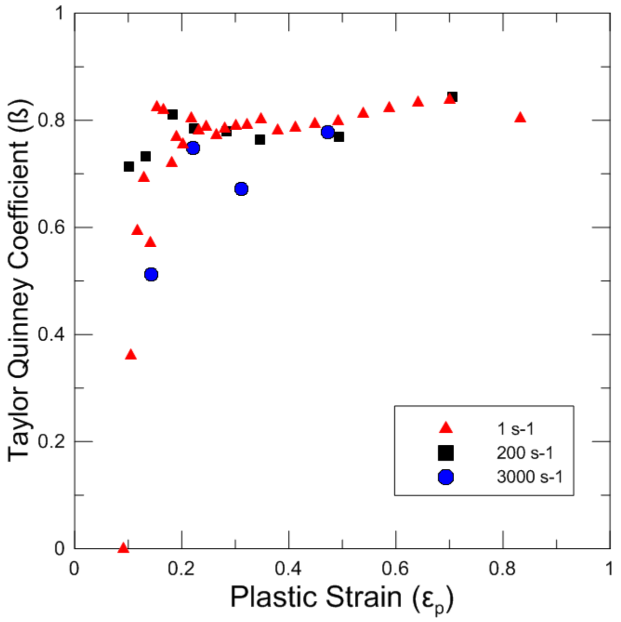

Fig. 13. Taylor-Quinney coefficient for 316L stainless steel.

2 Conclusions

The Taylor-Quinney coefficient can be determined in tensile tests from simultaneous measurements of strain and temperature in the necking region. Results from testing AISI 316L austenitic stainless steel at strain rates of 1.0 s^{-1}, 200 s^{-1} and 3,000 s^{-1} show an average value of 0.8.

The research was supported by the U.S.A. Federal Aviation Administration, Grant No. 11-G-004. One of the authors (VTK) wishes to thank the Finnish Cultural Foundation for partial funding of his sabbatical leave at OSU. The authors are grateful to Mr. William Emmerling, and Dr. Chip Queitzsch from the FAA for their support and involvement.

References

1. W.S. Farren, G.I. Taylor, Proc. R. Soc. **A107**, 422–451 (1925)
2. G.I. Taylor, H. Quinney, Proc. R. Soc. London **143**, 307–326 (1934)
3. J.J. Mason, A.J. Rosakis, and G. Ravichandran, Mech. Mater., **17**, pp. 135–145, (1994)
4. J. Hodowany, G. Ravichandran, a Rosakis, and P. Rosakis, Exp. Mech., **40**, no. 2, pp. 113–123, (2000)
5. R. Kapoor, S. Nemat-Nasser, Mechanics of Materials, **27**, pp. 1-12, (1998)
6. D.A.S, Macdougall, J. Harding, Int. J. Impact Eng. **21**, 473–488, (1998)
7. D. Rittel, L.H. Zhang, S. Osovski, J the Mech and Physics of Solids **107**, 96–114, (2017)
8. A. Gilat, J.D. Seidt, T.A. Matrka, K.A. Gardner, Experimental Mechanics, online, (2019)

Temperature Dependent Compressive Characteristics of Additively Manufactured Stainless-steel Auxetic Lattices at High Strain-rate

Petr Koudelka[1,*], *Tomas* Fila[1], *Jan* Falta[1], *Jan* Sleichrt[1], *Petr* Zlamal[1], *Anja* Mauko[2], *Marcel* Adorna[1], *Michaela* Neuhauserova[1], *Ondrej* Jirousek[1]

[1]Czech Technical University in Prague, Faculty of Transportation Sciences, Konviktska 20, 11000 Praha 1, Czech Republic
[2]Faculty of Mechanical Engineering , University of Maribor, Smetanova ul. 17, 2000 Maribor, Slovenia

Abstract. Specimens based on re-entrant honeycomb auxetic lattice were printed from powdered austenitic steel using selective laser sintering and subjected to dynamic compression using Split Hopkinson Pressure Bar (SHPB). To study the influence of strain-rate and temperature on mechanical properties of the lattices, heating and cooling devices integrated into the SHPB apparatus were developed and the experiments were performed at two different strain rates given by different striker impact velocities. As a result, the dynamic compression was performed at two strain rates and three temperature levels (reduced, room, and elevated temperature) with 5 specimens for each combination. The specimen were observed by a pair of high-speed CMOS optical cameras and a high-speed thermal imaging camera. Optical cameras were used for evaluation of strain fields of the compressed samples using digital image correlation and for inspection of experiment validity. Thermograms were used for qualitative evaluation of heat distribution within the sample microstructure during its deformation. It has been found out that increase of strain-rate results in increase of plateau stress together with decrease of densification strain. The difference in specimen temperature led to changes in the mechanical properties, the absolute temperature of the fully compressed sample and increase of maximum measured temperature during the experiment.

1 Introduction

Recent development in additive manufacturing methods, particularly the practical means for production of metallic constructs, has opened new possibilities in the field of materials for deformation energy mitigation by introduction of microstructures with functionally graded properties tailored for specific application. As an important advancement, the new manufacturing processes allowed to introduce a new type of cellular materials, where the internal structure is deliberately designed to exhibit negative Poisson’s ratio [1, 2]. Furthermore, the Poisson’s ratio can be advantageously engineered using the optimization techniques to be strain and/or strain-rate dependent, depending on the microarchitecture and the material used for its production[3 - 5]. The resulting so called auxetic meta-material exhibits beneficial energy absorption properties in case of dynamic impacts and penetration protection capabilities. In our recent experimental studies, mechanical properties of selected auxetic materials were evaluated at both quasi-static loading conditions and during dynamic impacts using Hopkinson bar [6, 7]. Strain-rate sensitivity of the additively manufactured auxetic structures together with strain dependence of the Poisson’s ratio were observed. For better understanding of deformation behavior of auxetics and for successful implementation of optimization procedures [8], strain-rate and temperature dependent effects have to be analyzed as one comprehensive physical system [9, 10]. In this paper, we investigated temperature dependence of material properties of a selected additively manufactured auxetic lattice having planar re-entrant honeycomb unit-cell geometry during dynamic compression in the Split Hopkinson Pressure Bar (SHPB) apparatus. The samples of the auxetic lattice were tested using the SHPB at different strain-rates and temperatures. High-speed optical and thermal imaging was used for the characterization of the material behavior during the impact.

2 Materials and methods

2.1. Specimens

The re-entrant honeycomb auxetic lattice with relatively thick struts (ratio of strut thickness to dimension of a unit-cell approximately 0.125) was selected for the study. The cubic-shaped specimens were additively manufactured from SS316L-0407 powdered austenitic steel using the selective laser sintering method (SLS). Dimensions of the specimens were 14.15 × 14.15 × 15.19 mm at the nominal strut thickness of 0.6 mm. Visualization and dimensions of the specimen are shown in Fig. 1.

The identical structure was used in our previously published study and its properties at room temperature are well known for both the quasi-static and dynamic loading conditions. Higher strut thickness was selected intentionally to increase heating dissipation effects to be reliably observable by the thermal imaging camera during the impact. The surface of the specimens was treated using a paint-brush to create a random speckle pattern for digital image correlation (DIC) on the side observed by the optical cameras. The opposite face of

---

[*] Corresponding author: koudelka@fd.cvut.cz

the samples, in every case the bottom face during the SLS printing procedure, with matt optical properties was left untreated to prevent reflections strongly affecting the infrared imaging.

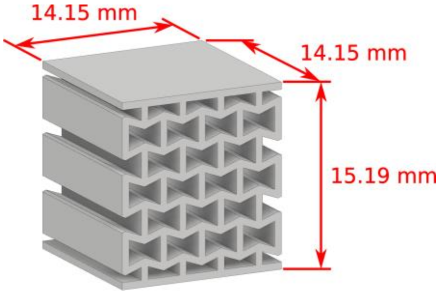

Fig. 1. Visualization and dimensions of the 2D re-entrant specimen printed using SLS.

2.2 SHPB setup

Conventional SHPB apparatus was used for the compression of the specimens at two different strain-rates. High-strength aluminum alloy bars (EN-AW-7075) with diameter of 20 mm were used in the experiments. Striker bars with length of 500 mm (for higher strain-rate) and 750 mm (for lower strain-rate) were accelerated using a gas-gun system. Striker impact velocities used in the experiments were 30 m/s and 45 m/s. The incident and the transmission bar had the same length of 1600 mm. Each bar was supported by four low friction polymer housings (drylin series, IGUS, Germany). The bars were instrumented using foil strain gauges 3/120 LY61 (HBM, Germany) with active length 3 mm wired in the Wheatstone half-bridge arrangement. Both bars were equipped with one measurement point located in the middle of the bar to prevent forward-going and backward-going wave superposition at the strain gauge location. Pulse-shaping technique using cylindrical soft copper shapers mounted on the incident bar impact face was employed to reduce wave dispersion effects and undesirable high-frequency oscillations in the bars. The specimen was in direct contact with both bars while contact faces were lubricated by a small amount of grease. The impact was observed by a pair of high-speed cameras Fastcam SA-Z (Photron, Japan). One camera was used to record the in-plane auxetic deformation of the specimen at a resolution of 256 x 168 px and approx. 252 kfps. Images of this camera were used for the DIC analysis to calculate the displacement and strain fields. Speckle pattern was applied on both ends of bars for DIC of their movement during the experiment. The second camera provided general overview of the experiment and served as a mean for inspection of the behavior of the experimental apparatus at the moment of impact. Its resolution was set to 512 x 424 px resulting in 80 kfps. Lighting of the scene was performed using a pair of high-performance LED light sources MULTILED QT (GS Vitec, Germany). Overview of the imaging part of the SHPB setup is shown in Fig. 2.

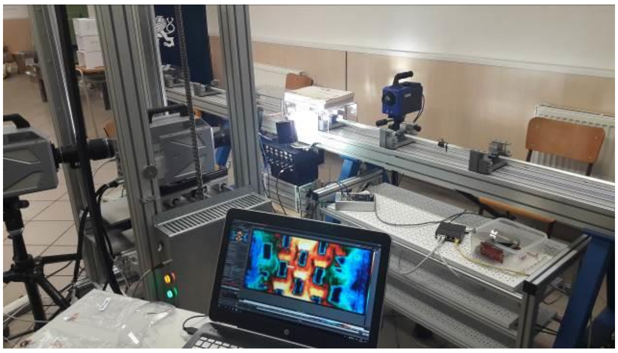

Fig. 2. SHPB setup showing both optical high-speed cameras, the thermal imaging camera, specimen chamber and a thermogram of a sample subjected to heating procedure.

2.3 Cooling and heating procedure

At both strain-rates, the specimens were tested at three temperature levels distinguished by different initial temperatures at the moment of start of the measurement. According to capabilities of the used heating/cooling setups, particularly the achievable speed of temperature changes, and thermal conductivity of the samples, the low temperature of -5 °C, the room temperature of 25 °C, and the elevated temperature of 120 °C were selected for the measurement. In total, five specimens were tested at a given strain-rate and temperature.

The heating setup consisted of a pair of two ceramic heating elements having rated power 40 W each that are commonly used for construction of HotEnds (printing heads of thermal-based 3D printers). The heating elements were placed into movable aluminum clamps to provide proper contact with the heated specimens. Movement of the clamps was provided by two independently regulated (RC) servo drives controlled by in-house developed electronics. Temperature was regulated by an open-loop control system using pulse-width modulation signal to achieve the desired temperature of the sample up to approx. 220 °C. The integrated heating device together with the thermal imaging camera is depicted in Fig. 3.

To warm up the specimen, the heating clamps were set in contact with the upper and bottom face of the specimen prior to the experiment. After the target temperature had been reached, the clamps were moved away from the specimen and the SHPB experiment was started.

The cooling setup was designed as a gas cooling system with CO_2 as an active medium. From a pressure vessel with volume of 6.7 l containing 5 kg of liquid CO_2, gas was released through a reduction valve at 15 bars and fed through a silicon low-temperature certified hose into the cooling stage. The cooling stage was composed of a thermally isolated box containing dry ice, i.e. carbon dioxide in solid state with temperature -78 °C, and another smaller vessel filled with a combination of dry ice and 1 l of pure ethanol. The silicon hose from the pressure vessel was led in the first instance through the dry ice and then through the cooled ethanol vessel. The lengths of the hose segments in the dry and ethanol part of the cooling stage were 2 m and 0.3 m respectively. The supercooled gas was then led directly to the specimen area, while the specimen was cooled from its top and bottom side by a pair of nozzles to reach the specimen temperature of -27 °C before start of the experimental procedure. The discrepancy between this temperature and nominal temperature -5 °C of the specimen at the start of the measurement was given by thermal conductivity of the samples leading to rapid raise of the temperature before SHPB experiment could have been started. The cooling setup in a position before the start of the experiment is shown in Fig. 4.

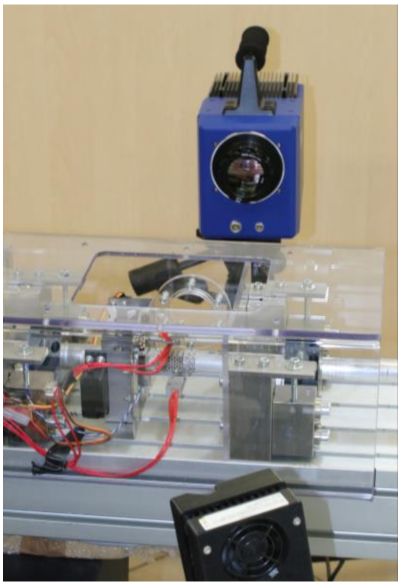

Fig. 3. Overview of the thermal setup showing the heating device, protection window and the high-speed thermal imaging camera.

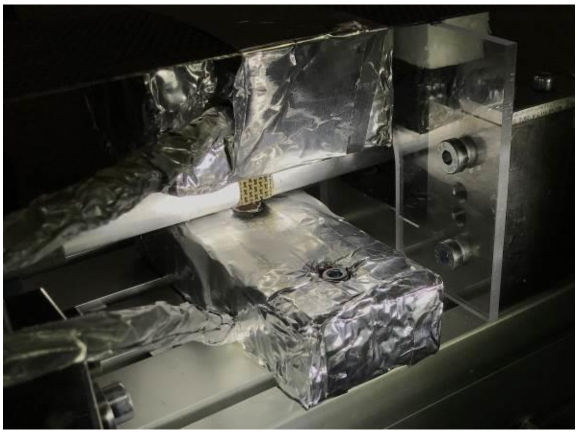

Fig. 4. Cooling setup with both cooling gas outlets in working position near the specimen.

2.4 Thermal imaging

Simultaneously with the optical-imaging, the impacts were observed by the thermal imaging camera to evaluate the thermal effects induced by the rapid compression of the samples. The SC 7600 high-speed thermal imaging camera (FLIR, USA) equipped with an actively cooled focal plane array (FPA) with full-frame resolution of 640 x 512 px and pixel pitch 15 µm was attached to 50 mm f/2 lens with anti-reflection coated silicon glass optics. The camera uses photon counting Indium Antimonide (InSb) detector operating in 1.5 – 5 µm spectral range (SWIR to MWIR band). The lens-camera assembly was calibrated for the temperature range from -20 °C to 300 °C, where the thermal response of samples to loading was anticipated. To achieve maximum possible frame-rate at a reasonable resolution, FPA windowing to 96 x 44 px was used to perform imaging at ~2 kfps for the room and elevated temperature experiments, while the cooled samples were observed at ~1.9 kfps given by the integration time necessary for imaging of samples at such low temperatures. During all the experiments, MgF_2 infrared-transparent protective window was used to guarantee safety of the thermal imaging optics. For verification of the cooling procedure and the sensitivity of the high-speed thermal-imaging camera, microbolometric LWIR thermal imager i7 (FLIR, USA) was used.

2.5 Digital image correlation procedure

Digital image correlation method was used for verification of strain-gauge signal and for general overview of specimen during the experiment as a mean for inspection of experiment validity. The two-stage DIC procedure with sub-pixel precision based on full affine transformation was then applied and strain fields were evaluated using a set of Matlab tools. The Fig. 5 depicts image of specimen captured using the high-speed camera with the generated pattern of correlation points.

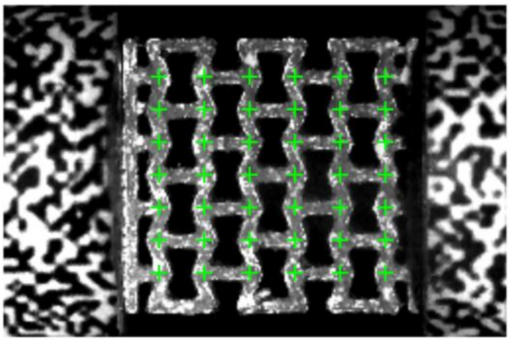

Fig. 5. Image from high-speed camera showing specimen located between the incident and the transmission bar with applied speckle patterns. The green markers represent correlation pattern used for DIC procedure.

3 Results

The re-entrant honeycomb construct exhibiting in-plane negative Poisson’s ratio were subjected to dynamic compression using SHPB apparatus at two strain-rates and at three temperature levels to reveal strain-rate and temperature dependent mechanical characteristics. DIC procedure was applied on series of images captured by the optical high-speed camera and showed good agreement with strain-gauge based evaluation.

According to the striker bar velocities used in the experiments, strain-rates of approx. 1200 s^{-1} and 2250 s^{-1} were used in the experiments. At first, the influence of strain-rate itself on the stress at the plateau region together with the densification strain was studied. It was assessed that the minor strain-rate effect is present at all the three temperature levels. Fig. 6 shows the results in terms of strain-rate and stress plotted against compressive strain for the samples at the reduced temperature.

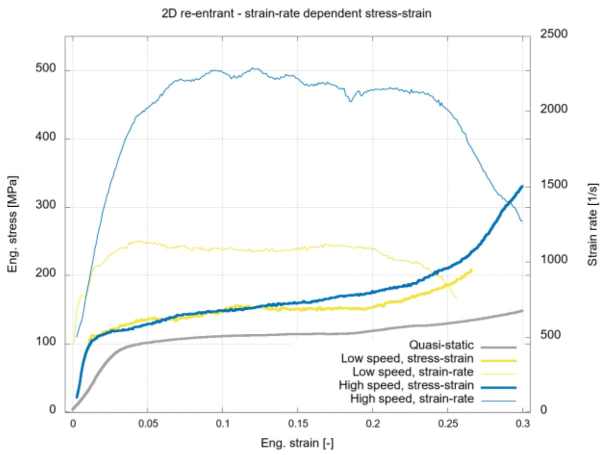

Fig. 6. Strain-rate and engineering stress plotted against engineering strain of the impacts at low temperature showing strain-rate dependence of the specimens.

It can be seen that with the increase of strain-rate the plateau stress increases and the densification strain decreases. The differences are the most apparent between the quasi-static compression (strain rate approx. 0.003 s^{-1}) and the low-strain rate dynamic experiments, where the plateau stress increased by 40 % and densification can be observed at as low as 0.25 strain.

Then, the temperature dependence of the structure was evaluated both on the basis of its mechanical response captured using the SHPB instrumentation and using analysis of the captured thermograms. Fig. 7 shows strain-rate and stress plotted against compressive strain for the samples measured using lower strain-rate at the different temperature levels together with the quasi-static results at the room temperature. Even though the comparison of the quasi-static and dynamic results comprises both the effect of temperature and strain-rate dependence of mechanical properties, it is apparent that the temperature dependence is present. Aside from the increase in plateau stress and decrease of densification strain between the quasi-static and dynamic response as a result of strain-rate effect, the temperature of the specimen at the beginning of the experiment influences all the plateau stress, densification strain, and the achieved strain rate. By comparing the dynamic results, it was observed that cooling of the sample causes increase of plateau stress, decrease of densification strain, and decrease of strain rate. Conversely, the exactly inverse effects can be observed for the elevated temperature levels.

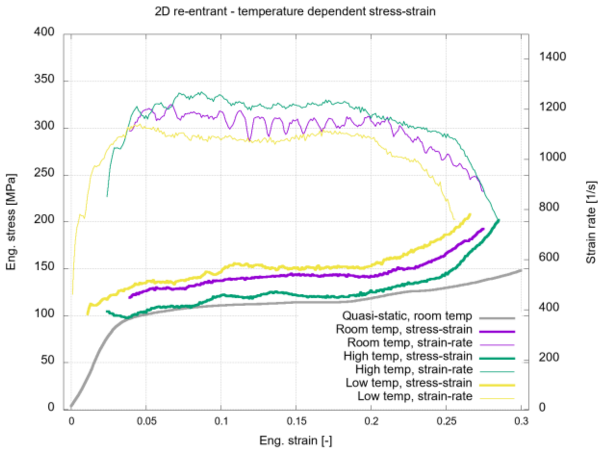

Fig. 7. Strain-rate and engineering stress plotted against engineering strain of the low energy experiments showing temperature dependence of the specimens.

Qualitative analysis of the deformation processes was performed by studying the distribution of heat in the acquired thermograms. The data show that the initial temperature of the sample not only trivially influences the highest observable temperature of the deforming microstructure, but more importantly affects the difference between the initial and the highest measured temperature during the given experiment. As such, highest temperature difference was calculated for the room temperature samples, while the lowest difference was assessed for the elevated-temperature samples loaded at a lower strain-rate. Furthermore, the thermograms can be used as mean for inspection of concentration of deformation within the specimen microstructure as can be seen in Fig. 8.

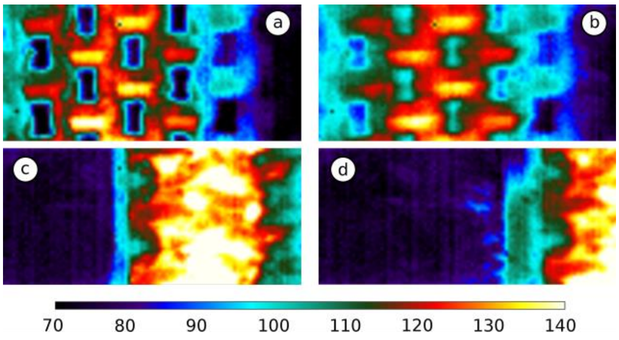

Fig. 8. Series of thermograms showing the heated specimen subjected to low strain-rate loading showing concentration of deformation to the first two layers of unit cells on the side of impacting incident bar. The scale bar indicates temperature in degrees centigrade. The thermograms were captured at 0 ms (a), 0.506 ms (b), 1.012 ms (c), and 1.518 ms (d) from start of the experiment.

Here, it is possible to reveal e.g. localized heating in the joints of struts and overall distribution of deformation over the microstructure including possible localization of deformation to certain layers of unit-cells.

To summarize the influence of temperature on the mechanical properties of the studied auxetic constructs, the stress in the plateau region was plotted against strain-rate (see Figure 9) depicting both the strain-rate and temperature dependency of mechanical properties of the constructs.

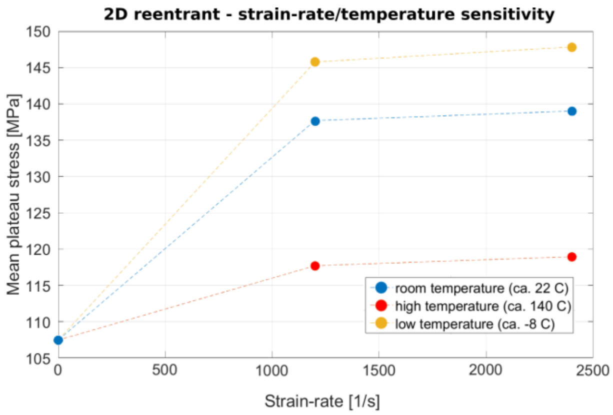

Fig. 9. Average plateau stress plotted against strain-rate showing its dependence on temperature.

Conclusion

SHPB strain gauge signals were used to evaluate the material behavior at the given strain-rate and temperature. Good quality dynamic equilibrium was achieved in all experiments. Images captured using the high-speed cameras were used for the visual evaluation of the experiment and were processed using DIC algorithm. To reach strain corresponding to the plateau region of the stress-strain curve, relatively high impact velocities and thus strain-rates had to be used. The influence of strain-rate and initial temperature of the specimens on the resulting mechanical properties, particularly the plateau stress and densification strain, was assessed. The thermograms were used to inspect heat distribution in the specimen microstructure related to localization of deformation during dynamic compression.

The research has been supported by Operational Programme Research, Development and Education in the project INAFYM (reg. no. CZ.02.1.01/0.0/0.0/16_019/0000766). The authors acknowledge the financial support from the Slovenian Research Agency (research core funding No. P2- 0063).

References

1. K. K. Saxena, R. Das, E. P. Calius, Adv. Eng. Mater., **18**, 1847–1870 (2016)
2. H. M. A. Kolken, A. A. Zadpoor, RSC Advances, **7**, 5111-5129 (2017)
3. Y. Jiang, Y. Li, Adv. Eng. Mater., **19**, 1600609 (2017)
4. Y. Jiang, Y. Li, Adv. Eng. Mater., **20**, 1700744 (2018)
5. T. Li, Y. Chen, X. Hu, Y. Li, L. Wang, Mater. Des. 2018, **142**, 247-285 (2018)
6. T. Fila, P. Zlamal, O. Jirousek, J. Falta, P. Koudelka, D. Kytyr, T. Doktor, J. Valach, Adv. Eng. Mater., **19**, 1700076 (2017)
7. T. Fila, P. Koudelka, P. Zlamal, J. Falta, M. Adorna, M. Neuhauserova, J. Luksch, O. Jirousek, Adv. Eng. Mater., available online, 1900204 (2019)
8. N. Novak, L. Starcevic, M. Vesenjak, Z. Ren, Compos. Struct., **40**, 210, 167-178 (2019)
9. A. Jung, A. D. Pullen, W. G. Proud, Compos Part A Appl Sci Manuf, **85**, 1-11 (2016)
10. A. Jung, S. Bronder, S. Diebels, M. Schmidt, S. Seelecke, Mater. Des., **160**, 363-370 (2018)

DYMAT2019 P14

Viscoplastic response of high manganese steels at a wide range of temperatures

Wojciech Moćko[1,*], *Magdalena* Jabłońska[2]

[1]Motor Transport Institute, Jagiellońska 80, 03-301 Warsaw, Poland
[2]Silesian University of Technology, Krasińskiego 8, 40-019 Katowice, Poland

Abstract. The paper presents a mechanical response of two grade of steels, containing a high manganese addition under a compressive loading condition at wide range of strain rates and temperatures. The high strain rate experiments were carried out at a range of temperatures from 23°C to 600°C. Rusinek-Klepaczko constitutive equation was calibrated on the basis of the acquired data. The thermally activated component of the overall stress determined at quasi-static loading conditions was suspended at room temperature. At dynamic loadings thermally activated component was observed below temperatures equal to 500°C and 600°C for X29MnAlSi26-3-3 and X55MnAl25-5 steels, respectively.

1 Introduction

Due to good ductility and high strength TWIP (twinning induced plasticity) steels exhibits an outstanding impact energy absorbing properties. Moreover, their excellent strength to weight ratio enable to design structures with high stiffness and reduced overall mass. As a consequence TWIP steels are used in automotive industry, especially in construction of vehicle bodies. Application of TWIP steels with other types of advanced high strength steels (AHSS), i.e. DP and TRIP enables to increase passengers safety during crash and at the same time reduce vehicle weight, therefore lower fuel consumption and CO2 emission.

The TWIP steel, typically is a face-cantered cubic (FCC) alloy with low stacking fault energy (SFE) ranging from 20 to 40 mJ/m^2. In conventional FCC metals, i.e. Al, Cu and Ni at low strain rate plastic deformation mechanism is based on dislocation movement. Increase of strain rate enhances dislocation evolution by promoting the dislocation generation and suppressing the dislocation annihilation [1]. As a result a strain rate sensitivity of work hardening is observed. The reason of such behaviour is the athermal generation of structural defects (dislocations), while at the same time collision and partial annihilation of dislocations occurs with the assistance of thermal activation [2]. Increase of strain rate activates twins generation as a second mechanism of plastic deformation. The deformation twins increase the work-hardening rate by acting as obstacles for gliding dislocations [3]. Despite the same crystalline structure of TWIP steels and FCC metals, strain rate effect on mechanical behaviour observed in steels is slightly different than mechanisms founded for FCC metals. The work hardening rate, controlled by evolution of dislocation and deformation twins in TWIP steels decreases at high strain rates [4]. This behaviour suggests that one or both deformation mechanisms are suppressed. Experimental investigation carried out with use of transmission electron microscopy on the pre-strained specimens proved that the density of twin boundaries decreases with strain rates increasing from 10^{-4}s^{-1} to 100s^{-1}. Reduction in the twining intensity may be related to dissipative heating which increases SFE and as a consequence diminishes generation of deformation twins [4]. Recently, similar analysis were conducted using X-ray diffraction experiments to determine influence of strain rate on dislocation density. It was found that in TWIP steels with FCC crystalline structure increase of strain rate induces lowering of the dislocation evolution which is in opposite to the FCC metals behaviour. This suppression of dislocation evolution has been attributed to the temperature increase due to dissipative heating at high strain rate deformation [5].

2 Experimental methodology

2.1 Tested steels

Analysis were carried out using two grades of the austenitic steel with high manganease content, i.e X29MnAlSi26-3-3 oraz X55MnAl25-5. Both steels were fabricated using casting in the copper die. Subsequently steels were forged at a temperature range from 1150°C ÷ 1000°C to obtain square forgings with a side equal to 45 mm. Further the materials were forged into 15 mm diameter rods at temperature 1150 ÷ 900°C . Finally, obtained rods were supersaturated thru 2 hours at temperature equal to 1150°C with water quenching. Both steels reveals single phase microstructure (Fig. 1). Cylindrical specimens for purposes of quasi-static and dynamic tests were cut-off from rods using electro-discharging machine. Diameter and length of specimens were equal to 5 mm and 3 mm respectively.

2.2 Quasi static and high strain rate testing

In order to obtain stress-strain curves of selected materials two various methods were applied. At low strain rate compression tests were conducted using a servo-hydraulic testing machine at room temperature. An electro-mechanical extensometer was applied for the axial strain measurements. The specimens had the following dimensions: diameter d_0=5 mm and length

---

[*] Corresponding author: wojciech.mocko@its.waw.pl

l_0=3 mm . The samples used in all of the tests performed were machined from round bars using the machining. Interfaces were lubricated using MoS2 in order to reduce friction effects between the anvil and the specimen under compression. Inertial, frictional and adiabatic heating effect usually observed in the dynamic compression tests were minimized using analytical solution introduced by Malinowski and Klepaczko [6, 7] Three specimens were tested at each given loading conditions. Average values of those measurements are presented in the paper.

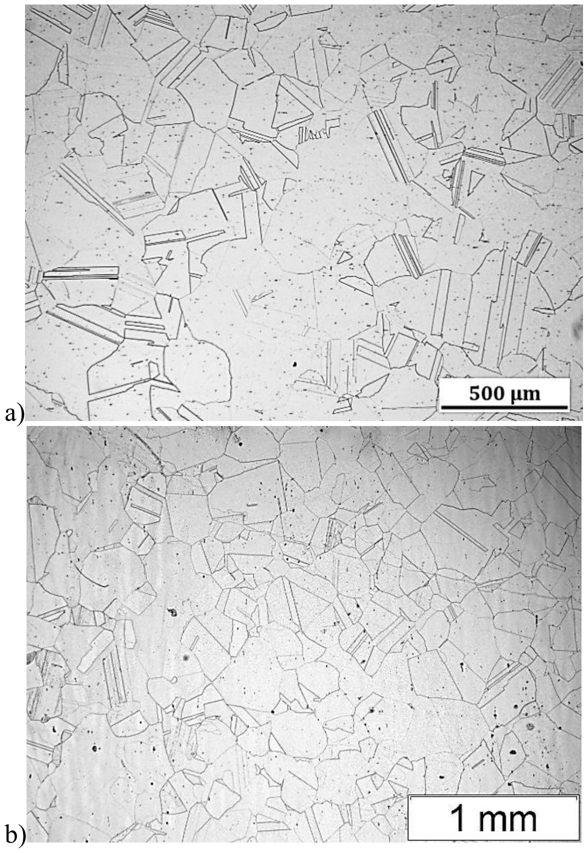

Fig. 1. Microstructure of a) X552MnAl25-5 and b) X29MnAlSi26-3-3 steel.

At high strain rates Split Hopkinson Pressure Bar methodology was applied [8]. The apparatus was equipped with temperature chamber to enable testing at elevated temperatures. The results obtained at high temperatures were corrected to avoid errors due to temperature gradients in elastic bars [9]. The test stand, presented in Fig. 2 and Fig. 3, was equipped with incident (8) and transmitter (9) bars 20 mm in diameter and 1000 mm in length, which were made of high strength maraging steel, σ_y = 2100 MPa [10]. The signals acquired from the strain gauges (7) were amplified by the wideband bridge circuit (3) and digitized by an oscilloscope (4). The initial velocity of the striker (5), which was accelerated in a pressure gas launcher (1) was measured by two sets of diodes and photo detectors coupled to a digital counter (2). Based on the waveforms recorded by a digital oscilloscope for transmitted $\varepsilon_T(t)$ and reflected $\varepsilon_R(t)$ waves and the known cross sectional area of the bars A and the specimen A_S, the speed of the elastic wave propagation in the material of the bars C_0 and the specimen length L, it is possible to determine stress σ(t), strain ε(t) and strain rate $\dot{\varepsilon}(t)$ in the specimen using the following formulas:

$$\sigma(t) = E\left(\frac{A}{A_S}\right)\varepsilon_T(t) \tag{1}$$

$$\varepsilon(t) = -\frac{2C_0}{L}\int \varepsilon_R(t)dt \tag{2}$$

$$\dot{\varepsilon}(t) = \frac{d\varepsilon(t)}{dt} = \frac{-2C_0}{L}\varepsilon_R(t) \tag{3}$$

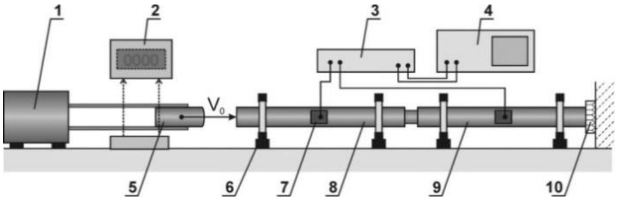

Fig. 2. Scheme of the test bench for tests by Hopkinson bar method, 1 - pneumatic gun, 2 - optoelectronic system for measuring striker velocity, 3 – broadband tensometer bridge, 4 - digital oscilloscope, 5 – striker, 6 - bar bearings, 7 - tensometers, 8 – incident bar, 9 – transmitter bar, 10 – wave damper.

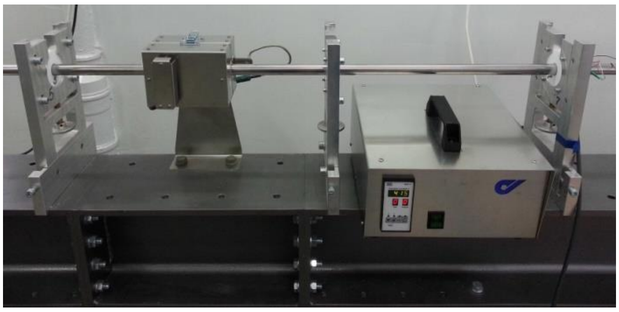

Fig.3. Temperature chamber mounted on the elastic bars.

2.3 Rusinek-Klepaczko constitutive equation

Viscoplastic mechanism of deformation was investigated using Rusinek-Klepaczko equation. The overall flow stress in the RK model [11] were decomposed into three stress components: the internal stress $\bar{\sigma}_\mu\left(\bar{\varepsilon}^p, \dot{\bar{\varepsilon}}^p, T\right)$, the effective stress $\bar{\sigma}^*\left(\dot{\bar{\varepsilon}}^p, T\right)$ and the drag stress $\bar{\sigma}_d\left(\dot{\bar{\varepsilon}}^p\right)$, as shown in Eq. 4.

$$\bar{\sigma}\left(\bar{\varepsilon}^p, \dot{\bar{\varepsilon}}^p, T\right) = \frac{E(T)}{E_0}\left[\bar{\sigma}_\mu\left(\bar{\varepsilon}^p, \dot{\bar{\varepsilon}}^p, T\right) + \bar{\sigma}^*\left(\dot{\bar{\varepsilon}}^p, T\right)\right] + \bar{\sigma}_d\left(\dot{\bar{\varepsilon}}^p\right) \tag{4}$$

3 Analysis of the influence of temperature on the plastic deformation mechanism

Stress-strain characteristic of X29 and X55 steels are shown in Fig. 4. Tests were carried out at wide range of strain rates from $10^{-4}s^{-1}$ to $3.7x10^3s^{-1}$ and from $10^{-4}s^{-1}$ to $3.7x10^3s^{-1}$, respectively, for X29 and X55 steel. Quasi-static offset yield strength determined at ε = 5% to is equal to 420 MPa for X29 steel. As a consequence of modification of the chemical composition of steel value of the offset yield strength rise to 436 MPa. Similar behaviour is observed at dynamic loading conditions. Offset yield strength of X29 steel determined at strain rate equal to at $1.5x10^3s^{-1}$ is equal to 693 MPa, whereas in the case of X55 steel its value increases up to 710 MPa. Both steel grades reveals similar positive strain rate sensitivity effect. However, some differences may be found analysing work hardening behaviour, i.e. X29 steel shows typical behaviour of TWIP steel, whereas X55 stress-strain curve is close to structural metallic alloys mechanical response.

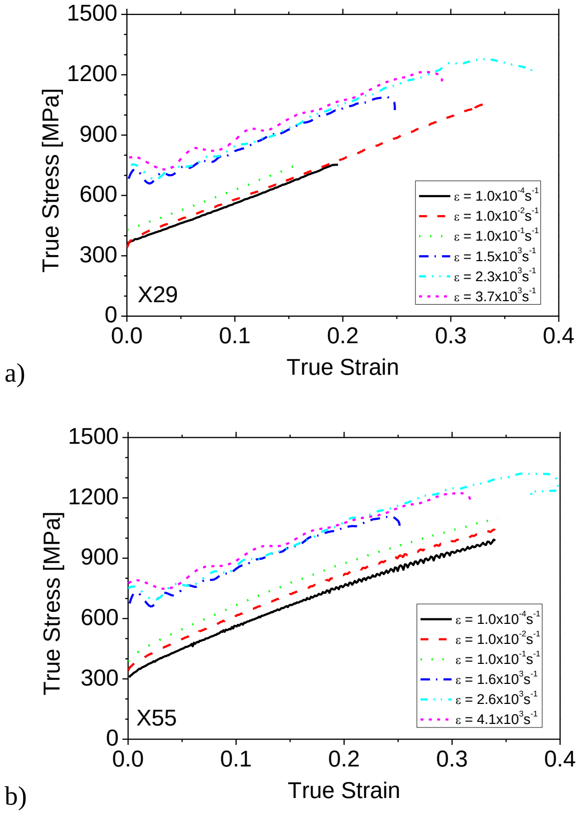

Fig.4. True stress-strain curves of a) X29 and b) X55 steels determined at various strain rates.

Influence of the temperature on the stress-strain behaviour of investigated steels determined at high strain rates is shown in Fig. 5. It may be observed that both grades of steel, i.e. X29 and X55 reveals similar thermal softening effect. Offset yield stress (ε = 10%) of X29 steel determined at 600oC drops to 500 MPa in comparison with value equal to 800 MPa estimated at RT. In the case of X55 steel offset yield strength is lowered from 786 MPa to 450 MPa, with increase of temperature from 23°C to 600°C, respectively. Moreover, temperature has no effect on the shape of compressive curve, i.e. plastic hardening modulus and exponent as well are comparable within applied range of temperatures. Due to low SFE plastic deformation of TWIP steels is govern by slip and twining interactions. Available analysis of SFE value determined using Alain's approach shows that increase of temperature from RT to 400oC induces growth of SFE from 21 mJ/m2 to 76 mJ/m2 in TWIP steel [12]. Since with the rise of temperature SFE value also increases therefore generation of twins is prohibited and stress component coming from twinning is suppressed [13]. It may be observed as thermal softening effect in Fig. 5.

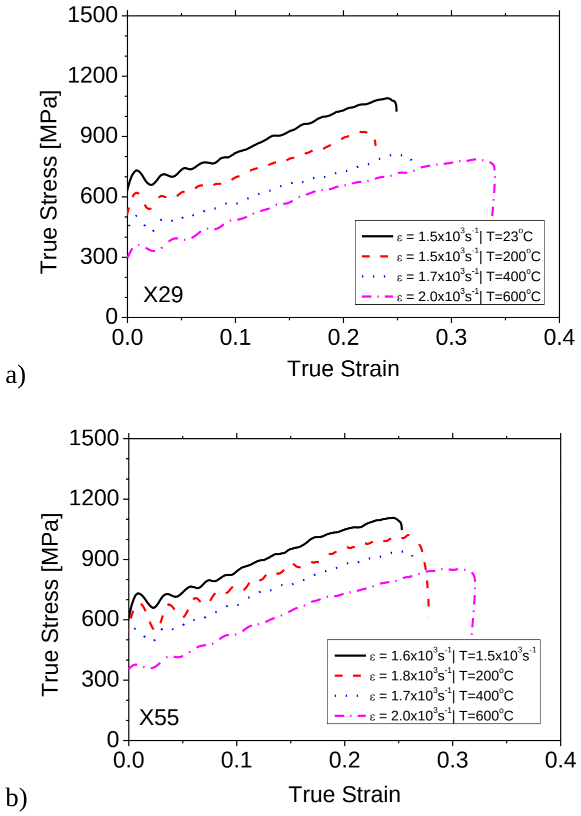

Fig.5. True stress-strain curves of a) X29 and b) X55 steels determined at various temperatures.

Comparison between experimental stress-strain curves and RK model based data estimated at wide range of strain rates is shown in Fig. 6. It may be seen that applied constitutive equation gives a good correlation between mechanical characteristics. Parameter n0 used in RK model to predict behaviour of X29 steel is equal to 1.0. In fact local minimum (stage B) and maximum (stage C) of work hardening values shown in Fig. 4 are very close, 1860 MPa and 2150 MPa, respectively. As a consequence application of constant rate of hardening in constitutive model gives a good fit to experimental data. X55 steel reveals typical work behaviour, i.e. the hardening rate decreases with strain, thus initial strain hardening exponent n0 was assumed to be 0.6.

Comparison of thermal softening effect influence of on flow stress of X29 and X55 steels is shown in Fig. 7. The rate of thermal softening is comparable for both tested steels. It may be found that inclination of the characteristic decreases at temperature around 500°C. Experimental data are reproduced by RK model with reasonable agreement.

Influence of temperature on the value of thermally activated effective stress component is illustrated in Fig. 8. It may be seen that according to RK model predictions at quasi-static deformation regime ($10^{-4}s^{-1}$) effective stress has a significant contribution to overall stress only for negative temperatures. At RT overall stress value is equal to 0 MPa. Moreover, drop of the overall stress with increase of temperature is governed by Young's modulus temperature dependence (Eqn. 4). At high strain rate loadings ($1.7x10^{-4}s^{-1}$) effective stress share in the overall stress is meaningful, i.e. it is equal to 300 MPa at RT. With the increase of temperature the effective stress value is reduced until 0 MPa at T=500°C.

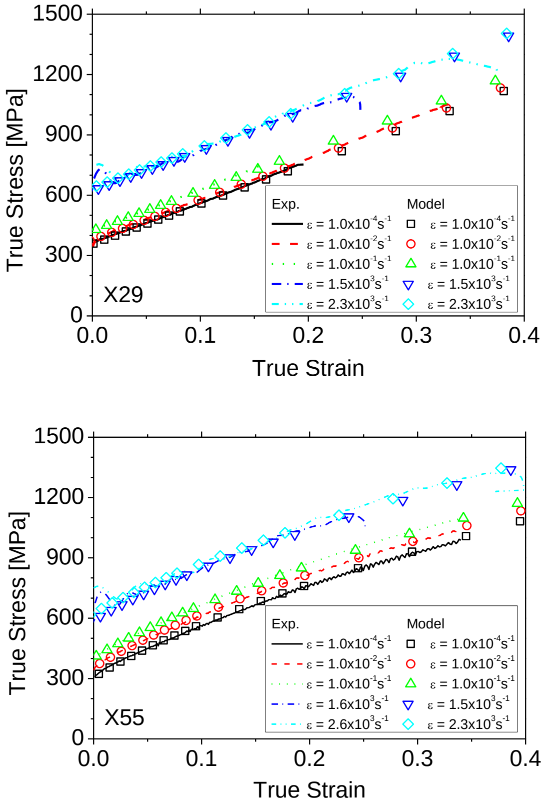

a)

b)

Fig.6. Comparison of true stress-strain curves of a) X29 and b) X55 steels determined experimentally and calculated using RK model at various strain rates.

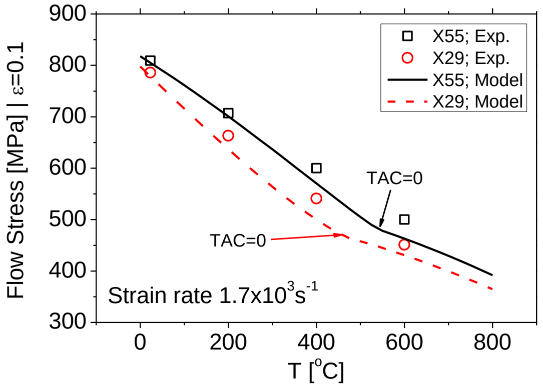

Fig.7. Temperature sensitivity of the flow stress of X29 and X55 steel determined experimentally and calculated on the basis of RK constitutive model; TAC – thermally activated component of the constitutive relation.

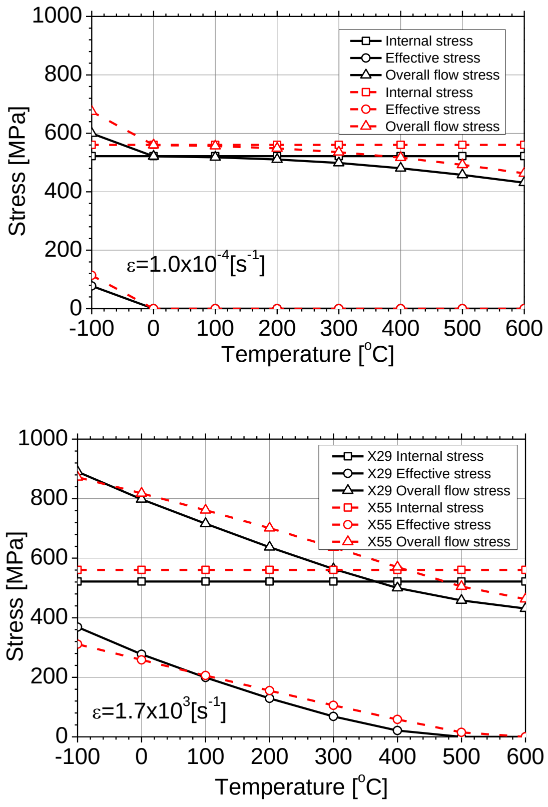

a)

b)

Fig.8. Influence of the temperature on the RK overall stress components of X29 and X55 steels at (a) quasi-static and (b) dynamic loading conditions.

Conclusions

The following conclusions were drawn on the basis of analysis of mechanical, microstructural and analytical properties of X29 and X55 steels:

- Plastic deformation mechanism of both analysed steels is based mainly on slip at quasi-static loading regime. Increase of a strain rate activates additional plastic deformation mechanism, i.e. twining. Moreover at dynamic loading conditions shear bands were identified. Despite the fact that microstructural analysis clearly shows increase of twins at high strain rate loadings, quasi-static and dynamic stress-strain curves are similar in terms of work hardening modulus and exponent. As a consequence rate and temperature dependent coefficients B and n in the case of analysed material were almost constant over investigated range of strain rates and temperatures.

- X29 steel shows typical behaviour of TWIP steel, whereas X555 stress-strain curve is close to structural metallic alloys mechanical response. The first one shows local minimum of work hardening rate at range of strain form 0.05 to 0.10, whereas for the latter one minimum (stages B and C) is absent in the chart representing work hardening. Strain rate hardening exponent n0 determined for X29 steel is equal to 1, therefore work hardening rate of TWIP type material is represented in the RK model by a constant value. This approach gives a good agreement with an experimental results, since difference between local minimum and maximum is very limited.

- At room temperature thermally activated effective stress is activated at strain rate equal to $10^{-2}s^{-1}$ in the case of X29 steel, whereas for the X55 it is observed at rates higher than $10^{-3}s^{-1}$. Moreover the intensity of the effective stress increase with deformation rate is higher for the X29 steel . Finally, strain rate sensitivity of X55 is almost linear in the investigated range of strain rates, whereas a curve representing X29 steel may be split into two regions of lower and higher sensitivity at quasi-static and dynamic loading conditions, respectively.

References

1. G.T. Gray, Annu. Rev. Mater. Res. 42, 285 (2012)
2. J.R. Klepaczko, C.Y. Chiem, J. Mech. Phys. Solids 34, 29 (1986)
3. O. Bouaziz O, N. Guelton, Mater. Sci. Eng. A 319–321, 246 (2001)
4. H.K. Yang, Z.J. Zhang, F.Y. Dong, Q.Q. Duan, Z.F. Zhang, Mater. Sci. Eng.: A607, 551 (2014)
5. Z.Y. Liang, W. Huang, M.X. Huang, Mater. Sci. Eng. A 628, 84 (2015)
6. J. Z. Malinowski, J. R. Klepaczko, Z. L. Kowalewski, Exp. Mech. 47, 451 (2007)
7. W. Moćko, Metrol. Meas. Syst 20, 555 (2013)
8. H. Kolsky, Proc. Phys. Soc. 62B, 647 (1949)
9. U. Lindholm, L. Yeakley, Exp. Mech. 8, 1 (1968)
10. W. Moćko, J.A. Rodriguez-Martinez, Z.L. Kowalewski, A. Rusinek, Strain 48, 498 (2012)
11. A. Rusinek, J.R. Klepaczko, Int. J. Plast. 17, 87 (2001).
12. S.H. Wang, Z.Y. Liu, W.N. Zhang, G.D. Wang, Acta Metall. Sin. 45, 573 (2009)
13. X.M. Qin, L.Q. Chen, H.S. Di, W. Deng, Acta Metall. Sin. 47, 1117 (2011)

Analysing and modelling the yield-strength anomaly at high strain-rates

Rafael Sancho[1,*], *Francisco* Gálvez[1]

[1]Department of Materials Science, Universidad Politécnica de Madrid, C/Profesor Aranguren 3, 28040, Madrid, Spain

Abstract. The present work aims to propose a constitutive equation to model the mechanical performance under high strain-rate and different temperatures of materials that present yield-strength anomaly (YSA). Experimental-data analysis, from nickel-based and cobalt-based superalloys, show that the shape of the anomalous temperature dependence of the yield strength fairly depends on the type of superalloy (material and composition). Moreover, high strain-rate tests at, 1000s^{-1}, confirm that the sudden temperature increment due to adiabatic heating does not lead to YSA because the mechanisms need some time to activate. The response model is formulated by considering the underlying micro-mechanisms responsible for the YSA along with some phenomenological equations, such as the Johnson-Cook model, to make it applicable to different alloys. Finally, experimental data from nickel-based and cobalt-based superalloys are fitted with the proposed model, demonstrating that is able to accurately capture the response of both alloys.

1 Introduction

The aerospace manufacturers are constantly in search of improving the performance of the aircrafts, either by aerodynamics enhancements [1] or by using new materials [2, 3] which allow companies to fabricate lighter components, more efficient engines [4], etc. Good mechanical properties at high temperatures (up to 800ºC), corrosion and wear resistance are examples of the working conditions that the materials used in some parts of the aircraft or power-generation engines, such us the turbine blades, must withstand, being Nickel-based high-performance alloys [5], also called Ni-based superalloys, and the promising Co-based superalloys [6], the ones that fulfil the aforementioned requirements.

The good performance of this alloys at high-temperatures is grounded in its microstructure (Figure 1), a face-centered-cubic (FCC) matrix (γ phase) and the L1$_2$ intermetallic precipitates (γ' phase), since the thermal softening of the matrix is offset by the thermal hardening of the precipitates, keeping almost constant the yield strength evolution of the alloy or even getting higher values at some range of temperatures.

The yield-strength anomaly (YSA) observed in the L1$_2$ compound have been widely studied [7, 8] and the well-accepted conclusion is that Kear-Wilsdorf (KW) locking is the responsible mechanism, in which screw dislocations get stuck when they move from the octahedral {111} to the cube {100} planes. As cross-slip is a thermally-activated process, the probability of pinning dislocations increases with the temperature and therefore, the yield-strength increases.

From the numerical point of view, some authors have studied the K-W lock mechanism and have stablished some constitutive equations, based on dislocation dynamics, to imitate the response of L1$_2$ intermetallic crystals [9, 10] and the behaviour of Ni-based superalloys by homogenizing the γ+γ' microstructure (hierarchical crystal plasticity models) [11].

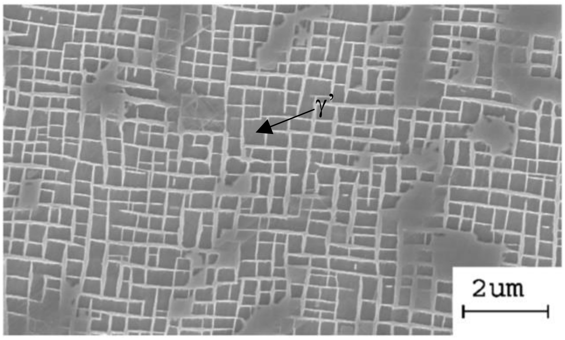

Figure 1. γ/γ' microstructure of a nickel-based superalloy with rectangular precipitates. Image obtained from [5].

Nevertheless, to simulate real components, saving time and money during the designing process, macro-material constitutive equations are needed. The Johnson-Cook model [12] is an example of one of these macro-constitutive equations that are widely used in the impact-dynamic field. The equation relates the evolutions of the yield strength with respect to the plastic strain ε_p, plastic strain-rate $\dot{\varepsilon}_p$ and temperature T. These types of models were formulated according to the standard mechanical behaviour of metals, i.e. thermal softening, so they cannot be used with YSA alloys unless defining different yield strengths for different temperatures or in other words, defining different materials for each temperature.

The scope of this work is twofold. First of all, using experimental data at high strain-rates and different temperatures from two different superalloys (Ni-based and Co-based superalloys), the shape change of the YSA is analysed depending on the type of material and the lack of applicability of some dislocations-dynamic-based equations is discussed too. Moreover, calculating the increment of temperature during the high-strain-rate tests, the effect of the adiabatic heating on triggering the K-W mechanism is examined. Finally, taking into account the information from the tests and K-W mechanism, authors

---

[*] Corresponding author: rafael.sancho@upm.es

propose a phenomenological constitutive equation that reproduce the effect of the strain rate $\dot{\varepsilon}_p$, testing temperature T and adiabatic heating ΔT on the mechanical response of YSA alloys.

2 Materials

Experimental data from the MAR-M247 nickel-based superalloy [13] and from a cobalt-based superalloy [14] was used to model different yield-strength dependences on temperature. Data from the split-Hopkinson-bar set-up was chosen to analyse the effect of the adiabatic heating on YSA.

2.1 MAR-M247 nickel-based superalloy.

MAR-M247 is a casting nickel-based superalloy that was developed in the early 1970's [15] but that it's still of great interest. The composition of the alloy in weight percentage can be seen in Table 1. For more information about the specimen's preparation and testing procedure, refer to [13].

Table 1. Chemical composition of MAR-M247 (wt. %)

Cr	**Co**	**Al**	**Ti**	**W**	**Ta**
8.00	10.0	5.50	1.00	10.0	3.00
Mo	**C**	**B**	**Zr**	**Hf**	**Ni**
0.60	0.15	0.01	0.03	1.5	Bal.

2.2 Cobalt-based superalloy.

Cobalt-based superalloys have better resistance against corrosion and oxidation at high temperatures than the nickel-based superalloys, so they are of great interest since 2006, when Sato et al. [16] discovered that it is possible to have a stable γ/γ' microstructure and therefore, YSA, in Co-Al-W alloys.

In this study, the nominal chemical composition of the chosen alloy is Co-12Al-10W-2Ti-2Ta (at.%). The alloy was processed by powder metallurgy and the mechanical properties were obtained by means of the split-Hopkinson bar. For more information about the alloy or the mechanical tests, see [14].

3 Constitutive equations and modelling

In the present section the authors explain the origin of the yield-strength anomaly (YSA) in detail, to continue with the equations needed to model the behaviour of $L1_2$ intermetallic compounds (γ' phase) and to finish with the explanation of the constitutive equation that is used to model the whole alloy (matrix + precipitates).

3.1 The yield-strength anomaly (YSA).

The origin of the positive temperature dependence of yield strength in the superalloys has to do with the presence of precipitates with a $L1_2$ lattice. This type of lattice, as can be seen in Figure 2, has FCC structure, so plastic deformation occurs in a similar way to the conventional FCC lattice but with certain dissimilarities.

In the $L1_2$ structure the slip vector ½<110> is not lattice translation, so a surface disorder is left behind when a dislocation glide. The energy associated to this disorder is called antiphase-boundary energy (APB energy). The order in the structure is restored again when another dislocation passes in the same direction of the same plane. As a consequence, a perfect dislocation in $L1_2$ lattice is composed by two partial ½<110> dislocations with an associated APB.

In the *traditional* FCC structures, dislocations only glide on the octahedral planes {111}, but in this case, they can glide on the cube {100} planes too. Since the APB energy associated to the {100} planes is lower than the one associated to {111}, it may occur that a screw dislocation ½<110> in {111} cross-slips to {100}. However, the Peierls stress on cube planes is higher than on octahedral planes. Thus the perfect dislocation get stuck and a higher external stress must be applied to keep the plastic flow (Kear-Wilsdorf mechanism) [7, 8].

Finally, the effect of the temperature on the mechanism has to do with the increment of thermal energy available for cross-slip. Increasing the temperature, increases the probability of K-W mechanism.

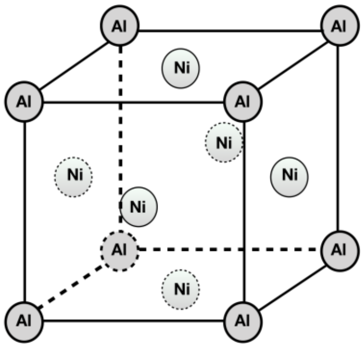

Figure 2. Schematic representation of the $L1_2$ unit cell for the case of the intermetallic compound Ni_3Al, which is responsible for the YSA in nickel-based superalloys. The unit cell of $Co_3(Al, W)$ is the same but changing nickel by cobalt and aluminium by aluminium or tungsten.

3.2 Constitutive equations.

3.2.1 The γ' precipitate

Many authors have studied and proposed models to reproduce the behaviour of Ni_3Al single crystals [9-11]. Mainly, all authors expound that the strength of γ' (τ_p) is due to the contribution of the resistance of the octahedral planes {111} to the movement of dislocations $(\tau_{\{111\}})$, the increment of flow stress due to cross-slip pinning mechanism (τ_{cs}) and the slip resistance of cube planes $\{100\}(\tau_{\{100\}})$.

Figure 3 shows an example of the experimental yield strength of a Ni_3Al single-crystal (γ' precipitate), highlighting three main regions. At low temperatures (region I), the mechanical response of the compound has its main source in the octahedral slip $\tau_{\{111\}}$ because there is not enough thermal energy to activate the cross-slip mechanism significantly. While increasing the temperature (region II), the cross-slip event become more important progressively and the K-W locking lead to an increase of the flow stress ($\tau_{\{111\}} + \tau_{cs}$). The end of the region II is well-defined and occurs at the temperature T_p. At this point the L-W locking is maximum and consequently, a flow-stress peak appears. In the end, going above T_p (region III) means activating dislocations slip in {100} planes and a sudden decrease of the mechanical performance.

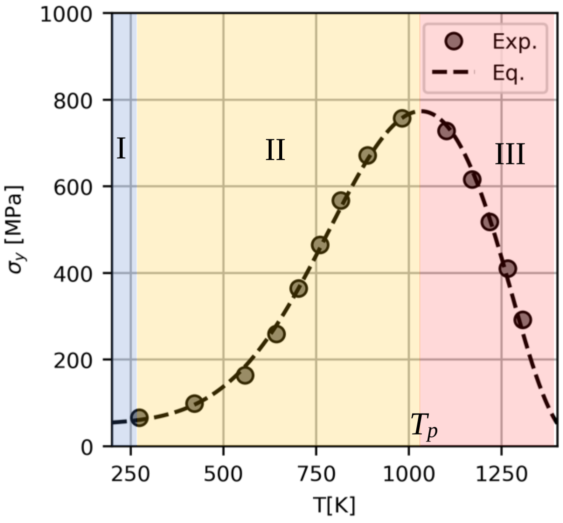

Figure 3. Variation of the Ni_3Al yield-strength with temperature. Experimental dots (data from [10]) and the fitting curve by using the equation (3).

The shape of the yield-strength evolution with the temperature have been described by some authors [9-11] with the combination of an Arrhenius-type function (thermal activation of cross-slip mechanism) and a natural-exponential function (thermal softening).

On the other hand, other authors [17, 18] says that the probability of the L-W lock mechanism follows a normal distribution and therefore, it can be used to model the response of γ'.

In the present work, authors have checked that the normal-distribution solution is more suitable for fitting macroscopic experimental data.

Hence, the critical stress due to cross-slip-pinning mechanism (τ_{cs}) can be written as:

$$\tau_{cs}=\tau_{cs0}\exp\left(-\frac{(T-T_p)^2}{w^2}\right) \qquad (1)$$

where τ_{cs0} is the maximum stress increment due to K-W mechanism (define the height of the distribution), w is a constant with units of temperature that is responsible for the width of the temperature range of K-W lock and T_p is the temperature at which the flow-stress peak appears (see Figure 3).

Besides the cross-slip contribution, the γ' response is also a function of $\tau_{\{111\}}$, so the yield strength of region I and II can be modelled as:

$$\tau_{\{111\}}+\tau_{cs0}\exp\left(-\frac{(T-T_p)^2}{w^2}\right) \qquad (2)$$

while the region III (loose of mechanical performance due to {100}-slip activation) may be defined with a phenomenological law. We have decided to use a Johnson-Cook type [12] thermal softening in pursuit of being able to adjust several types of distributions. So, the final equation for τ_p reads:

$$\left(\tau_{\{111\}}+\tau_{cs0}\exp\left(-\frac{(T-T_p)^2}{w^2}\right)\right)\left(1-\left(\frac{T-T_r}{T_m-T_r}\right)^m\right) \qquad (3)$$

where T_r and m are constants to be adjusted and T_m is the temperature at which the material does not offer resistance to plastic deformation.

Finally, the quality of the equation (3) was tested by fitting some experimental data (see Figure 3). To obtain the values different parameters (Table 2) the next procedure was followed:

- The parameters that are easy to identify, such as $\tau_{\{111\}}$ and T_p, were set directly.
- To reduce the number of constants to be fitted, T_r was set to zero. In this case, the shape of the region III can be controlled with just T_m and m.
- The rest of constants were obtained by means of a least-square-fitting route.

Table 2. Parameters of equation (**3**) to fit experimental Ni_3Al data.

$\tau_{\{111\}}$	τ_{cs0}	**w**	**T_p**	**T_m**	**m**
50MPa	752MPa	391.2K	1067K	1500K	15

3.2.2 The YSA alloy

The mechanical behaviour of the superalloys is based on the contribution of the matrix (γ) and the precipitates (γ'). The matrix behaves similar to other metallic alloys so, applying the Orowan relation, we can write the plastic strain-rate as:

$$\dot{\varepsilon}_p=\rho_m b\bar{v} \qquad (4)$$

where ρ_m is the density of mobile dislocations, b is the magnitude of the Burger's vector and $\bar{v}$ is the mean velocity of dislocations.

Applying the dislocation-thermal-activation theory [19], the mean velocity of dislocations can be expressed as an Arrhenius-type equation:

$$\bar{v}=\bar{v}_o\exp\left(\frac{-\Delta G}{k_B T}\right) \qquad (5)$$

where ΔG is the energy associated to the obstacles that can be overcome by using only thermal energy, $\bar{v}_o$ is a fitting constant, k_B is the Botzmann constant and T is the temperature. If an external stress τ_{ext} is applied to the material, ΔG decreases its value as:

$$\Delta G = \Delta G_o \left(1 - \left(\frac{\tau_{ext} - \tau_a}{\tau_t}\right)^p\right)^q \tag{6}$$

where τ_a is the non-thermal component of the resistance of the material(the minimum amount of external work that must be applied to start dislocation gliding) and τ_t the thermal one. The values $0<p<1$ and $1<q<2$ defines the shape of the energetic barrier.

Combining equations (**4**), (**5**) and (**6**), the thermo-viscoplastic law of the matrix reads:

$$\tau_m = \tau_a + \tau_t \left(1 - \left(\frac{k_B T}{\Delta G_o} ln\left(\frac{\dot{\varepsilon}_o}{\dot{\varepsilon}_p}\right)\right)^{1/q}\right)^{1/p} \tag{7}$$

being $\dot{\varepsilon}_o$ a reference strain-rate that does not have an important influence on the output values of the equation and therefore, it can be set equal to $1\text{x}10^8$ s^{-1} for metallic alloys [20]. Moreover, depending on the type of alloy that we want to model, τ_a may be a constant value or a function that depends on the temperature.

Finally, the superposition law adopted in [18] can be used to determine the response of the whole alloy from γ+γ'.

$$\tau^n = {\tau_m}^n + {\tau_p}^n \tag{8}$$

where $1<n<2$.

Typically, we only have the experimental data of the YSA alloys that we want to simulate and not any information about the behaviour of the matrix and or the precipitates. In this situation, fitting all the constants, at least 12, become a difficult task because of two main reasons: more than 12 experimental points are needed and there would strong interactions among some parameters like $\tau_{\{111\}}$ and τ_a that preclude the fitting procedure.

Therefore, from the point of view of the authors, equation (3) can be simplified as:

$$\tau_p = \tau_{cs0}\exp\left(-\frac{(\text{T-T}_\text{p})^2}{\text{w}^2}\right) \tag{9}$$

just to model the region where the peak flow stress appears, while the general shape of the flow-stress evolution is defined by τ_m. As it will be shown in the next section, the high temperatures that are achieved with the superalloys lead to an important drop of their mechanical response, so it is necessary to define a temperature-dependent τ_a, i.e. a Johnson-Cook-type thermal softening. Moreover, if all the experimental data are from tests at the same strain-rate, the right-hand side of equation (**7**) must be disregarded and the simplified equation reads:

$$\tau^n = \left[\tau_a\left(1\text{-}\left(\frac{\text{T}}{\text{T}_\text{m}}\right)^\text{m}\right)\right]^n + \left[\tau_{cs0}\exp\left(-\frac{(\text{T-T}_\text{p})^2}{\text{w}^2}\right)\right]^n \tag{10}$$

3.2.3 Sensitivity analysis of the model

In this sub-section, a variance-based sensitivity analysis, also known as Sobol's sensitivity analysis [21], is presented to examine the influence of each parameter on the output of equation (10). The study was done with the SALib module for Python language [22].

The parameter T_p was disregarded from the analysis because it can be well determined with the flow-stress peak. The rest of the parameters were analysed in a range of feasible values taking into account the experimental data that is presented in the next section. The range of the temperature parameter was changed twice to cover the whole temperature range from room to high temperature and just to study what happens in the flow-stress-peak region.

From the results of the sensitivity analysis (Figure 4) we can infer that *m* is of great importance to control the "shape" of equation (10) as a function of *T*. The next two parameters that have a higher index are again related to the matrix response. Somehow this result was expected since the precipitates contribution was simplified and only is important to define YSA in a short range of temperatures. Therefore, from the global response of the model the influence of such parameters are low but locally, they are going to be important to reproduce the increment of flow stress.

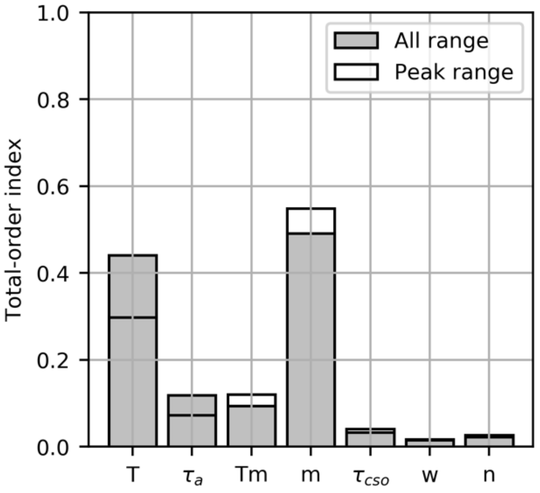

Figure 4. Sobol's sensitivity analysis of the model parameters (equation (**10**)). The total-order index is expressed as a decimal.

4 Experimental data and discussion

To check the flexibility of the constitutive equation (equation (10)), two different YSA behaviours, based on experimental data from a cobalt-based [14] and a nickel-based superalloy [13], were used.

All experimental data were fitted by means of least-square methods.

4.1. The cobalt-based superalloy

Figure 5 depicts that the model is able to reproduce, with the constants gathered in where χ is the Taylor-Quiney coefficient, C_p is the specific heat of the alloy and ρ the mass density. The values 0.9, 420J/kg/K and 9110kg/m^3 were used for the alloy., the yield-strength dependence on temperature during the three main stages. In the first stage, in which the material decrease its 0.2% flow-stress from room temperature until 1000K, the model takes advantage of the first part of equation (10). Then, the K-W lock mechanism activates, between 970K and 1070K, leading to the flow-stress peak. This zone is narrow and therefore the *w* needs to have a low value. Finally, above the peak-stress temperature T_p, the response of the material drops, and the thermal-softening part of the equation is the responsible for model the trend.

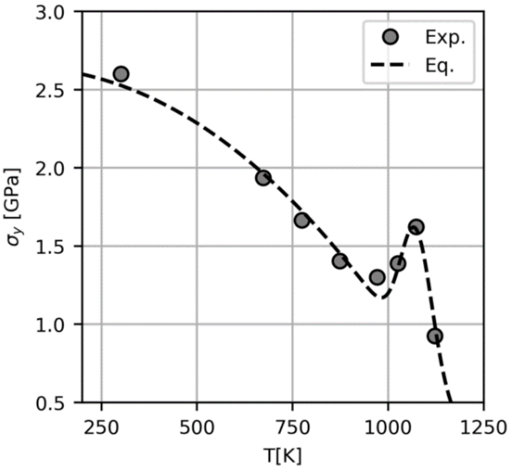

Figure 5. Yield-strength evolution of the Co-based superalloy with temperature. Experimental data (dots) and numerical model (dashed line)

As the authors of the present article mentioned in section 3.1.1, it is known that the cross-slip mechanism (basis of the YSA) is a thermally-activated process. This means that dislocations need enough temperature and time to cross-slip and therefore, it may be assumed that the adiabatic heating does not activate the L-W mechanism.

This assumption is sustained by Figure 6, where we can see that the sample tested at 973K does not increase its flow stress in spite of "entering" in the temperature range of YSA due to the adiabatic heating. Moreover, analysing the test at 1073K we can also check that the sudden softening also needs some time to play its role. From the point of view of the authors, these ideas must be clear in mind when programming user-material subroutines in finite element codes to avoid non-real material responses under impact events.

The temperature evolution of the samples where determined with the equation:

$$T = T_0 + \frac{\chi}{C_p \rho} \int_0^{\varepsilon p} \sigma d\varepsilon_p \qquad \textbf{(11)}$$

where χ is the Taylor-Quiney coefficient, C_p is the specific heat of the alloy and ρ the mass density. The values 0.9, 420J/kg/K and 9110kg/m^3 were used for the alloy.

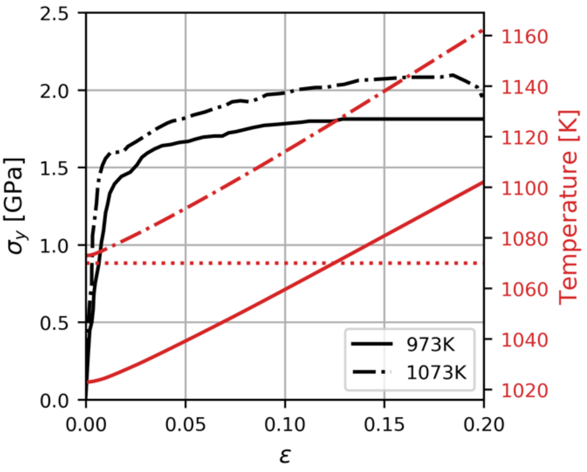

Figure 6. Stress-strain curves of the Co alloy at 973K and 1073K and at 1000s^{-1}. The temperature evolution of the sample is also presented. The dotted horizontal line corresponds to T_P.

Table 3. Parameters to fit Co-based experimental data.

τ_a	T_m	m	τ_{cso}
2.65GPa	1267K	2.13	0.92GPa

T_p	w	n
1073K	58.3K	1.1

4.1. The MAR-M247 alloy

Figure 7 shows the experimental data and the numerical fit for the nickel-based superalloy. The dots corresponds to tests performed with the Hopkinson-bar set-up (Exp.D) and to quasi-static tensile test (Exp.QS).

Firstly, it is important to note that the behaviour of the alloy is totally different from the one studied previously. In this case, there is no a clear YSA zone with a peak but just a slightly increase around 500K at high-strain rates. Due to this reason, authors decided to do two adjustments of the experimental data.

On the one hand, only data from the dynamic tests were considered and the equation (10) was used. The agreement between the experimental data and the model is good and hence, reinforced the idea that the propose model can be applied for different types of superalloys.

On the other hand, equation (10) was coupled with equation (7) with the aim of modelling the YSA and the effect of the strain-rate together. As can be seen (dotted lines) the strain-rate and temperature effect on the yield strength is reasonably well-captured. The different trend of the quasi-static data with respect to the dynamic data in the temperature range between 295K and 750K makes it impossible to get a better result, because we have to decide between a flat evolution (quasi-static) or a small peak of flow stress (high strain-rates). The authors chose to extrapolate the behaviour at high strain-rates to have a more complex temperature dependence and check the capabilities of equation (10).

Finally,

Table **4** and Table 5 collect the values of the constants that were used in the model.

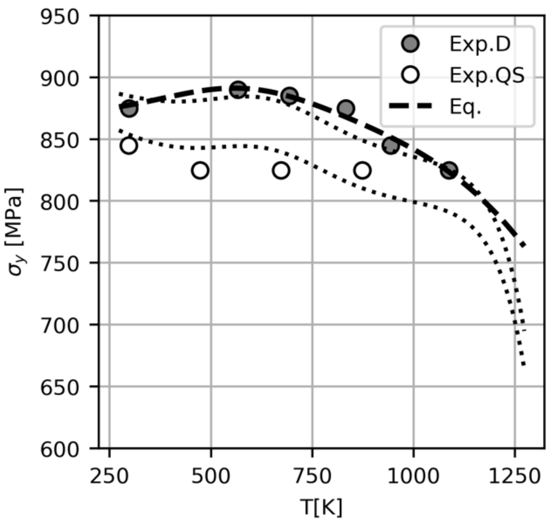

Figure 7. Yield-strength evolution of MAR-M247 alloy with temperature at two different strain-rates (D=1000s-1 and QS=1.4x10-4 s-1). The dashed line corresponds to only fitting dynamic data, while the dotted line is the result of fitting both data.

Table 4. Parameters to fit MAR-M247 experimental data under high strain-rates.

τ_a	T_m	m	τ_{cso}
870MPa	1964K	3.98	33.6MPa

T_p	w	n
573K	279K	1.1

Table 5. Parameters to fit MAR-M247 experimental data under high and low strain-rates.

τ_a	T_m	m	τ_t
788MPa	1130K	14.78	124.4MPa
ΔG_o	q	p	τ_{cso}
4.6x10^{-17} J	1	0.01	39.2MPa

T_p	w	n
573K	206K	1.1

Conclusions

In the present work, the authors analyse the YSA behaviour of superalloys and propose a constitutive equation to model it for impact applications. The model is used to fit the response of a cobalt-based and a nickel-based superalloy, getting a good agreement although the yield-strength temperature dependence is different. Finally, it is verified that the effect of adiabatic heating on the mechanism that preclude the YSA effect is null.

References

1. A. Abbas, J. De Vicente, and E. Valero. Aerosp Sci Technol. **28**, 100-132 (2013).
2. P. Immarigeon, et al. Mater Charact. **35**, 41-67 (1995).
3. R. J. Bucci, C. J. Warren, and E. A. Starke. J Aircraft. **37**, 122-129 (2000)
4. D. G. Backman, J. C. Williams. Science. **255**, 1082-1087 (1992)
5. T. M. Pollock, S. Tin. J Propul Power. **22**, 361-374 (2006).
6. A. Suzuki, G. C. DeNolf, T. M. Pollock, T. M. Scr Mater. **56**, 385–388 (2007).
7. P.H. Thornton, R.G. Davies, Metall. Trans. **1A** 549 (1970).
8. S. Takeuchi, E. Kuramoto, Acta Metall. **21**, 415 (1973)
9. A. M. Cuitiño, M. Ortiz. Mater Sci Tech-Lond. **A170**, 111-123 (1993).
10. S. Keshavarz, S. Ghosh. Philos. Mag. **95:24**, 2639-2660 (2015)
11. R.G Weber, S. Ghosh. Mater High Temp. **33**, 401-411 (2016)
12. G.R Johnson. Proc. 7th Inf. Sympo. Ballistics. 541-547(1983)
13. B. Erice. *Flow and fracture behaviour of high performance alloys.* (2012)
14. R. Casas. *Design of high temperature cobalt-based alloys processed by powder metallurgy route* (2019)
15. K. Harris, G. L. Erickson, and R. E. Schwer. *MAR M 247 derivations—CM 247 LC DS alloy, CMSX® single crystal alloys, properties and performance*. 5th Int. Symp. (1984).
16. J. Sato, T. Omori, K. Oikawa, I. Ohnuma, R. Kainuma, K. Ishida. Science. **312** (2006)
17. K. Aoki, O. Izumi. J. Mater. Sci. **14**, 1800–1806. (1979)
18. J. Wang, et *al*. Mech Mater. **94**, 79-90 (2016)
19. D Caillard, JL Martin. *Thermally activated mechanisms in crystal plasticity.* **8** Elsevier (2003).
20. D. Rodríguez-Galán, I. Sabirov, and J. Segurado. Int J Plasticity. **70,** 191-205 (2015)
21. M. Sobol. Math Comput Simulat. **55,** 271-280 (2001)
22. J. Herman, W. Usher. JOSS. **2(9),** 97 (2017)

DYMAT2019 P16

Dynamic Temperature-Dependent Tensile Behavior of Soft Ferromagnetic Alloy Fe-Co-2V

Brett Sanborn*[1], *Bo* Song[1], *Don* Susan[1], *Kyle* Johnson[1], *Jeff* Dabling[1], *Jay* Carroll[1], *Adam* Brink[1], *Scott* Grutzik[1], *Andrew* Kustas[1]

[1]Sandia National Laboratories, 1515 Eubank SE, Albuquerque, NM 87108 USA

Abstract. Fe-Co-2V is a soft ferromagnetic alloy used in electromagnetic applications due to excellent magnetic properties. However, the discontinuous yielding (Lüders bands), grain-size-dependent properties (Hall-Petch behavior), and the degree of order/disorder in the Fe-Co-2V alloy makes it difficult to predict the mechanical performance, particularly in abnormal environments such as elevated strain rates, high/low temperatures, and combinations of these. Thus, experimental characterization of the high-strain-rate stress-strain properties of the Fe-Co-2V alloy at high/low temperatures is desired, which are used for material model development in numerical simulations. In this study, the high-rate tensile response of Fe-Co-2V is investigated with a pulse-shaped Kolsky tension bar from cold to hot temperatures. Effect of temperature on yield stress, ultimate tensile stress, and elongation to failure are discussed.

1 Introduction

Applications such as magnetic bearings and rotors require soft ferromagnetic alloys such as Fe-Co-2V because of their high magnetic saturation. During the applications, soft ferromagnetic alloys may be required to bear sufficient mechanical loads under a wide range of environments, such as extreme ranges of temperature and loading rate. Currently, limited studies are available regarding the mechanical response of Fe-Co-2V alloys, with most focusing on the response under elevated temperatures. Ren et al. measured the tensile stress-strain response of Fe-Co-2V over a temperature range from ambient to 800°C [1]. Ren et al. found that the Fe-Co-2V displayed a linear elastic response, followed by a Lüders band (flat plateau) before linearly work hardening until failure. Below about 300°C, Ren et al. [1] found that the yield strength decreased with increasing temperature. The decrease in yield strength became insignificant when the temperature was between 300-700°C. Grain size within the material affected the yield strength and followed a Hall-Petch relationship [1]. Duckham et al. investigated Fe-Co-2V over a wide range of grain sizes and temperatures ranging from ambient to 500°C [2]. Their study reinforced the assertion that the Fe-Co-2V followed a Hall-Petch relationship between yield stress and grain diameter and added that both ordered and disordered Fe-Co-2V followed the same relationship. In terms of temperature, Duckham et al. [2] also concurred that the yield stress decreased with increasing temperature. The work hardening rate of the material with grain sizes between 100-150 nm was found to be fairly constant at temperatures up to approximately 300°C, but the material with grain sizes of 290 nm experienced a decrease in hardening rate when the temperature was elevated only to 100°C.

All the available studies have presented the tensile properties of Fe-Co-2V alloys at elevated temperatures but were limited to quasi-static strain rates. Ren et al. did vary the strain rate within the quasi-static regime and discovered a strain rate effect [1]. No information is available on the stress-strain relationship at high strain rates. Furthermore, no investigation has been undertaken to study Fe-Co-2V at low temperatures. Such high-rate, high- or low-temperature material property information of the Fe-Co-2V is critical for the performance assessment under abnormal extreme environments to which materials in magnetic applications may be exposed.

In this study, we use a Kolsky tension bar with an environmental chamber to simultaneously subject the Fe-Co-2V alloy to both extreme temperatures from -100 to 100°C and a high strain rate of 230 s^{-1}. Effects of temperature on yield stress, flow stress, and ductility are explored.

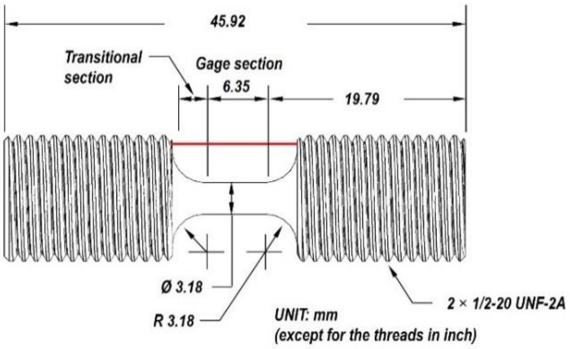

Fig. 1. Specimen Design

2 Materials and Methods

The Fe-Co-2V alloy studied was manufactured by Metal Werks Inc. Dog-bone tensile specimens were machined with the geometry shown in Fig. 1. Dynamic tensile experiments were conducted at temperatures of -100, -50, 23, and 100°C. The strain rate was held constant at approximately 230 s^{-1} for all experiments to determine the temperature effect. Five experiments were conducted

---

[*] Corresponding author: bsanbor@sandia.gov

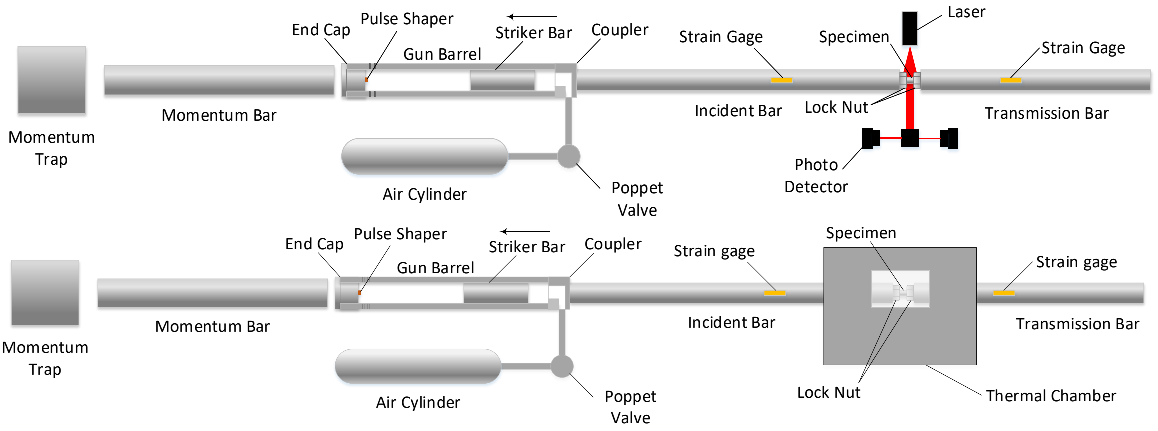

Fig. 2. a) Kolsky tension bar for ambient temperatures. b) Kolsky bar for high and low temperatures

at each temperature condition.

A Kolsky tension bar as shown in Fig. 2 was used for dynamic tensile experiments. The incident and transmission bars were 3.66 and 2.13 m long, respectively, and were made of C300 maraging steel. In this configuration, a solid cylindrical striker is contained inside the gun barrel [3]. When the striker is launched by releasing compressed gas from the cylinder, the striker is propelled toward the opposite end of the gun barrel and strikes an end cap. The generated tensile wave travels through the gun barrel and into the incident bar through a coupler. The tensile wave then propagates along the incident bar until it reaches the specimen which is threaded into the incident and transmission bars and locked into place using two lock nuts. While the specimen is being loaded in dynamic tension, part of the incident pulse is reflected into the incident bar as a reflected pulse, and part of the pulse is transmitted into the transmission bar. The primary benefit of a Kolsky tension bar with this design is that traditional pulse shaping techniques for general dynamic compression tests are easily implemented for dynamic tensile tests. In this study, annealed C11000 copper disks were placed on the inside of the end cap as pulse shapers. Like compression experiments, the dimensions of the pulse shaper can be changed to tailor the profile of the loading pulse for different temperature conditions.

For experiments at high and low temperatures, an environmental chamber was installed at the specimen location to locally heat or cool the specimen and bar ends. A thermocouple was placed on the bar a few centimeters away from the sample. The temperature of the bar and the specimen was assumed to be equilibrated. The material properties of the bars were assumed to be constant within the temperature range (-100 to 100 °C) investigated in this study.

At ambient temperatures, the specimen strain was measured using a linear laser and detector configuration. Shown in Fig. 2a, this configuration used a single beam laser split into two separate high-speed photodetectors using a mirror prism [4]. This allowed displacements of the incident (L_1) and transmission (L_2) bars to be tracked independently during the experiment to calculate the strain history of the specimen. The laser measurement eliminates the possible error in specimen displacement measurement with a traditional method using strain gage signals due to wave reflection at the complicated interfaces, i.e., threads, between the specimen and the bars. However, a previous study showed that when sufficient torque is applied to the lock nuts experimental error is minimal when stain gage signals were used to calculate the displacements at both ends of the specimen [5]. For the experiments where the thermal chamber was used (Fig. 2b), using the laser system was not possible. With proper torque applied to the lock nuts, the specimen strain was therefore calculated using the strain gage signal

$$L_1 - L_2 = \Delta L = C_0 \cdot \int_0^t \left(\varepsilon_i(t) - \varepsilon_r(t) - \varepsilon_t(t)\right) dt \qquad (1)$$

where C_0 is the bar wave speed and ε_i, ε_r, and ε_t are incident, reflected, and transmission bar strains, respectively.

For either the laser or strain gage strain measurements, the deformation of both the gage and non-gage sections were recorded. Thus, the specimen strain must be corrected to include only the gage section. Because the Fe-Co-2V material has an elastic, followed by linear hardening behavior, the specimen strain correction method developed by Song et al. [6] is applicable to correct the specimen strain. Details of the linear hardening strain correction method were presented in [6], however, the general method is summarized here. The correction method divides the stress-strain curve into four regions, shown in Fig. 3.

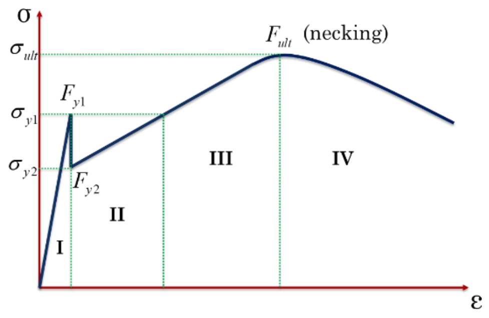

Fig. 3. Idealized linear elastic, work hardening material [6].

In Fig. 3, σ_{y1} and σ_{y2} are the upper and lower yield strengths, and σ_{ult} is the ultimate tensile strength. Forces F_{y1}, F_{y2}, and F_{ult} correspond to upper yield, lower yield, and onset of necking. As will be shown later, the Fe-Co-2V specimens only require use of Regions I-III since no necking occurs. The specimen strain is calculated using Regions I-III from with the piecewise function [6],

$$\varepsilon = \begin{cases} c' \cdot \dfrac{\Delta L}{L_s} & \begin{pmatrix} \text{Region I} \\ \sigma < \sigma_{y1} \end{pmatrix} \\[2ex] \dfrac{\Delta L}{L_s} - \dfrac{F}{M} \cdot \left(\dfrac{1}{c'} - 1 \right) & \begin{pmatrix} \text{Region II} \\ \sigma_{y2} < \sigma < \sigma_{y1} \end{pmatrix} \\[2ex] \left. \begin{matrix} \dfrac{F_{y1}}{M} + \\ \dfrac{\Delta L - \dfrac{2 \cdot F}{E_s \cdot \pi} \cdot \displaystyle\int_{x_0}^{x_l} \dfrac{dx}{R_Q} - \dfrac{F_{y1}}{M} \cdot (2x_0 + L_s)}{\dfrac{2 \cdot F \cdot r_0^2 \cdot \displaystyle\int_0^{x_0} \dfrac{dx}{R_Q} - 2 \cdot F_{y2} \cdot x_0}{F - F_{y2}} + L_s} \end{matrix} \right\} & \begin{pmatrix} \text{Region III} \\ \sigma > \sigma_{y1} \end{pmatrix} \end{cases} \quad (2)$$

R_Q and M are defined as

$$R_Q = \left(R + r_0 - \sqrt{R^2 - x^2} \right)^2 \quad (3)$$

$$M = E_s \cdot \pi \cdot r_0^2 \quad (4)$$

Where R and r_0 are the radii of the shoulder and gage sections of the specimen, respectively. For the geometry used in this study, $x_1 = R = r_0 = 3.18$ mm. L_s is the length of the straight gage section, and F is the force generated by the specimen as a function of time. The specimen Young's modulus is denoted E_s, while c' is a constant also derived from the specimen geometry,

$$c' = \frac{1}{1 + 2 \cdot \dfrac{r_0^2}{L_s} \cdot \displaystyle\int_0^{x_l} \dfrac{dx}{R_Q}} \quad (5)$$

The elastic/plastic boundary, x_0, increases with increasing applied force, F,

$$x_0 = r_0 \sqrt{\left(\sqrt{\frac{F}{F_{y1}}} - 1 \right) \cdot \left[2 \cdot \frac{R}{r_0} - \left(\sqrt{\frac{F}{F_{y1}}} - 1 \right) \right]} \quad (6)$$

The specimen stress history was calculated using

$$\sigma(t) = E_0 \cdot \varepsilon_t(t) \cdot \frac{A_0}{A_s} \quad (7)$$

where E_0 is the Young's modulus of the bar, A_0 is the bar cross-sectional area, and A_s is the specimen cross-sectional area.

3 Results and Discussion

A typical set of strain signals from a Kolsky tension bar experiment on Fe-Co-2V alloy are shown in Fig. 4. Figure 4 shows a uniquely-shaped incident pulse compared to most Kolsky bar experiments. Achieved through pulse shaping, this nearly linear hardening incident pulse was required to deform the specimen at a near constant strain rate, rather than the usual trapezoidal incident pulse. The specimen response shown in Fig. 4 displays high and low yield stresses followed by linear hardening until abrupt failure. The corresponding displacements of the incident and transmission bar ends are shown in Fig. 5.

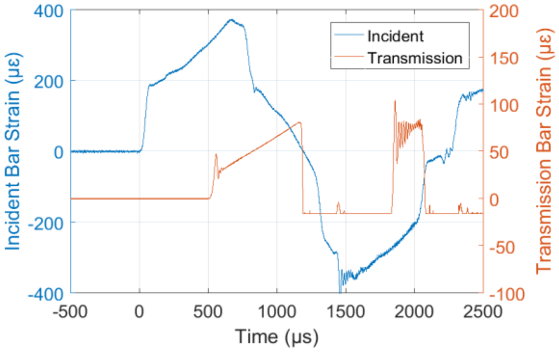

Fig. 4. Original experimental record for Fe-Co-2V under dynamic tension

Using the displacement histories in Fig. 5, the linear hardening strain correction method of Song et al. [6] was applied to calculate strain and strain rate histories, the results of which are shown in Fig. 6. In this case, the specimen was subjected to a nearly constant strain rate of approximately 230 s^{-1}, which was achieved through pulse shaping. At an engineering strain of approximately 5%, a decrease in strain rate was observed which was caused by the beginning of plastic deformation in the shoulders of the specimen, after which the strain rate returned to a similar level [6].

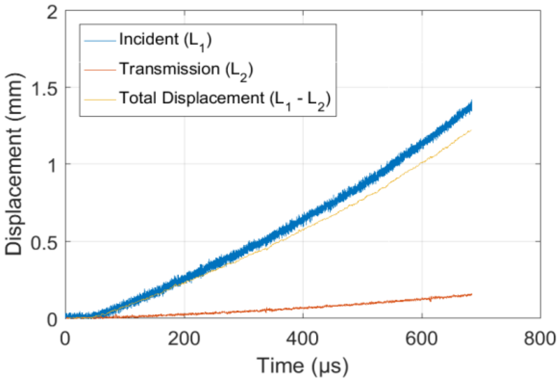

Fig. 5. Displacement history

Overall, the general shape of the stress-strain curve at high rate is like the quasi-static behavior, but some differences are noticeable. The dynamic stress-strain curve has a distinct upper and lower yield response prior to onset of linear hardening. This contrasts with the quasi-static case where yield occurred, followed by a flat plateau (Lüders banding) prior to hardening [1,2].

Using the same process, the temperature of the thermal chamber was varied from -100 to 100°C. The strain rate was held constant at approximately 230 s^{-1} for all experiments. The average engineering stress-strain curves are shown in Fig. 7, which represent an average of five experiments under each condition. Notably, both the high and low yield stresses increased with decreasing temperature. The rate of hardening was independent of temperature. The behavior at ambient temperature and 100°C was nearly identical, but higher strain to failure and ultimate stress was observed at 100°C.

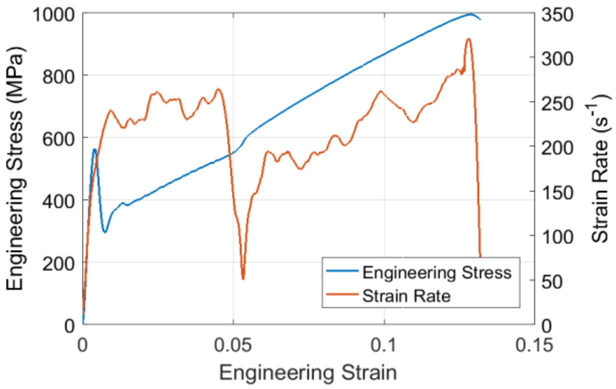

Fig. 6. Engineering stress-strain and strain rate behavior of Fe-Co-2V at 23°C

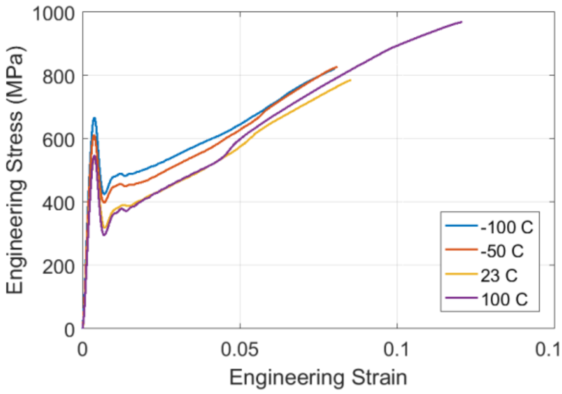

Fig. 7. Temperature effect on stress-strain behavior of Fe-Co-2V. Averaged curves at 230 s^{-1}

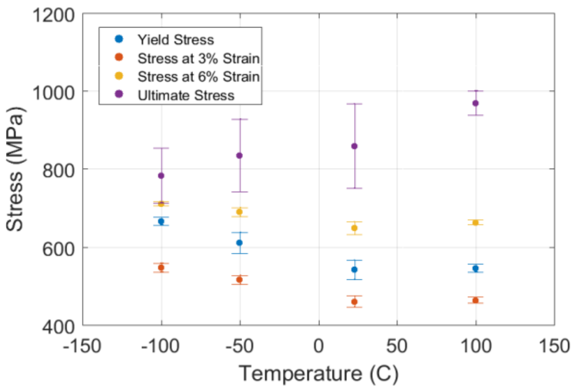

Fig. 8. Temperature effects on yield, flow, and ultimate stress. Error bars represent one standard deviation.

Further temperature effects are shown in Fig. 8 at different strains. As was noted earlier, the yield stress was the highest at -100°C and decreased with increasing temperature. The flow stresses at both 3% and 6% strains were also the highest at -100°C and decreased with increasing temperature. The ultimate tensile stress showed the opposite trend where the average value at 100°C was about 24% higher than at -100°C. This is most likely linked to the increase in overall ductility with increasing temperature, which is shown in Fig. 9. The Fe-Co-2V had 65% higher average failure strain at 100°C compared to -100°C.

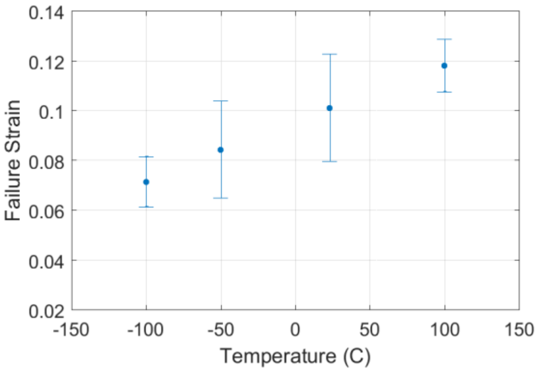

Fig. 9. Temperature effect on failure strain. Error bars represent one standard deviation.

Comparisons of these results to any literature data are difficult to make since to our knowledge, no studies are available to address temperature effects over this range for Fe-Co-2V. Duckham et al. [2] investigated a similar Fe-Co-V alloy under quasi-static tension but mainly looked at the elevated temperature behavior. In general, the behavior found in this study at ambient temperature and 100°C agrees with Duckham et al. [2], where only a minor difference was measured over that temperature range. Duckham et al. similarly noted that the hardening rate of the tensile stress-strain curve did not change with temperature until the temperature reached about 300°C, though this was a grain size dependent relationship.

Though temperature-dependent behavior of Fe-Co-2V is sparse in the literature, the tensile stress-strain behavior of a few different steel types has been studied at cold temperatures which may be used for rough comparison. The temperature effect measured here for Fe-Co-2V is somewhat less dramatic compared to 304 stainless steel. Zheng and Yu saw an increase in ultimate stress of 304 stainless steel by about 24%, under quasi-static conditions when the temperature was dropped from 27°C to -100°C [7]. The ultimate strain was also about 40% lower at -100°C compared to 27°C [7]. Another quasi-static study on mild and high-strength S690 steels showed similar behavior from 30°C to -80°C [8]. Yan et al. [8] found that the mild steel had approximately 18% higher ultimate tensile strength at low temperature while the high-strength steel was only about 9% stronger at low temperature. Unlike the Fe-Co-2V alloy, the failure strain of both types of steel remained relatively constant over the temperature range [8].

Post-test failure analysis of the Fe-Co-2V samples showed that the material underwent brittle fracture. This was observed in all cases regardless of temperature. Each of the specimens failed within the gage section, but no necking was noticeable in any case. This agrees with the stress-strain behavior shown in Fig 5, since no localized necking was observed prior to fracture.

Conclusion

A Kolsky tension bar with an environmental chamber was used to measure the temperature dependent properties of the soft ferromagnetic alloy Fe-Co-2V at high strain rate. A specimen strain correction was applied to the measured displacement data to accurately calculate the strain over the gage section. Tensile stress-strain curves were presented for temperatures of -100, -50, 23, and 100°C at the same strain rate of 230 s^{-1}.

Overall, the dynamic tensile stress-strain behavior was similar over the temperature range. The flat Lüders band plateau usually seen for this material at quasi-static strain rates was absent at high rate. Instead, the material displayed a high and low yield behavior prior to hardening. Notably, the post-yield hardening rate remained constant despite varying the temperature. In general, the upper yield stress and flow stresses at the same strain levels increased with decreasing temperature. An opposite effect was observed for ultimate stress wherein the ultimate stress increased with increasing temperature. This is most likely due to the higher ductility at higher temperatures.

In all cases, the material underwent brittle fracture at high strain rate. Each of the specimens failed within the gage section but maintained a circular cross section with no signs of necking.

This study serves as a first look into the dynamic temperature dependent tensile properties of soft ferromagnetic alloys such as Fe-Co-2V.

Sandia National Laboratories is a multimission laboratory managed and operated by National Technology and Engineering Solutions of Sandia, LLC, a wholly owned subsidiary of Honeywell International, Inc., for the U.S. Department of Energy's National Nuclear Security Administration under contract DE-NA0003525. The views expressed in the article do not necessarily represent the views of the U.S. Department of Energy or the United States Government.

References

1. L. Ren, S. Basu, R.H. Yu, A. Parvizi-Majidi, J. Mater. Sci. **36**, (2001)
2. A. Duckham, D.Z. Shang, D. Liang, V. Luzin, R.C. Cammarata, R.L Leheny, C.L. Chien, T.P. Weihs, A. Mater. **51**, (2003)
3. B. Song, B.R. Antoun, K. Connelly, J. Korellis, W.Y. Lu, Meas. Sci. Technol. **22** (2011)
4. X. Nie, B. Song, C.M Loeffler, J. Dyn. Behav. Mater. **1**, (2015)
5. Y. Qiu, C.M. Loeffler, X. Nie, B. Song, Meas. Sci. Technol. **29,** (2018)
6. B. Song, B. Sanborn, D. Susa, K. Johnson, J. Dabling, J. Carroll. A. Brink, S. Grutzik, A. Kustas. Int. J. Impact. Eng. (submitted 2019)
7. C. Zheng, W. Yu, Mater. Sci. Eng. A, **710** (2018)
8. J.B. Yan, J.Y.R. Liew, M.H. Zhang, J.Y. Wang. Mater. Des. **61**, (2014)

Non-monotonous strain rate dependence of yield stress for tungsten heavy alloy

Christoph Sauer[1,*], *Andreas* Heine[1], *Werner* Riedel[1], *Nadine* Hartmann[1], *Wilfried* Harwick[1], *Sebastian* Kilchert[1], *Noah* Ledford[1], *Martin* Sauer[1]

[1]Fraunhofer Institute for High-Speed Dynamics, Ernst-Mach-Institut, EMI, Ernst-Zermelo-Straße 4, 79104 Freiburg, Germany

Abstract. In this work, the mechanical behavior of a tungsten heavy alloy is investigated under tensile loading over a strain rate range from approximately 10^{-3} to 10^{3} 1/s. In the strain rate regime around 10^{3} 1/s, the material response to compressive loading is tested as well. In tension, we find roughly constant true failure strains between 0.07 and 0.11, while no failure occurs in compression. For the strain rate dependence of the yield stress, a non-monotonous behavior is observed, exhibiting maximum values around 10^{1} 1/s. The unexpected negative strain rate sensitivity above 10^{2} 1/s is addressed by discussing thermal softening and dynamic strain aging as two possible explanations.

1 Introduction

In order to establish predictive modeling capabilities for crash and impact scenarios, the behavior of the involved materials has to be studied under the appropriate high rate loading conditions [1]. Generally, transient dynamic deformation is often linked with a simultaneous increase of temperature due to adiabatic heating as a consequence of plastic work. Hence, it can be quite difficult to distinguish between rate and temperature effects when material strength and failure are investigated. A well known example for this issue is a (partial) compensation of strain rate hardening by simultaneous thermal softening in metals [2].

Tungsten heavy alloy (WHA) is a material that has to sustain high-rate impact loading in certain applications [3]. In this composite material, a high density is achieved by its major constituent tungsten (W) that contributes usually above 90 weight percent. Embedding these W-grains in a metal alloy matrix creates a much larger ductility than in pure W. A particular microstructure of this metal composite is produced by liquid-phase sintering and subsequent heat treatment and swaging processes [4-6]. The abundance of W leads to comparatively large W-grains (several tenths of µm) either in direct vicinity to each other or separated by smaller matrix regions. Thus, both W-W and W-matrix interfaces exist in this material. In addition to the distribution of these interfaces, the shape of the W-grains determines the meso-structure of WHA, and consequently, its macro-mechanical properties.

The motivation for performing material characterization experiments with WHA is to develop and enhance constitutive models for numerical simulations, which are capable of describing the mechanical behavior of this material over a wide range of strain rates. For the sake of simplicity, a homogenous and isotropic material model is favored. This means that the composite nature of WHA and its consequences for the strength and failure behavior have to be included into a homogenized description. Whether or not such a numerical model is capable of properly predicting the response of WHA to different loading scenarios has to be tested by comparison to experimental data. For this model validation, thorough material testing over an appropriate region of loading conditions and strain rates is necessary, since the complexity of the meso-structure of WHA might result in unexpected mechanical behavior.

The scope of this work is to investigate the strain rate dependence of strength and failure in tension of a WHA material of the tungsten-nickel-cobalt (W-Ni-Co) type. Moreover, a comparison of tensile and compressive loading at elevated strain rates is performed. For that purpose, tensile tests at two different strain rates, Split Hopkinson Tension Bar (SHTB) tests, and Split Hopkinson Pressure Bar (SHPB) tests, are conducted. First, the experimental aspects and the derivation of the true stress vs. true strain curves are discussed. Then, we present the resulting curves and the obtained strain rate dependence of yield stress and failure strain. Finally, effects of thermal softening and dynamic strain aging [7] are discussed in order to find a possible explanation for the observed non-monotonic strain rate dependence of the yield stress.

2 Experimental

All samples were machined from identical cylindrical rods. Due to the swaging process a possible inhomogeneity of the W-grain-matrix meso-structure can occur (see for example [8]). This means that in axial and radial direction, but also with changing distance from the middle of the rod, differences in mechanical properties might be present. In order to ensure that the same meso-structure is investigated in the different experimental techniques, all samples exhibit rotational symmetry and were extracted in axial direction along the center axes of the cylindrical rods. The sample geometries are shown as insets in Fig. 1 and Fig. 2.

In all tensile tests, the gauge area was cylindrical with a diameter of 5.0 mm and a length of 30.0 mm. The quasi-static (QS) tensile tests were performed on a hydraulic testing machine with a velocity of 0.08 mm/s

---

[*] Corresponding author: christoph.sauer@emi.fraunhofer.de

resulting in a mean technical (nominal) strain rate of 2.7×10^{-3} 1/s. In these QS measurements, the engineering strain of the sample results from measuring the extension of the sample with a clip gauge exhibiting a gauge length of 10 mm and an effective measurement range of 5 mm. The force was measured with a load cell with a maximum range of 250 kN. The mechanical motion of the piston was detected with a linear variable displacement transformer (LVDT).

Medium rate tensile tests (velocity of 800 mm/s and nominal strain rate of 27 1/s) were performed on a high-speed hydraulic testing machine. Here, the engineering strain was measured optically with a digital high-speed-camera (rate of 75,000 frames per second and a resolution of 152 x 768 pixels) on the surface of the specimen. The specimen strain has been calculated by relating the overall elongation to the initial length (l_0 = 27 mm). The engineering stress in the medium rate tensile tests is obtained by force measurements with a piezo-electric force sensor (with a calibrated force of 35 kN) divided by the initial section. The detection of the piston position is identical to the quasi-static test setup.

The SHTB specimens were tailored cylinders with a gauge length of 3 mm and a diameter of 4 mm in the gauge section. At its ends, the sample was threaded into the titanium bars with M16x1.5 threads. The force was measured at 4 MHz with four strain gauges 300 mm away from the specimen. The measured voltage change on strain gauges was converted into force using calibrated load cells to increase traceability and remove additional uncertainties. The force was then divided by the measured area before testing to determine the technical stress. The strain was measured locally on the gauge length of the specimen using high-speed imaging and Digital Image Correlation (DIC). The camera took images at 442,105 frames per second with an image size of 256 x 64 pixels. The DIC followed two points as close as possible to the failure point. Very little necking was observed and failure propagated very quickly through the specimens.

Pressure tests at high strain rates were carried out at a Direct Impact Hopkinson Pressure Bar facility (DIHPB). The DIHPB setup differs from a classical SHPB setup in having no incident bar. An accelerated striker bar directly impacts the specimen and generates a compressive stress pulse (see [9, 10] for detailed description). Cylinder specimens with a height of 2 mm and a diameter of 2 mm were used. The technical strain rates calculated from the initial impact speed of the striker bar divided by the specimen height ranged between 2000 1/s and 3000 1/s. The force signal was measured via a PVDF sensor attached on the tip of the output bar (accuracy of measurement ±3 %) between sample and bar. A PVDF sensor is basically a piezoelectric film that is a very thin and flexible electromechanical transducer which can convert about 12 % of mechanical energy into electrical energy. For redundancy, a second force signal was measured on the basis of a strain gauge on the transmitter bar (positioned in 1500 mm distance from the location of impact). This strain measurement allows calculating the force signal on the basis of the elastic response of the transmitter bar. The longitudinal deformation of the specimen was measured optically using a high-speed camera system that tracks the movement of two black-and-white edges attached to the tips of striker bar and transmitter bar. The engineering strain was calculated by dividing the specimen deformation by the initial specimen height.

From the resulting stress vs. strain data, the true stresses ($\sigma_{true} = \sigma_{tech} \cdot (1+\varepsilon_{tech})$) and true strains ($\varepsilon_{true} = \ln(1+\varepsilon_{tech})$) were calculated for all experimental techniques.

3 Results and Discussion

Fig. 1 displays exemplary true stress vs. true strain curves under tensile loading. The strain rate range of the tensile tests and SHTB experiments spans from roughly 10^{-3} to almost 10^{3} 1/s. The presented curves show that a constant flow stress is realized until tensile failure. Hence, there is basically no visible strain hardening in tension for these deformation rates. However, since strain rate and temperature can vary by some degree during such plastic deformations, there is also the theoretical possibility of a cancelation of hardening (strain and strain rate increase) and softening (temperature increase) effects. Considering the observed almost ideally plastic behavior, such a cancellation for each of these three different strain rate domains seems unlikely. Consequently, this data is described within a simplified elastic-perfectly plastic model for the consideration of yield stresses. For the QS tensile test and the SHTB data, the shape of the curves in Fig. 1 makes this a reasonable simplification. The medium rate tensile tests (blue curve in Fig. 1a)) show some oscillations due to vibrations of the experimental setup, so that observing small deviations from this model might be hindered. Substantial hardening or softening, however, would be clearly visible even with these oscillations.

A comparison of the observed behavior in Fig. 1 with literature on other types of WHA-compounds shows that the almost perfectly constant flow stress until tensile failure is quite unique for such a large strain rate range. For example, Scapin [11] finds hardening with increasing strain for strain rates from 10^{-3} to 10^{3} 1/s. Moreover, Weerasooriya et al. [12] first observe an almost constant flow stress until failure for the range between 10^{-4} and 10^{-1} 1/s and then find significant softening with increasing strain at a strain rate of 750 1/s. Additionally, the tensile tests presented in Rohr et al. [13] show a moderate hardening at 10^{-5} 1/s, which for higher strain rates gradually transforms to a constant flow stress at 10^{-1} 1/s. Consequently, a large variety of mechanical behavior of different WHA-compounds is found in literature, which shows that drawing conclusions from investigations of one type of WHA for a different type can be troublesome.

The exemplary compressive true stress vs. true strain curve from the SHPB data displayed in Fig. 2 shows that the above discussed simplified elastic-perfectly plastic model is acceptable up to a true strain of approximately

0.2. Beyond that there appears to be softening, but possible barreling of the samples makes a definite statement difficult. As for the medium rate tensile test in Fig. 1a), oscillations of the experimental system are present and limit the experimental accuracy. Nevertheless, a careful comparison to the tensile data up to true strains of 0.1 seems possible. As for the tensile loading, different behavior under compression is observed in literature [11, 14, 15] for different WHA-compounds.

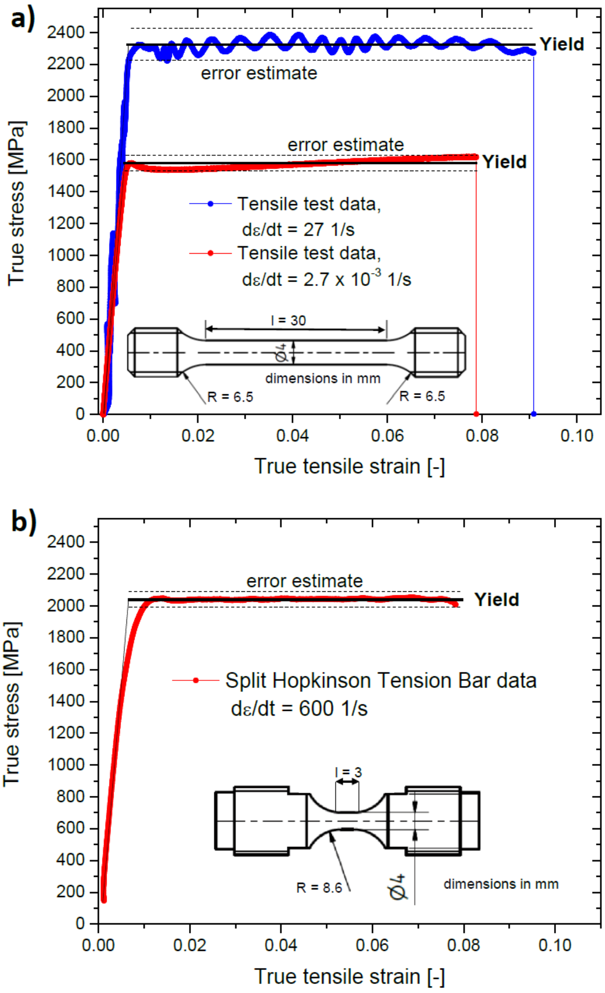

Fig. 1 Exemplary true stress vs. true tensile strain curves from tensile tests at two different nominal strain rates (panel a)) and a Split Hopkinson Tension Bar test (panel b)). The derivation of the yield stress (solid thick curves) and the corresponding error estimate (dashed lines) are demonstrated.

In each of the exemplary curves in Fig. 1 and Fig. 2, a straight thick line marks the true stress value, which is interpreted as the yield stress. The accuracy of determining this value within the assumed simplified elastic-perfectly plastic model is considered in the given error estimate (dashed thin line). In Fig. 3a) the obtained yield stress values and corresponding error bars are presented as a function of strain rate. From the QS tensile tests at a strain rate of roughly 10^{-3} 1/s to the medium rate tensile tests in the range of 10^{1} 1/s, a large increase of the yield stress is observed. Then, going to larger strain rates around 10^{3} 1/s, the yield stress values decrease again. This unexpected non-monotonous strain rate dependence of the yield stress has (to the best of our knowledge) not been observed in literature so far (some examples are given in [11-15]).

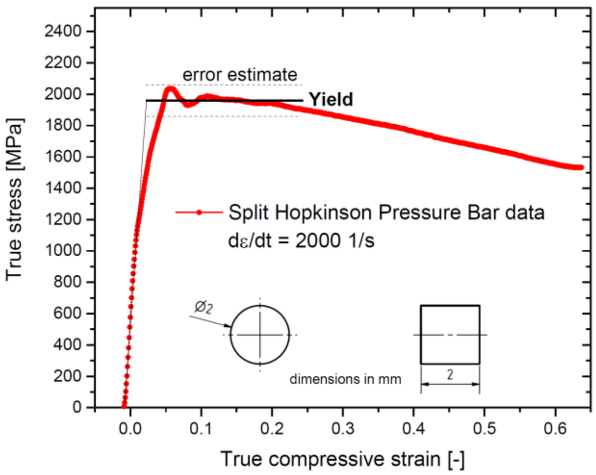

Fig. 2 Exemplary true stress vs. true compressive strain curve from a Split Hopkinson Pressure Bar test. The derivation of the yield stress (solid thick curve) and the corresponding error estimate (dashed line) are demonstrated.

Comparing the yield stresses around 10^{3} 1/s for true strains up to approximately 0.1, there is no significant difference for tensile and compressive loading (within the experimental accuracy). For failure strains, the situation is very different. Since none of the SHPB experiments led to material failure, a quantitative comparison is not possible. It can only be stated that the compressive failure strain is much larger than the tensile strain to failure. The latter is shown as a function of strain rate in Fig. 3b) for all conducted tensile and SHTB tests. Considering the experimental scatter of the data points, a roughly constant true tensile failure strain is observed for strain rate variations in the investigated regime of 10^{-3} to 10^{3} 1/s.

Since usually an increase of the yield stress is expected with increasing strain rate for metals, the question arises how the surprising non-monotonous strain rate dependence of the yield stress, shown in Fig. 3a), can be explained. One possible explanation is thermal softening due to adiabatic heating, which commences somewhere around strain rates of 10^{2} 1/s. However, the presence of a strong thermal softening should be visible in the shape of the presented curves, so that with increasing strain beyond the onset of plastic flow, the stress values should decrease. Especially the almost perfectly constant true stress for true strain values from 0.01 to 0.08 in the SHTB data (Fig. 1b)) stand in stark contrast to this expectation. The presence of an almost perfect compensation of thermal softening by strain and/or strain rate hardening over this entire strain interval appears unlikely.

A second possible explanation of a negative strain rate sensitivity is dynamic strain aging, which is the origin of the Portevin-Le Chatelier effect [7]. Both the characteristic serrated flow and a negative strain rate sensitivity have been reported for different WHA-materials [15-18]. However, these effects appear in those studies within an interval of elevated temperatures and at much lower strain rates. Thus, it is not the same situation as found in this work. Nevertheless, the existence of dynamic strain aging in the material investigated here, which causes an onset of a negative strain rate sensitivity at strain rates beyond 10^2 1/s, is generally possible. In this scenario the absence of serrated flow in the curves within the regime of negative strain rate sensitivity would have to be explained somehow. If such serrations exhibited an amplitude larger than 1 kN and occurred on a time scale larger than 250 ns, they should be observable in the employed SHTB setup.

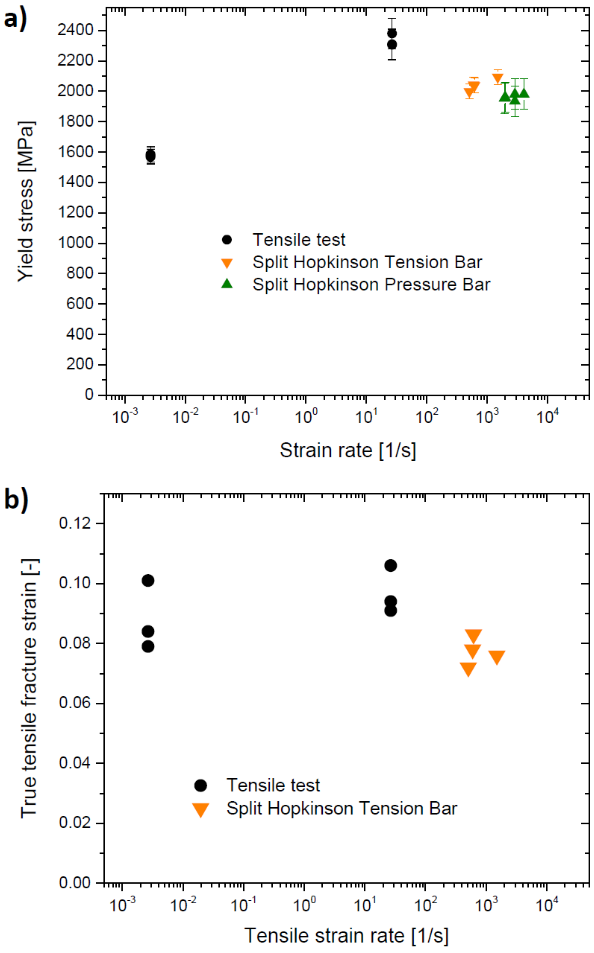

Fig. 3 Strain rate dependence of the yield stress (panel a)) and the true tensile fracture strain (panel b)). The determination of the yield stress values is shown in Fig. 1 and Fig. 2.

Conclusion

A tungsten heavy alloy (WHA) material of the tungsten-nickel-cobalt type was investigated with tensile tests, Split Hopkinson Tensile Bar (SHTB) tests, and Split Hopkinson Pressure Bar (SHPB) tests. Under tensile loading, we find true stress vs. true strain curves that exhibit an almost perfectly constant flow stress until failure. Thus, these curves are approximated by an elastic-perfectly plastic model. For the SHPB data, this approximation is acceptable up to true strains of 0.2. Comparing SHTB and SHPB tests, much smaller failure strains are observed in tensile than in compressive loading, in which no failure occurred up to strains of 0.9. Moreover, almost constant tensile failure strains were found in a strain rate region from 10^{-3} to 10^3 1/s. In the same strain rate regime, the yield stress values show an unexpected non-monotonous variation. Initially, the values rise from approximately 1600 MPa at strain rates around 10^{-3} 1/s to roughly 2300 MPa at around 10^1 1/s and subsequently decline towards 2000 MPa at strain rates around 10^3 1/s. As possible explanations for this negative strain rate sensitivity above 10^2 1/s, thermal softening and dynamic strain aging are discussed. A definite conclusion, however, cannot be drawn at this point, since the curves around 10^3 1/s lack the characteristic features of both discussed effects. Further experimental studies including microstructure analysis of this particular WHA material will have to clarify this interesting finding in the future.

We would like to thank H. Paul, M. Isakov, F. Bagusat, and F. Kölble for stimulating discussions. Furthermore, we thank BMVg and BAAINBw for funding and H. Sohn for his support.

References

1. S.J. Hiermaier, Structures Under Crash and Impact (Springer Science+Business Media, 2008)
2. M.A. Meyers, Dynamic Behavior of Materials (John Wiley & Sons, Inc., 1994)
3. L.S. Magness, T.G. Farrand, in: Proc. 1990 Army Sci. Conf., 465 (1990)
4. B.H. Rabin, A. Bose, R.M. German, Int. J. Powder Metall. **25**, 1 (1989)
5. J. Das, G.A. Rao, S.K. Pabi, M. Sankaranarayana, T.K. Nandy, Mater. Sci. Eng. A **613**, 48–59 (2014)
6. A. Bose, D. Sims, R.M. German, Metall. Trans. A, **19A**, 487–494 (1988)
7. R.C. Picu, G. Vincze, F. Ozturk, J.J. Gracio, F. Barlat, A.M. Maniatty, Mater. Sci. Eng. A **390**, 334–343 (2005)
8. T.J. Vogler, J.D. Clayton, J. Mechan. Ph. Solids **56**, 297–335 (2008)
9. C.K.H. Dharan, F.E. Hauser, Expe. Mech. **10**, 370–376 (1970)
10. H. Couque, Philo. Tran. R. Soc. London A **372**, 2023 (2014)
11. M. Scapin, Int. J. Refract. Met. H. **50**, 258–268 (2015)
12. T. Weerasooriya, J. Clayton, Proceedings of the 2006 Int. Conf. on Tungsten (2006)
13. I. Rohr, H. Nahme, K. Thoma, C.E. Anderson Jr., Int. J. Impact Engng. **35**, 811–819 (2008)

14. Z. Xu, F. Huang, Int. J. Plasticity **40**, 163–184 (2013)
15. J. Das, G.A. Rao, S.K. Pabi, M. Sankaranarayana, B. Sarma, Mater. Sci. Eng. A **528**, 6235– 6247 (2011)
16. S. Kumar, E. Pink, R. Grill, Scr. Mater. **35**, 1047–1052 (1996)
17. E. Pink, S. Kumar, R. Grill, Int. J. Refract. Met. H. **15**, 301–309 (1997)
18. E. Pink, S. Kumar, Mater. Sci. Eng. A **234-236**, 102–105 (1997)

DYMAT2019 P18

Characterisation of material behaviour at low temperatures using Split Hopkinson Pressure Bar for calibrating cryogenic machining numerical simulations

G. Haugou[1*], *H. Morvan*[1], *E. Markiewicz*[1], *R. Bertolini*[2], *S. Bruschi*[2]

[1]Univ. Polytechnique Hauts-de-France, CNRS, UMR 8201-LAMIH, F-59313 Valenciennes, France
[2]Department of Industrial Engineering, University of Padova, Via Venezia 1, 35131, Padova, Italy

Abstract. Recently, cryogenic machining of difficult-to-cut alloys has been adopted to increase tool life and improve the machined components surface integrity. Numerical models of cryogenic machining are being developed to evaluate the influence of the different process parameters. Up to now, their calibration in terms of material flow stress is fulfilled using data at conventional temperatures, whereas the material sensitivity to temperatures lower than the environment one should be taken into account. To this regard, the paper objective is to present material data, obtained through a Split Hopkinson Tension Bar setup at cryogenic temperatures and high strain rates to properly calibrate cryogenic machining numerical models.

1 Introduction

Nowadays, cryogenic machining of the so-called difficult-to-cut metal alloys appears more and more to be the best way to reduce the tool wear and to increase the part in-service performances [1]. The former is fulfilled thanks to the drastic reduction of the cutting temperature, which, in turn, limits adhesion and diffusion wear phenomena to a great extent [2]; whereas, the latter is usually achieved thanks to the attainment of machining-altered layer characterized by ultra-fined microstructure and compressive residual state of stress [3]. The influence of the cutting parameters and of the layout of the liquid nitrogen delivery system can be evaluated by means of either machining trails or numerical simulations. While the former are costly and time-consuming, the latter are still far from being an established procedure due to the difficulties that can be encountered in calibrating the numerical models devoted to machining operations. Attempts for the numerical modelling of cryogenic machining have been done recently, as in [4] and [5] where flow stress data of the workpiece material were coupled with microstructural features evolution to give a proper description of the machined surface integrity. Usually, flow stress data for machining simulations are gained from tests carried out at elevated strain rate values, being the latter relevant to cutting operations, making use of either tensile or compressive testing apparatuses, such as the Split Hopkinson Tension or Pressure Bars at dynamic regime (see [6] and [7]). Most of these tests are carried out at room temperature, in some cases at higher temperatures to account for the cutting temperature increase, but none at sub-zero temperatures that the workpiece surface encounters during cryogenic machining. However, at very low temperature this kind of dynamic tests remains challenging and only few data are available in the open literature.

The objective of this paper is then to analyse how the material behaviour of a Ti6Al4V titanium alloy, in terms of flow stress and strain at fracture as well as surface fracture features, is affected when loaded at sub-zero temperatures and elevated strain rates. For sake of comparison, quasi-static tests were carried out with a strain rate of 0.008 s^{-1} at room temperature.

2 Material and experimental procedures

2.1 Material under investigation

The material used in this study is a Ti6Al4V titanium alloy supplied in form of 1 mm thick sheets. The sheets were provided in annealed condition, characterized by an equiaxed α + β microstructure. According to the supplier's specification, the chemical composition of the Ti6Al4V alloy is reported in Table 1.

Table 1. Chemical composition of Ti6Al4V (%wt).

Ti	Al	V	Fe	O	C	N
Balance	6	4	<0.3	0.2	<0.08	<0.07

2.2 Split Hopkinson Tension Bar tests

To characterize the material behaviour at high rate of strains, experimental tests were carried out using a Split Hopkinson Tension Bar (SHTB) apparatus. During the test, the sheet specimen is sandwiched between the incident bar and the transmitter bar; a tensile load is produced by the release of a pre-stretched load at the free

---

[*] Corresponding author: gregory.haugou@uphf.fr

end of the incident bar. More details about the experimental procedure and analytical technique used to evaluate the dynamic mechanical response of the impacted specimens are presented in [8]. To match geometrical/material properties of the bars and the strain rates attended in this study, the shape of the specimens was accurately designed by means of analytical approaches [8].

Fig. 1 shows the drawing of the specimen used in this study. The specimens were laser cut from the as-received sheet along the rolling direction.

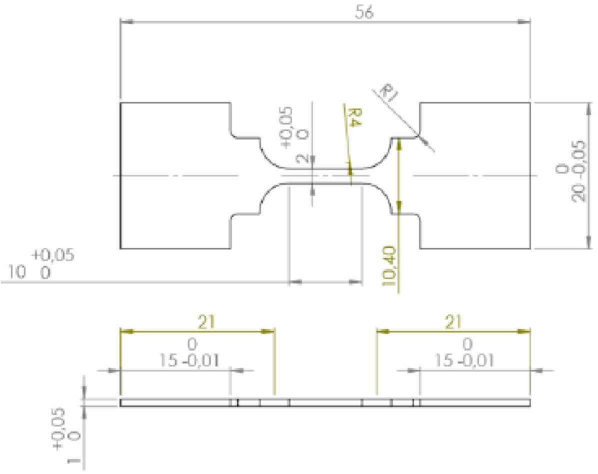

Fig. 1. Drawing of the Ti6AlV tensile sheet specimen used in this study (dimensions in mm).

Tests were performed at different strain rates and temperatures. In particular, strain rate values of 200 s^{-1} and 1000 s^{-1} were chosen as representative of machining processes, while the temperature was varied from 25°C to -150°C at steps of 50°C. In order to achieve sub-zero temperatures, a refrigeration chamber was specifically designed. The chamber is composed of an upper part and a lower part, in which both the cylindrical bars and the sample are located in between. K-thermocouples are spot-welded on the surface of the tensile specimen to measure the temperature during tests.

The experimental procedure adopted for sub-zero testing consists of the following three stages:

1. The lower part is placed below the connectors/bars set and the liquid nitrogen is completely spilled in. Then, the upper part is positioned over the lower part and a locking system assures the contact of the two parts. Five minutes of contact with the liquid nitrogen assures the specimen temperature to be close to -195°C.
2. The upper part is removed with the temperature still controlled by heat exchange with the environment. A mechanism is used to discharge the liquid nitrogen so that the connectors/sample set is no more immersed into the liquid nitrogen.
3. When the desired testing temperature is reached, the test is launched and data are collected.

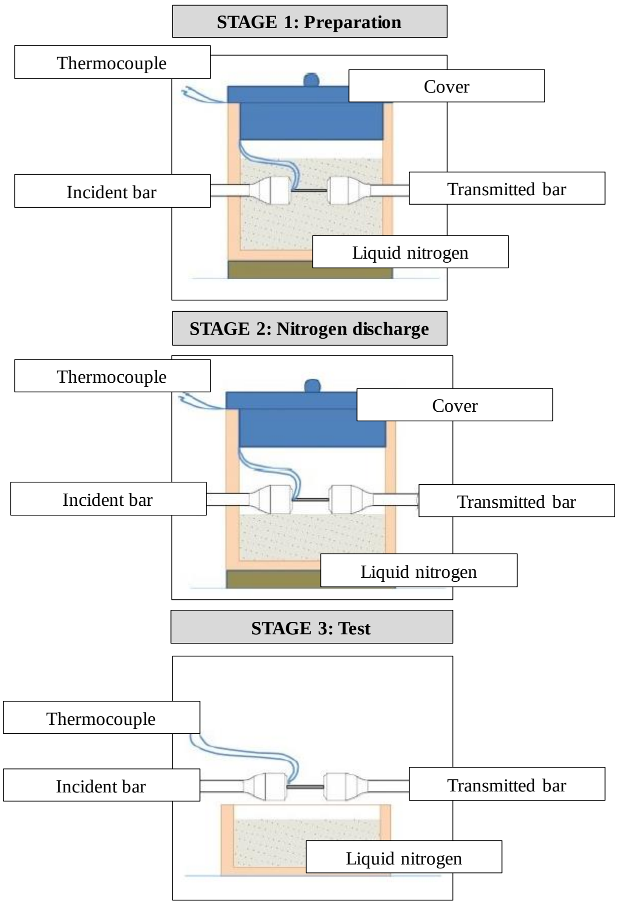

Fig. 2. Experimental stages of SHTB tests under low temperatures regime.

The aforementioned three stages are schematically described in Fig. 2, while images of the experimental apparatus are reported on Fig. 3. From the latter, it can be seen that the refrigeration chamber is large enough to ensure a constant temperature in the environment of the specimen.

It is supposed that a homogeneous temperature is obtained at the gauge area of the specimen thanks to its reduced dimensions. However, this information cannot be checked since the thermocouple is bonded at the surface of the specimen. It is also worth adding that the actual temperature during the test cannot be measured due to the very short time at break (less than 1 ms).

Normally, a set of 3 tests was performed for each testing condition to ensure an acceptable repeatability of results and highlight possible material data dispersion at the same time.

For sake of comparison, quasi-static tests were carried out on a ElectroPuls^{TM} Instron E3000 machine with a strain rate of 0.008 s^{-1} at room temperature.

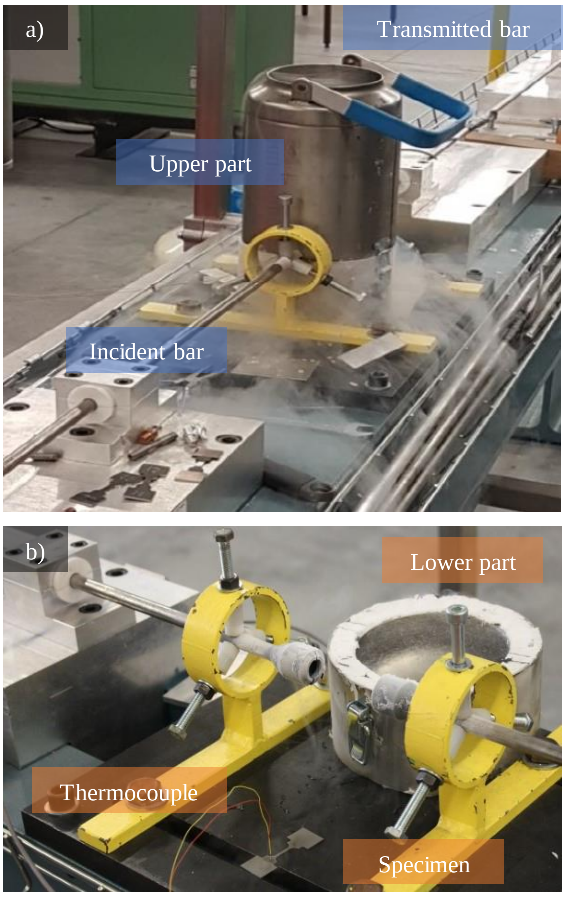

Fig. 3. SHTB experimental setup apparatus: a) setting of the testing temperature in the refrigeration chamber; b) configuration after testing.

2.3 Characterization after SHTB tests

After SHTB tests, the specimens fracture surface was analysed by means of a FEI™ QUANTA 450 Scanning Electron Microscope (SEM) using the Secondary Electron (SE) probe. Images at different magnifications, namely 5000X, 2000X and 1000X, were acquired. Low magnification images of the fracture surfaces were acquired by SEM and the area was accurately measured by means of the length tool of the microscope.

3 Results and discussion

3.1 True stress–strain curves and strain at fracture

In this section, the Ti6Al4V mechanical behaviour is presented with respect to different strain rates and temperatures. The flow stress relations are obtained using David^{TM} software [9] on the basis on the governing equations mentioned in a previous paper [10]. For all the conditions, it is assumed a Poisson's coefficient of 0.34 and no visco-elasticity effect is considered.

Fig. 4 reports the effect of strain rate on the flow stress at room temperature. The tensile tests performed under dynamic conditions showed higher values of the fracture strength compared to the flow stress under quasi–static conditions, confirming the strain rate hardening effect at elevated strain rates. It is worth noting that the changes of the tensile tests strain rate do not influence significantly the elastic modulus of the investigated material: Young's modulus is 80 GPa in quasi-static conditions and close to 90 GPa under dynamic loadings. However, in the latter case, the elastic modulus cannot be accurately confirmed [11].

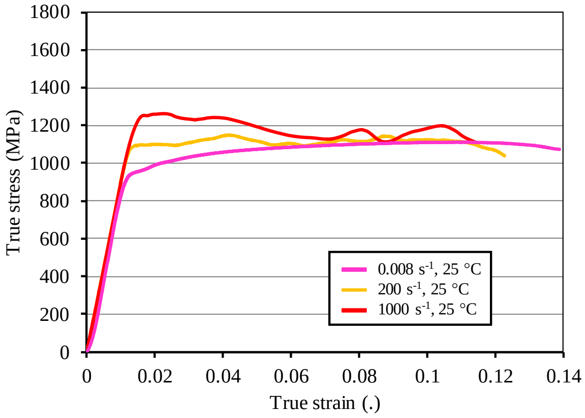

Fig. 4. Ti6Al4V true stress–true strain curves as a function of strain rate at room temperature.

Fig. 5 a and b presents the Ti6Al4V true stress–strain curves at strain rate of 200 s^{-1} and 1000 s^{-1}, respectively, and at temperatures varying from -150°C to 25°C.

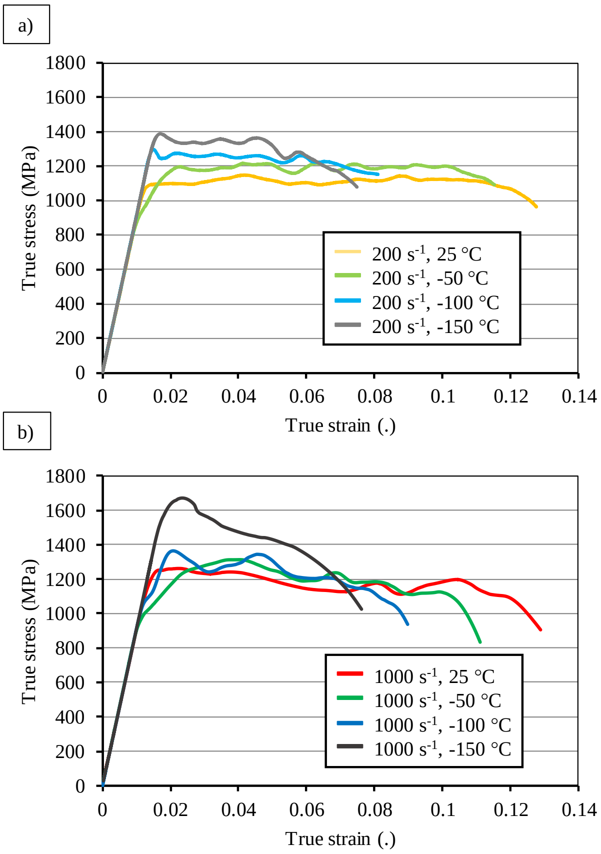

Fig. 5. Ti6Al4V true stress–true strain curves as a function of temperature at a) 200 s^{-1} and b) 1000 s^{-1}.

It can be clearly seen that the flow stress depends on both the strain rate and temperature. Specifically, at a given constant temperature, the flow stress increases quickly at increasing strain rate, while at a given constant strain rate, the flow stress increases gradually at decreasing temperature [12]. For instance, at a fixed true plastic strain of 0.03 and strain rate of 200 s^{-1}, the flow stress increases from 1100 MPa to 1320 MPa as the temperature decreased from 25°C to -150°C. Similarly, at the highest strain rate of 1000 s^{-1}, the flow stress increases from 1210 MPa to 1580 MPa. The curves shown in Fig. 6 show that the strain rate governs not only the flow stress, but also the fracture strain.

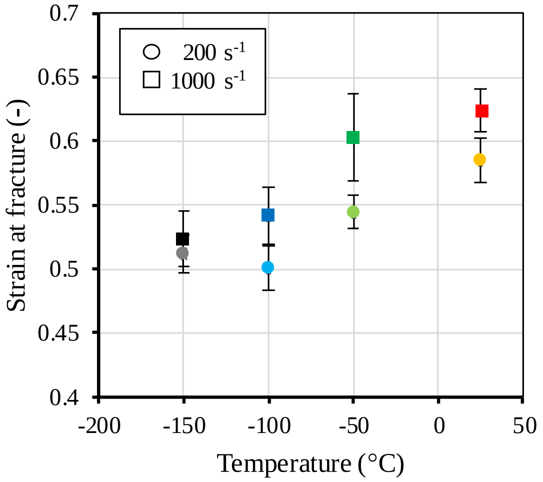

Fig. 6. Ti6Al4V strain at fracture as a function of temperature at a) 200 s^{-1} and b) 1000 s^{-1}.

Specifically, at a given constant temperature, the fracture strain increases for increasing strain rates, but the effect is less significant at the lowest testing temperature. Furthermore, at a given constant strain rate, the fracture strain reduces drastically at decreasing temperature from 25°C to -100°C, even if no sensible difference can be found between -100°C and -150°C. We can then conclude that the strain rate and temperature effect on the strain at fracture is opposite.

3.2 Fracture surfaces

Figs. 7 and 8 report the SEM images of the specimens' fracture surfaces as a function of the strain rate and temperature at two different magnifications. Surface fractures are arranged in dimple-like features regardless of the testing parameters, thus indicating always a ductile fracture mechanism. It should be expected, that fracture nucleates in the area of α phase nucleation, then plastic flow occurs in the areas of β phase – much more ductile, close to α phase areas [13].

.

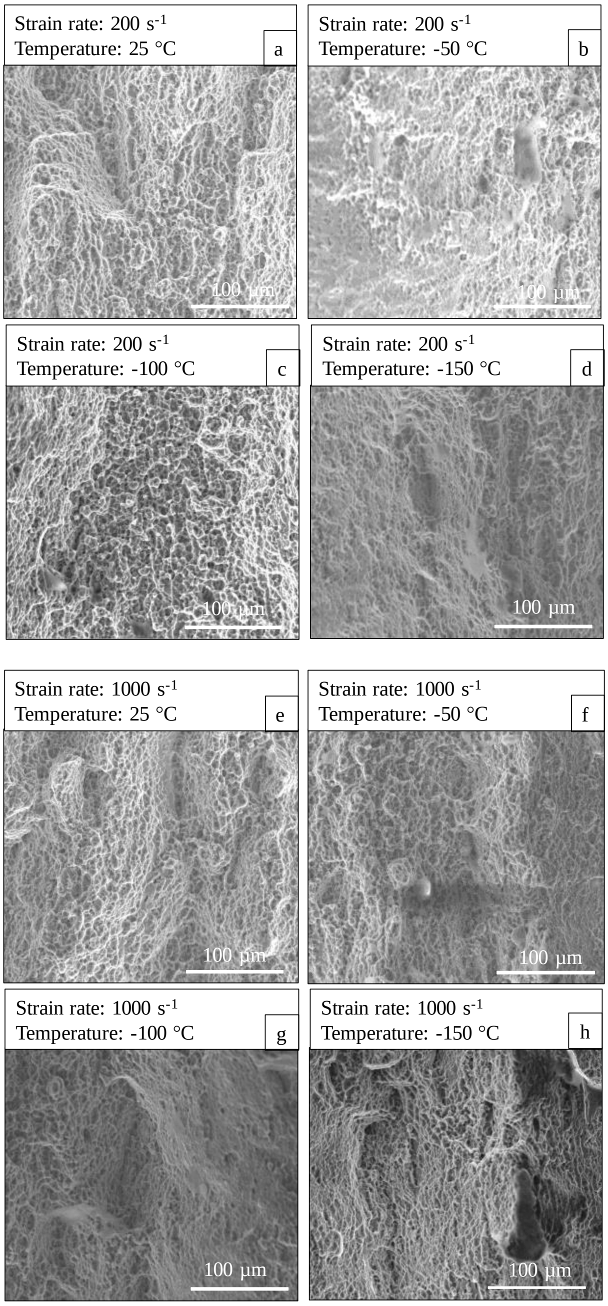
Strain rate: 200 s-1
Temperature: 25 °C
a
100 µm
Strain rate: 200 s-1
Temperature: -50 °C
b
100 µm
Strain rate: 200 s-1
Temperature: -100 °C
c
100 µm
Strain rate: 200 s-1
Temperature: -150 °C
d
100 µm
Strain rate: 1000 s-1
Temperature: 25 °C
e
100 µm
Strain rate: 1000 s-1
Temperature: -50 °C
f
100 µm
Strain rate: 1000 s-1
Temperature: -100 °C
g
100 µm
Strain rate: 1000 s-1
Temperature: -150 °C
h
100 µm

Fig. 7. Fracture surfaces of the Ti6Al4V specimens deformed at different strain rates and temperatures (magnification 1000X).

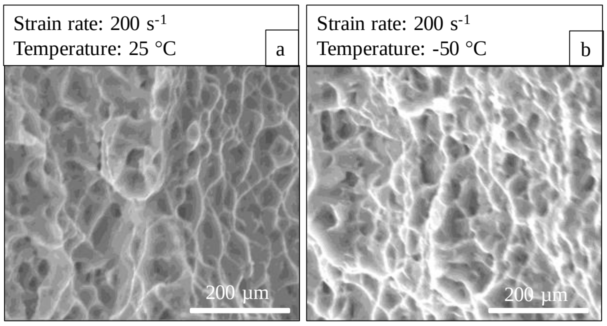
Strain rate: 200 s-1
Temperature: 25 °C
a
200 µm
Strain rate: 200 s-1
Temperature: -50 °C
b
200 µm

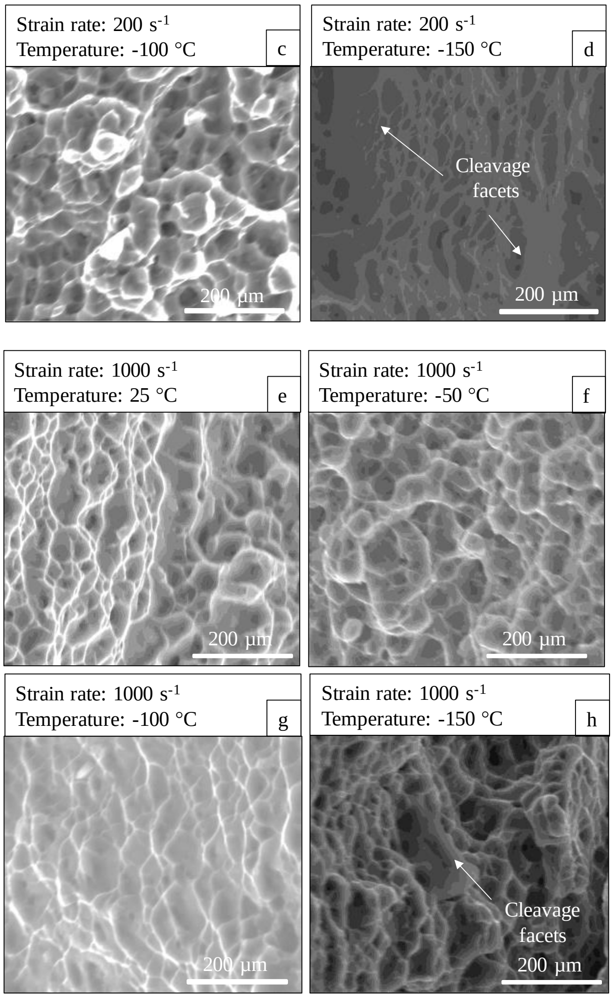

Fig. 8. Fracture surfaces of the Ti6Al4V specimens deformed at different strain rates and temperatures (magnification 5000X).

Fig. 7 a and b presents the fractographies of the two specimens deformed at a temperature of 25 °C and strain rates of 200 s^{-1} and 1000 s^{-1}, respectively.

The comparison of the two fracture surfaces shows that the dimple density increases at increasing strain rate. Similar tendencies are noted for the other testing temperatures and shown in in Fig. 7b, c and d. On the contrary, the dimple density reduces and the number of flat cleavage planes increases as the temperature reduces. These more brittle features at the fracture surface are indicative of the hardening effects occurred when deforming at low temperatures and are a sign of reduced ductility. These findings are in accordance with the strain at fracture values reported in Fig. 6.

Conclusion

In this study the effect of the strain rate, up to 1000 s^{-1}, and temperature, in the range between 25°C and -150°C, on the Ti6Al4V mechanical behaviour was investigated.

To this purpose, a newly designed refrigeration chamber was designed to cool down the specimen for sub-zero testing and applied to the Split Hopkinson Tension Bar experimental apparatus.

The main findings can be summarized as follows:

- The material behaviour is sensitive to both strain rate and temperature. The flow stress increases with increasing strain rate and decreasing temperature. The strain rate and temperature effect on the strain at fracture is opposite.
- The SEM observations of the fracture surfaces show dimple structure indicative of a ductile rupture mechanism regardless of the strain rate and temperature adopted in this study. However, the dimple density increases as the strain rate is increased, while is reduced when deforming at sub-zero temperatures. Actually, at the lowest testing temperature cleavage surfaces are shown.

References

1. IS. Jawahir, H. Attia, D. Biermann, J. Duflou, F. Klocke, D. Meyer, ST. Newman, F. Pusavec, M. Putz,, J. Rech, V. Schulze, D. Umbrello, Cryogenic manufacturing processes. CIRP Annals-Manuf Tech, 65/2:713–36, (2016).
2. S. Sartori, A. Bordin, S. Bruschi, A. Ghiotti, Machinability of the EBM Ti6Al4V in Cryogenic Turning. Key Eng Mat, 651:1183-88, (2015).
3. S. Bruschi, R. Bertolini, A. Ghiotti, E. Savio, W. Guo, R. Shivpuri, Machining-induced surface transformations of magnesium alloys to enhance corrosion resistance in human-like environment. CIRP Annals - Manuf Tech, 67:579–582, (2018).
4. D. Umbrello, A. Bordin, S. Imbrogno, S. Brusch, 3D finite element modelling of surface modification in dry and cryogenic machining of EBM Ti6Al4V alloy. CIRP J Manuf Sci Tech., 18:92–100, (2017).
5. G. Rotella, D. Umbrello, Finite element modeling of microstructural changes in dry and cryogenic cutting of Ti6Al4V alloy, CIRP Annals – Manuf Tech, 63/1:69–72, (2014).
6. LA. Denguir, JC. Outeiro, G. Fromentin, V. Vignal, R. Besnard, A physical-based constitutive model for surface integrity prediction in machining of OFHC copper. J Mat Process Tech, 248:143–160, (2017).
7. W. Cheng, J. Outeiro , JP. Costes, R. Saoubi, H. Karaouni, L. Denguir, V. Astakhov, F. Auzenat, Constitutive model incorporating the strain-rate and state of stress effects for machining simulation of titanium alloy. Procedia CIRP, 77:344-7, (2018).
8. G. Haugou, N. Leconte, H. Morvan, Design of a pre-stretched tension Hopkinson bar device: Configuration, tail corrections, and numerical validation. Int J Impact Eng, 97:89–101, (2016).

9. G. Gary, V. Degreef ., DAVID, Users' manual version, Labview version. LMS Polytechnique, Palaiseau, France, version 12341.
10. J. Achenbach, Wave propagation in elastic solids. North-Holland, (1973).
11. K. Safa, G. Gary Displacement correction for punching at a dynamically loaded bar end. Int J Impact Eng,37/4:371-384 (2010).
12. WS. Lee, TH. Chen, SC. Huang. Impact deformation behaviour of Ti–6Al–4V alloy in the low-temperature regime. J Nucl Mat, 402:1-7, (2010).
13. M. Wojtaszek, T Sleboda, , A. Czulak, G. Weber, WA. Hufenbach. Quasi-Static and Dynamic Tensile Properties of Ti-6Al-4V Alloy. Arch. Met. and Mat., 58:1261-5, (2013).

DYMAT2019 A01

Investigation of a Severe Plastic Deformation process of structural hardened aluminum grades using a heated direct impact technique to annihilate Adiabatic Shear Bands formation

J. Mespoulet, P.L. Hereil*, H. Couque, A. Hocini, P. Langlois, G. Dirras

Abstract. Alloying and thermomechanical treatments are widely used to improve the mechanical properties of metallic materials. This is done by building obstacles that restrict dislocation propagation. Among them, increasing the fraction of grain boundaries via grain refinement [1] [2] is of particular importance and easy to implement. Indeed, the grain size reduction effect can be super-imposed to other strengthening mechanisms such as solid solution, plastic deformation and precipitate hardening.

Conventional techniques to generate Ultra Fine Grain (UFG) by Severe Plastic Deformation (SPD) such as High-Pressure Torsion, Equal Channel Angular Pressing or Multi-Axial Forging have demonstrated their abilities to strengthen materials such as steels, aluminum-based or titanium-based alloys [3].

The plastic deformation of metals and metal alloys remains marked by two important properties, namely the strain hardening rate and strain rate sensitivity. In the dynamic regime, a strain rate sensitivity of the flow stress is observed, which is most often accompanied by a dynamic softening due to a localized deformation within adiabatic shear bands (ASB). Without incorporating additional heat treatment steps, occurrence of ASBs limits further processing and therefore grain refinement.

However, the advantage of using Dynamic SPD in a single step opens new opportunities for material engineering by mastering the different physical parameters (strain, strain rate, temperature) with the help of numerical simulations that gives in-situ information that cannot be obtained experimentally.

To this end, a Dynamic Plastic Deformation (DPD) process based on a direct impact technique has been investigated. This study aimed to evaluate and demonstrate the feasibility of using high strain rate to enhance the mechanical properties via grain refinement under adiabatic condition. Several specimen dimensions have been employed to ensure parametric studies at reduced scales (Ø 19 mm and Ø 40 mm) in order to optimize the conditions of the tests (projectile weight and velocity) at large scale (up to Ø 100 mm). Nickel, copper [4] and aluminum grade materials have been investigated. Strain limitation due to Adiabatic Shear Band (ASB) formation for aluminum grades has initially limited the level of achievable strain. A preliminary heating step helped to overcome those problems [5] and a specific configuration has been developed to get rid of ASB formation during the dynamic process in the intermediate scale (Ø 40 mm).

This paper describes the methodology employed and the numerical works performed during this intermediate scale DPD campaign on three structural hardened aluminum grades (2000 and 6000 series). A post-mortem mechanical behavior and microstructure analysis of the 6000 series has also been done to complete this study by evaluating the induced microstructure and mechanical behaviour after DPD at room temperature or initial hot conditions.

This work was supported by Délégation Générale à l'Armement (DGA) in the framework of the ANR-14-ASTR-0029 "MAUDE" project operated by the French National Research Agency (ANR).

---

* Corresponding author: hereil@thiot-ingenierie.com, THIOT INGENIERIE

References

1. Hall E.O., Proc. Phys. Soc. London. 64 p747–753, (1951)
2. Petch N.J., J. Iron Steel Inst. London. 173, p25–28 (1953)
3. Azushima A., Kopp R., Korhonon A., Yang D.Y., Micari F., Lahot G.D., Yanagimoto J., Tsuji N., Rosochowski A and Yanagida A., CIRP Annuals – Manuf. Tech., 57, p716-735 (2008)
4. Mespoulet J., Beucia B., Tingaud D., Hereil P.L., Dirras G., EPJ Web Conf., 183, p3023-3029 (2018)
5. Beucia B., Tingaud D., Couque H., Chauveau T., Brinza O., Mespoulet J., Hereil P., Dirras G., Euromat - Thessalonique, Greece – (2017)

Thermomechanical properties of hexagonal close-packed metals under high strain rate loading: a novel approach to diagnostic and full-field measurements of temperature and strain fields

L. Farbaniec[*], D.E. Eakins

Abstract. In dynamic and impacts events, metals are often subjected to large deformations and high strain rates. Under these extreme loading conditions, the conventional stress relaxation mechanisms that generally lead to homogeneous plastic deformation are suppressed due to time constraints, and the deformation occurs in the form of localised deformation bands (the so-called adiabatic shear bands). Although the adiabatic shear bands (ASBs) have been studied for many years, the underlying mechanisms of ASB formation are not well understood. This is due to the limited ability of conventional experimental approaches to visualize and quantify this dynamic failure mode. Thus far, a major challenge in studying dynamic and impact problems is capturing crucial data, such as local temperature and strain fields, at the rates and resolutions corresponding to the time and length scales of ASBs formation. Although, the state-of-the-art high-speed cameras are able to capture the early stage of dynamic shear localisation, the corresponding infrared camera technologies are still too slow to measure the temperature fields with required temporal and spatial resolutions.

In this study, we propose a novel diagnostic tool with which a conventional high-speed camera can be used to determine both the full-field strain and temperature fields in the miniaturised test specimens undergoing dynamic shear deformation. The experiments have been performed using a modified split-Hopkinson pressure bar technique for compression testing. However, the geometry of the specimen has been designed such that the shear deformation is promoted and remains stable to large strains at high strain-rates. This approach is based on simultaneous non-contact surface measurements on the test specimens and involves additional sample preparation steps, such as sputter-coating with gold and ink-speckling of the visualized surface of the specimen during the test. The evolution of the temperature fields has been obtained based on the changes in optical properties of gold that occurs as the temperature of the specimen rises with subsequent deformation. This was accomplished by measuring the changes in reflected light from the gold coated surface in the visible light spectrum of interest. The evolution of the strain and strain rate fields has been obtained by Digital Image Correlation (2D DIC) measurements. To this end, the capability of this diagnostic tool to observe the formation of shear bands with sub-micron spatial and sub-microsecond temporal resolutions has been demonstrated on two model hcp material systems (titanium and magnesium alloys). The results showed non-uniform temperature and strain fields in the gage section of the specimen resulting from the applied load. The evolution of temperature and strain fields has been found to vary as a function of strain rate and strain. For example, the investigation of ASB formation in titanium alloys Ti-6Al-4V showed the average temperature rise of at least 200 °C near the deformation bands, and locally above $0.4-0.5T_m$. The maximum shear strain and shear strain rate measured by the DIC technique in this experiment was ~0.2 and 4.5x104 s^{-1}, respectively. This novel experimental approach can help to better understand the early stage of ASB formation and provide experimental data for further evaluation of competing mechanisms (i.e., strain-rate hardening vs. thermal softening) on the formation of ASBs in this class of materials.

---

[*] Corresponding author: lukasz.farbaniec@eng.ox.ac.uk, University of Oxford

Dynamic properties of honeycomb liner materials Hastelloy X and Haynes 214

S. Ulan kyzy*, R. Völkl, O. Munz, T. Fischer, U. Glatzel

Abstract. The efficiency of gas turbines is closely associated with sealing systems between rotor and stator. Most widely used are labyrinth seals with honeycomb liners, which allow for minimum leakage and tolerate rub events. In order to avoid a severe damage of the rotor, the wear during rub-in should only occur on the honeycomb side. The interaction between the blade and honeycomb can lead to strain rates higher than 10^3 s^{-1} and temperatures up to the melting point of the material.

Some scholars reported during the rub-in event in abradable seals the formation of a so-called plastic shear mix layer. Bill and Wisander [1] suggested that all the wear-controlling processes occur within this layer. The shear mix layer has a thickness of 10 – 250 µm [2] and consists of very fine recrystallized grains [1]. Bill and Wisander [1] indicated the correlation between the formation of the plastic shear mix layer and the hot-working behaviour as well as recrystallization kinetics of the materials. Marscher [2] proposed that the shear mix layer has “dynamic characteristics” and recommended to study the strain rate behaviour of the materials.

Cremisio and McQueen [3] studied the hot-workability of Hastelloy X at strain rate of 20 s^{-1} at temperatures from 870 to 1200°C. They reported a ductility peak at 1100°C and decreasing ductility at higher temperatures as result of the grain boundary liquation. Aghaie-Khafri et al. [4] studied hot-workability of Hastelloy X at temperatures 900–1150°C and strain rates of $1\cdot10^3$ and $5\cdot10^0$ s^{-1}. Hastelloy X has demonstrated a dynamic strain aging at intermediate temperatures. Miner [5] found the solute drag effect at intermediate temperatures. According to Sakthivel et al. [6] Hastelloy X shows a serrated flow behaviour because of molybdenum migration within the matrix at strain rates from 10^{-3} to 10^{-5} s^{-1} and at temperatures 200-700°C. They reported activation energy for Hastelloy X of 106 kJ/mol. For Haynes 214 only the mechanical properties under quasi-static loading condition was reported by Deevi [5] and Haynes International [7]. The influence of intermediate strain rates and temperatures on the dynamic properties of both alloys is not investigated yet.

For the prediction of rub-in effect, it is important to understand the dynamic material properties, microstructural changes and the wear mechanisms at high strain rates and high temperatures. However, complex stress, strain and temperature loadings in jet engines hinder the analysis of the main influencing parameters on wear of honeycomb seals. The goal of this research is to study the material behaviour close to the real application conditions of the honeycomb liners. The dynamic properties of the honeycomb liner materials Hastelloy X and Haynes 214 were investigated on foils (0.3 and 0.5 mm) at intermediate strain rates (1, 10 and 50 s^{-1}) and a wide range of temperatures (20-1300°C) using a servo-hydraulic test machine Gleeble 3500. Using the Norton power law the relationship between ultimate tensile strength, UTS, and the strain rate was extrapolated to high strain rates. The activation energy was determined for the temperatures above 1100°C. Moreover, the microstructure examination of the tensile samples was studied using Electron Channelling Contrast Imaging and Electron backscatter diffraction.

---

* Corresponding author: sonun.ulan-kyzy@uni-bayreuth.de, University of Bayreuth

References

1. R.C. Bill, D. Wisander, Recrystallization as a controlling process in the wear of some f.c.c. metals, Wear. 41 (1977) 351–363.
2. W.D. Marscher, A phenomenological model of abradable wear in high performance turbomachinery, Wear. 59 (1980) 191–211. doi:10.1016/0043-1648(80)90278-1.
3. R.S. Cremisio, H.J. McQueen, Some Observations of Hot Working Behavior of Superalloys According to Various Types of Hot Workability Tests, Superalloys 1972 (Second Int. Symp. (1972) G-1-G-36. doi:10.7449/1972/Superalloys_1972_G-1_G-36.
4. M. Aghaie-Khafri, N. Golarzi, Forming behavior and workability of Hastelloy X superalloy during hot deformation, Mater. Sci. Eng. A. 486 (2008) 641–647. doi:10.1016/j.msea.2007.11.059.
5. R. V. Miner, M.G. Castelli, Hardening mechanisms in a dynamic strain aging alloy, HASTELLOY X, during isothermal and thermomechanical cyclic deformation, Metall. Trans. A. 23 (1992) 551–561. doi:10.1007/BF02801173.
6. T. Sakthivel, K. Laha, M. Nandagopal, K.S. Chandravathi, P. Parameswaran, S. Panneer Selvi, M.D. Mathew, S.K. Mannan, Effect of temperature and strain rate on serrated flow behaviour of Hastelloy X, Mater. Sci. Eng. A. 534 (2012) 580–587. doi:10.1016/j.msea.2011.12.011.
7. S.C. Deevi, V.K. Sikka, Nickel and iron aluminides: An overview on properties, processing, and applications, Intermetallics. 4 (1996) 357–375. doi:10.1016/0966-9795(95)00056-9.

DYMAT2019 A04

Interplay of temperature, strain rate and orientation: Case study on elevated temperature, high strain rate micromechanical tests on fcc metallic systems

G. Mohanty*, A. Lambai, R. Ramachandramoorthy, J. Michler

Abstract. Testing polycrystalline metals at high strain rates provides an overview of the average plastic deformation of all the grains. While micro plasticity is important in such cases (e.g. strain localization, slip transfer, etc.), this phenomenon is mostly studied as a consequence of a performed test and not as a design variable that can be studied systematically. Such tests are interesting as they allow deformation mechanisms to be studied in a systematic manner as a function of crystal orientation, temperature and strain rates. Although it is possible to perform these tests on multiple single crystals with varying crystal orientations, they are expensive and suffer from limited material availability. Consequently, literature data on high strain rate testing exploring the influence of crystal orientation on temperature and strain rate effects is sparse. This has been the state-of-the-art since high strain rate testing has focused mostly at macro length scales.

One way to get around this problem is to perform high strain rate tests at small length scales, especially in the micro regime. A polycrystalline sample can be mapped for grain orientations using electron backscatter diffraction (EBSD) and localized mechanical tests can be performed as a function of temperature and strain rates on different grain orientations. The inherent advantage of this approach is its high throughput nature, obtaining sufficient statistics and avoid sample-to-sample variations. Due to the controlled nature of such tests, the repeatability of microscale tests is excellent as various sources of scatter like grain boundaries, grain size distribution, etc. are eliminated. This work will present application of such an approach using nanoindentation on polycrystalline metallic systems to study the interplay of grain orientation, temperature and strain rate to study the deformation mechanisms. Additionally, the work will also demonstrate reliable extraction of deformation activation parameters – activation volumes, apparent activation energies – to determine the rate controlling deformation mechanisms.

Nanoindentation is an instrumented indentation technique that measures the load and displacement with micronewton and nanometer resolution respectively. This versatile technique is used to study not only hardness and modulus, but it has been adapted for studying various mechanical properties like yield strength, strain rate sensitivity [1,2], stress relaxation [3], fracture, cycling fatigue behavior, etc. In combination with focus ion beam (FIB) milled microstructures, the same technique can be extended to perform micropillar compression and microcantilever bend tests. Its further extension to high temperatures upto 800°C [4] and high strain rates (up to 1000/s) is a relatively recent development and presents an interesting opportunity to undertake systematic studies as a function of crystal orientation.

This work will present the microscale high strain rate tests on two different metallic systems – microcrystalline Cu and nanocrystalline Ni. The rationale for material selection was to start with simple fcc metals, with well understood deformation mechanisms but with different microstructural length scales – Cu sample with grains sizes of ~ 100 µm and nanocrystalline Ni with grain sizes of 30nm. The orientation of the individual grains in Cu was mapped using EBSD and micropillars were fabricated in individual grains (with

---

[*] Corresponding author: gaurav.mohanty@tuni.fi, Materials Science and Environmental Engineering, Faculty of Engineering and Natural Sciences, Tampere University

varying orientations). The micropillars were FIB milled keeping the height-to-diameter aspect ratio of 3. The micropillar tests in Cu can be considered to be single crystal tests. On the contrary, each micropillar fabricated in nanocrystalline Ni comprised of more than 100,000 grains, resulting in a "bulk test". No size effects were observed in case of tests performed on nanocrystalline Ni and the engineering stress-strain curves corresponded well to bulk high strain rate data from literature. These tests comprised the validation of the high strain rate micropillar test methodology and data analysis protocols. The Cu micropillars were compressed over wide range of temperatures (25 - 500°C) and strain rates (1e-4/s to 1000/s) to study the interplay of temperature, strain rate and orientation. The emerging trends in this dataset with respect to yield, hardening rate, etc., will be discussed. Extracted activation parameters like activation volume and apparent activation energy for deformation will be discussed in the light of the operative deformation mechanisms in both the metallic systems. It is hoped that this study will pave the way for more such tests on different material systems and will advance our understanding of micro-plasticity at small length scales.

References

1. Mohanty G, Wheeler JM, Raghavan R, Wehrs J, Hasegawa M, Mischler S, et al. Elevated temperature, strain rate jump microcompression of nanocrystalline nickel. Philosophical Magazine 2015;95:1878-95.
2. Wehrs J, Mohanty G, Guillonneau G, Taylor AA, Maeder X, Frey D, et al. Comparison of In Situ Micromechanical Strain-Rate Sensitivity Measurement Techniques. JOM 2015;67:1684-93.
3. Mohanty G, Wehrs J, Boyce BL, Taylor A, Hasegawa M, Philippe L, et al. Room temperature stress relaxation in nanocrystalline Ni measured by micropillar compression and miniature tension. Journal of Materials Research 2016;31:1085-95.
4. T.E.J. Edwards, F. Di Gioacchino, G. Mohanty, J. Wehrs, J. Michler, W.J. Clegg, Acta Mater. 148 (2018) 202–215.

Micromechanical exploration of the combined effects of high strain rate and high temperature: A novel experimental technique

R. Ramachandramoorthy*, G. Mohanty, J. Schwiedrzik, D. Frey, J.-M. Breguet, J. Michler

Abstract. Smaller is stronger. A well-known statement used to explain the fact that when the size of sample is reduced to micro- and nano-levels, their physical properties are enhanced. Nevertheless, after half a decade of intense research, the mechanical properties of metals, ceramics and other materials, in general, at the micro- and nano-scale are only known at quasi-static strain rates[1] and nominal temperatures,[2] despite being used in applications under extreme conditions. Thus, there is a lack of mechanical and metrological capabilities for the assessment of deformation and failure of micro- and nano-scale materials at high strain rates and extreme temperatures. This also directly affects the society and business world, since even with extreme levels of miniaturization in electronics which are being used in modern gadgets, there is still a lack of research on the robustness of such miniaturized components under both time-dependent and impact-dependent (accidental drop, vibrations) conditions.

Specifically, silicon is a ubiquitous material with applications in a plethora of small scale electronics that use micro electromechanical systems (MEMS) based devices.[3] Till date, the only experimental data available on them in the micro and nano scale is at quasi-static strain rates upto 0.1/s.[4] On the other hand, there are several atomistic simulations that are able to identify the nanomechanical properties of silicon at very high strain rates at ~10^5/s or higher.[5] Unfortunately, these simulations cannot be validated due to the absence of experiments at such high strain rates. Thus, until now, a true one-to-one comparison between experiments and MD simulations has not been possible, thus motivating the development of experimental platforms that can close this gap in knowledge.[6]

Macroscale dynamic mechanical testing of materials as a function of strain rate above ~100/s is a well-established field, which traditionally uses specialized equipment such as Kolsky bars, split Hopkinson bars and plate impact testers for conducting the experiments. Unfortunately, as mentioned earlier, micromechanical testing has been limited to strain rates below ~0.1/s[7] and even fewer literature data is available for the combination of high strain rate and high temperature testing at this small scale. This limitation in strain rate is due to the fact that conducting micromechanical testing at such an extreme combination of strain rate and temperature requires a testing system capable of high speed actuation and precise displacement, and load sensing with microscale resolution, while simultaneously capable of heating the sample and the tip to high temperatures upto 800°C.[2] Also, in commercially available microscale testing systems, there are hardware limitations such as low resonance frequencies and low bandwidth data acquisition/control electronics that prevent testing at strain rates beyond 0.1/s. These are the main reasons behind the unknown mechanical properties of microscale materials at high strain rates.

This presentation will report, for the first time, a piezo-based experimental setup,[8] protocols and testing methodology for conducting high strain rate in situ micropillar (of gage length ~25um) compression testing inside a scanning electron microscope at rates up to ~400/s and at temperature ranges between room temperature and 800°C. This will also include the calibration protocols developed to protect the piezo actuators and sensors from damage due to thermal conduction and radiation. This will render the polarization

---

* Corresponding author: rajaprakash.ramachandramoorthy@empa.ch, Empa - Swiss Federal Laboratories for Materials Science and Technology

and consequently the piezo-constants to be immune to changes in sample temperature. The strain rate achieved in this study is an increase of approximately three orders of magnitude compared to the current state-of-the-art micromechanical testing. There are several benefits associated with microscale mechanical testing at these harsh loading conditions including higher stain rates due to smaller sample size, lower thermal drift, lower magnitude of inertial contributions and faster stress wave equilibration times.[9] So intrinsically, exploring the high strain rate mechanical properties at the microscale could potentially be more advantageous compared to their macroscale counterparts.

As a case study, single crystal silicon micropillars tested in situ at high strain rates up to ~400/s and temperatures of 600°C in a scanning electron microscope will be presented. The stress-strain response of silicon micropillars at strain rates across 6 orders of magnitude will be presented as a function of pillar size from 3.4µm to 8.6µm and a temperature range between room temperature and 600°C. At high temperatures, a ductile-to-brittle transition in failure mode can be seen in silicon micropillars as the strain rate is increased from quasi-static to 400/s. The current study will be compared against a previous study where identical silicon micropillars were tested as a function of temperature from room temperature to 500°C but at quasi-static strain rates. This comparison will be used to show that increasing the strain rate by one order of magnitude is equivalent to cooling down the silicon micropillars by ~70°C. Finally, there will be a discussion on the atomistic mechanisms behind the deformation behavior of silicon micropillars via the extracted parameters of strain rate sensitivity and activation volumes.

References

1. Ramachandramoorthy, R., et al., High strain rate tensile testing of silver nanowires: rate-dependent brittle-to-ductile transition. Nano letters, 2015. 16(1): p. 255-263.
2. Kang, W., M. Merrill, and J.M. Wheeler, In situ thermomechanical testing methods for micro/nano-scale materials. Nanoscale, 2017. 9(8): p. 2666-2688.
3. Zhang, D., et al., In situ tensile testing of individual Co nanowires inside a scanning electron microscope. Nanotechnology, 2009. 20(36): p. 365706.
4. Wheeler, J. and J. Michler, Elevated temperature, nano-mechanical testing in situ in the scanning electron microscope. Review of Scientific Instruments, 2013. 84(4): p. 045103.
5. Guénolé, J., J. Godet, and S. Brochard, Deformation of silicon nanowires studied by molecular dynamics simulations. Modelling and Simulation in Materials Science and Engineering, 2011. 19(7): p. 074003.
6. Ramachandramoorthy, R., et al., Design of piezoMEMS for high strain rate nanomechanical experiments. Extreme Mechanics Letters, 2018. 20: p. 14-20.
7. Jennings, A.T., J. Li, and J.R. Greer, Emergence of strain-rate sensitivity in Cu nanopillars: Transition from dislocation multiplication to dislocation nucleation. Acta Materialia, 2011. 59(14): p. 5627-5637.
8. Guillonneau, G., et al., Nanomechanical testing at high strain rates: New instrumentation for nanoindentation and microcompression. Materials & Design, 2018. 148: p. 39-48.
9. Jia, D. and K. Ramesh, A rigorous assessment of the benefits of miniaturization in the Kolsky bar system. Experimental Mechanics, 2004. 44(5): p. 445.

Fast X-ray imaging as a diagnostic tool for high temperature high strain rate loaded materials

A. Cohen[*], A. Yosef-Hai, D. Levi-Hevroni, M. Oblinado, A. Rack

Abstract. In the field of high strain rate plastic flow and failure investigation, fast imaging is a major tool for tracking and visualization of damage evolution. High speed imaging and Digital Image Correlation (DIC) are widely used to characterized the surface pattern motion of the sample. These tools are inherently limited to the surface behavior and to the surface image quality. In situ X-ray radiography can supplement surface measurements by probing into the bulk material and thus allow to investigate inner damage evolution.

Temperature is known as a significant factor influencing mechanical and damage behavior. We suggest using fast X-ray real time imaging as a diagnostic tool to study this influence in high-rate, high temperature experiments.

Based on our new SHPB system installed at the European Synchrotron Radiation Facility (ESRF), which was developed for dynamic X-ray imaging, we aim at adding a temperature control system. We plan to incorporate it into our future ESRF beam time proposal. This new Split Hopkinson Pressure Bar (SHPB), equipped with traditional strain gages diagnostic, is situated at beamline ID19 – ESRF Grenoble, to facilitate real time X-ray radiography imaging. Its high spatial and temporal resolution enables deep damage and failure development tracking. Careful synchronization of all signals enables good matching between traditional stress-strain measurements and radiography. The flexible system design allows a wide range of experiments such as conventional compression tests with 1/2"" steel or aluminium bars or 1/4"" steel bars and direct impact for higher strain rate experiments.

We will present some of our recent experiments results at the ESRF to demonstrate the capabilities of the system: shear failure of Ti-6Al-4V (AM vs. conventional material), concrete failure under compression, and Al2O3 cracking*.

Expected benefit of phase contrast used in the X-ray radiography when compared to surface imaging is high spatial resolution that is less affected by the sample temperature. The high temporal resolution is expected not to be affected by the sample temperature at all.

*part of these experiments were carried out under European Synchrotron Radiation Facility granted beam time in the frame of long-term proposal MI1252.

---

[*] Corresponding author: Cohen.amitay@gmail.com, Department of Physics, NRCN, Israel

On the impact behavior of aluminum alloy AA7020-T6

C. C. Roth [*], T. Fras and D. Mohr

Abstract. High strength 7xxx series aluminum alloys are being increasingly considered in high performance structures due to their superior specific strength compared to 6xxx series alloys. The present focuses on the impact behavior of an AA7020-T6. Ductile fracture experiments ranging from shear to biaxial stress states are carried out on 1mm thick sheet samples at low (0.001/s), intermediate (1/s) and high (> 1000/s) as well as temperatures ranging from room temperature to more than 180°C. Both optical and infrared high speed measurements are used to observe the specimens during the test. While the material exposes a negligible (partially negative) strain rate sensitivity at room temperature, a strong positive strain rate hardening is observed at elevated temperatures. The material microstructure is analyzed using electron-backscatter diffraction (EBSD) pre and post mortem for shear and biaxial stress states. The results from the comprehensive experimental program are used to calibrate a strain rate and temperature dependent plasticity and fracture model. Impact experiments with differently shaped MARS300 impactors are performed on 4mm thick AA7020-T6 plates and different fracture mechanism are observed. Numerical simulations of the impact event using the aforementioned modelling approach are preformed and compared to the experimental results.

---

[*] Corresponding author: ccroth@ethz.ch , Department of Mechanical and Process Engineering, ETH Zurich

Fracture of Dual Phase Steel under Extreme Loading Conditions: Experiments and Simulations

X. Li [*], C. C. Roth, D. Mohr

Abstract. There has been an ongoing quest to determine the strain to fracture for sheet metals for a wide range of stress states, strain rates and temperatures. Good results have been obtained for slow, intermediate and high strain rate conditions, while a high degree of uncertainty remains at high temperatures. In the present work, a recently developed induction heating system is used to examine the material response of a dual phase steel DP780. Temperature experiments ranging from 25°to 1000°C at different strain rates in an attempt to shed some light on the material response under these conditions. Low (0.001/s) and intermediate (~1/s) strain rate experiments are performed on a hydraulic universal testing machine, while high strain rate tests (~1000/s) are carried out on a modified split Hopkinson pressure bar system. Planar digital image correlation as well as (high speed) infrared imaging is used to access the surface strain and temperature fields. A (counterintuitive) non-monotonic temperature response is identified that cannot be captured by classic modelling approaches such as Johnson-Cook. A visco-plastic rate and temperature dependent plasticity model based on a recently developed machine learning approach with combined Swift-Voce strain hardening is calibrated based on the response of the tested materials. The loading histories of the simulations are extracted, identifying the ductility as a function of stress state, strain rate and temperature.

---

[*] Corresponding author: lixue@ethz.ch , ETH Zurich

DYMAT2019 A09

Thermomechanical behavior of UHMWPE during Cold-spray process

C. Bernard[*], K. Ravi, K. Ogawa, O. Lame, J.-Y. Cavaillé

Abstract. During the last decades, additive manufacturing processes gain of lost of interest from the material sciences and engineering communities thanks to their abilities to use native powder, reduce the material consumption, elaborate complex geometry at low cost... Among them, the interest in Cold-Spray (CS) process comes from that the particles are not melted and remain in a solid-state throughout the whole process. It is commonly used to repair structures and perform coating using materials which are difficult to manufacture otherwise. Cold-spray process consists in the high velocity impact of micrometric particles which are accelerated through a De-Laval nozzle using a pressurized heated gas. Because of the impact, the particle will deform plastically and adhere onto the substrate to obtain a coating. During the process and under the gas effect, the particles heat-up (but remain below their melting temperature) leading to a thermal gradient inside the particle [1]. Moreover, due to the high-velocity impact of the particle onto the substrate, between 100 and 400 $m.s^{-1}$, the particles undergo important self-heating. The process was initially developed for metallic materials but was recently extended to polymers [2], especially ultra-high molecular weight polyethylene (UHMWPE). However, the obtained coating exhibits a rather porous microstructure reducing the excellent wear and impact properties of UHMWPE. It is due to the important viscoelastic behavior of the polymer below its melting temperature.

To improve the process, better understanding of the particle deformation mechanisms is needed. During the polymer plastic deformation, important evolution of the microstructure is observed. In absence of loadings, the polymer microstructure consists in regular stacking of crystalline lamellae and confined amorphous phase. Because the important molecular weight of UHMWPE, the very long macromolecular chains can belong to both crystalline lamellae structure and amorphous confined phase. During the material deformation, fragmentation and fibrillation of the crystalline lamellae and elongation and recrystallization of the amorphous chains are observed leading to a reorganization of the microstructure [3]. Thus, the different crystalline blocks size acts as entanglement nodes within the amorphous microstructure delaying the flow of the polymer. To predict such behavior, the numerical model should take into account the evolution of microstructure from crystalline structure to fibrillar one during the plastic deformation of the material. To predict the thermomechanical behavior of UHMWPE in order to improve the UHMWPE coating formation during CS, Bernard et al. [4] recently developed a three-dimensional numerical model able to report the evolution of microstructure observed during the plastic deformation of the polymer. The model is based on (i) a repartition of strain according to the crystalline ratio φ

$$F=F_a^{(1-\varphi)}\,F_c^{\varphi} \tag{1}$$

where F is the deformation gradient and the subscript 'a' and 'c' represent respectively the confined amorphous phase and the crystalline lamellae, and (ii) an evolving mechanical coupling between the crystalline lamellae and the amorphous confined phase

---

[*] Corresponding author: chrystelle.bernard@rift.mech.tohoku.ac.jp , Frontier Research Institute for Interdisciplinary Sciences

$$F_c=(F_f)^{\zeta} \tag{2}$$

where the parameter ζ representing the mechanical coupling evolves during the plastic deformation of the crystalline lamellae.

Predicting results in agreement with the uniaxial compressive loadings at different strain rates and temperatures, this three-dimensional numerical model has been implemented in the finite element software ABAQUS/Explicit to simulate high velocity of the particle onto the substrate. The approach used to simulate the cold-spray process consists in a three-step approach: (i) influence of the gas temperature and pressure on the polymer particle thermal and velocity history is investigated, (ii) according to the evolution of the gas temperature [2], the temperature gradient inside the particle is simulated, (iii) according to steps (i) and (ii), high-velocity impact of the polymeric particle onto the substrate is performed.

First results of the particle thermal gradient during cold-spray highlighted a difference of around 15°C between the particle core and its surface for 60 µm diameter particle. In the other hand, high-velocity impact simulations, at 150 $m.s^{-1}$ and 500 $m.s^{-1}$, of polymeric particle at room temperature (homogeneous temperature of the particle) shows important local plastic deformation (around 100% in less than 1 ms). It results of an important self-heating of the particle because of the impact.

References

1. Bernard et al., Influence of the gas pressure and gas temperature of the in-flight polymer particle history during Cold-Spray: Effect of non-continuous nozzle, on going
2. Ravi et al., Development of ultra-high molecular weight polyethylene (UHMWPE) coating by cold spray technique, Journal of Thermal Spray Technology 24(6), 2015
3. J. Defebvin et al., In situ SAXS/WAXS investigation of the structural evolution of poly (vinylidene fluoride) upon uniaxial stretching, Polymer 84, 2016.
4. Bernard et al., From rheological to original three-dimensional mechanical modelling of semi-crystalline polymers: application to a wide strain rate range and large deformation of Ultra-High Molecular Weight semi-crystalline polymers, Submitted to International Journal of Plasticity, January 2019.

---

[*] Corresponding author: chrystelle.bernard@rift.mech.tohoku.ac.jp , Frontier Research Institute for Interdisciplinary Sciences

Microstructure prediction in high strain-rate deformation of Al6063-O using artificial neural network and finite element analysis

C. Montenegro*, J. Osorio, J. Casas, S. Abolghasem

Abstract. The final microstructure of materials under interactive effects of critical elements of deformation: strain, strain-rate, and temperature, often follows complex trajectories. Capturing the existing process–structure linkages is fundamental for controlling product outcomes, yet it calls for establishing the constitutive relationships that describe material behavior. In this paper, backpropagation Artificial Neural Network (ANN) is proposed for microstructure prediction in different deformation ranges. Quasi-static universal testing apparatus, Drop Weight Impact Tester (DWIT), and Split Hopkinson Pressure Bar test (SHPB) are performed to study the microstructure response (grain size) in low strain and high strain-rate regimes at elevated temperature. Next, Plane Strain Machining (PSM) is performed to probe the resulting microstructure (subgrain size) for the high strain, high strain-rate and the accompanied temperature rise conditions. Two ANNs are established to predict microstructure responses, grain and subgrain sizes, in low and high strain regimes, respectively. Additionally, the results obtained from the low strain regime are used to calculate the Johnson-Cook (J-C) material constants which are incorporated in the finite element (FE) simulation along with the ANN, to obtain microstructure response (subgrain size) for PSM. The performance of the ANNs and the FEM are evaluated using statistical indices. The comparative assessment of the model's outcomes indicates close agreements with the experimental results in both low- and high-level deformations. The accurate predictions from PSM conditions can potentially be applicable for microstructural prediction of the machined surface.

---

* Corresponding author: ca.montenegro11@uniandes.edu.co, Universidad de los Andes

Thermal softening and rate sensitivity of bcc metals: experiments and mechanism-based modeling

K. T. Ramesh *

Abstract. The temperature-dependent rate sensitivity of metals is obviously related to dislocation motion within the metal, and there have been a variety of experimental and theoretical works that have examined this behavior. The vast majority of these works have examined face-centered-cubic (fcc) metals, but a significant number of efforts have also considered body-centered-cubic (bcc) metals over the last three decades. This paper examines the available data on several bcc metals (including vanadium, tungsten and tantalum) at high rates and high temperatures, and presents high strain rate experiments conducted in the compression Kolsky bar, the torsional Kolsky bar, and using the high strain rate pressure-shear plate impact technique.

We then present a mechanism-based approach to developing a general constitutive model for such metals with the specific intent of accurately capturing the response at high strain rates and low homologous temperatures. The model is based on an approximation of the traditional kink nucleation mechanism for the motion of screw dislocations. The predictions of the model are compared with the results of a variety of experimental measurements on several bcc metals. The model is able to describe high strain rate experimental data for a number of bcc metals using this single mechanism. A form of the model amenable to application using available experimental information is presented. The model is able to effectively describe high-rate response up to homologous temperatures of the order of 0.3. We note that several challenges remain for modeling even such simple cubic systems, primarily because of a lack of experimental data in well-characterized metals at high strain rates and high temperatures.

---

* Corresponding author: ramesh@jhu.edu, The Johns Hopkins University

High-Speed Infrared investigations of local heating in a Graphite-Fiber-PDMS Composite material Under dynamic loading

S. Boubanga-Tombet*, S. Ravindran, A. Kidane, F. Marcotte

Abstract. Infrared full field temperature measurement techniques have been used as a non-contact and real-time method for measuring the temperature evolution during inelastic deformation of materials [1-3]. Jordan and Sandor, for example, have used a differential temperature measurement for monitoring the elastic-plastic behavior of metals in 1978 [4]. Following recent developments in thermographic techniques [5], quantitative stress measurements became possible by measuring the change in infrared photon emission produced by mechanical deformation.

Experimental temperature measurement is essential to understand the physics of many mechanic’s problems. For example, the physics of accidental explosions of polymer bonded explosives are not very well understood. However, it is believed that the highly localized temperature regions called hot spots are the causes of such material behavior. However, the understanding of its formation and the dynamics of hotspot evolution are very limited. This requires high spatial resolution and high temporal resolution temperature measurements. Latest high-speed IR cameras provide high temporal and spatial resolution, which helps in understanding the challenging problems.

In the present work, we used the Telops FAST M3k combined with a microscope lens to investigate potential hot-spot formation in polymer bonded explosives. Split Hopkinson pressure bar was used to load the sample at higher strain rate. The Telops FAST M3k was used with sub-portions of 64 × 64 and 128 × 40 pixels at frame rates of 20 KHz and 19 KHz respectively. A microscopic lens with 1x magnification, designed by Telops, was used for the experiments, leading to a spatial resolution of the order of the pixel pitch (30 μm). The striker bar of the Split-Hopkinson bar set-up was fired from a gas gun at a pressure of 5 psi. The samples in this experiment were made of graphite cylindrical rods embedded in a polydimethylsiloxane (PDMS).. The sample dimensions are measured to be about 8 mm × 8 mm × 8 mm. The graphite rods were about 500 μm in diameter, aligned parallel to the PDMS cube edges or at a 45° angle. All samples were treated with a black coat layer before the test to minimize the temperature variations induced by emissivity difference between graphite and epoxy. For our experiments, we selected a camera field of view covering only the region of the sample containing the fibers inclusions.

Figure 1 depicts the experimental results for the PDMS sample with an inclusion of three graphite rod aligned parallel to the loading direction. A sub-portion of the FPA detector of 64 × 64-pixel with a frame rate of 20 KHz was used for the test. Selected infrared images recorded before and after the stress wave enters the sample are shown. The deformation of the sample due to the stress wave loading induced temperature increase is therefore shown in Fig.1. The images recorded before were used as a reference for image subtraction. Subtracting the reference image from the subsequent images gives the net temperature increase in the sample.

When the sample is deforming due to the stress wave, the temperature plot shows a negligible temperature increase in the binder. Net temperature increase in the binder away from the inclusion is than 2 OC. Interestingly, significantly higher temperature was observed near the inclusions indicating the rigid inclusions have significant effect on the temperature evolution in composites. Figure shows the dynamics of the inclusions in the

---

* Corresponding author: stephane.boubanga@telops.com, Telops INc

binder. Such movement of the crystal causes significant relative movement of inclusions and the binder which could cause high friction between the binder and inclusion. The temperature near the inclusion is nearly 22 times the temperature in the regions away from the binder. However, further investigation is required to confirm the deformation mechanism that causes the temperature rise.

References

1. REIFSNIDER, K.L. and WILLIAMS, R.S., “Determination of Fatigue related Heat Emission in Composite Materials”, Experimental Mechanics, 14(12), 479-485, 1974.
2. MARCUS, L.A. and STINCHCOMB, W., “Measurement of Fatigue Damage in Composite Materials”, EXPERIMENTAL MECHANICS, 15(2), 55-60, 1975.
3. CHARLES, J.A., APPL, F.J. and FRANCIS, I.E., “Using the Scanning Infrared Camera in Experimental Fatigue Studies”, EXPERIMENTAL MECHANICS, 15(4), 133-138, 1975.
4. JORDAN, E.H. and SANDOR, B.I., “Stress Analysis from Temperature Data”, J. Test. and Eval., 6(6), 325-331, 1978.
5. MOUNTAIN, D.S. and WEBBER, J.M.B., “Stress Pattern Analysis by Thermal Emission (SPATE)”, Proc. Sac. Photo-Opt. Inst. Engrs., 164, 189-196, 1978.